

# **Optimization of 100 Gb/s Short Range Wireless Transceivers under Processing Energy Constraints**

Von der Fakultät für Elektrotechnik und Informationstechnik  
der Rheinisch–Westfälischen Technischen Hochschule Aachen  
zur Erlangung des akademischen Grades  
einer Doktorin der Ingenieurwissenschaften  
genehmigte Dissertation

vorgelegt von  
M.Sc. Gaojian Wang  
aus Liaocheng, China

Berichter: Universitätsprofessor Dr.-Ing. Gerd Ascheid  
Universitätsprofessor Dr. sc. techn. Renato Negra

Tag der mündlichen Prüfung: 12.11.2021

Diese Dissertation ist auf den Internetseiten  
der Universitätsbibliothek online verfügbar.



# Abstract

---

The current development of smart electronic devices (e.g., smartphones and tablets) and multimedia applications leads to tremendous data traffic growth, which is an enormous challenge for future wireless communication systems due to the spectrum scarcity. In such a context, the 60 GHz band, due to the several GHz of unlicensed bandwidth worldwide, is a promising option to serve the ever-increasing demands of local and personal area networks for higher data rates and higher spatial reuse. This dissertation's subject is the scientific investigation of new concepts for short-range radio transceivers that work with carrier frequencies of 60 GHz and bandwidth between 1 and 10 GHz.

For a given amount of processing energy per information bit, the overall power consumption increases with the data rate. When targeting data rates beyond 100 Gb/s, the system's overall power consumption soon exceeds the power which can be dissipated without forced cooling. In order to achieve a maximum data rate under this power constraint, the processing energy per information bit must be minimized. Therefore, in this dissertation, a novel processing efficient transmission scheme, i.e., using joint analog/digital signal processing architectures, is proposed. As a prerequisite, the wireless channel characteristics at 60 GHz are well studied, and the implementation of a 60 GHz channel model for system simulations is done. The major baseband signal processing tasks such as beamforming/MIMO techniques, channel estimation, equalization, matched filtering (pulse shaping at the transmitter) are investigated. Each of the transceiver tasks is studied both concerning the high-level power consumption and the communication performance impact. Except that, the low complexity algorithms with acceptable performance loss are investigated to guarantee the strict power limit.

The overall methodology is energy-driven. For instance, all design decisions like transmission scheme selection, analog/digital partitioning, and algorithms optimization, are driven by energy efficiency. There is a strong relationship between energy efficiency and communication performance. Thus, power estimation is performed for the components identified to be suitable for a system that meets the overall throughput, communication performance, and power constraints. This applies to components in both the analog as well as the digital part. Besides, an analysis of the relation

between energy and spectrum efficiency is also performed to guide the practical energy/spectrum efficiency trade-off for the millimeter-wave system design.

Finally, as proof of concept for the methodology and because of its high relevance, the proposed approach is applied towards systems operating beyond the 100 GHz carrier frequency range. The impact of an extension to 120 GHz carrier frequency ranges and an extension from the point-to-point MIMO transmission to multi-user case are addressed. In this dissertation, all novel designs and analytical evaluations in system design aspects are validated via simulations. The results demonstrate the performance advantage of millimeter-wave systems, which positions 60GHz technology as a critical component in the forefront of Gbps wireless communications.

# Kurzfassung

---

Die derzeitige Entwicklung intelligenter elektronischer Geräte (z.B. Smartphones und Tablets) und Multimedia Anwendungen führt zu einem enormen Wachstum des Datenverkehrs, was aufgrund der Knappheit des Spektrums eine enorme Herausforderung für zukünftige drahtlose Kommunikationssysteme darstellt. In einem solchen Kontext ist das 60 GHz Band eine vielversprechende Option, um die ständig steigenden Anforderungen lokaler und persönlicher Netzwerke nach höheren Datenraten und höherer räumlicher Wiederverwendung aufgrund der weltweit nicht lizenzierten Bandbreite von mehreren GHz gerecht zu werden. Der Gegenstand dieser Dissertation ist die wissenschaftliche Untersuchung neuer Konzepte für Nahbereichs-Funktransceivers, die mit Trägerfrequenzen von 60 GHz und einer Bandbreite zwischen 1 und 10 GHz arbeiten.

Bei einer bestimmten Menge an Verarbeitungsenergie pro Informationsbit steigt der Leistungsverbrauch mit der Datenrate. Wenn Datenraten über 100 Gbit/s angestrebt werden, übersteigt der Gesamtleistungsverbrauch des Systems bald die Leistung, die ohne erzwungene Kühlung verbraucht werden kann. Um unter dieser Leistungsbeschränkung eine maximale Datenrate zu erreichen, muss die Verarbeitungsenergie pro Informationsbit minimiert werden. Daher wird in dieser Dissertation ein neues verarbeitungseffizientes Übertragungsschema vorgeschlagen, das auf gemeinsame analogen/digitalen Signalverarbeitungsarchitekturen benutzt. Die Voraussetzung ist, dass die Eigenschaften des Funkkanals bei 60 GHz gut untersucht sind und die Implementierung eines 60 GHz Kanalmodells für Systemsimulationen erfolgt. Die Hauptaufgaben der Basisbandsignalverarbeitung wie Strahlformungs/MIMO Techniken, Kanalschätzung, Entzerrung und angepasste Filterung (Impulsformung am Sender) werden untersucht. Jede der Transceiver Aufgaben wird sowohl hinsichtlich des hohen Stromverbrauchs als auch der Auswirkungen auf die Kommunikationsleistung untersucht. Abgesehen davon werden die Algorithmen mit geringer Komplexität und akzeptablem Leistungsverlust untersucht, um die strenge Leistungsgrenze zu gewährleisten.

Die Gesamtmethode ist energiegetrieben. Zum Beispiel, alle Entwurfsentscheidungen wie Auswahl des Übertragungsschemas, analoge/digitale Partitionierung und Optimierung von Algorithmen, hängen von der Energieeffizienz ab. Es besteht ein

enger Zusammenhang zwischen Energieeffizienz und Kommunikationsleistung. Die Leistungsschätzung wird für die Komponenten durchgeführt, die als für ein System geeignet identifiziert wurden, das den Gesamtdurchsatz, die Kommunikationsleistung und die Leistungsbeschränkungen erfüllt. Dies gilt sowohl für Komponenten im analogen als auch im digitalen Teil. Darüber hinaus wird eine Analyse der Beziehung zwischen Energie und Spektrumseffizienz durchgeführt, um den praktischen Kompromiss zwischen Energie und Spektrumseffizienz für das Design von Millimeterwellensystemen zu bestimmen.

Schließlich wird der vorgeschlagene Ansatz als Proof of Concept für die Methodik und aufgrund seiner hohen Relevanz auf Systeme angewendet, die außerhalb des 100 GHz Trägerfrequenzbereichs arbeiten. Die Auswirkungen einer Erweiterung auf 120 GHz Trägerfrequenzbereiche und einer Erweiterung von der Punkt zu Punkt MIMO Übertragung auf den Mehrbenutzerfall werden angesprochen. In dieser Dissertation werden alle neuartigen Designs und analytischen Bewertungen in Bezug auf Systemdesignaspekte durch Simulationen validiert. Die Ergebnisse zeigen den Leistungsvorteil von Millimeterwellensystemen, die die 60 GHz Technologie als kritische Komponente an der Spitze der drahtlosen Gbit/s Kommunikation positionieren.

# Acknowledgements

---

This dissertation is the result of my work as a research assistant at the Institute for Integrated Signal Processing Systems (ISS) at RWTH Aachen University. During my time at ISS, I have been so pleased and fortunate to work with many brilliant people and obtained involvement and generous support from them. At this point, I would like to express my great appreciation to all of you.

Firstly, I wish to express my deep gratitude to my doctoral supervisor, Professor Gerd Ascheid, for his support over the years regarding scientific research and personal life. I am very grateful for his patient guidance, enthusiastic encouragements, and many inspiring discussions during my research in the project LP100. All these helped me to develop ideas and passion for doing research. I particularly appreciate that he has provided me opportunities to participate in exciting scientific and industrial projects, attend various international conferences, and practice my teaching skills.

Furthermore, I would like to thank all my colleagues at ISS, especially, Dan Zhang, Adrian Ispas, Xitao Gong, Professor Guido Dartmann, Aamir Ishaque, Huijun Li, Kaifeng Guo, Daniel Günther, Stephan Schlupkothen, Sebastian Birke, Zekai Liang for many fruitful and countless inspiring discussions and also for their openness in sharing their knowledge. A special appreciation goes to Sebastian Birke for his motivating suggestions and brainstorming on our research topics during the LP100 project. I would also like to extend my thanks to staff members of ISS, Elisabeth Böttcher, Christoph Vogt, Michael Rieb, Gabi Reimann, and Christoph Zörkner, for providing a pleasant working environment. Many thanks go to my students, Dara Khajavi, Shaghayegh Aghabozorgi Naeimi, Jiaxin Sun, Jiaping Jing, Na Cui, and Jingyu Su, for their significant contributions to this dissertation.

Last but not least, I want to thank my parents, husband, and my little boy, Haoyu. Without their patience and faith in me, this work would not have been completed. During the dissertation writing at home, thank my little boy for his lovely 'accompany' and all those pleasant moments and thank my husband for his constant and great patience to my late ending of work and the little boy.

Gaojian Wang, on November 25, 2021





# Contents

---

<b>1</b>	<b>Introduction</b>	<b>1</b>
1.1	Project LP100 . . . . .	2
1.2	Research Objectives . . . . .	2
1.2.1	Channel Modeling . . . . .	3
1.2.2	Transmission Schemes . . . . .	4
1.2.3	Power Estimation . . . . .	5
1.3	Outline . . . . .	5
1.4	Notation . . . . .	7
<b>2</b>	<b>Preliminaries</b>	<b>9</b>
2.1	State of the Art of Relevant Research Topics . . . . .	9
2.2	60 GHz Wireless Standards . . . . .	12
2.3	60 GHz Radio Channel Modeling . . . . .	14
2.3.1	Scenarios . . . . .	14
2.3.2	Large Scale Channel Characterization . . . . .	15
2.3.3	Small Scale Channel Characterization . . . . .	16
2.4	Summary . . . . .	20
<b>3</b>	<b>Transmission Schemes: Hybrid Beamforming Approach</b>	<b>21</b>
3.1	Hybrid Beamforming with Time Delay Compensation . . . . .	22
3.1.1	Propagation Scenario . . . . .	23
3.1.2	Capacity of Time-Delay Compensation based MIMO System . . . . .	25
3.1.3	Performance Evaluation . . . . .	28
3.2	Best Possible Beam Separation Algorithm . . . . .	32
3.2.1	System Model . . . . .	32

3.2.2	Best Possible Beam Separation Algorithm Design . . . . .	36
3.2.3	Performance Evaluation . . . . .	40
3.3	Summary . . . . .	43
<b>4</b>	<b>Performance Analysis on Hybrid Beamforming Approach</b>	<b>45</b>
4.1	Joint Pre-/Post-Processing Design . . . . .	46
4.1.1	Fully-connected Structure . . . . .	46
4.1.2	Array-of-subarray Structure . . . . .	55
4.1.3	Performance Evaluation . . . . .	61
4.2	Channel Estimation Based on DFT for Short Range Communication . .	67
4.2.1	System Model . . . . .	68
4.2.2	Formulation of the mmWave Channel Recovery Problem . . . . .	70
4.2.3	Adaptive Estimation Algorithm for a Sparse mmWave Channel .	75
4.2.4	Performance Evaluation . . . . .	78
4.3	Low Complexity Equalization Algorithms . . . . .	80
4.3.1	60 GHz Wideband MIMO Fading Channel . . . . .	82
4.3.2	Problem Statement . . . . .	83
4.3.3	Time-Delay Compensation based Time Domain Equalizer . . . . .	85
4.3.4	Phase-Shift Compensation based Frequency Domain Equalizer .	87
4.3.5	Performance Evaluation . . . . .	89
4.4	Summary . . . . .	92
<b>5</b>	<b>Power Efficiency Analysis of Millimeter Wave Transmission Systems</b>	<b>95</b>
5.1	Introduction . . . . .	95
5.2	Spectrum Efficiency . . . . .	96
5.3	Power Consumption Model . . . . .	99
5.4	Energy Efficiency . . . . .	101
5.4.1	The Energy Efficiency Optimization Algorithm . . . . .	101
5.5	Performance Evaluation . . . . .	104
5.5.1	Parameters in Power Consumption Model . . . . .	104
5.5.2	Impact of Increase in Antennas . . . . .	106
5.5.3	Influence of SIR Threshold in EE and SE . . . . .	107
5.6	Summary . . . . .	108

<b>6</b>	<b>Energy-Efficient Design of Multi-user Millimeter Wave and sub-THz System</b>	<b>111</b>
6.1	Introduction to Terahertz Band . . . . .	111
6.2	Channel Model and System Model . . . . .	113
6.2.1	Channel Model at 120 GHz . . . . .	113
6.2.2	System Model . . . . .	116
6.2.3	Nanonetwork Architecture . . . . .	118
6.3	Hybrid Beamforming Design . . . . .	120
6.3.1	System Configuration . . . . .	120
6.3.2	Problem Formulation . . . . .	122
6.3.3	Optimization Algorithms with Perfect CSI . . . . .	122
6.3.4	Optimization Algorithm without CSI . . . . .	130
6.4	Performance Evaluation . . . . .	132
6.4.1	Performance and Complexity Comparison . . . . .	133
6.4.2	Performance Analysis . . . . .	135
6.5	Summary . . . . .	139
<b>7</b>	<b>Conclusion and Outlook</b>	<b>141</b>
7.1	Summary and Contributions . . . . .	141
7.2	Outlook . . . . .	144
	<b>Appendix</b>	<b>145</b>
	<b>Glossary</b>	<b>145</b>
	<b>Bibliography</b>	<b>147</b>
	<b>Publication List</b>	<b>157</b>
	<b>Curriculum Vitae</b>	<b>159</b>



## Chapter 1

# Introduction

---

The current development of smart electronic devices (e.g., smartphones and tablets) and multimedia applications leads to tremendous data traffic growth, which is an enormous challenge for future wireless communication systems due to the spectrum scarcity. The 60 GHz band is a promising option to serve the ever-increasing demands of local and personal area networks for higher data rates and higher spatial reuse [58]. When considering commercial mobile devices, the forced cooling of integrated circuits is out of scope. This limits the power consumption for signal processing to a few Watts. Assuming, e.g., a 1 W limit, a simple calculation shows that for an information rate of 100 Gb/s, this results in a limit of 10 pJ of processing energy for one information bit ( $1 \text{ W} / 100 \text{ Gb/s}$ ). Thus, energy-efficient processing is critical for achieving data rates beyond 100 Gb/s. When optimizing the communication system architecture for maximum achievable data rates under a processing energy constraint, different architectures result. Due to the different propagation conditions of millimeter-wave (mmWave), multiple-input multiple-output (MIMO) processing in mmWave systems differs significantly from the ones for lower frequencies (below 10 GHz). At mmWaves, the channel is, for instance, sparse in the angular domain [76,96].

The focus of our research is on communication system architectures for data rates of 100 Gb/s and beyond under a processing energy constraint. As a scenario, short-range wireless transmitters working at carrier frequencies around 60 GHz and bandwidths between 1 GHz and 10 GHz are assumed. One of the critical challenges is the partitioning into analog and digital signal processing tasks, particularly since analog to digital converter (ADC) and digital to analog converter (DAC) typically are power-hungry operations for high data rates. The partitioning must be capable of supporting the required throughput and, at the same time, fulfill the overall energy constraints.

Target is the design of innovative high-frequency architectures, mixed-signal architectures, and digital signal processing architectures to support a very high energy, bandwidth, and implementation efficiency. To achieve these goals, several aspects are considered in this work, including higher-order modulation, multiple antenna systems, digitally adjusted and switched analog signal processing, compensation of the impact of hardware imperfection on the signals as energy-efficient implementations. Key issues for all concepts are the ability to achieve the highest data rates and to study their impact on the overall energy consumption.

It is well known that larger bandwidth and higher power efficiency require more elaborate signal processing and, thus, higher processing energy per information bit. This motivates our approach to consider implementation efficiency already in the communication system design. Achieving data rates beyond 100 Gb/s requires a

design of space exploration considering jointly wireless communication performance and implementation efficiency. Based on this, suitable high-frequency transmission schemes together with energy-efficient architectures and their implementations are investigated in a true cross-layer approach.

## 1.1 Project LP100

The project LP100<sup>1</sup> was conducted by the institute for communication technologies and embedded systems (ICE) and the institute for high frequency electronics (HFE) of RWTH Aachen university together with the institute for microelectronic systems design (EMS) of TU Kaiserslautern. This work was funded by the German Research Foundation (Deutsche Forschungsgemeinschaft, DFG<sup>2</sup>). The project's focus is the investigation of near field wireless transmitters working on a carrier frequency of 60 GHz and bandwidth between 1 GHz and 10 GHz. For a given energy per information bit, the overall energy consumption increases with the data rate. When targeting data rates in the region of 100 Gb/s, the overall system's power consumption has a severe problem. Therefore, transceivers should be optimized to achieve a maximum data rate under a strict overall energy constraint, which implies that the transmit energy, as well as processing energy, is limited for a given data rate.

In this project, there are close interrelations between the requirements on high frequency, mixed-signal, and digital sides from a communications and implementation point of view. To achieve the ambitious project goals, the intensive interdisciplinary collaboration of researchers from the different fields is essential. **The research for this thesis was carried out as part of the LP100 project.** Throughout the whole project LP100, the algorithm-hardware co-design approach is adopted. This thesis addresses the ultra-high throughput wireless communication system under constrained processing power only at the algorithmic level. Various techniques were applied, e.g., performance vs. complexity trades-off, transmission schemes to reduce hardware cost, designs to relax power amplifier requirements, and exploitation of unique channel characteristics occurring in systems. An important technology required for the design of space exploration is a high-level power estimation, which is, therefore, studied as well.

## 1.2 Research Objectives

As already introduced, the objective of our research is on wireless communication systems design for data rates of 100 Gb/s and beyond under a processing energy

<sup>1</sup> LP100 - "Optimization of 100 Gb/s near field wireless transmitters under consideration of power limits" as part of SPP 1655/0 - Wireless ultra-high data rate communication for mobile internet access "Wireless 100 Gb/s and beyond".

More detailed information and project-related publications about the LP100 project can be found on the website: <https://www.wireless100gb.de/index.html>.

<sup>2</sup> Duration: 1st June 2013 until 30th September 2019

constraint. The overall power consumption increases with the data rate for a given amount of processing energy per information bit. When targeting data rates beyond 100 Gb/s, the system's overall power consumption soon exceeds the power which can be dissipated without forced cooling. To achieve a maximum data rate under this power constraint, we must minimize the processing energy per information bit. Therefore, transceivers should be optimized to achieve a maximum data rate under a strict overall energy constraint, which implies that the transmit energy and processing energy are limited for a given data rate.

The main challenges are the investigation of methods to reach data rates of 100 Gb/s and the partitioning into analog and digital signal processing tasks. In this dissertation, we mainly address the following questions:

- How to make the choice of the scenario (e.g., the carrier frequency around 60 GHz) and why? What are the characteristics of the wireless channel at such carrier frequency? Because it lays the foundation for the investigations in the following research scopes (e.g., to study the transceiver methods and algorithms).
- What is the processing energy optimized system architecture at 60 GHz? How to develop suitable transmit and receive strategies (e.g., beamforming/MIMO, beam steering)?
- How can the information bit rate be maximized under a given processing power constraint? How to trade-offs between analog and digital processing, as well as trade-offs between power and bandwidth efficiency?

The exploration of these questions and the corresponding research items are explained explicitly in the following. In this dissertation, the information bit rate (to be maximized) is the most important metric of the system communication performance. Here, the information bit rate of a digital communication channel is the channel capacity, also known as the Shannon capacity, which is a theoretical upper bound for the maximum net bitrate in bits/s/Hz.

### 1.2.1 Channel Modeling

The best trade-off between the carrier frequency choice and the available bandwidth is accomplished with a carrier frequency of around 60 GHz. Several GHz of unlicensed bandwidth is available worldwide, e.g., 57~66 GHz are available in Europe. The main downside is the severe signal attenuation and penetration loss at 60 GHz. Therefore, one objective is to evaluate and counter the adverse effects of propagation and channel at millimeter-wave (mmWave) frequencies. Thus, we consider a carrier frequency of 60 GHz for an indoor environment, with the perspective to go up to 120 GHz, and aim to identify a suitable trade-off between high throughput and high energy/power efficiency. In this work, target use cases are initially short-range wireless transmitters working at carrier frequencies around 60 GHz and bandwidths between 1 GHz and 10 GHz.

In order to identify a suitable transmission scheme that allows achieving a throughput of more than 100 Gb/s within the given energy budget, the characteristics of the wireless channel at 60 GHz have to be well studied, and the implementation of a 60 GHz channel model for system simulations has to be done. Since many groups already work on sounding and characterizing the 60 GHz channel, our work's focus is on the derivation of suitable channel models based on published work. A corresponding software model is also implemented to enable further investigations of communication algorithms.

### 1.2.2 Transmission Schemes

An essential topic of this part consists of re-evaluating the analog/digital partitioning of the whole system [33], which can yield some flexibility in the trade-off between the requirements of high data rates and low energy consumption.

The channel modeling studies show that frequency selectivity will already be relevant for signal bandwidths in the MHz-range. The most common way to enable feasible equalization is orthogonal frequency division multiplexing (OFDM). In [83, 102, 103], for example, different criteria were proposed to design an RF beamformer for frequency selective channels by employing OFDM. However, OFDM is very costly in terms of power consumption. Due to its high peak to average power ratio (PAPR), OFDM requires high-resolution AD- and DA-converters and high linearity ranges of the amplifiers. Both lead to excessive power consumption (e.g., 3 W for 1 Gsamples/s, 10 bits, see [www.ti.com](http://www.ti.com)) and is, thus, not a suitable approach for getting the highest data rate under a processing power constraint. Another option to combat the frequency selective fading is single carrier modulation with frequency domain equalization (SC-FDE). In [63], hybrid beamforming for frequency-selective MIMO channels using SC-FDE is proposed. Compared with multicarrier OFDM systems, single-carrier systems can achieve a better power efficiency in AD-/DA- conversion and the RF front-end and better synchronization robustness. Yet, for the targeted data rates above 100 Gb/s, frequency selectivity is so severe that equalization becomes exceptionally complicated.

Since antennas are small at 60 GHz, multi-antenna transceivers can be implemented efficiently. Thus, the channel can be made frequency-flat by RF domain beamforming, separating the dominating paths and per-beam time delay compensation (TDC). For paths separable by the transmitter, pre-transmission delay compensation is managed. For paths separable by the receiver, beamforming at the receiver side is employed. This architecture can now be used to trade-off data rates and processing energy. For example, more antennas per beam provide a better separation (less interference) and higher gain, but at the cost of more processing power (more RF chains). Different paths may be combined in the receiver to get a higher gain or be used for spatial multiplexing.

This confirms that a processing energy optimized transceiver architecture differs from an architecture where only communication performance is optimized. Thus, a novel transmission scheme, i.e., joint analog/digital signal processing architectures, is



proposed in this work [107]. The major baseband signal processing tasks are wide topics, which include many modules such as channel estimation, Beamforming/MIMO techniques, equalization, matched filtering (pulse shaping at the transmitter)<sup>3</sup>. Each of the transceiver tasks should be studied both concerning the power consumption and the communication performance impact. Except that, the low complexity algorithms with acceptable performance loss should be investigated to guarantee the strict power limit.

### 1.2.3 Power Estimation

The overall methodology is energy-driven, i.e., all design decisions like transmission scheme selection, analog/digital partitioning, algorithms optimization, etc. will be driven by energy efficiency. There is a strong relationship between energy efficiency and communication performance. Power estimation is performed for the components identified to be suitable for a system that meets the overall throughput, communication performance, and power constraints. This applies to components in both the analog and the digital part.

The power estimation for the analog blocks and the RF front-end can be found precisely through circuit-level simulations. However, to explore the design space of different suitable architectures and the optimum partitioning between analog and digital functionality, system-level models will be created for the entire front-end. The behavioral models will be built in such a way to allow for estimation of the power consumption of the individual building blocks. These will then be used in system-level simulation setups.

For the digital part, power estimation for the critical components will be conducted based on the number of operations (addition and multiplication) but not a simulation of synthesized gate-level netlists annotated with timing delay information extracted from the physical chip layout. The hardware implementation is out of scope for the author. Here, we focus on the energy efficiency maximization algorithms to obtain the optimal system setting<sup>4</sup>.

## 1.3 Outline

The remainder of the thesis, which tries to meet the challenges and answer the problems as mentioned in Section 1.2, is organized as follows.

Since the performance of the physical layer strongly depends on the analog front end characteristics, the choice of the carrier frequency and the available bandwidth is studied at the start of our research. In Chapter 2, we first introduce the state of the art of 60 GHz technology, such as worldwide regulatory and frequency allocations, and potential indoor applications. Next, various standardization efforts for the 60 GHz

<sup>3</sup> The demapping of symbols (i.e., detection of bits) and decoding algorithms and the corresponding software models are contributed by other members in the Project LP100.

<sup>4</sup> The specific simulation of synthesized gate-level netlists for critical components is performed by other project members.

band already developed by multiple international standards groups and industry alliances are discussed. After that, to design a suitable transmission scheme that allows us to achieve a throughput of more than 100 Gb/s within the given energy budget, as a prerequisite, wireless channel models at 60 GHz are identified. For link-level simulations, a precise knowledge of the radio channel is essential. These provide the basis of the remainder of the thesis.

The channel modeling studies show that the 60 GHz band suffers from extremely high propagation loss. Therefore, at mmWave systems, hybrid beamforming, in which the precoding and combining are split into analog and digital domains, can be employed to provide ultra-high data rates and satisfy the hardware constraint. Moreover, to mitigate the effect of frequency selectivity, making the channel frequency flat over a wide bandwidth has to be performed in mmWave system architecture. In Chapter 3, we first propose a new method to combat the frequency selectivity named time delay compensation, which, if implemented precisely, provides no delay differences between different paths and achieves flat channel over a wide bandwidth. In order to further achieve a flat fading channel, the best possible beam separation is necessary. We propose an average signal-to-interference ratio (SIR) constrained design to achieve the best possible beam separation. As is known, the SIR of a particular beam is related to the number of antennas used. In this design algorithm, we optimize the number of antennas to achieve the best possible directivity and, simultaneously, satisfy the SIR constraint, which also minimizes the processing power.

In Chapter 4, we mainly focus on performance analysis on the hybrid beamforming approach proposed in Chapter 3, such as MIMO pre-/post-processing, channel estimation, and equalization for such large scale MIMO systems. To obtain the maximum information rate, we propose a joint design of digital baseband pre- and post-processing based on a weighted minimum mean square error (MMSE) criterion on the transmit power constraint. Further, the optimization in the RF domain is specified into three criteria by taking various error weights into account. We also develop a transceiver with lower complexity for ease of hardware implementation, where pre-processing in the RF domain after up-conversion is implemented merely using analog phase shifters. While employing such large antenna arrays, it becomes challenging to estimate the mmWave channel using conventional algorithms. Hence, we develop two novel multi-resolution mmWave channel estimation algorithms that exploit two dimensional discrete Fourier transform (DFT) technique inspired by the sparse nature of the mmWave channel. The proposed algorithms take into account practical radio frequency (RF) hardware limitations and computational complexity reduction during the training phases. Except that, we propose two frequency selective hybrid precoding solutions, namely time delay compensation (TDC) based time-domain equalization (TDE) and phase shift compensation (PSC) based frequency domain equalization (FDE).

As mentioned in Section 1.2.3, the overall methodology is energy-driven. Therefore, the trade-off relationship between energy efficiency and spectrum efficiency is essential for mmWave systems design, which is addressed in Chapter 5. In Chapter 5, the spectrum efficiency of the hybrid beamforming approach is introduced. After

that, a power consumption model for such a system is presented and analyzed, including a detailed literature review. The total average power consumption along the signal path can be divided into two main components: the power consumption of all the circuit blocks in the analog part and the power consumption of baseband combiner. Except that, we optimize the overall system's energy efficiency over different parameters. The optimization of energy efficiency is a crucial factor in system optimization and the design of power-hungry devices. Meanwhile, the spectral efficiency goes through a reduction with the increasing energy efficiency. Thus, an analysis of the relation between energy and spectral efficiency is also performed to guide the practical energy/spectrum efficiency trade-off for the mmWave system design.

Until now, the research focuses on the 60 GHz range, in particular, for the radio frequency (RF) architecture and channel characteristics. In Chapter 6, the impact of an extension to 120 GHz carrier frequency ranges is considered. Except that, an extension from the point-to-point MIMO transmission to multi-user case (MIMO multiple access channel for uplink and broadcast channel for downlink) is addressed. This chapter has first studied the channel characteristics and channel models at 120 GHz published in the literature. Compared to 60 GHz, the shorter wavelength of 120 GHz allows more antennas employed, and larger bandwidth used in the system. Based on literature research, we employ the ray-tracing method to generate the channel model. Moreover, the planar antenna array is used instead of the linear antenna array. After comparing different system architectures, a multi-user low RF complexity hybrid beamforming MIMO system at 120 GHz is applied in our work, with two structures: fully-connected structure and array-of-subarray structure. Several algorithms with CSI are proposed to maximize the capacity of such systems. Besides, we propose an iterative power precoding algorithm without CSI. Its performance seems better since the complexity of the hardware is much higher. Finally, we explore the influence of some parameters on the system performance, such as the number of antennas, the number of users, and quantization-bits.

Finally, Chapter 7 gives a conclusion of this thesis and points out potential research directions for future work.

## 1.4 Notation

In general, we use the following notations: small and large bold fonts are used to denote vectors and matrices, respectively;  $(\cdot)^*$ ,  $(\cdot)^T$  and  $(\cdot)^H$  denote conjugate, transpose and conjugate transpose respectively;  $(\mathbf{A})_+$  denotes the fact that the negative elements of  $\mathbf{A}$  are replaced by zero;  $|\mathbf{A}|$  is the determinant of  $\mathbf{A}$ ;  $\text{Tr}(\mathbf{A})$  is the trace of  $\mathbf{A}$ ;  $\angle \mathbf{A}$  returns the phase of the elements of  $\mathbf{A}$ ;  $\lceil \mathbf{A} \rceil$  rounds the elements of  $\mathbf{A}$  to the nearest integers towards infinity;  $\text{round}(\mathbf{A})$  rounds each element of  $\mathbf{A}$  to the nearest integer;  $\mathbf{I}_N$  is the  $N \times N$  identity matrix;  $\mathcal{CN}(\mathbf{a}, \mathbf{A})$  denotes a complex Gaussian vector with mean  $\mathbf{a}$  and covariance matrix  $\mathbf{A}$ ;  $\mathcal{Q}_N$  denotes the set  $\{1, \dots, N\}$ .



## Chapter 2

# Preliminaries

---

For future cellular networks and local area networks, the millimeter-wave (mmWave) spectrum in the 30-300 GHz carrier frequency will be used to meet the ever-increasing demand for higher transmission rates [10]. Here, the mm-wave frequency range at 60 GHz is of particular interest, as the 60 GHz band (57 - 66 GHz) offers a continuous bandwidth of at least 5 GHz in many countries worldwide. A primary challenge of the mmWave spectrum is the severe atmospheric absorption, which results in extremely high propagation losses. Fortunately, small wavelengths of mmWave frequencies enable installing numerous antenna elements array, which can give substantial array gains and produce highly directional beams. Beamforming can concentrate the transmit/receive signal power in the desired direction to improve the link budget. Despite the beamforming gain, the propagation losses are still so severe that the potential 60 GHz systems will be limited to operate in single rooms and at distances of less than 10 meters [93]. Thus, mm-wave systems are well suited for indoor networks for ubiquitous communication coverage, either in the home environment or at public places like hotels, restaurants, and office buildings. This thesis aims to design, optimize, and link-level simulations of the physical layer algorithms for indoor mmWave systems.

In this chapter, we first introduce the state of the art of 60 GHz technology, such as worldwide regulatory and frequency allocations, and potential indoor applications in Section 2.1. Next, various standardization efforts for the 60 GHz band already developed by multiple international standards groups and industry alliances are discussed in Section 2.2. At last, wireless channel models at 60 GHz are identified in Section 2.3 as a prerequisite of designing a suitable transmission scheme that allows us to achieve a throughput of more than 100 Gb/s within the given energy budget. These provide the basis of the remainder of the thesis.

## 2.1 State of the Art of Relevant Research Topics

Although current wireless technologies give us almost near maximum theoretical achievable capacity, most of them work under 10 GHz frequency bands. One of the emerging wireless technologies is mmWave technology to overcome the spectrum shortage at the microwave band. It is important to note that applying the mmWave band for broadband indoor wireless communication systems has already been proposed around 1990 [99]. However, it was to spend about 20 years before the first commercial products have been available. The improvements in process technologies and low-cost integration solutions have made mmWave technology become possible

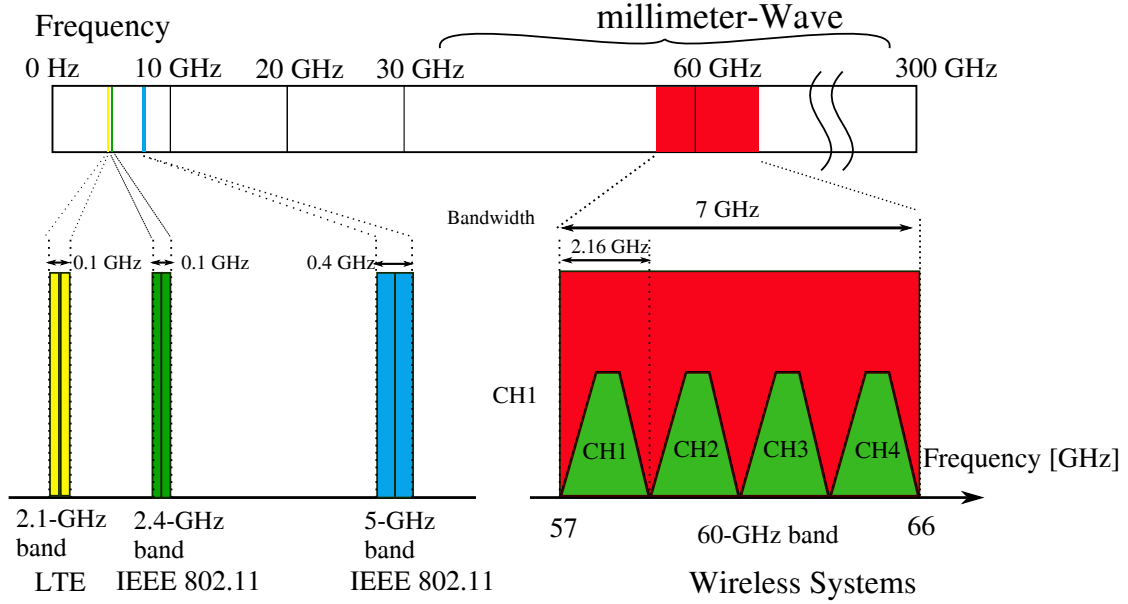


**Figure 2.1:** mm-Wave vs. conventional ISM bands

and begun to attract enthusiastic interest from academia, industry, and standardization bodies.

The mmWave band from 30 to 300 GHz offers a 10 or 100 times larger bandwidth than the conventional Industrial, Scientific and Medical bands (ISM) [78] where we can squeeze more data and transmit with higher data rates. Fig. 2.1 illustrates the available bandwidth in both conventional and mmWave systems. In this thesis, however, we will focus specifically on 60 GHz radio, which enables many new ultra-high throughput applications that are difficult to offer by wireless systems at lower frequencies. Unless otherwise specified, the terms 60 GHz and mmWave are used interchangeably in the following.

One primary reason for the recent interest in 60 GHz technology is the large unlicensed bandwidth. The US Federal Communication Commission (FCC) first proposed establishing an unlicensed band at 59–64 GHz in 1994 since radio regulatory organizations around the world have already done many types of research in these areas. In recent years, an unlicensed spectrum allocation method in the 60 GHz band has been approved by many countries such as the EU, the US, Canada, China, South Korea, Australia, and Japan. As shown in Fig. 2.2, at least 5 GHz of continuous bandwidth is available in many countries worldwide.

In [122], the author made a comparison between the typical 60 GHz system with other unlicensed systems: ultra-wideband (UWB) systems and IEEE 802.11 systems that operate near the US FCC regulatory limit, as shown in Table 2.1. Compared with the UWB system, the typical 60 GHz system is less restricted in terms of power limits since the UWB system is an overlay system and thus is subject to stringent

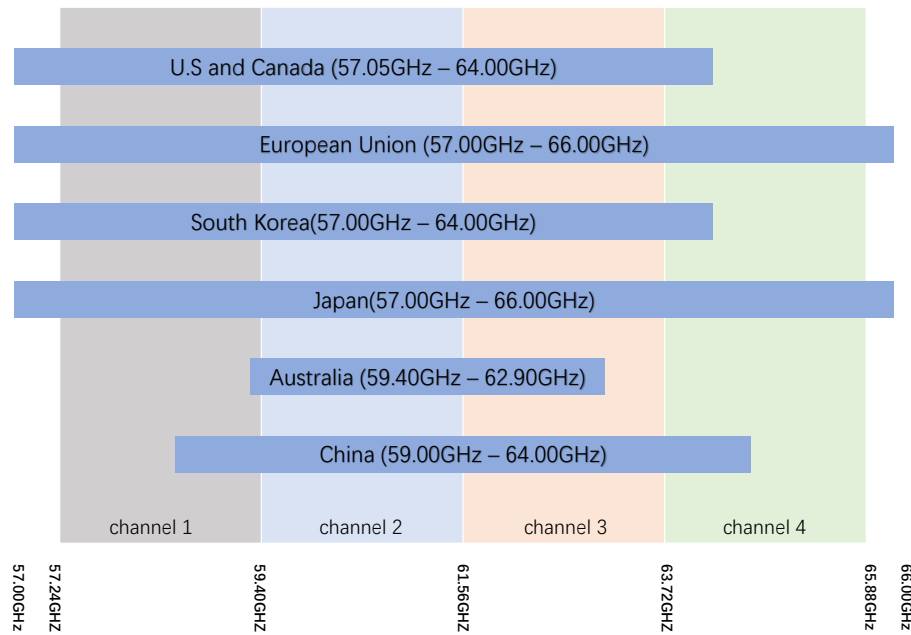


**Figure 2.2:** Worldwide frequency allocation for 60 GHz band and operation.

**Table 2.1:** Comparison of the typical implementation of 60 GHz, UWB and 802.11n systems in terms of their output power, antenna gain and EIRP output

Technology	60 GHz	UWB	IEEE 802.11n
Frequency [GHz]	57.0-66.0	3.1-10.6	2.4/5.0
PA output [dBm]	10.0	-11.5	22.0
Antenna gain [dBi]	25.0	1.5	3.0
EIRP output [dBm]	35.0	-10.0	25.0
Bandwidth [MHz]	2000	528	40
Efficiency 1 Gbps [bps/Hz]	0.5	2.0	25.0
Target data rate [Mbps]	4000	480	600
Efficiency required [bps/Hz]	2.0	1.0	15.0

and different regulations [4]. The bandwidth at 60 GHz is one of the largest unlicensed bandwidths ever to be allocated. We can see that, compared to other existing WLAN and WPAN systems, 60 GHz regulation allows much higher transmit power – equivalent isotropic radiated power (EIRP).

In order to overcome the higher path loss at 60 GHz, the higher transmit power is necessary. The steep path attenuation limits the 60 GHz transmission to the indoor environment (the delay spread of the channel under study is another limiting factor).

Hence, the interference levels for 60 GHz are less severe than those systems located in the bands less than 10 GHz, which turns its drawbacks into benefits.

As we know, the huge bandwidth also simplifies the design of the systems that deliver a multi-Gigabytes transmission with much lower spectral efficiency (i.e., low cost and simple implementation). Table 2.1 also shows the spectral efficiency required by the 60 GHz, UWB, and IEEE 802.11 systems to achieve 1 Gbps transmission. The spectral efficiency is the throughput divided by the bandwidth. For example, a typical 60 GHz system with 2GHz bandwidth requires efficiency only 0.5 bps/Hz to achieve 1 Gbps, and even for target data rate 4 GHz, the required efficiency is only 2.0 bps/Hz. This makes it an ideal candidate for ultra-high data rate (e.g., 100 Gbps and beyond) transmission systems with strict power limitation. Therefore, the target use cases in this work are initially short-range wireless transmitters working at carrier frequencies around 60 GHz. Though the UWB system only requires 2.0 bps/Hz to achieve 1 Gbps, its actual throughput is limited to 480 Mbps at 1 m operating range with required efficiency 1.0 bps/Hz. IEEE 802.11n systems will require 25 bps/Hz to achieve 1 Gbps due to the narrower bandwidth, making the extension of such a system to beyond 1 Gbps unappealing in terms of cost and implementation.

Several potential indoor applications are listed in the following:

- Cable replacement or uncompressed high definition (HD) video streaming is emerging as one of the most attractive applications and related products based on the WirelessHD specification are currently available on the market from companies such as Panasonic, LG Electronics and Toshiba [8].
- Typical WLAN applications and Gigabit Ethernet cable replacement that permits multi-Gigabit Ethernet traffic.
- ‘synch and go’ file transfer that enables Gigabytes of file transfer in a few seconds.
- wireless gaming ensures high-quality performance and low latency for an excellent user experience similar to today’s DLNA (Digital Living Network Alliance), AirPlay [2,3].

## 2.2 60 GHz Wireless Standards

Driven by the potential applications, various standards for 60 GHz band have been already developed by multiple international standards groups and industry alliance.

**IEEE802.15.3c:** In March 2005, the IEEE802.15.3c Task Group (TG3c) was formed to develop a mmWave based alternative physical layer (PHY) for the IEEE 802.15.3 WPAN standard 802.15.3-2003 [1]. IEEE 802.15.3c is the first standard that addresses multi-Gigabit short-range wireless systems. IEEE 802.15.3c standard has been explicitly designed for WPAN, meaning that it focuses on indoor environment propagation. IEEE 802.15.3c can provide a multi-Gigabit data rate (up to 5.67 Gbps) in the range of a few meters with five usage models.



**Table 2.2:** Overview of 60 GHz standards

System	Frequency Band	Bandwidth	Max. Data Rate	Published	Ref.
ECMA-387	60 GHz	2 GHz	6.35 Gbps	2008	[4]
IEEE 802.15.3c			5.67 Gbps	2009	[1]
WirelessHD			7.1 Gbps	2010	[8]
WiGig			7 Gbps	2010	[7]
IEEE 802.11ad			6.8 Gbps	2012	[9]

**ARIB-STD T69 and ARIB-STD T74:** The Association of Radio Industries and Business (ARIB) in Japan developed two standards related to the 60 GHz band for specified low-power radio stations (point-to-point systems): the ARIB-STD T69 [6] and ARIB-STD T74 [5]. The ARIB STD-T69 was released in July 2004 and was reviewed in November 2005, which is the standard for mm-wave video transmission equipment. While the ARIB-STD T74 is the standard for mmWave ultra-high-speed WLANs. Both of them cover the 59–66 GHz band, defined in Japan.

**ECMA-387:** In August 2006, European Computer Manufacturers Association (ECMA International) Technical Committee Task Group (TG20) provided a PHY and a MAC for short-range transmission up to 10Gb/s WPAN transport for bulk data transfer and also multimedia streaming [4]. The ECMA-387 standard can provide a data rate of up to 6.35 Gbps with a single channel and 25.41 Gbps with four bonded channels.

**WirelessHD:** In October 2006, the WirelessHD consortium was formed by many key consumer electronics companies to deliver a specification for high-speed, high-quality, uncompressed audio/video (A/V) streaming using 60 GHz technology [8]. The data rates can amount to up to 7.1 Gbps supporting 3D TV and 4K resolution.

**WiGig:** The Wireless Gigabit Alliance (WiGig) was formed in May 2009 to build a unified specification for 60 GHz wireless technology, which focuses on connectivity among PCs, consumer electronics, and handheld devices. The specifications were finalized in 2010 which define data rates of up to 7 Gbps [7].

**IEEE802.11ad:** Since 2009 within the IEEE 802.11 working group, Task Group ‘ad’ (TGad) developed the successor standard of IEEE 802.11n and IEEE 802.11ac, aiming to provide WLAN both the 802.11 physical layers (PHY) and the 802.11 Medium Access Control Layer (MAC) at 60GHz frequency band with very high throughput (VHT) [9]. This standard employs a single carrier(SC, data rate up to 4.620 Gbps) and OFDM (data rate up to 6.756 Gbps) modulation techniques with a beamforming method to maximize the throughput. The final specifications were published in 2012.

Table 2.2 shows the overview of 60 GHz standards and comparison with established systems.

## 2.3 60 GHz Radio Channel Modeling

The huge bandwidth, high EIRP limit, and unified regulation and frequency allocation globally have positioned 60 GHz the ideal carrier frequency for ultra-high throughput wireless communication systems. This can be confirmed by the extensive standardization effort and industry alliance formation to promote 60 GHz technology. Therefore, when we intend to investigate the near-field wireless transmitters with 100 Gbps and beyond under power constraints, the 60 GHz band is the first choice as the start point.

Realistic channel modeling, which closely approximates real propagation environments, is the first step to be performed before any system design, such as in IEEE 802.15.3c [1], and IEEE 802.11ad [9]. In the context of 60 GHz, we consider indoor environments with wideband systems. Due to the directional nature (employing many antennas array) of 60 GHz communications systems, the channel models developed also include the effect of the antenna array, namely the radio channel model. When the effect of the antenna array is removed, the channel model is referred to as the propagation channel [97]. To the best of our knowledge, all the proposed 60 GHz channel models to date are radio channels and can be modeled using various modeling approaches.

Usually, propagation channel models can be broadly classified into two main categories: deterministic and stochastic, as specified introduced in [77]. For all the modeling approaches, a propagation channel can be characterized in two ways, namely large-scale and small-scale channel characterizations. Large-scale fading characteristics of the wireless channel attribute dispersion and attenuation features in the channel detailed in Section 2.3.2. In contrast, the small-scale fading describes the multipath effect, time dispersion, power delay profile, power azimuth spectrum, and amplitude fading features, as addressed in Section 2.3.3.

In this section, we mainly focus on the discussion of IEEE 802.15.3c industry-standard channel models, since they are the fundamental models used for the evaluation of a 60 GHz communications system in the literature.

### 2.3.1 Scenarios

The TG3c has developed and provided a group of models for channels in the 60 GHz frequency band in various indoor environments. The structure of these models is based on clustered rays and implements both small and large scale fading channel characterization. The TG3c group has recommended five different indoor environments, including Residential, Office, Library, Desktop, and Kiosk, that for each environment a Line of sight (LOS) and Non-Line of Sight (NLOS) scenario has been considered. In a LOS case, there is a direct dominant path between the transmitter (Tx) and receiver (Rx) that no object blocks while in the NLOS case, there is no dominant path between the Tx and Rx. Table 2.3 summarizes all the environments for different scenarios [123].

**Table 2.3:** Various environments in indoor mmWave channel model

Channel Model	Scenario	Scenario	Descriptions
CM1	LOS	Residential	Typical Home environments with rooms, walls, ceiling made of wood/concrete, windows, beds, carpet etc.
CM2	NLOS		
CM3	LOS	Office	Typical Office environments with chairs, desks, computers, bookshelves, white-board. The walls are made by metal or concrete and covered with plasterboard with windows and door.
CM4	NLOS		
CM5	LOS	Library	Typical small library with many desks, bookshelves filled with books, computers, chairs.
CM6	NLOS		
CM7	LOS	Desktop	Typical office desktop and computer clutter with partitioning.
CM8	NLOS		
CM9	LOS	Kiosk	Typical Kiosk serves portable devices.

### 2.3.2 Large Scale Channel Characterization

The essential parameters for large scale channel characterization are path Loss and shadowing.

#### 2.3.2.1 Path Loss

Path loss denotes the attenuation of the transmit signal over a certain distance and is defined as the proportion of the received signal strength to the power of the transmit signal. Path loss in dB for the mmWave systems is

$$PL_{dB}(d) = \overline{PL}(d) + X_\sigma \quad (2.1)$$

Where  $\overline{PL}(d)$  is the path loss at a certain distance  $d$  in dB, which depends on the environment, and  $X_\sigma$  is the statistical model for shadowing, which is zero-mean,

**Table 2.4:** The path loss exponent and standard deviation for shadowing defined in IEEE 802.15.3c [123]

Channel Model	Scenario	$n$	$PL_0$	$\sigma_s$	Comment	Ref.
CM1	LOS	1.53	75.1	1.5	Tx-72° HPBW, Rx-60° HPBW	[67]
CM2	NLOS	2.44	86.0	6.2	Tx-72° HPBW, Rx-60° HPBW	[67]
CM3	LOS	1.16	84.6	5.4	Tx-Omni, Rx-Horn (30° HPBW)	[57]
CM4	NLOS	3.74	56.1	8.6	Tx-Omni, Rx-Horn (30° HPBW)	[57]

Gaussian distribution and with a standard deviation of  $\sigma$  dB. Hence, resulting the PL rewritten as [26]

$$PL_{dB}(d) = \overline{PL} \left( \frac{4\pi d_0}{\lambda} \right) + 10 \log_{10} \left( \frac{d}{d_0} \right)^n + X_\sigma \quad (2.2)$$

Where  $d_0$  denotes the reference distance, and  $\lambda$  is the wavelength. The exponent  $n$  achieved based on measurements done in [26] for mmWave channel and varies from 1.2 to 2.0 for LOS cases and 1.97 to 10 when there is no dominant path between the transmitter and receiver (NLOS). Table 2.4 demonstrates the values of  $n$  for different environments with LOS and NLOS cases. Here the distance value is  $d_0 = 1m$ .

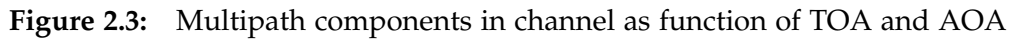
### 2.3.2.2 Shadowing

The effect where the received power fluctuates due to objects obstructing the propagation path between the transmitter and the receiver is called shadowing.

By various measurement results, it has been observed that shadowing in the mm-Wave range is log-normal distributed, i.e.,  $X_\sigma[\text{dB}] = N(0, \sigma_s)$ , where  $X_\sigma$  denotes a Gaussian random variable with zero mean and standard deviation  $\sigma_s$  and  $X_\sigma$  is measured in dB. The standard deviation  $\sigma_s$  varies as a function of the antenna beamwidth and Tx-Rx height. Human movement has a significant effect on shadowing. Measurements have shown that human movement is significant and ranges between 18-36dB [97, 123]. This can even altogether remove the LOS path. In Table 2.4 different values for  $\sigma_s$  are given for various environments and scenarios.

### 2.3.3 Small Scale Channel Characterization

As mentioned before, the significant parameters for small scale channel characterization are amplitude statistics, delay properties (e.g., power delay profile (PDF), RMS delay spread, mean excess delay), angle-of-arrival/departure (AOA/AOD) properties, and Doppler spreading. In the mmWave frequency range, the generic statistical



### 2.3.3.1 Saleh-Valenzuela Channel Model

$$\begin{cases} p(T_l|T_{l-1}) = \Lambda \exp[-\Lambda(T_l - T_{l-1})], & l > 0 \\ p(\tau_{k,l}|\tau_{(k-1)l}) = \lambda \exp[-\lambda(\tau_{k,l} - \tau_{(k-1)l})], & k > 0. \end{cases} \quad (2.3)$$
$$h(t) = \sum_{l=0}^{L-1} \sum_{k=0}^{K_l-1} \beta_{k,l} e^{j\theta_{k,l}} \delta(t - T_l - \tau_{k,l}), \quad (2.4)$$

where  $L$  is the total number of clusters in the channel, and  $K_l$  is the total number of rays within each  $l$ th cluster.  $\beta_{k,l}$  are discrete, mutually independent and identically distributed variables with Rayleigh distribution having uniform phase shift and are strictly decaying as a function of  $T_l$  and  $\tau_{k,l}$

$$\begin{aligned}\overline{\beta_{k,l}^2} &\equiv \overline{\beta^2(T_l, \tau_{k,l})} \\ &= \overline{\beta^2(0,0)} e^{-\frac{T_l}{\Gamma}} e^{-\frac{\tau_{k,l}}{\gamma}},\end{aligned}\quad (2.5)$$

where  $\overline{\beta^2(0,0)}$  is the average power gain of the first multipath component (ray) of the first cluster and  $\Gamma$ , and  $\gamma$  are cluster decay and ray decay factors respectively. As shown in Fig. 2.4, typically  $\Gamma > \gamma$  meaning clusters decay faster than and rays also the multipath components in each cluster are decreasing quicker than the first ray in the next cluster (i.e.,  $\Delta T \equiv T_l - T_{l-1}$ , with  $e^{-\frac{\Delta T}{\Gamma}} \gg e^{-\frac{\Delta T}{\gamma}}$ ).

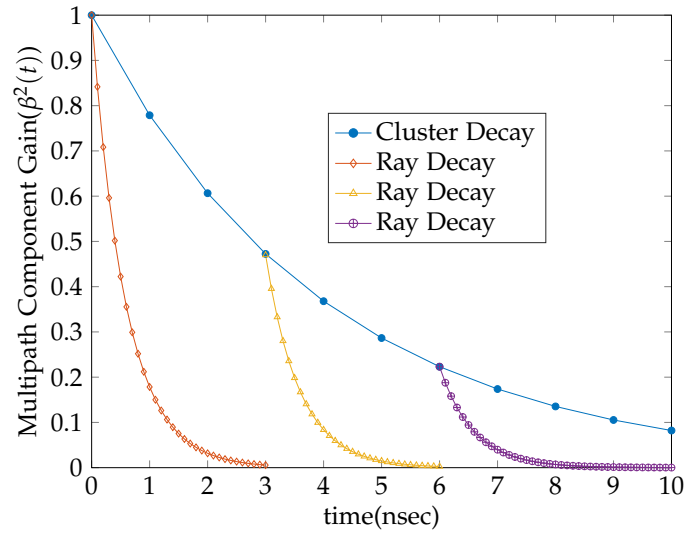


Figure 2.4: Cluster and ray decay representation

### 2.3.3.2 Angle of Arrival Extended S-V Model

This model has been developed for the mmWave range( 55 - 65 GHz) channels to perfectly represent an indoor channel's characteristics at this frequency range. In this model, in addition to all key parameters of the S-V model, *Angle of Arrival* (AoA) of multipath components arriving in the channel has been considered. In [27, 55, 96], all emphasize that rays and clusters arrive with discrete time and angle of arrival (ToA)

and (AoA). And measurements are taken to realize these parameters. Thus, the channel impulse response derived in 2.4 can be rewritten [55]

$$h(t, \phi) = \sum_{l=0}^{L-1} \sum_{k=0}^{K_l-1} \beta_{k,l} e^{j\theta_{k,l}} \delta(t - T_l - \tau_{k,l}) \delta(\phi - \Psi_l - \psi_{k,l}), \quad (2.6)$$

where  $\Psi_l$  is the mean angle of arrival of the  $l$ th cluster and  $\psi_{k,l}$  is AoA of the  $k$ th ray within the  $l$ th cluster. It is assumed that the arrival times of rays and clusters and AoAs are independent variables. Mean value of AoA of clusters is zero  $\Psi = 0$ .  $\Psi$  has a uniform distribution over  $[0, 2\pi]$  [123]

$$p(\Psi_l | \Psi_{l-1}) = \frac{1}{2\pi}, \quad l > 0 \quad (2.7)$$

Also ray AoAs have a Gaussian distribution with  $\sigma_G$  standard deviation and is given by

$$p(\psi_{k,l}) = \frac{1}{\sqrt{2\pi}\sigma_s} e^{-\left(\frac{\psi_{k,l}}{\sqrt{2}\sigma_G}\right)^2} \quad (2.8)$$

The number of clusters in a particular environment can be described by a Poisson distribution. However, most of the time, the type of distribution of the clusters is not known. The mean number of clusters  $\bar{L}$  gives an indication of the density of things in the environment. For example, the higher the value of  $\bar{L}$  indicates the presence of a large amount of furnishing.

### 2.3.3.3 60 GHz Channel Parameterization

All the parameters for the 60GHz channel characterization are summarized in the Table 2.5.

**Table 2.5:** Key Parameters of Extended S-V model

	Description		Description
$h_1/h_2$	Tx/Rx height	$G_T/G_R$	Tx/Rx gain
$P_{L0}$	PL at a distance of 1m	$\sigma_s$	Shadowing standard deviation
$n$	PL exponent	$\beta$	Amplitude of the first arrival path
$\Lambda$	Cluster arrival rate	$\sigma_c$	Cluster log-normal standard deviation
$\Gamma$	Cluster decay rate	$\sigma_r$	Ray log-normal standard deviation
$\lambda$	Ray arrival rate	$\sigma_\phi$	Angle spread
$\gamma$	Ray decay rate	$\bar{L}$	Average number of clusters
$\Delta k$	Ray Rician factor	$\Omega$	First ray's average power of the cluster
$d$	Tx-Rx separation		

The parameters mentioned above are valid for the 57-66 GHz range. It can be used to describe different channel models. A few examples employed in this thesis for numerical simulation for the different channel models are given in Appendix A.1 for Residential, Office, Desktop, and Library environments, respectively. All the channel model parameters are extracted from measurement data over a certain specified range of distance and around a particular frequency range.

## 2.4 Summary

In this chapter, we have first presented an introduction to 60 GHz technology, which started with the worldwide regulatory and frequency allocation of the 60 GHz band. The direct comparisons between typical 60 GHz system and other Gigabits systems such as UWB and IEEE 802.11n technologies have been shown in terms of the transmit power, bandwidth, and spectrum efficiency. The large bandwidth simplifies the design of the systems that deliver a multi-Gigabytes transmission with much lower spectral efficiency. This makes it an ideal candidate for ultra-high data rate (e.g., 100 Gbps and beyond) transmission systems with strict power limitation. Therefore, our target use cases in this work are initially short-range wireless transmitters working at carrier frequencies around 60 GHz.

Next, various standardization efforts for the 60 GHz band already developed by multiple international standards groups and industry alliances have been discussed, and a comparison of their physical layer features has been provided in Table 2.2.

After that, we have presented an overview of 60 GHz channel modeling, which lays the foundation of the investigation of 60 GHz based wireless communications system design in the following chapters. In particular, the PL and shadowing effects impose huge losses on the communication link at the mmWave band. Take the path loss for an example, in the residential environment (NLOS case) in the IEEE 802.15.3c channel model for example, at a distance of 10 m, a total of 110.4 dB loss is incurred. Such high PLs need to be compensated to achieve ultra-high data rate transmission [92]. By employing beamforming technology, it can provide significant directivity gain over the space of interest at one end of the link, if a large scale antennas array is employed. Therefore, beamforming technology is very critical to 60 GHz communications design (see Chapter 3).

Finally, a few examples of the different channel models proposed by IEEE 802.15.3c have been given for Residential, Office, Desktop, and Library environments, respectively, which will be used in this thesis for the numerical simulations in the following chapters. All the channel model parameters are extracted from measurement data over a specific range of distances and around a particular frequency range.



## Chapter 3

# Transmission Schemes: Hybrid Beamforming Approach

---

The 60 GHz band suffers from extremely high propagation loss due to the limited dominant scatterers and reflections, and strong oxygen absorption. In order to overcome this, MIMO through large scale antenna arrays can be exploited to provide sufficient gain considering the small wavelength in mmWave band [16]. MIMO pre- and post-processing in mmWave systems are generally different compared with traditional microwave systems. One differentiating feature is that, in traditional microwave systems, spatial multiplexing is often implemented at the digital baseband. Also, each antenna has its complete radio frequency (RF) chain, including a digital-to-analog converter (DAC) at the transmitter or analog-to-digital converter (ADC) at the receiver. However, in mmWave systems due to a large number of antennas, this arrangement will result in highly complex, expensive hardware implementation and high power consumption. This makes the traditional system architecture infeasible. Another differentiating feature is that the mmWave system utilizes huge bandwidth, meaning that the fading channels suffer from severe frequency selectivity, which further leads to sophisticated equalization. Moreover, the channel characteristics at mmWave differ drastically from micro frequencies. Based on the indoor channel measurements [55, 96], the MIMO channel is not rich at mmWave and is sparse in the angular domain. Owing to all these differentiating factors, it becomes necessary to develop new transceiver architectures for mmWave systems.

Inspired by the hardware constraint [19] at mmWave, hybrid beamforming, in which the precoding and combining are split into analog and digital domains, can be employed. Compared to pure analog beamforming, the digital beamforming layer provides more freedom for the pre- and post-processing design problem. This enables hybrid beamforming to provide high data rates and achieve better performance for multi-stream transmission.

In order to mitigate the effect of frequency selectivity, in the literature, OFDM has been widely used to convert the frequency selective fading channel into several parallel flat channels. Different criteria to design the RF beamformer for frequency selective channels by employing OFDM have been proposed in [83, 103]. However, since OFDM puts substantial linearity requirements onto the front end, single-carrier schemes are preferable for processing energy-efficient transmission. The sparse channel characteristics at mmWave can be leveraged to flatten the channel by utilizing efficient RF domain beamforming with time-delay compensation (TDC) technology. Hence, a novel transmission scheme, namely hybrid beamforming with TDC, is developed in this chapter.

In this chapter, we first propose a new method to combat the frequency selectivity named time delay compensation, which, if implemented precisely, provides no delay differences between different paths and achieves flat channel over wide bandwidth as described in Section 3.1. In order to achieve a flat fading channel, the best possible beam separation is necessary. We propose an average signal-to-interference ratio (SIR) constrained design to achieve the best possible beam separation. As is known, the SIR of a particular beam is related to the number of antennas used. In this design algorithm, we optimize the number of antennas to achieve the best possible directivity and, simultaneously, satisfy the SIR constraint, which also minimizes the processing power shown in Section 3.2. Finally, we validate the efficiency of the proposed strategy via simulations and comparisons with the full digital case.

The results presented in the chapter have been published in part by the author in [107, 110, 112].

### 3.1 Hybrid Beamforming with Time Delay Compensation

In this section, we propose a new method to combat the frequency selectivity named time delay compensation, which, if implemented precisely, provides no delay differences between different paths and achieves flat channel over a wide bandwidth. Based on the indoor channel measurements, the geometric modeling approach [55, 96, 104] consists of multiple clusters, each with multiple rays. In order to reduce the delay spread at both intra- and inter-cluster, we introduce beamforming in the RF domain and the buffer in the baseband. Firstly, the local scatterers in each cluster introduce very minor delay variations, and we can even further reduce the delay spread in the cluster by employing RF beamforming techniques. With increasing the number of antennas, a narrower beam can be obtained, which leads to lesser delay spread. The effect which large antenna arrays bring about is that we can assume each cluster to be frequency flat over a wider bandwidth. Secondly, we compensate for the inter-cluster relative time delay by using a buffer in digital baseband. The channel's frequency selectivity depends on the resolution of the buffer, and a flat channel can be obtained with a sufficiently high resolution. Then we consider a MIMO wireless zero-padded (ZP) block transmission system, where the transmitter antennas are partitioned into sub-arrays to reduce the intra-cluster delay spread and support the required gain. A minimum mean-square-error (MMSE) equalization with fixed tap-length is used at the receiver to recover the received signal. Furthermore, We investigate the influence of the delay spread on the ergodic capacity and the outage capacity. This section concludes by validating the efficiency of the time delay compensation via simulations and comparisons with the frequency-selective case.

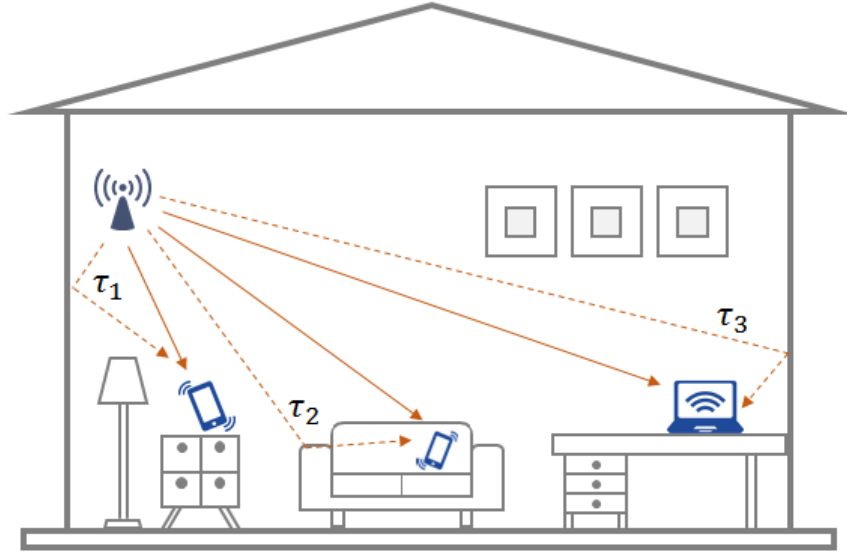


**Figure 3.1:** An illustration of wireless applications in the 60 GHz frequency band (typically 57-66 GHz) capable of very high throughput

### 3.1.1 Propagation Scenario

Consider a system with a single access point in an indoor environment, as illustrated in Fig. 3.1. We assume such a propagation environment that there are finite scatterer clusters, and the paths emanating from the same cluster suffer smaller delay differences. For the sake of simplicity, we restrict our attention to the downlink case here. The results for the uplink case are similar, which means the time delay compensation can be done at the access point side for both the uplink and downlink transmission. Obviously, the complexity of such a system only lies in the access point side. This section presents the channel model for broad-band MIMO fading channels based on previous work reported in [55, 96, 104].

#### 3.1.1.1 Channel Model

For our case of indoor propagation at 60 GHz, we use the modified Saleh-Valenzuela (S-V) model [55, 96, 104] for channel modeling.  $L$  number of clusters are assumed in the model with each channel cluster being composed of multiple rays, which is due to scattering from objects in vicinity or reflecting surfaces. The channel impulse response considered is given by

$$h[n, \phi] = \sum_{l=0}^{L-1} \sum_{k=0}^{K_l-1} \alpha_{k,l} \delta(nT_s - \tau_l - t_{k,l}) \delta(\phi - \Psi_l - \psi_{k,l})$$

where  $L$  denotes the number of clusters, and  $K_l$  represents the number of multipath components in the  $l$ th cluster.  $\alpha_{k,l}$  is the multipath gain coefficient of the  $k$ th multipath component in the  $l$ th cluster, which follows a log-normal distribution.  $\tau_l$  denotes the arrival time of the first ray in the  $l$ th cluster. And the delay of the  $k$ th multipath

component within the  $l$ th cluster relative to the first path arrival time  $\tau_l$  is denoted as  $t_{k,l}$ . The mean angle of arrival of  $l$ th cluster, which follows uniform distribution  $U[0, 2\pi)$ , is represented as  $\Psi_l$ . Further, we use  $\psi_{k,l}$  to denote the angle of arrival of the  $k$ th multipath component within the  $l$ th cluster. It follows a zero mean Laplacian distribution given by [96]

$$p(\psi_{k,l}) = \frac{1}{\sqrt{2}\sigma_G} \exp(-|\sqrt{2}\psi_{k,l}/\sigma_G|)$$

where  $\sigma_G$  is the standard deviation.

For the convenience of our simulations, the power delay profile of the channel used here is derived from the non-line-of-sight (NLOS) channel model for the residential scenario based on the measurements by the IEEE task group 802.15.3c [124].

It is known that the number of clusters  $L$  gives an indication about the number of dominant paths. Our model also considers that there are  $L$  significant scatterer clusters, and each of the paths within the same cluster experiences the same delay. In practice, however, local scatterers in the cluster introduce micro delay variations ( $\tau_{k,l}$  is small). As illustrated in Fig. 3.1, those micro delay variations can be further reduced by employing beam steering for each cluster, which focuses the power in the direction of the dominant path. The result of beam steering is that less delay spread in each cluster is obtained due to a narrower beam. Based on that, we, therefore, consider each cluster to be frequency flat over a wider bandwidth. This assumption leads to a result that all the rays in the cluster constructively contribute to the channel gain of the  $l$ th cluster, and then we seem to have one dominant path in each cluster.

In ultra high throughput systems, the symbol duration  $T_{sym}$  is much smaller (e.g., 1ns) than the inter-cluster root mean square (RMS) delay spread [38]. This results in significant frequency selectivity of the channel. Hence, time-delay compensation is implemented as compensation by using time-shifted beams on each path. Under this modified model, the discrete-time channel impulse response  $h[n]$  at the time instant  $n$  is given by

$$h[n] = \sum_{l=0}^{L-1} \alpha_l \delta(nT_s - \tau_l + \hat{\tau}_l) \quad (3.1)$$

where  $\alpha_l$  denotes the channel gain of the  $l$ th path and is simply the summation of  $\alpha_{k,l}$ . The time delay of the  $l$ th path is denoted as  $\tau_l$  and  $\hat{\tau}_l$  represents the time delay compensation of the  $l$ th path.

To summarize, by using transmit multi-antenna directivity, power is focused in the direction of dominant paths, and time delay on each path is compensated by time-shifted beams. We achieve a flat channel over a wide bandwidth with the guarantee of sufficient resolution in terms of time delay compensation.

### 3.1.1.2 Beam Steering

We assume a uniform linear array (ULA) at both the access point and the user side, each consisting of identical antenna elements. At the access point side, a large antenna

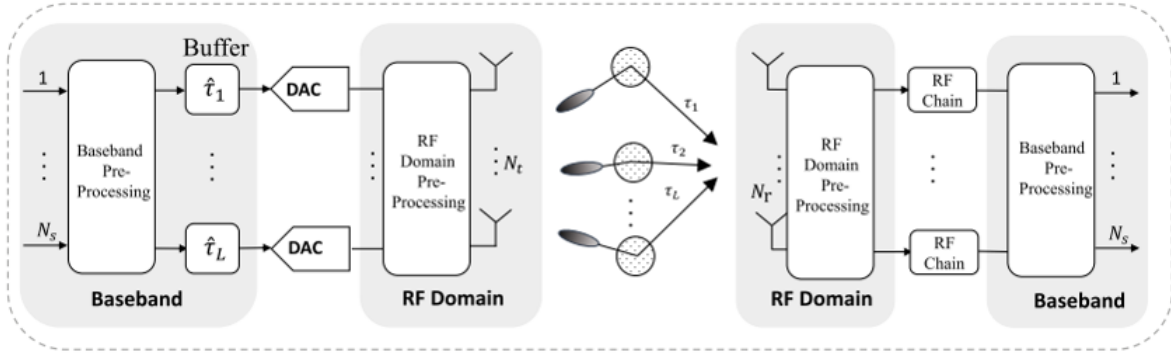


**Figure 3.2:** Block diagram of a large mmWave system employing hybrid beamforming and time-delay compensation

array is divided into  $L$  linear subarrays. Here, the concept of beam steering is applied to achieve high directionality. Shifting the radio-frequency phase is a very practical and feasible approach for achieving beam steering, especially considering the low-power consumption and low-complexity structure for 60 GHz compliant devices. To obtain the best weighting vectors for the transmitter antennas, we choose a uniform-weighting based codebook design [129]. The weighting vector is then described as follows

$$w_m = e^{-j \frac{2\pi}{\lambda} m d \sin(\theta_{max})}$$

The array factor now can be derived as

$$AF(\theta) = \sum_{m=0}^{M-1} w_m e^{j \frac{2\pi}{\lambda} m d \sin(\theta)} \quad (3.2)$$

where  $d$  is the antenna spacing,  $\lambda$  is the wavelength,  $M$  denotes the number of antennas in each sub-array, and  $\theta_{max}$  is the desired direction. Here  $\theta_{max}$  can be set to the direction of the dominated path, which is  $\Psi_l$  for different sub-arrays.

### 3.1.2 Capacity of Time-Delay Compensation based MIMO System

The following considerations focus on the realization of time delay compensation at the access point side. Then we employ linear equalization at the user side to recover the transmitted signal. The impact of time resolution of the time delay compensation on the ergodic and outage capacity of the system [24, 52] is also studied at the end of this section.

#### 3.1.2.1 RF Beamforming with Time-delay compensation

We consider a single user mmWave MIMO system, as shown in Fig. 3.2. The  $N_t$  transmitter antennas are partitioned into  $L$  subarrays. Analog phase shifters are used to adjust the signal phase such that a constructive interference in the respective direction

is obtained. Beam steering technique is employed to minimize the delay spread in respective clusters, as well as help focus the power in the direction of dominant paths. This further helps in reducing frequency selectivity and making the channel as flat as possible. The number of antennas in each subarray is denoted as  $M = \lceil N_t/L \rceil$ . With larger antenna number  $M$ , narrower beams are obtained, which bring less delay spread. Meanwhile, higher beamforming gain can be achieved.

The time delay on each path is compensated by time-shifted beams, as illustrated in Fig. 3.2. The time delay compensation can be easily implemented by the input buffer. Denote the time delay vector  $\tau$  as follows

$$\tau = [\tau_1, \dots, \tau_l, \dots, \tau_L]^T$$

In order to reduce the implementation complexity, we consider the relative time delay with reference to the first path in the cluster rather than the absolute time delay. Then, via simple manipulations, we obtain

$$\tau = \tau_1 + [0, \tilde{\tau}_2, \dots, \tilde{\tau}_l, \dots, \tilde{\tau}_L] \quad (3.3)$$

where  $\tilde{\tau}_l = \tau_l - \tau_1$  with  $l = 2, \dots, L$ .

Now the quantized relative path delay can be defined as

$$\hat{\tau} = \text{round}(\tilde{\tau}/T_s) \cdot T_s \quad (3.4)$$

Obviously, the precision of the buffer is related to the sample duration  $T_s$ . It is noteworthy that the use of interpolation is avoided due to its higher complexity and being out of the scope of this article. The quantization error vector is calculated by

$$\tau_e = \tilde{\tau} - \hat{\tau} \quad (3.5)$$

A flatter channel is generated as the quantization error  $\tau_e$  decreases. In this way, time-delay compensation proves to be a more feasible method to avoid frequency selectivity.

### 3.1.2.2 Zero-padded Block Transmission System and Linear Equalization

To mitigate the effects of frequency-selective channels, we consider point-to-point wireless zero-padded block transmissions over time-flat but frequency-selective fading channels. It is clear that the frequency selectivity of the equivalent channel depends on the time resolution of the buffer. Defining the maximum delay spread as  $\tau_{max} := \max\{\tau_l\}$ , the maximum channel order is then given by  $\mathcal{L} := \lceil \tau_{max}/T_{sym} \rceil$ . Here a MIMO system with  $N_t$  transmitter antennas and  $N_r$  receiving antennas is built. The information bearing sequence is grouped into blocks  $\mathbf{x}(n) = [x(M_c n + 1), \dots, x(M_c n + M_c)]^T$  of size  $M_c$ , where  $n$  denotes the block index and  $M_c$  denotes the block size. As a compensation for the inter block interference (IBI),  $M_0$  zeros are padded to each information block to obtain transmitted blocks of size  $M_b = M_c + M_0$ .

Collecting the  $N_r$  received symbol blocks corresponding to all received antennas, the output can be expressed as follows

$$\mathbf{y}(n) = \sum_{i=1}^L \sum_{j=1}^{N_r} \mathbf{H}^{(i,j)} \mathbf{x}(n) + \mathbf{v}(n) \quad (3.6)$$

where  $\mathbf{H}^{(i,j)}$  is a  $M_b \times M_b$  circulant matrix with first column

$$\mathbf{h} = [h_{i,j}(1), \dots, h_{i,j}(\mathcal{L}), 0, \dots, 0]^T \quad (3.7)$$

and the additive white Gaussian noise (AWGN) with variance  $\sigma_n^2 \mathbf{I}$  is denoted as  $\mathbf{v}(n)$ .

IBI is completely removed under the constraint  $M_0 \geq \mathcal{L}$ . Assuming that perfect channel state information is available at the receiver and omitting the block index  $n$  in (3.6) for notational simplicity. We now consider a minimum mean square error (MMSE) equalization for our model to recover the transmitted signal. The MMSE equalizer is given as

$$\mathbf{G}_{MMSE} = \mathbf{H}^H (\mathbf{H}\mathbf{H}^H + \sigma_n^2 \mathbf{I})^{-1} \quad (3.8)$$

### 3.1.2.3 Capacity derivation

Suppose  $\mathcal{P}$  denotes the total transmit power per block, and equal transmit power allocation is employed, the channel capacity averaged over the random channel  $\mathbf{H}$  is defined as follows

$$\mathcal{C}_e = \frac{1}{M_b} \mathbb{E} \left[ \log \det (\mathbf{I}_{M_b} + \frac{\bar{\mathcal{P}}_0}{\sigma_n^2} \mathbf{H}\mathbf{H}^H) \right] \quad \text{bits/s/Hz} \quad (3.9)$$

where  $\bar{\mathcal{P}}_0 = \frac{\mathcal{P}}{M_b L}$  is the normalized power.

Now the correlation matrix is defined as follows

$$\mathbf{R}_h = \mathbb{E}[\mathbf{h}\mathbf{h}^H] \quad (3.10)$$

Let  $\Delta$  times the wavelength be the spacing between the antenna elements and  $\tau_e$  be the delay spread quantization error,  $\mathbf{R}_h$  can be further expressed as

$$\mathbf{R}_h = \mathbb{E}(\Delta, \tau_e) \quad (3.11)$$

Note that we have absorbed the delay spread quantization error, depending on power delay profile and sample duration of the buffer, of the channel into the correlation matrix. By factoring the  $M_b \times M_b$  correlation matrix  $\mathbf{R}_h$  according to  $\mathbf{R}_h = \mathbf{R}_h^{1/2} \mathbf{R}_h^{1/2}$ , the channel matrix  $\mathbf{H}$  can be expressed as [64]

$$\mathbf{H} = \mathbf{R}_h^{1/2} \mathbf{H}_G \quad (3.12)$$

where the  $\mathbf{H}_G$  is the uncorrelated  $M_b \times M_b$  matrix with independently Gaussian distributed  $\mathcal{CN}(0,1)$  entries. Taking into account the correlation matrix  $\mathbf{R}_h$ , the ergodic capacity [74] is obtained as

$$\mathcal{C}_e = \frac{1}{M_b} \mathbb{E} \left[ \log \det \left( \mathbf{I}_{M_b} + \frac{\bar{\mathcal{P}}_0}{\sigma_n^2} \mathbf{R}_h \mathbf{H}_G \mathbf{H}_G^H \right) \right] \quad \text{bits/s/Hz} \quad (3.13)$$

$M_b$ , when at a large scale, follows the law of large numbers, namely  $1/M_b \mathbf{H}_G \mathbf{H}_G^H \rightarrow \mathbf{I}_{M_b}$  [117]. Hence, in the large  $M_b$  limit, we get

$$\mathcal{C}_e = \frac{1}{M_b} \mathbb{E} \left[ \log \det \left( \mathbf{I}_{M_b} + \frac{\bar{\mathcal{P}}_0 M_b}{\sigma_n^2} \mathbf{R}_h \right) \right] \quad \text{bits/s/Hz} \quad (3.14)$$

Since the distribution of quantized delay spread error can not be determined, its impact on the ergodic capacity and outage capacity can just be validated by Monte Carlo simulations. The results will be illustrated in section 3.1.3.

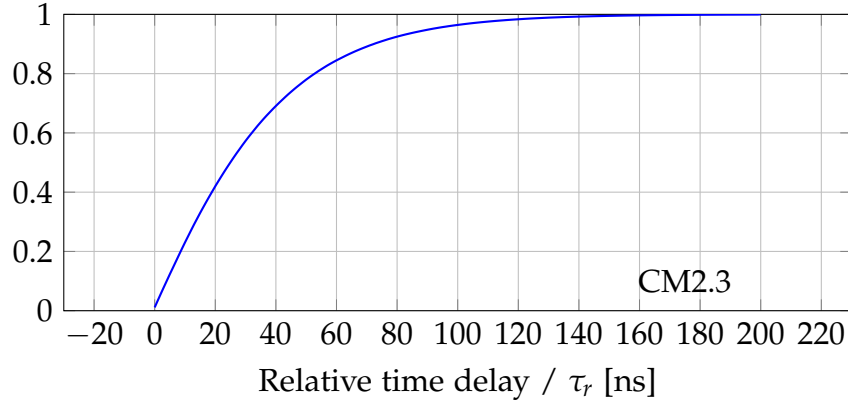
### 3.1.3 Performance Evaluation

The proposed technique of time delay compensation (TDC) is validated in this section by means of the simulation results. Consider a wireless transceiver system operating at 60 GHz in an indoor non-line-of-sight (NLOS) environment. For demonstration purposes, the total transmit power per block is assumed to normalize to unity with  $\mathcal{P} = 1$ , and a rectangular 16-QAM modulation with Gray mapping is used. As mentioned earlier, the channel realization  $\mathbf{H}$  is assumed to be perfectly known at both the transmitter and receiver side. In addition, each channel impulse response is generated using the 60 GHz NLOS multipath channel model for the residential scenario CM2.3 [124].

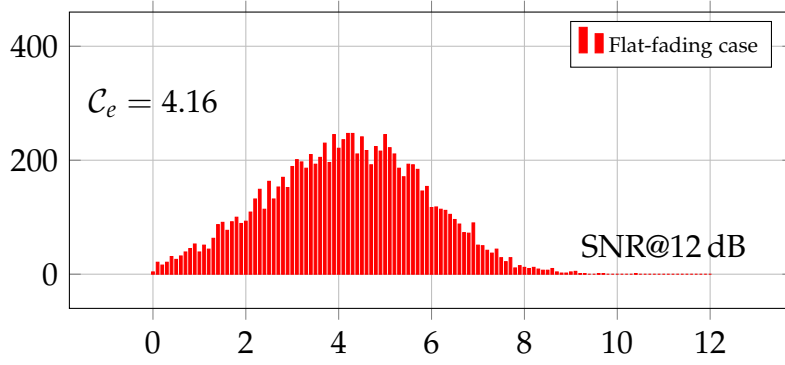
#### 3.1.3.1 Buffer Length

Fig.3.3 depicts a cumulative graph describing the probability distribution of the relative time delay. Based on this distribution, the buffer length can be defined as  $\mathcal{L}_b := \lceil \tau_r / T_s \rceil$ , where  $T_s$  is the sample duration of the buffer. It is observed that the probability that the relative time delay is less than 50 ns is 0.8 and that it is less than 100 ns is 0.96. According to Fig. 3.3, strictly considering the probability of 1, the minimum relative time delay is 150 ns. However, when the requirement is relaxed, for example, 0.96, we can get the relative time delay to be 100 ns. And then, the length of the buffer can be defined accordingly. The lower the buffer length, the lesser is the complexity, and a trade-off is consequently observed between the complexity of the buffer and the performance. In the following, the buffer length is defined to be  $\mathcal{L}_b = 100\text{ns}/T_s$ .

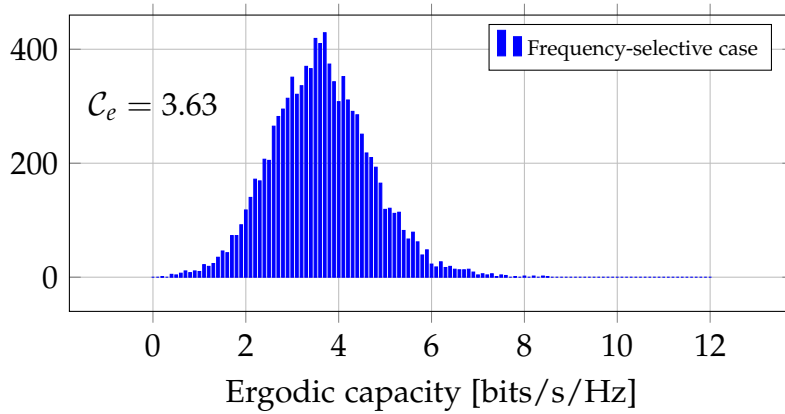




**Figure 3.3:** The cumulative distribution function of the relative time delay for the NLOS residential scenario CM2.3 [124].



**(a)** Mutual information in the flat fading case (Channel order  $\mathcal{L} = 1$ ) with  $T_s = 0.1T_{sym}$



**(b)** Mutual information in the frequency selective case (Channel order  $\mathcal{L} = 12$ ) without time delay compensation

**Figure 3.4:** Example histogram of the ergodic capacity in bits/s/Hz in (a) the flat-fading case and (b) the frequency-selective case.

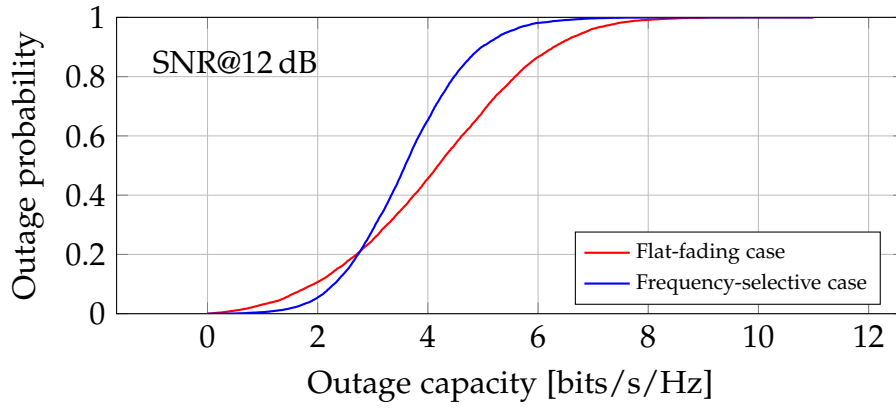


**Figure 3.5:** Outage probability of the outage capacity in bits/s/Hz in the flat-fading case and the frequency-selective case.

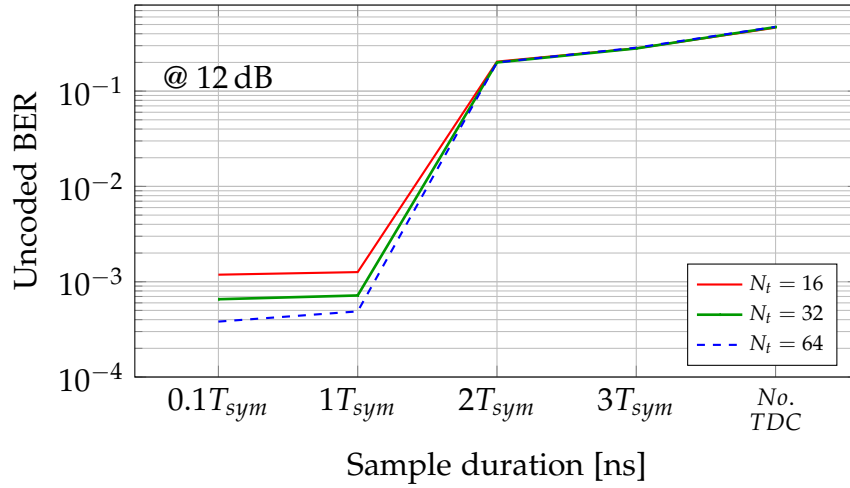
### 3.1.3.2 Influence of delay spread on ergodic and outage capacity

The ergodic capacities are firstly considered for the case of flat fading channel as well as frequency selective channel. As shown in Fig.3.4a and Fig.3.4b, the distribution of the mutual information for the frequency selective case ( $\mathcal{L} = 12$ ) is significantly more concentrated around the mean as compared to the flat fading case. Additionally, the ergodic capacity for the flat fading case is 4.16 bits/s/Hz at 12dB. It is higher than the frequency selective case, which is 3.63 bits/s/Hz under the same system setting. Therefore, the flat fading case offers an advantage over the frequency selective case in terms of ergodic capacity.

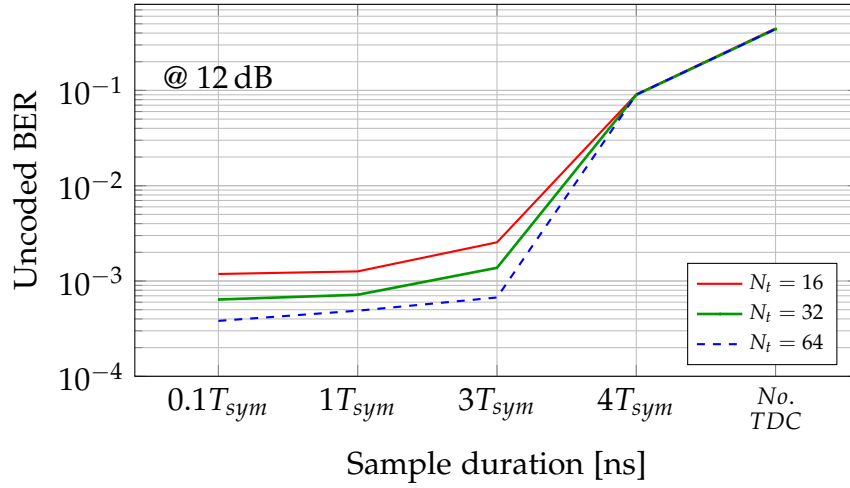
In the next step, the impact of delay spread on the outage capacity of the system is investigated. Under the same system setting, Fig.3.5 shows the outage probability for channel order  $\mathcal{L} = 1$  and 12 at an SNR of 12dB. It can be seen that for the mutual information above 2.75 bits/s/Hz, the outage probability for flat fading case is much lower than for the frequency selective case, probably due to the constructive channel gain of different paths. However, for the mutual information lower than 2.75 bits/s/Hz, the outage probability for frequency selective case is slightly lower than for the flat fading case. It may attribute to the decrease in spatial diversity. Such observations indicate that the flat fading channel obtained by time-delay compensation has the advantage of both of the ergodic and outage capacity.

### 3.1.3.3 Influence of time resolution of the buffer on BER Performance

Here, the influence of resolution of the buffer has been analyzed on the BER performance of the system mentioned above with a different number of transmit antennas  $N_t$ . In Fig.3.6, the effect of different sample duration of the buffer on the BER performance is illustrated. Finite tap-length MMSE equalizer at the receiver side is employed to fix the complexity at the user side for the purpose of fairness comparison. It is clearly shown in Fig.3.6 that decreasing the resolution of the buffer has an adverse effect on



(a) Un-coded BER performance with One-tap MMSE equalizer



(b) Un-coded BER performance with Three-tap MMSE equalizer

**Figure 3.6:** Average un-coded BER of a MIMO system with various resolution of the buffer and different number of antennas at access point side with finite tap-length MMSE equalizer.

the BER performance. As depicted in Fig.3.6a, for one-tap MMSE equalizer when the sample duration equals the symbol duration, the BER performance is comparable to that when the sample duration equals  $0.1T_{sym}$ , but as we increase the sample duration, the performance becomes worse, and eventually, the data cannot be recovered.

Now, the influence of the tap-length of the MMSE equalizer on the BER performance is studied. As observed from Fig.3.6a and Fig.3.6b, increasing the number of taps of the MMSE equalizer results in better BER performance even at a lower resolution which implies lower complexity at the transmitter side. Therefore, as the complexity at the receiver side is increased, it reduces the complexity at the transmitter side and vice versa. It is also demonstrated that the BER performance in frequency selective case highly depends on the tap-length of MMSE equalizer.

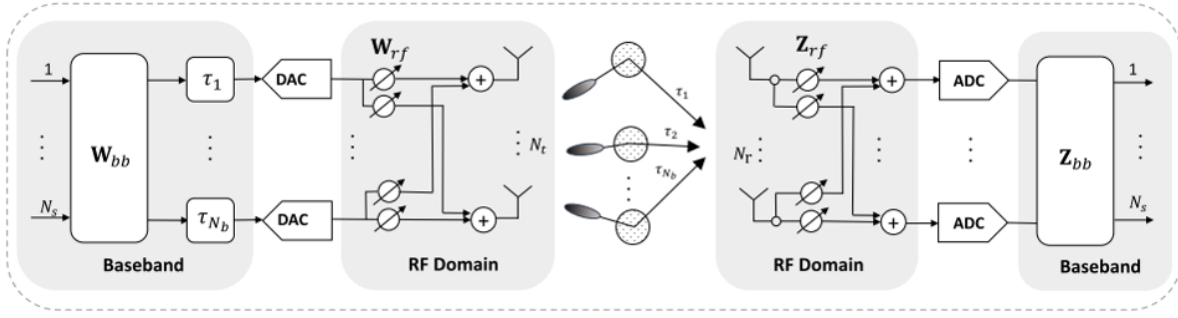


**Figure 3.7:** Block diagram of a large mmWave system employing hybrid beamforming and time-delay compensation

For illustration purposes, we adopt a frequency selective channel, which is the case where no time delay compensation has been applied as a benchmark for the comparisons. It can be observed from Fig.3.6 that the BER performance is worse than all the previous cases. Such high-frequency selectivity of the channel requires a high number of taps at the equalizer for an acceptable BER performance. This supports our proposal that time delay compensation makes the channel flat, reduces the receiver complexity, and improves the system performance.

In addition, we assess the relation of the number of transmitter antennas  $N_t$  and the uncoded BER. As shown in Fig.3.6, as the number of antennas is increased, the BER performance improves significantly. This is due to the fact that higher  $N_T$  has higher beamforming gain.

## 3.2 Best Possible Beam Separation Algorithm

To flatten the fading channel over a wide bandwidth and maximize the capacity of the proposed system, we propose a signal-to-interference ratio (SIR) constrained capacity maximization algorithm to jointly design the precoder and combiner in this section. On the one hand, to realize the effective TDC implementation for flattening the fading channel, it is essential to achieve the best case beam separation. This leads us to the optimization of RF beamforming at the transmitter side. Here we use the average signal-to-interference ratio (SIR) as a performance measure to maintain the signal quality for each beam. The implementation of this SIR constrained RF beamforming design is twofold, namely path selection and RF beamforming design. On the other hand, after obtaining the flattened fading channel, the optimization of the remaining precoder and combiner is formulated based on the capacity maximization criterion under a total transmit power constraint. Finally, we validate the efficiency of the proposed strategy via simulations and comparisons with the full digital case.

### 3.2.1 System Model

The classical single-user MIMO system model is as illustrated in Fig. 3.7. It shows an access point (AP) with  $N_t$  antennas communicating  $N_s$  data streams to a user with

$N_r$  antennas. The focus of this section will be put on the downlink transmission. The data streams are preprocessed by an  $N_b \times N_s$  baseband precoder  $W_{bb}$ . At last,  $N_b$  flat beams are obtained. The  $N_b$  flat beams are time-shifted by the input buffer and then processed by an  $N_t \times N_b$  RF precoder,  $W_{rf}$ . With efficient TDC and RF domain beamforming, the equivalent flattened fading channel can be expressed as follows

$$\tilde{\mathbf{H}} = \mathbf{A}_R \text{diag}(\boldsymbol{\alpha}) \mathbf{A}_T^H \mathbf{W}_{rf} \quad (3.15)$$

where  $\boldsymbol{\alpha} = \sqrt{\frac{N_t N_r}{\bar{L}}} [\alpha_1, \dots, \alpha_l, \dots, \alpha_{\bar{L}}]$  and where  $\bar{L}$  represents the number of survived paths after path selection. Note that  $N_b$  does not need to be constant rather than be optimized and equals to the number of survived path. The matrix  $\mathbf{A}_R$  contains the user side array response vector with  $\mathbf{A}_R = [\mathbf{a}_r(\phi_1), \dots, \mathbf{a}_r(\phi_l), \dots, \mathbf{a}_r(\phi_{\bar{L}})]$  while  $\mathbf{A}_T$  represents the AP side with  $\mathbf{A}_T = [\mathbf{a}_t(\theta_1), \dots, \mathbf{a}_t(\theta_l), \dots, \mathbf{a}_t(\theta_{\bar{L}})]$ .

The discrete-time transmitted signal is then

$$\mathbf{x} = \tilde{\mathbf{H}} \mathbf{W}_{bb} \mathbf{s} \quad (3.16)$$

where  $\mathbf{s}$  is the  $N_s \times 1$  vector of transmitted symbols such that  $\mathbb{E}[\mathbf{s}\mathbf{s}^H] = (\mathcal{P}_o/N_s)\mathbf{I}_{N_s}$ , and the total transmit power is denoted as  $\mathcal{P}_o$ . Since the RF beamforming is implemented using only analog phase shifters, we assume  $|\mathbf{W}_{rf}(m, l)|^2 = M_l^{-1}$ . The total power constraint is enforced by normalizing  $\mathbf{W}_{bb}$  such that  $\|\mathbf{W}_{rf} \mathbf{W}_{bb}\|_F^2 = N_s$ .

The received signal at the user side is first combined in the RF domain employing the  $N_b \times N_r$  combining matrix  $\mathbf{Z}_{rf}$  followed by an  $N_s \times N_b$  baseband combiner  $\mathbf{Z}_{bb}$ . The constraints on the entries of RF combiner  $\mathbf{Z}_{rf}$  are similar to the RF precoder. If  $\mathbf{Z} = \mathbf{Z}_{bb} \mathbf{Z}_{rf}$ , the received signal after processing can be then written as

$$\hat{\mathbf{s}} = \mathbf{Z} \tilde{\mathbf{H}} \mathbf{W}_{bb} \mathbf{s} + \mathbf{Z} \mathbf{n} \quad (3.17)$$

where  $\mathbf{n}$  denotes the  $N_r \times 1$  noise vector of i.i.d.  $\mathcal{CN}(0, \mathbf{R}_{nn})$ .  $\mathbf{R}_{nn} = \sigma_n^2 \mathbf{I}_{N_r}$  stands for the noise covariance matrix. In this section, we assume that the channel state information (CSI) is perfectly known at both the transmitter and receiver. In addition, we implicitly assume perfect synchronization. In literature, mmWave-specific channel estimation has been proposed [14]. The important channel parameters such as AoDs, AoAs, time delay and path loss can be estimated by sparse channel estimation.

### 3.2.1.1 Some Basics of RF Domain Beamforming

MmWave channels are expected to have limited scattering while the paths emanating from the same cluster suffer smaller delay differences. Let  $L$  be the number of clusters. The number of clusters  $L$  gives an indication of the number of dominant paths. Our model assumes that there are  $L$  significant clusters, and the intra-cluster delay spread is minimal. Fundamentally, however, micro delay variations are introduced by the local scatterers in the cluster. Beam steering can then be employed, which focuses the power in the direction of the dominant path and further reduces the delay variations. The narrower the resultant beam is, the lesser the delay spread in each cluster will

appear. Each cluster after beam steering can be considered to be frequency flat over a wide bandwidth. Hence we consider that there is one dominant path in each cluster since all the rays in a cluster constructively add the channel gain of the  $l$ th cluster.

The most widely used modified Saleh-Valenzuela (S-V) model for channel modeling at 60 GHz [55, 96] is considered here. Under this model, the  $N_r \times N_t$  dimensional frequency-selective MIMO channel between the AP and the user can be defined as

$$\mathbf{H} = \sqrt{\frac{N_t N_r}{L}} \sum_{l=1}^L \alpha_l \mathbf{a}_r(\phi_l) \mathbf{a}_t^T(\theta_l) \delta(t - \tau_l) \quad (3.18)$$

where  $\alpha_l$  is the complex gain of the  $l$ th path which follows the log-normal distribution with  $\mathbb{E}[|\alpha_l|^2] = \bar{\alpha}$ , and  $\phi_l$  and  $\theta_l$  are the angles of arrival and departure (AoAs/AoDs) of the  $l$ th dominant path respectively. The array response vectors of the uniform linear arrays can be denoted as  $\mathbf{a}_r(\phi_l) \in \mathbb{C}^{N_r \times 1}$  for the receiver and  $\mathbf{a}_t(\theta_l) \in \mathbb{C}^{N_t \times 1}$  for the transmitter. A Laplacian distribution with uniformly distributed mean over  $[-\pi, \pi)$  and angular standard deviation of  $\sigma_{AS}$  is used to model AoAs and AoDs. In this section, a non-line-of-sight (NLOS) channel model for the residential scenario is applied based on the measurements by IEEE task group 802.15.3c [124].

The symbol duration  $T_{sym}$  is much smaller (e.g. 1ns) than the inter-cluster root mean square (RMS) delay spread in ultra high throughput systems. Thus there is significant frequency selectivity in the channel, which makes it important to implement time delay compensation in such a way that the beams are time shifted with the help of an input buffer. This modification leads to the discrete channel matrix given by

$$\mathbf{H} = \sqrt{\frac{N_t N_r}{L}} \sum_{l=1}^L \alpha_l \mathbf{a}_r(\phi_l) \mathbf{a}_t^T(\theta_l) \delta(t - \tau_l + \hat{\tau}_l) \quad (3.19)$$

where  $\hat{\tau}_l$  denotes the time delay compensation of the  $l$ th path, which is a quantized value given by  $\hat{\tau}_l = k_l \cdot T_b$ , where  $T_b$  is the sample duration of the buffer and  $k_l$  is an integer. The efficiency of the time delay compensation is validated in [107]. Employing even just a one-tap MMSE equalizer at the user side, comparable BER performance to the flattened fading case can be achieved when the sample buffer duration is equal or less than the symbol duration which is not a challenge for hardware implementation at 60 GHz.

Before introducing the RF domain beamforming design, some basics involved would be firstly clarified. Here we use the term beamforming more classically to refer to a steered beam, as described in Fig. 3.8. The high propagation loss at 60 GHz makes it necessary to obtain highly directional antenna patterns. In order to achieve efficient TDC, separation of individual rays at transmitter as well as receiver is required. Thus beamforming can be employed at both sides to achieve proper beam separation in the respective dominant paths.

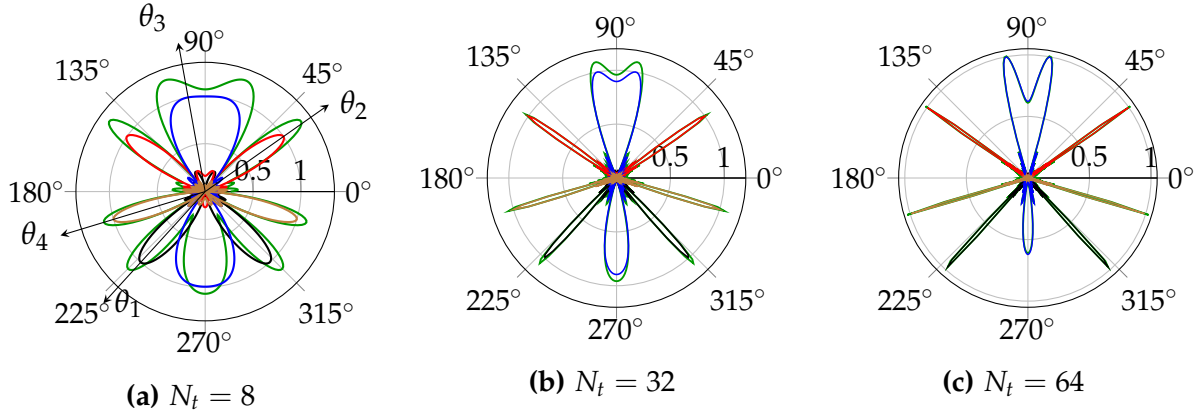


**Figure 3.8:** An example beam patterns with AoDs  $\theta_l \in [\theta_1, \dots, \theta_4]$ . The individual antenna patterns pointing in four different AoDs are normalized to 1. Subplots show the beam patterns for various number of transmitter antennas. Higher antenna employed, narrower beamwidth.

Suppose that the antennas in uniform linear array (ULA) are all identical and that the coupling effects among antennas can be neglected. By the antenna array theory, the RF array factor (RAF) for the  $l$ th dominant path is thus expressed as

$$\mathcal{AF}^l(\theta) = \sum_{m=1}^{M_l} w_m^l e^{j \frac{2\pi}{\lambda} (m-1)d \sin(\theta)} \quad (3.20)$$

where  $d$  is the antenna spacing which is set to  $d = \frac{\lambda}{2} = 2.5$  mm,  $\lambda$  is the wavelength and  $M_l$  denotes the number of active antennas for the  $l$ th beam.

Given the target direction  $\theta_l$  for the  $l$ th dominant path, ideally, we can set

$$w_m^l = e^{-j \frac{2\pi}{\lambda} (m-1)d \sin(\theta_l)} \quad (3.21)$$

to maximize  $\mathcal{AF}^l(\theta)$  in the direction of  $\theta_l$ , which allows us to steer the main beam of (3.20) so that it points in the desired directions. These  $w_m^l$  form the elements of the beamforming matrix  $\mathbf{W}_{rf}$  of order  $N_t \times N_b$ , if the  $l$ th output of the BB processing module is routed to the  $m$ th antenna  $m \in \mathcal{Q}_{M_l}$ . Otherwise  $\mathbf{W}_{rf}(m, l) = 0$ . Here,  $N_b$  denotes the number of flat beams.

As illustrated in Fig. 3.7, all the phase shifted data streams are combined and distributed through all the transmitting antennas via  $L$  dominant paths by the RF beamformer. The side lobes and grating lobes of beam patterns affect each other by introducing interference in the other beam patterns. The whole array factor after combination can then be expressed as

$$\mathcal{AF}(\theta) = \sum_{m=1}^{M_l} \left( \sum_{l=1}^L w_m^l \right) e^{j \frac{2\pi}{\lambda} (m-1)d \sin(\theta)} \quad (3.22)$$

In Fig 3.8, different dominant paths are illustrated by means of normalized RAFs

$\frac{|\mathcal{AF}^l(\theta)|}{\max_{\theta} |\mathcal{AF}^l(\theta)|}$  with  $L = 4$  and different number of antennas  $N_t = 8, 32, 64$ . The individual antenna patterns pointing in four different AoDs are depicted in the figure each represented with the help of different colors. The summation of all these paths, i.e.  $\mathcal{AF}(\theta)$  is represented by the pattern with green color. The difference between summation and the respective individual patterns depicts the interference in that particular path. As it can be observed, the beams become narrower with increasing number of antennas and leads to a reduction of interference. Thus better beam separation can be obtained with a higher number of antennas.

To obtain a high SIR, there needs to be minimum interference from all the other dominant paths in the corresponding path, which is obtained for a suitable value of  $M_l$ . Another important factor that needs to be considered is beam spacing. We can say that if beam spacing is very small for a particular set of beams, then they tend to interfere more with each other. In such cases, more processing of these corresponding beams needs to be done, as opposed to the sufficiently spaced beams. Given the number of antennas at the transmitter side, path selection is necessary if the beam spacing is too narrow to distinguish the individual beams. Therefore, the optimization of  $\mathbf{W}_{rf}$  to achieve the best beam separation depends on the dominant path selection, and the optimization of the number of active antennas for the survived paths.

### 3.2.2 Best Possible Beam Separation Algorithm Design

The focus of this section is twofold, firstly, to achieve a flat fading channel and, secondly, to maximize the capacity of the system. In order to flatten the frequency selective fading channel, RF domain beamforming with TDC is employed, and to maximize the capacity of the system, digital baseband pre- and post-processing is used. Best case beam separation is necessary in order to achieve a flat fading channel. In this section, the average signal-to-interference ratio (SIR) is applied as a performance metric to maintain the signal quality for each beam. Based on that, a SIR constrained design has been proposed in this section to achieve the best possible beam separation. As we know, the SIR of a particular beam is related to the number of antennas used. In this design algorithm, we try to optimize the number of antennas to achieve the best possible directivity and, at the same time, satisfy the SIR constraint.

#### 3.2.2.1 Problem Formulation

As mentioned earlier, the optimization problem can be formulated based on the functionality of different beamformers. RF domain beamforming with TDC is utilized as the first step to flatten the frequency selective fading channel. Therefore RF precoders  $\mathbf{W}_{rf}$  and  $\mathbf{Z}_{rf}$  are designed to maximize the channel gain  $\|\tilde{\mathbf{H}}\|^2$  under the SIR constraint. The optimization problem can be expressed as

$$\max_{\mathbf{W}_{rf}} \|\tilde{\mathbf{H}}\|^2 \quad (3.23)$$



$$\begin{aligned}
\text{s.t. } \mathcal{S}_l &\geq \delta, \quad l \in \mathcal{Q}_L \\
\mathbf{W}_{rf}(m, l) &= w_m^l, \quad m \in \mathcal{Q}_{M_l}, l \in \mathcal{Q}_L \\
\mathbf{Z}_{rf}(n, l) &= \frac{1}{\sqrt{N_r}} e^{j\psi_{n,l}}, \quad n \in \mathcal{Q}_{N_r}, l \in \mathcal{Q}_L
\end{aligned} \tag{3.24}$$

where  $\psi_{n,l} = -\frac{2\pi}{\lambda}(n-1)d \sin(\phi_l)$ . The notation  $\mathcal{S}_l$  labels the SIR in the direction of  $\theta_l$  and  $\delta$  denotes the SIR threshold in dB. After obtaining an effective flat fading channel, we focus on maximizing the information rate of the system. The optimization problem for the information rate achieved by this system can be formulated as

$$\begin{aligned}
\max_{\mathbf{W}_{bb}, \mathbf{Z}_{bb}} \mathcal{I} &= \log_2 \left| \mathbf{I} + \frac{(\mathbf{Z}\tilde{\mathbf{H}}\mathbf{W}_{bb})^H (\mathbf{Z}\tilde{\mathbf{H}}\mathbf{W}_{bb})}{(\mathbf{Z}\mathbf{R}_{nn}\mathbf{Z}^H)} \right| \\
\text{s.t. } \text{Tr}(\mathbf{W}_{bb}\mathbf{W}_{bb}^H) &\leq \mathcal{P}_0
\end{aligned} \tag{3.25}$$

### 3.2.2.2 RF Domain Beamforming Design

The RF domain beamforming design is basically the design of the matrices  $\mathbf{W}_{rf}$  and  $\mathbf{Z}_{rf}$ . According to (3.20), the interference introduced by the  $l$ th beam on the  $k$ th beam, represented by  $\mathcal{A}\mathcal{F}^l(\theta_k)$ , is influenced by the number of active antennas  $M_l$  for the  $l$ th beam. Now an attempt of optimizing the number of antennas is carried out in order to meet the SIR constraint in the direction of each dominant path. The SIR in the direction of  $\theta_l$  is denoted by

$$\mathcal{S}_l = 10 \log_{10} \frac{|\mathcal{A}\mathcal{F}^l(\theta_l)|}{\sum_{k=1, k \neq l}^{k=L} |\mathcal{A}\mathcal{F}^k(\theta_l)|} \quad [\text{dB}] \tag{3.26}$$

where the denominator denotes the interference introduced by all other beams in the direction of  $\theta_l$ .

For illustrating the relation between the number of active antennas and the SIR, Fig. 3.9 shows the SIR at beam spacing  $\theta_s = 5^\circ$  or  $10^\circ$ . It is observed that large number of antennas are required to distinguish between the beams for an extremely small beam spacing. In the following, we present the optimization of number of active antennas for each beam.

**1) Initialization:** The number of active antennas collected to form a set  $\mathcal{M}$  for each beam is initialized to  $N_t$ , i.e.  $M_l = N_t$ ,  $l \in \mathcal{Q}_L$ . Let  $\bar{L}$  denote the number of survived paths. Based on  $\mathcal{M}$ , we calculate all the  $\mathcal{S}_l$  from (3.26) and no further processing is needed in the current channel realization if the constraint in (3.24) is satisfied.

According to (3.26) and (3.24), we can derive the following inequality

$$\sum_{k=1, k \neq l}^{k=L} |\mathcal{A}\mathcal{F}^k(\theta_l)| \leq \frac{|\mathcal{A}\mathcal{F}^l(\theta_l)|}{10^{\frac{\delta}{10}}} \tag{3.27}$$

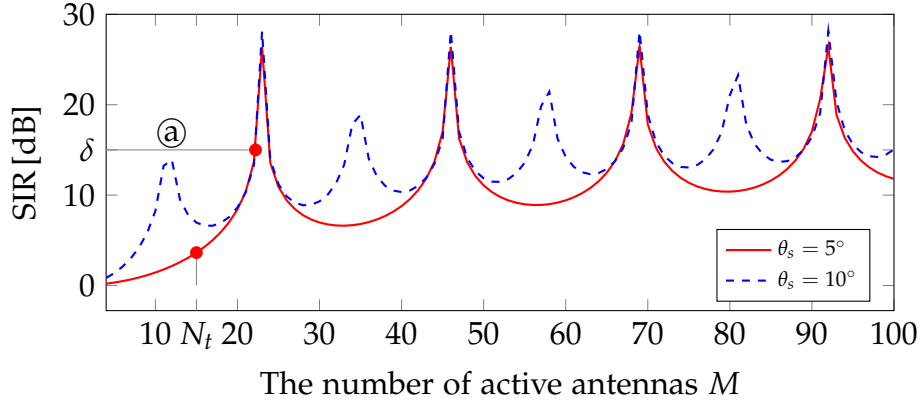


**Figure 3.9:** Relation between the number of active antenna  $M$  and the beam spacing  $\theta_s$ , where the target direction  $\theta_{max} = 0^\circ$ . For the case ①, the number of antennas  $N_t = 16$ , beam spacing  $\theta_s = 5^\circ$  and SIR threshold  $\delta = 15$  [dB].

Thus the upper bound for the interference is represented by  $\frac{|\mathcal{AF}^l(\theta_l)|}{10^{\frac{\delta}{10}}}$ . Each element  $\mathcal{AF}^k(\theta_l)$  is weighted against the above mentioned constraint. When the interference is observed to be greater than the threshold, the corresponding index pairs are collected into a set as follows

$$\mathcal{A}_{\text{con}} \triangleq \left\{ (k, l) \middle|_{k \neq l} \quad k, l \in \mathcal{Q}_L, |\mathcal{AF}^k(\theta_l)| > \frac{|\mathcal{AF}^l(\theta_l)|}{10^{\frac{\delta}{10}}} \right\}$$

**2) Path Selection:** Path selection needs to be proceeded after identifying  $\mathcal{A}_{\text{con}}$ . It is nothing but path elimination and is carried out based on the individual path gains. Thus, the first step here is to arrange the path gains in a descending order. This process is called sorting of the path gains. Obviously priority is given to the paths with higher path gains.

**Phase 1 - Compulsory Path Removal:** The SIR depends on the number of antennas as well as the beam spacing. In the case, if beam spacing is too narrow and also the number of antennas is not large enough, the SIR threshold can never be achieved for such small  $N_t$  even if the number of antennas is changed. This case is similar to the case ① shown in Fig. 3.9.

Here, we consider a vector  $\mathcal{F}$  in which the indices of the paths are stored in a descending order respective of their path gains. Depending on whether  $\mathcal{F}_i$ , namely the  $i$ th element in  $\mathcal{F}$ , is included in the set  $\mathcal{A}_{\text{con}}$ , the following cases are observed.

- If it is observed that  $\mathcal{F}_i = l$ , i.e.  $l$  is also included in the non-empty set  $\mathcal{A}_{\text{con}}$ , then all the paths introducing intolerable interference on  $\mathcal{F}_i$  are collected to form a new set

$$\mathcal{B}_{\text{con}} \triangleq \left\{ (k, \mathcal{F}_i) \middle|_{k \neq \mathcal{F}_i} (k, \mathcal{F}_i) \in \mathcal{A}_{\text{con}} \right\}$$

And then the further processing for path selection is done. On the other hand, if  $\mathcal{F}_i$  is not included in the non-empty set  $\mathcal{A}_{\text{con}}$ , then we go to  $\mathcal{F}_{i+1}$  until  $\mathcal{F}_{\bar{L}}$  is reached.

- We define the value SIR between two beams as

$$\mathcal{S}_{(k, \mathcal{F}_i)} = 10 \log_{10} \frac{|\mathcal{A}\mathcal{F}^{\mathcal{F}_i}(\theta_{\mathcal{F}_i})|}{|\mathcal{A}\mathcal{F}^k(\theta_{\mathcal{F}_i})|} \quad [\text{dB}] \quad (3.28)$$

The calculation of this for different values of number of active antennas as depicted in Fig. 3.9. As can be observed from the figure, if

$$\max \{ \mathcal{S}_{(k, \mathcal{F}_i)} |_{M=\{4, \dots, N_t\}} \} < \delta \quad (3.29)$$

the threshold can never be met. Therefore, from the paths  $k$  and  $\mathcal{F}_i$ , the path with the lower path gain, i.e. path  $k$  is dropped.

- By clearing out all the dropped paths, the sets  $\mathcal{A}_{\text{con}}$ ,  $\mathcal{F}$ ,  $\bar{L}$  and  $\mathcal{M}$  are updated. Then we go to the next iteration  $\mathcal{F}_{i+1}$ .

**Phase 2 - Selective Path Removal:** From (3.26) we find that  $\mathcal{S}_l$  depends on the set of number of active antennas for all the survived paths after phase 1. Then if an exhaustive search optimization algorithm is employed, it makes complexity of the algorithm intolerable and thus we consider a new metric as substitute,  $\hat{\mathcal{S}}_l$ , which is

$$\hat{\mathcal{S}}_l = 10 \log_{10} \frac{|\mathcal{A}\mathcal{F}^l(\theta_l)|}{\sum_{k=1, k \neq l}^{k=\bar{L}} |\mathcal{A}\mathcal{F}^l(\theta_k)|} \quad [\text{dB}] \quad (3.30)$$

where the denominator denotes the interference introduced by the  $l$ th path on all the other paths. Here,  $\hat{\mathcal{S}}_l$  depends solely on  $M_l$  and not the entire set and  $\mathcal{M}$  reduces the algorithm complexity. The aim is to determine  $M_l$  in order to minimize this interference and thus maximize  $\hat{\mathcal{S}}_l$ . Then  $\mathcal{S}_l$  is calculated from (3.26) according to the updated set  $\mathcal{M}$ . For the paths which do not fulfill the constraint in (3.24), the set can be determined as

$$\mathcal{L} \triangleq \{ l \mid l \in \mathcal{Q}_{\bar{L}}, \mathcal{S}_l < \delta \}$$

- If it is observed that  $\mathcal{F}_i = l$ , i.e.  $l$  is also included in the non-empty set  $\mathcal{L}$ , we proceed to path removal based on the interference introduced by all the beams  $i$ , with path gains  $\alpha_i < \alpha_l$  on the  $l$ th path. On the other hand, if  $\mathcal{F}_i$  is not included in the non-empty set  $\mathcal{L}$ , we go to  $\mathcal{F}_{i+1}$  until  $\mathcal{F}_{\bar{L}}$  is reached.
- For all the beams  $i$  which satisfy the interference bound when the  $i$ th beam is not considered, a set can be expressed as

$$\mathcal{C} \triangleq \left\{ i \mid \alpha_i < \alpha_l, l \in \mathcal{L}, \sum_{k=1, k \neq l, i}^{k=\bar{L}} |\mathcal{A}\mathcal{F}^k(\theta_l)| \leq \frac{|\mathcal{A}\mathcal{F}^l(\theta_l)|}{10^{\frac{\delta}{10}}} \right\}$$

The path with the lowest path gain is removed in the case of a non-empty set. Otherwise, we discard the weakest path from the set  $\mathcal{F}$ .

- With the help of all eliminated paths, the sets  $\mathcal{F}$ ,  $\bar{L}$  and  $\mathcal{M}$  are updated. Then the next iteration  $\mathcal{F}_{i+1}$  is executed.

The process in Phase 2 is repeated until we obtain a set  $\mathcal{M}$  which maximizes  $\hat{S}_l$  and makes  $S_l$  as well as  $l \in \mathcal{Q}_L$  satisfy the SIR constraint.

**3) RF Domain Beamforming Optimization:** The set  $\mathcal{M}$ , obtained in the previous part, maximizes  $\hat{S}_l$  and  $l \in \mathcal{Q}_L$ . In this section, a set  $\mathcal{O}_l$ , which consists of all the possible  $M_l$  satisfying the constraint,  $\hat{S}_l > \delta$ , is firstly obtained. Denote the length of  $\mathcal{O}_l$  as  $N_l$ , then there are  $N = \prod_{l=1}^L N_l$  candidate sets of  $\mathcal{M}$  which fulfill  $\hat{S}_l > \delta$ . All the candidate sets of  $\mathcal{M}$  are listed in  $\mathcal{C}_C$  and arranged in descending order of the summations of  $\mathcal{M}$ , with the motivation here being the maximization of number of antennas to improve the transmitter diversity.

- For a candidate set  $\mathcal{C}_C^i$ , the optimum set  $\mathcal{M}_{opt} = \mathcal{C}_C^i$  can be achieved if  $S_l \geq \delta$  is satisfied.
- Otherwise, we move on to the next iteration  $\mathcal{C}_C^{i+1}$ .

### 3.2.2.3 Baseband Beamforming Design

The optimization problem (3.25) can be solved according to the well known water-filling solution. The closed form solution of  $\mathbf{W}_{bb}$  and  $\mathbf{Z}$  is given by [112]. The optimum combiner  $\mathbf{Z}_{opt}$  is given by the flattened channel's left singular vectors. According to  $\mathbf{Z}_{rf}$ , the optimization of  $\mathbf{Z}_{bb}$  can be formulated as

$$\mathbf{Z}_{bb} = \arg \min_{\mathbf{Z}_{bb}} \|\mathbf{Z}_{opt} - \mathbf{Z}_{bb}\mathbf{Z}_{rf}\|_F^2 \quad (3.31)$$

The solution of this least squares problem is

$$\mathbf{Z}_{bb} = \mathbf{Z}_{opt}\mathbf{Z}_{rf}^H(\mathbf{Z}_{rf}\mathbf{Z}_{rf}^H)^{-1} \quad (3.32)$$

### 3.2.3 Performance Evaluation

In this section, the efficiency of our proposed algorithm is validated by means of decoding performance, i.e., the frame error rate (FER). Here we employ the standard soft-input soft-output maximum a-posteriori (MAP) demapper and decoder. A wireless transceiver system operating at 60 GHz is set up in an indoor non-line-of-sight (NLOS) environment. For demonstration purposes, it is assumed that the total transmits power across all transmit antennas is normalized to unity with  $\mathcal{P}_0 = 1$ . Without specific mention, the default system parameters are as follows: the code rate is set to  $r_c = 2/3$ , LDPC code, and a rectangular 16-QAM modulation with Gray mapping are employed for the transmission [87]. As mentioned earlier, each channel realization is

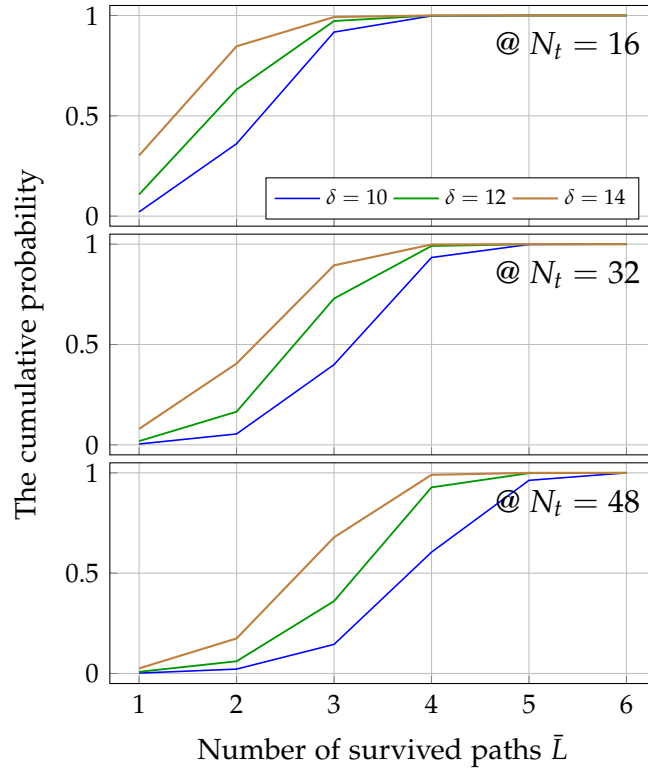
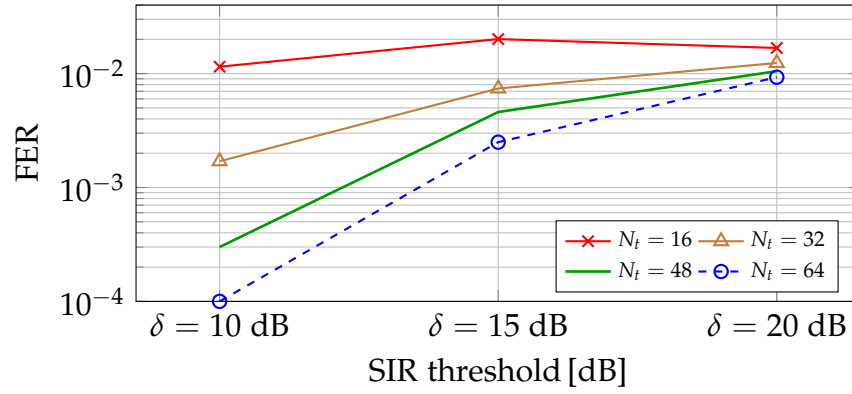


**Figure 3.10:** The CDFs of the number of survived paths under various number of antennas and SIR threshold.

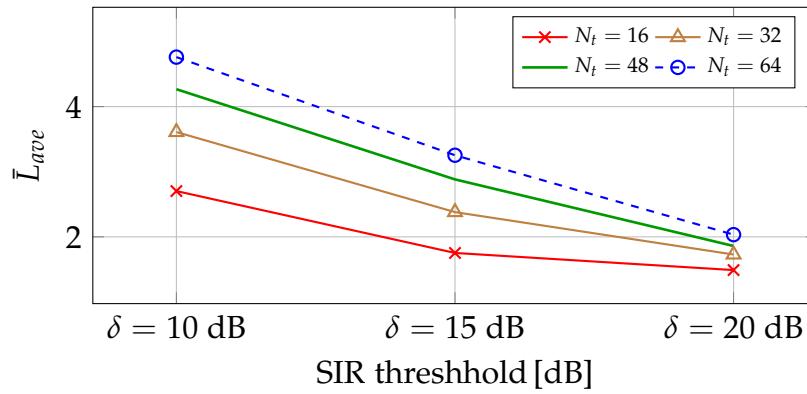
generated using the 60 GHz NLOS multipath channel model for the residential scenario CM2.3 [124]. In addition, the channel realization  $\mathbf{H}$  is assumed to keep invariant during one codeword transmission.

Fig. 3.10 depicts the dependence of the cumulative distribution functions (CDF) of the number of survived paths  $\bar{L}$  on the number of transmit antennas  $N_t$  and the SIR threshold  $\delta$ . It can be observed from the figures that the number of survived paths  $\bar{L}$  is proportional to the value of  $N_t$ . As we know, the larger the  $N_t$  is, the narrower the beam can be formed, and lesser interference is introduced in the other directions. Thus it can be noted that with the increasing number of antennas, the curve shifts towards the right side, representing the survival of more paths, i.e., higher  $\bar{L}$ . Another factor influencing the probability of  $\bar{L}$  is the SIR threshold  $\delta$ . A lower threshold indicates which is easier to be met leads to the survival of more paths as a consequence. As shown in Fig. 3.10, the curve shifts towards the right, indicating a higher  $\bar{L}$  as the SIR threshold decreases.

The effect of the SIR threshold on the decoding performance, i.e., FER, and the average survived paths,  $\bar{L}_{ave}$  is illustrated in Fig. 3.11, where different plots with various number of transmitter antennas  $N_t$ , are depicted. As it can be observed, the average number of survived paths is reduced with the increase of the threshold, since the tolerance for beam spacing is reduced to meet such high performance metric. Ow-



(a) Decoding Performance



(b) Average survived paths number

**Figure 3.11:** The effect of SIR threshold on FER and average number of survived paths where the codeword length is 576,  $N_r = 16$ ,  $N_s = 2$  and the SNR for  $N_t = 16, 32$  is @ 2 dB and for  $N_t = 48, 64$  is @ -2 dB for demonstration purpose.

ing to this, there is a degradation in channel gain, which further increases the FER. Moreover, this also results in the reduction of freedom of the channel, which further leads to lower data rates. On the other hand, increasing the SIR threshold can achieve higher received SNR and significant reduction in the frequency selectivity, with which the equalization complexity at the user side can be reduced. While the threshold is high enough, the frequency selectivity becomes negligible, and therefore the equalizer becomes unnecessary.

Considering another perspective, the gain on each subchannel is higher as the threshold raises. As a consequence of the increased capacity, higher-order modulation can be employed. This then results in an enhancement of the overall data rate. However, as previously mentioned, increasing the threshold reduces the channel rank and further the data rate. The overall effect is that the data rate is reduced with an increase of  $\delta$ , which is demonstrated in Fig. 3.12.

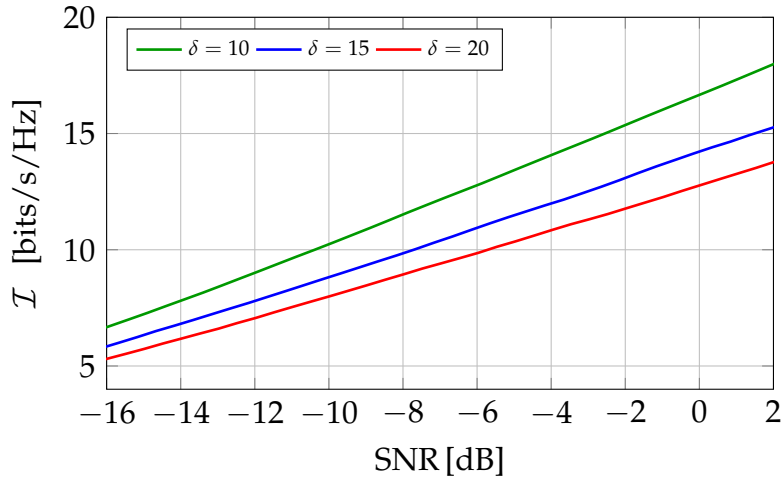


**Figure 3.12:** The effect of SIR threshold on the information rate in a  $16 \times 16$  MIMO system, where the number of data streams  $N_s = 2$ .

To conclude, a trade-off between the performance of the system, i.e., the data rates and the complexity of the equalizer, should be observed, aiming at the setting of the SIR threshold based on the system requirements.

### 3.3 Summary

In this chapter, we have proposed the TDC technology to mitigate the severe frequency selectivity effects at the 60 GHz band. The simulation results indicate that the approximate flat fading channel obtained by TDC has advantages for both the ergodic and outage capacity. Even just one-tap MMSE equalizer employed at the user side can achieve comparable BER performance to the flattened fading case when the sample duration is equal to or less than the symbol rate, which is not a challenge for hardware implementation at 60 GHz. This performance evaluation supports our proposal that TDC makes the channel flat, reduces the receiver complexity, and improves the system performance. Meanwhile, in order to achieve a flat fading channel, the best possible beam separation is necessary. A SIR constrained capacity maximization algorithm has been proposed, devoted to a joint design of the precoder and combiner, which is implemented with a two-fold aim of flattening the channel and maximizing the capacity. Numerical results to evaluate the performance of the proposed system, i.e., hybrid beamforming with TDC, have also been presented in terms of the FER and information rate.





## Chapter 4

# Performance Analysis on Hybrid Beamforming Approach

---

In this chapter, the investigation of PHY layer parameters and algorithms on the hybrid beamforming approach proposed in Chapter 3 has been performed. Digital baseband processing is a broad topic that includes many signals processing functionality modules such as baseband modulation schemes, channel estimation, MIMO pre-/post-processing, forward error correction, interleaving, and convolutional code. In this thesis, we mainly focus on MIMO pre-/post-processing, channel estimation, and equalization for large scale MIMO systems.

To obtain the maximum information rate, in Section 4.1, we propose a joint design of digital baseband pre- and post-processing based on a weighted minimum mean square error (MMSE) criterion under a transmit power constraint. Further, the optimization in the RF domain is specified into three criteria by taking various error weights into account. For ease of hardware implementation, we also develop a transceiver with lower complexity where pre-processing in the RF domain after up-conversion is implemented merely using analog phase shifters.

While employing such large antenna arrays, it becomes challenging to estimate the mmWave channel using conventional algorithms. In Section 4.2, we develop two novel multi-resolution mmWave channel estimation algorithms that exploit two dimensional discrete Fourier transform (DFT) technique inspired by the sparse nature of the mmWave channel. The proposed algorithms take into account practical radio frequency (RF) hardware limitations and computational complexity reduction during the training phases.

Due to broad bandwidth at 60GHz, the channel suffers severe frequency selectivity, making equalization much more complicated for SC modulation. To reduce the power consumption and the complexity of equalizer at the user side, we consider SC systems and try to make channels flat over a wide bandwidth. In Section 4.3, we propose two frequency selective hybrid precoding solutions, namely time delay compensation (TDC) based time-domain equalization (TDE) and phase shift compensation (PSC) based frequency domain equalization (FDE). First, we implement sectorized beamforming in the RF domain to compensate for the large path-loss at mmWave range and reduce the intra-cluster delay spread. Here, the RF precoder is assumed to be frequency flat during one block transmission due to the independence of RF precoder design on the time delay spread. Subsequently, adopting TDC for TDE and PSC for FDE in digital baseband to reduce frequency selectivity, the baseband precoder is designed to maximize the achievable capacity given in Section 4.1.

The results presented in the chapter have been published in part by the author in [22, 56, 105, 109, 111–113].

## 4.1 Joint Pre-/Post-Processing Design

In mmWave systems, the small wavelength enables pre-processing, exploiting large antenna arrays to provide the required gain [11]. Generally, in traditional microwave systems, pre-processing is done at the digital baseband. However, the cost and power consumption of a radio frequency (RF) chain, which translates RF and digital baseband, is too high for each antenna element to afford. This hardware limitation places additional constraints on pre-processing design. Therefore, we use hybrid spatial processing architecture within which the number of RF chains is lower than the number of antenna elements. There are two kinds of common structures: fully-connected structure and array-of-subarray structure.

**Fully-connected structure:** For the fully-connected structure in Fig. 4.1, each RF chain is connected to all antennas [18]. In order to decrease the system's complexity, a low complexity structure is defined in the following chapter, where the beam pattern is generated only by the phase shifter other than adjusting both the amplitude and phase of the signal. In this chapter, we employ a fully-connected structure with high complexity, which can achieve an optimal capacity, only as a benchmark for performance comparison.

**Array-of-subarray structure:** As shown in Fig. 4.2, the array-of-subarray structure is more practical for the antenna deployment of the base station in the 3G and 4G LTE systems [41], where each RF chain is generally connected to an antenna array [40]. The subarray antenna element spacing is assumed to be smaller than the wavelength. Thus there exists a high level of antenna correlation. We further assume the space between adjacent subarrays is much larger than the wavelength so that the channels of different subarrays are independent. In addition, the distance from any user to the AP is assumed to be much larger than the spaces among different subarrays. The complexity of the array-of-subarray structure is much reduced compared to the fully-connected structure, also, by only using the phase shifter as given in Fig. 4.2 instead of the combining of the phase shifter and PA can further decrease the complexity of the system, which is more realistic for mmWave systems.

### 4.1.1 Fully-connected Structure

#### 4.1.1.1 System Model

In this section, we construct a mmWave system model under a single-user scenario with digital baseband pre-processing followed by constrained RF pre-processing.

Our single user mmWave MIMO system model is presented in Fig. 4.1. The input bit streams are coded and modulated to generate  $N_s$  parallel data streams launched through  $N_t$  transmit antennas.  $N_{rf}^t$  RF chains are employed at the transmitter side

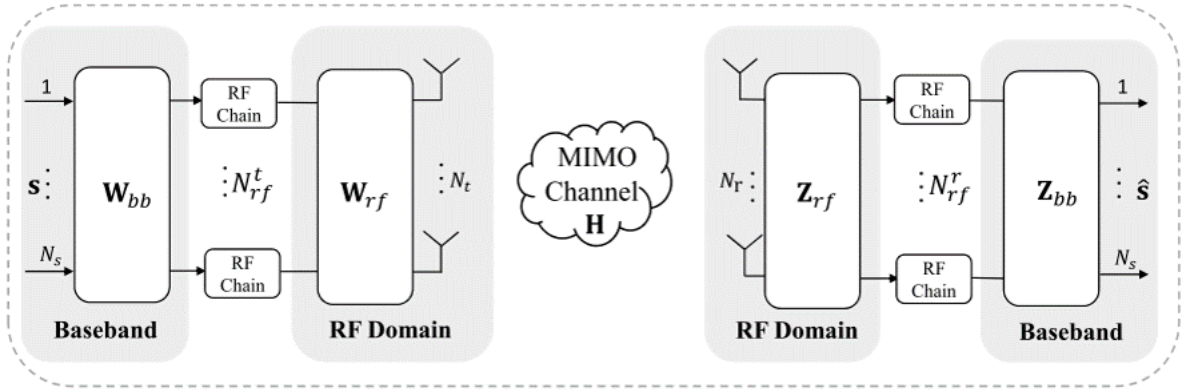


**Figure 4.1:** Block diagram of a large millimeter wave hybrid spatial processing system

with  $N_s \leq N_{rf}^t \leq N_t$ . The symbol vector  $\mathbf{s}$  is processed by the  $N_{rf}^t \times N_s$  digital baseband pre-processing  $\mathbf{W}_{bb}$ , followed by the  $N_t \times N_{rf}^t$  RF pre-processing  $\mathbf{W}_{rf}$ .

For a MIMO flat fading channel, the received signal is

$$\mathbf{y} = \mathbf{H}\mathbf{W}_{rf}\mathbf{W}_{bb}\mathbf{s} + \mathbf{n} \quad (4.1)$$

where  $\mathbf{y}$  is the  $N_r \times 1$  received vector,  $\mathbf{H}$  represents the  $N_r \times N_t$  channel matrix and  $\mathbf{n}$  stands for the  $N_r \times 1$  noise vector of i.i.d.  $\mathcal{CN}(0, \mathbf{R}_{nn})$ . In addition,  $\mathbf{R}_{nn} = \sigma_n^2 \mathbf{I}_{N_r}$  is noise covariance matrix. In order to simplify the optimization problem, we impose  $\mathbf{W}_{rf}^H \mathbf{W}_{rf} = \mathbf{I}_{N_{rf}^t}$ . In this manner, the total power constraint is  $\text{Tr}(\mathbf{W}_{bb} \mathbf{W}_{bb}^H) \leq \mathcal{P}_0$ , where  $\mathcal{P}_0$  is the total available transmitter power. In this thesis, we implicitly assume perfect synchronization. Moreover, we assume that

$$E(\mathbf{s}\mathbf{s}^H) = \mathbf{I}; \quad E(\mathbf{s}\mathbf{n}^H) = \mathbf{0} \quad (4.2)$$

Note that for simplicity of analysis, we have assumed uncorrelated input sources, each normalized to unit power and  $N_s \leq \text{rank}(\mathbf{H})$ . Besides, we assume that channel state information (CSI) is known to both the transmitter and receiver. Although large antenna arrays are employed, CSI can still be acquired smoothly by certain strategies, such as channel estimation based on reciprocity in time division duplex (TDD) systems.

The receiver is equipped with  $N_{rf}^r$  RF chains that are used to receive  $N_s$  data streams with  $N_s \leq N_{rf}^r \leq N_r$ . The processed signal is

$$\hat{\mathbf{s}} = \mathbf{Z}_{bb} \mathbf{G} \mathbf{W}_{bb} \mathbf{s} + \mathbf{Z}_{bb} \mathbf{Z}_{rf} \mathbf{n} \quad (4.3)$$

where  $\mathbf{G}$  represents the equivalent digital MIMO channel of size  $N_{rf}^r \times N_{rf}^t$  which is given by  $\mathbf{G} = \mathbf{Z}_{rf}^H \mathbf{H} \mathbf{W}_{rf}$ .  $\mathbf{Z}_{rf}$  is the  $N_{rf}^r \times N_r$  RF post-processing matrix and  $\mathbf{Z}_{bb}$  denotes the  $N_s \times N_{rf}^r$  digital baseband post-processing matrix.

At the mmWave carrier frequency, the high path loss leads to limited spatial selectivity, and signal propagations may exhibit intensive multipath trajectories phenomenon. Meanwhile, tightly packed large antenna arrays lead to higher antenna correlation. Therefore, the Rayleigh model is not suitable anymore. Instead, we consider the most popular channel model based on the modified Saleh-Valenzuela (S-V) Model in mmWave channel modeling [55, 96, 104]. The impulse response of the channel is considered as

$$h(t, \phi) = \sum_{l=0}^{L-1} \sum_{k=0}^{K_l-1} \alpha_{k,l} \delta(t - T_l - \tau_{k,l}) \delta(\phi - \Psi_l - \psi_{k,l}) \quad (4.4)$$

where  $L$  is the number of clusters and  $K_l$  is the number of multipath components in the  $l$ th cluster. The parameter  $\alpha_{k,l}$  represents multipath gain coefficient of the  $k$ th multipath component in the  $l$ th cluster, which follows a log-normal distribution.  $T_l$  denotes arrival time of the first ray in the  $l$ th cluster and  $\tau_{k,l}$  is delay of the  $k$ th multipath component within the  $l$ th cluster relative to the first path arrival time  $T_l$ . The mean angle of arrival of  $l$ th cluster  $\Psi_l$  is characterized by a uniform distribution  $U[0, 2\pi)$ . Then, within the active range of each cluster, the multipath component arrival angle  $\psi_{k,l}$  follows a zero mean Laplacian distribution with a standard deviation  $\sigma_G$  [96]

$$p(\psi_{k,l}) = \frac{1}{\sqrt{2}\sigma_G} \exp(-|\sqrt{2}\psi_{k,l}/\sigma_G|) \quad (4.5)$$

For simplicity of elaboration, we employ the  $N$ -element uniform linear array (ULA) in the following analysis. The array factor can be expressed by [20]

$$A^{ULA}(\phi) = \sum_{n=0}^{N-1} \exp(j2\pi nd \sin(\phi)/\lambda) \quad (4.6)$$

where  $d$  is the element spacing distance while  $\lambda$  represents the wavelength. And  $\phi$  corresponds to the polar angle with respect to  $x$ -axis since the antenna elements are located along  $y$ -axis.

The IEEE task group 802.15.3c has developed a channel model for a variety of indoor scenarios. Our emphasis of this section would be laid on the non-line-of-sight (NLOS) channel model for the residential scenario [121].

#### 4.1.1.2 Problem Formulation

In this section, we specify three criteria which help to optimize the pre-processing matrices  $\mathbf{W}_{bb}$ ,  $\mathbf{W}_{rf}$  and post-processing matrices  $\mathbf{Z}_{bb}$ ,  $\mathbf{Z}_{rf}$ . To simplify this optimization problem, we first derive a closed-form expression for digital baseband pre-processing and post-processing with a weighted MMSE criterion [28, 80, 81], under a constraint of certain total transmit power across all transmit antennas. Secondly, the optimization in RF domain is performed based on three criteria sorted by various error weights: 1) maximum information rate (MIR); 2) unweighted MMSE criterion; 3) SNR based

criterion (we show how to achieve any set of relative SNRs across subchannels). Afterward, with the help of the front-end phase rotation technique [68], a low complexity transceiver is attained so that the realization complexity accompanying the product costs are decreased.

As mentioned earlier,  $\mathbf{G}$  has been treated as an equivalent channel matrix. Therefore, our first aim is to derive the baseband pre-processing and post-processing matrices  $\mathbf{W}_{bb}$  and  $\mathbf{Z}_{bb}$ , respectively. The error vector is given by

$$\mathbf{e} = \mathbf{s} - \hat{\mathbf{s}} = \mathbf{s} - (\mathbf{Z}_{bb}\mathbf{G}\mathbf{W}_{bb}\mathbf{s} + \mathbf{Z}_{bb}\mathbf{Z}_{rf}\mathbf{n}) \quad (4.7)$$

According to  $\mathbf{e}$ , the weighted combination of symbol estimation errors can be represented by  $E[\mathbf{e}^H \mathbf{Y}^{H1/2} \mathbf{Y}^{1/2} \mathbf{e}]$ , where  $\mathbf{Y}^{1/2}$  is the  $N_s \times N_s$  square root of a diagonal positive definite error weight matrix  $\mathbf{Y}$ . Now, we denote the objective function as

$$\begin{aligned} \zeta(\mathbf{W}_{bb}, \mathbf{Z}_{bb}) &= E[\mathbf{e}^H \mathbf{Y}^{H1/2} \mathbf{Y}^{1/2} \mathbf{e}] \\ &= \text{Tr}[\mathbf{Y} \mathbf{R}_{ee}(\mathbf{W}_{bb}, \mathbf{Z}_{bb})] \end{aligned} \quad (4.8)$$

where  $\mathbf{R}_{ee}(\mathbf{W}_{bb}, \mathbf{Z}_{bb})$  is the error covariance matrix. Based on (4.7) and the assumption listed in (4.2), we can modify the error covariance matrix into

$$\begin{aligned} \mathbf{R}_{ee}(\mathbf{W}_{bb}, \mathbf{Z}_{bb}) &= (\mathbf{Z}_{bb}\mathbf{G}\mathbf{W}_{bb} - \mathbf{I})(\mathbf{Z}_{bb}\mathbf{G}\mathbf{W}_{bb} - \mathbf{I})^H \\ &\quad + \mathbf{Z}_{bb}\tilde{\mathbf{R}}_{nn}\mathbf{Z}_{bb}^H \end{aligned} \quad (4.9)$$

where  $\tilde{\mathbf{R}}_{nn} = \mathbf{Z}_{rf}\mathbf{R}_{nn}\mathbf{Z}_{rf}^H$ . To obtain  $\zeta(\mathbf{W}_{bb}, \mathbf{Z}_{bb})$ , we have used the fact that  $a = \text{Tr}(a)$  for scalar  $a$ ,  $\text{Tr}(\mathbf{AB}) = \text{Tr}(\mathbf{BA})$ , and the linearity of the expectation ( $E$ ) and the trace operators.

The optimization problem can be concluded by

$$\begin{aligned} \min_{\mathbf{W}_{bb}, \mathbf{Z}_{bb}} \quad & \zeta(\mathbf{W}_{bb}, \mathbf{Z}_{bb}) \\ \text{s.t.} \quad & \text{Tr}(\mathbf{W}_{bb}\mathbf{W}_{bb}^H) \leq \mathcal{P}_0 \end{aligned} \quad (4.10)$$

where the optimal solutions  $\mathbf{W}_{bb}$  and  $\mathbf{Z}_{bb}$  are shown in [80,81] respectively.

#### 4.1.1.3 Joint Pre- and Post-Processing Design

To describe the optimum  $\mathbf{W}_{bb}$  and  $\mathbf{Z}_{bb}$ , eigenvalue decomposition (ED) is applied to  $\mathbf{G}^H \tilde{\mathbf{R}}_{nn}^{-1} \mathbf{G}$  and the conduction is presented by

$$\mathbf{G}^H \tilde{\mathbf{R}}_{nn}^{-1} \mathbf{G} = (\mathbf{V} \quad \tilde{\mathbf{V}}) \begin{pmatrix} \Lambda & \mathbf{0} \\ \mathbf{0} & \tilde{\Lambda} \end{pmatrix} (\mathbf{V} \quad \tilde{\mathbf{V}})^H \quad (4.11)$$

where  $\mathbf{V}$  is an orthogonal matrix of size  $N_{rf}^t \times N_s$  which is constructed from the first  $N_s$  columns of singular vector matrix and  $\Lambda$  is a diagonal matrix in which the  $N_s$  eigenvalues are located on the diagonal following a decreasing order.  $\tilde{\Lambda}$  contains the zero

eigenvalues. Note that we assume  $N_s = \text{rank}(\mathbf{G})$ . For the case when  $N_s < \text{rank}(\mathbf{G})$ , it is likely that eigenmode transmission is still optimum. In this circumstance, the power is allocated to only those  $N_s$  eigenmodes.

**Lemma 1.** *The optimum  $\mathbf{W}_{bb}$  and  $\mathbf{Z}_{bb}$  minimizing (4.8) is given by [81]*

$$\mathbf{W}_{bb} = \mathbf{V}\Phi_f \quad (4.12)$$

$$\mathbf{Z}_{bb} = \Phi_w \mathbf{V}^H \mathbf{G}^H \tilde{\mathbf{R}}_{nn}^{-1} \quad (4.13)$$

where  $\Phi_f$  and  $\Phi_w$  are diagonal matrices given by

$$\Phi_f = (\mu^{-1/2} \Lambda^{-1/2} \mathbf{Y}^{1/2} - \Lambda^{-1})_+^{1/2} \quad (4.14)$$

$$\Phi_w = (\mu^{1/2} \Lambda^{-1/2} \mathbf{Y}^{-1/2} - \mu \Lambda^{-1} \mathbf{Y}^{-1})_+^{1/2} \Lambda^{-1/2} \quad (4.15)$$

The Lagrange multiplier is given by

$$\mu^{1/2} = \frac{\text{Tr}(\Lambda^{-1/2} \mathbf{Y}^{1/2})}{\mathcal{P}_0 + \text{Tr}(\Lambda^{-1})} \quad (4.16)$$

*Proof.* See [81]. □

By choosing an appropriate error weight matrix  $\mathbf{Y}$ , we can obtain different  $\mathbf{W}_{bb}$  and  $\mathbf{Z}_{bb}$  corresponding to different applications. While the error weight matrix  $\mathbf{Y} = \Lambda$ , the maximization of information rate could be achieved. While the error weight matrix  $\mathbf{Y} = \mathbf{I}$ , we obtain the jointly optimal linear pre-processing and post-processing that minimize the sum of symbol estimation errors, namely MMSE. This design criterion is well known in literature [85]. It is also possible to choose different error weight matrix  $\mathbf{Y}$  to obtain specific relative SNRs on each subchannel. A comprehensive description for these design criteria and the optimization of RF matrices  $\mathbf{W}_{rf}$  and  $\mathbf{Z}_{rf}$  are presented in the following subsections.

**Maximum Information Rate Criterion:** We aim at maximizing the information rate by using layered pre-processing  $\mathbf{W}_{bb}$  and  $\mathbf{W}_{rf}$ . The information rate is denoted by  $\mathcal{I}$  and equal to

$$\mathcal{I} = \log_2(|\mathbf{I}_{N_s} + (\mathbf{Z}_{bb} \mathbf{G} \mathbf{W}_{bb})^H (\mathbf{Z}_{bb} \tilde{\mathbf{R}}_{nn} \mathbf{Z}_{bb}^H)^{-1} \quad (4.17)$$

$$(\mathbf{Z}_{bb} \mathbf{G} \mathbf{W}_{bb})|) \quad (4.18)$$

Based on Lemma 1, the optimum pre-processing and post-processing diagonalize the equivalent channel matrix  $\mathbf{G}$  into eigenmodes for any set of error weight  $\mathbf{Y}$ . More specifically, we can get

$$\mathbf{Z}_{bb} \mathbf{G} \mathbf{W}_{bb} = \Phi_w \Lambda \Phi_f \quad (4.19)$$

$$\mathbf{Z}_{bb} \tilde{\mathbf{R}}_{nn} \mathbf{Z}_{bb}^H = \Phi_w^2 \Lambda \quad (4.20)$$

The information rate thereby is changed to

$$\mathcal{I} = \log_2(|\mathbf{I}_{N_s} + \mathbf{\Phi}_f^2 \mathbf{\Lambda}|) \quad (4.21)$$

To achieve maximum information rate,  $\mathbf{\Phi}_f$  should be chosen according to the well-known waterfilling solution [80,81,85]. While the error matrix  $\mathbf{Y} = \mathbf{\Lambda}$ , the  $\mathbf{\Phi}_f$  obtained from weighted MMSE design leads to the waterfilling solution given by

$$\mathbf{\Phi}_f^2 = \left( \frac{\mathcal{P}_0 + \text{Tr}(\mathbf{\Lambda}^{-1})}{N_s} \mathbf{I} - \mathbf{\Lambda}^{-1} \right)_+ \quad (4.22)$$

So far, we have calculated the optimum values for  $\mathbf{W}_{bb}$  and  $\mathbf{Z}_{bb}$ . Now, we extend the optimization problem to

$$\max_{\mathbf{W}_{rf}, \mathbf{Z}_{rf}} \mathcal{I} = \log_2 \left( \left| \frac{\mathcal{P}_0 + \text{Tr}(\mathbf{\Lambda}^{-1})}{N_s} \mathbf{\Lambda} \right| \right) \quad (4.23)$$

for the calculation of optimum matrices  $\mathbf{W}_{rf}$  and  $\mathbf{Z}_{rf}$ .

Maximizing the objective function (4.23) is a non-linear optimization problem. The proposed work in [86] suggests that the optimization results presented by applying determinant and trace are identical. Therefore, we propose to optimize the lower bound of the information rate defined by the trace. For a real convex function  $\phi(x) = 1/x, x > 0$ , according to Jensen's inequality, we have  $\text{Tr}(\mathbf{\Lambda}^{-1})/n \geq n/\text{Tr}(\mathbf{\Lambda})$ , where  $\mathbf{\Lambda}$  is a  $n \times n$  diagonal matrix. Then, the following equation holds

$$\left( \frac{\mathcal{P}_0 + \text{Tr}(\mathbf{\Lambda}^{-1})}{N_s} \right) \text{Tr}(\mathbf{\Lambda}) \geq 1 + \frac{\mathcal{P}_0 \text{Tr}(\mathbf{\Lambda})}{N_s} \quad (4.24)$$

Thus, the capacity maximization problem in (4.23) is simplified to

$$\max_{\mathbf{W}_{rf}, \mathbf{Z}_{rf}} \text{Tr}(\mathbf{\Lambda}) \quad (4.25)$$

with

$$\text{Tr}(\mathbf{\Lambda}) = \text{Tr}(\mathbf{G}^H \tilde{\mathbf{R}}_{nn}^{-1} \mathbf{G}) = \text{Tr}(\mathbf{W}_{rf}^H \mathbf{H}^H \mathbf{R}_{nn}^{-1} \mathbf{H} \mathbf{W}_{rf}) \quad (4.26)$$

According to maximum property of Ky Fan Theorem [36], the optimum RF matrix  $\mathbf{W}_{rf}$  is an isomorphic matrix containing the first  $N_{rf}^t$  eigenvectors of right singular vector matrix of  $\mathbf{H}$ . Note that  $\mathbf{Z}_{rf}$  can be an arbitrary invertible matrix since it does not form a part of the expression for the maximum information rate given by (4.25). For the sake of completeness, we can let  $\mathbf{Z}_{rf}$  be conjugate transpose of the matrix containing the first  $N_{rf}^r$  eigenvectors of the left singular vector matrix of channel matrix  $\mathbf{H}$ .

**Unweighted MMSE Criterion:** As mentioned before, unweighted MMSE design can be derived by setting error matrix  $\mathbf{Y} = \mathbf{I}$ . Based on Lemma 1, (4.19) and (4.20), the error covariance matrix  $\mathbf{R}_{ee}$  in (4.9) can be modified to

$$\mathbf{R}_{ee} = \mathbf{\Lambda}^{-1/2} \mu^{1/2} = \frac{\text{Tr}(\mathbf{\Lambda}^{-1/2})}{\mathcal{P}_0 + \text{Tr}(\mathbf{\Lambda}^{-1})} \mathbf{\Lambda}^{-1/2} \quad (4.27)$$

From (4.27), we derive one optimization criterion

$$\min_{\mathbf{W}_{rf}, \mathbf{Z}_{rf}} \text{Tr} \left( \frac{\text{Tr}(\mathbf{\Lambda}^{-1/2})}{\mathcal{P}_0 + \text{Tr}(\mathbf{\Lambda}^{-1})} \mathbf{\Lambda}^{-1/2} \right) \quad (4.28)$$

Given that  $\text{Tr}(\mathbf{AB}) \leq \text{Tr}(\mathbf{A})\text{Tr}(\mathbf{B})$ , where  $\mathbf{A}$  and  $\mathbf{B}$  are non-negative definite matrices, the following equation holds

$$\frac{\text{Tr}(\mathbf{\Lambda}^{-1/2})}{\mathcal{P}_0 + \text{Tr}(\mathbf{\Lambda}^{-1})} \text{Tr}(\mathbf{\Lambda}^{-1/2}) \geq \frac{\text{Tr}(\mathbf{\Lambda}^{-1})}{\mathcal{P}_0 + \text{Tr}(\mathbf{\Lambda}^{-1})} \quad (4.29)$$

Therefore, the optimization criterion can be modified to

$$\min_{\mathbf{W}_{rf}, \mathbf{Z}_{rf}} \text{Tr}(\mathbf{\Lambda}^{-1}) \quad (4.30)$$

In line with minimum property of Ky Fan Theorem [36], the optimization of RF matrices  $\mathbf{W}_{rf}$  and  $\mathbf{Z}_{rf}$  obtains the same solutions as in maximum information rate criterion. It is noteworthy that minimizing the MSE does not specifically mean a reduction in the probability of error (PoE). The unweighted MMSE design improves the overall system performance only by minimizing the sum of the symbol estimation errors across all subchannels. Again, it does not guarantee that the MSE and SNR on each subchannel is minimized. In contrast with maximum information rate criterion, more power is allocated to the weaker eigenmodes in unweighted MMSE criterion.

**SNR Based Criterion:** Consider a MIMO spatial multiplexing system through which independent data streams are transmitted on different subchannels. On one hand, for fixed rate systems in which the transmission of data streams requires identical modulation and coding strategy, all subchannels should have equal errors. On the other hand, while a multimedia application simultaneously transmits diverse types of information on multiple subchannels (e.g, videos typically require a higher SNR than audios for successful transmission), individual subchannels should have different SNRs. To satisfy the requirements of various applications, a SNR based criterion should be derived.

The SNR matrix is defined as

$$\mathbf{\Gamma} = (\mathbf{Z}_{bb} \mathbf{G} \mathbf{W}_{bb})^H (\mathbf{Z}_{bb} \tilde{\mathbf{R}}_{nn} \mathbf{Z}_{bb}^H)^{-1} (\mathbf{Z}_{bb} \mathbf{G} \mathbf{W}_{bb}) \quad (4.31)$$



According to Lemma 1, (4.19) and (4.20), equation (4.31) can be simplified to

$$\mathbf{\Gamma} = \mathbf{\Phi}_f^2 \mathbf{\Lambda} \quad (4.32)$$

Define a diagonal matrix  $\mathbf{S}$  in which the element  $s_{i,i}$  corresponds to relative SNRs across different subchannels with  $\sum_{i=1}^{N_s} s_{i,i} = 1$ . From (4.32), we can obtain

$$\mathbf{\Gamma} = \mathbf{Y}^{1/2} \mu^{-1/2} \mathbf{\Lambda}^{1/2} - \mathbf{I} = \gamma \mathbf{S} \quad (4.33)$$

where  $\gamma > 0$  is a scalar. Then the error weight matrix is given by

$$\mathbf{Y}^{1/2} = (\mathbf{I} + \gamma \mathbf{S}) \mathbf{\Lambda}^{-1/2} \mu^{1/2} \quad (4.34)$$

Substituting this expression for  $\mathbf{Y}^{1/2}$  into (4.16), we obtain

$$\gamma = \frac{\mathcal{P}_0}{\text{Tr}(\mathbf{\Lambda}^{-1} \mathbf{S})} \quad (4.35)$$

Then, we can further derive another optimization criterion based on (4.33)

$$\max_{\mathbf{W}_{rf}, \mathbf{Z}_{rf}} \text{Tr}(\gamma \mathbf{S}) = \frac{\mathcal{P}_0}{\text{Tr}(\mathbf{\Lambda}^{-1} \mathbf{S})} \text{Tr}(\mathbf{S}) \quad (4.36)$$

Using the fact that  $\text{Tr}(\mathbf{AB}) \leq \text{Tr}(\mathbf{A})\text{Tr}(\mathbf{B})$ , we can derive a lower bound

$$\begin{aligned} \frac{\mathcal{P}_0}{\text{Tr}(\mathbf{\Lambda}^{-1} \mathbf{S})} \text{Tr}(\mathbf{S}) &\geq \frac{\mathcal{P}_0}{\text{Tr}(\mathbf{\Lambda}^{-1}) \text{Tr}(\mathbf{S})} \text{Tr}(\mathbf{S}) \\ &= \frac{\mathcal{P}_0}{\text{Tr}(\mathbf{\Lambda}^{-1})} \end{aligned} \quad (4.37)$$

Now, the SNR based criterion can be reformed into

$$\min_{\mathbf{W}_{rf}, \mathbf{Z}_{rf}} \text{Tr}(\mathbf{\Lambda}^{-1}) \quad (4.38)$$

The optimum solutions  $\mathbf{W}_{rf}$  and  $\mathbf{Z}_{rf}$  are the same as determined by equation (4.30). Combined with the preceding analyses, it holds that the pre- and post-processing in the RF domain are identical for all the criteria. Obviously, the contribution of  $\mathbf{W}_{rf}$  and  $\mathbf{Z}_{rf}$  to the hybrid system is to decouple the MIMO channel into eigen subchannels. Therefore only the power allocations across the eigen subchannels which are implemented in digital baseband need to be computed depending on the different criterion.

#### 4.1.1.4 Low Complexity Transceiver

So far we have extracted the optimum pre-processing  $\mathbf{W}_{bb}$ ,  $\mathbf{W}_{rf}$  and post-processing  $\mathbf{Z}_{bb}$ ,  $\mathbf{Z}_{rf}$  corresponding to different design criteria. The RF domain pre-processing  $\mathbf{W}_{rf}$  and post-processing  $\mathbf{Z}_{rf}$  contain  $N_{rf}^t$  and  $N_{rf}^r$  columns of unitary matrix, respectively.

Therefore, for each transmitter and receiver antenna in RF domain, the proposed scheme requires  $N_{rf}^t$  and  $N_{rf}^r$  pairs of variable gain amplifier (VGA) and variable phase shifter (VPS), respectively. By taking into account the two important design parameters: low-power consumption and low-complexity structure, a feasible approach that involves just shifting RF phases, rather than adjusting both the amplitude and phase of each element in mmWave system, could be derived. To obtain this, we define

$$\tilde{\mathbf{W}}_{rf} = \frac{1}{\sqrt{N_t}} \exp(j \cdot \arg(\mathbf{W}_{rf})) \quad (4.39)$$

$$\tilde{\mathbf{Z}}_{rf} = \frac{1}{\sqrt{N_r}} \exp(j \cdot \arg(\mathbf{Z}_{rf})) \quad (4.40)$$

to be the new RF domain pre-processing and post-processing matrices. Using  $\mathbf{G} = \tilde{\mathbf{Z}}_{rf} \mathbf{H} \tilde{\mathbf{W}}_{rf}$ , we get a new equivalent digital MIMO channel. Then, (4.11) and Lemma 1 are applied to calculate the new baseband pre-processing matrix  $\mathbf{W}_{bb}$  and post-processing matrix  $\mathbf{Z}_{bb}$ . Up to now, the low complexity transceiver is derived. The setting in (4.39) and (4.40) may not be optimal. The further enhancement of RF domain pre-processing and post-processing which merely contain phase shift elements remains a future topic.

#### 4.1.1.5 Complexity Analysis

The complexity comparison of the proposed schemes and AS scheme is evaluated in the following twofold considerations: the complexity of pre- and post-processing operations and the complexity of the hardware implementation.

The complexity of the hybrid spatial processing is dominated by the singular value decomposition (SVD) of channel matrix  $\mathbf{H}$ . In order to obtain the pre- and post-processing matrixes in the RF domain, one SVD of channel matrix has to be computed. The complexity of one SVD is  $\mathcal{O}(\min(N_t \times N_r^2, N_r \times N_t^2))$ . For digital baseband processing, only  $N_s$  transmit power  $\phi_i^2$  need to be calculated. In the exhaustive search AS scheme,  $\binom{N_t}{N_{rf}^t} \times \binom{N_r}{N_{rf}^r}$  subchannel matrix have to be analyzed to find the optimum one. Then, one SVD with complexity  $\mathcal{O}(\min(N_{rf}^t \times (N_{rf}^r)^2, N_{rf}^r \times (N_{rf}^t)^2))$  has to be computed.

As to the complexity of the hardware implementation the optimum scheme requires  $(N_t \times N_s + N_r \times N_s)$  pairs of VGAs and VPSs in the RF domain and  $2 \times N_s$  VGAs in digital baseband. Furthermore,  $N_t$  combiners at transmitter and  $N_r$  splitters at receiver are required. The low complexity scheme does not require VGAs in the RF domain. The AS scheme only demands  $(N_{rf}^t \times N_s + N_{rf}^r \times N_s)$  pairs of VGAs and VPSs,  $N_{rf}^t$  combiners at transmitter and  $N_{rf}^r$  splitters at receiver. In the following sections, the performance of different criteria is evaluated.

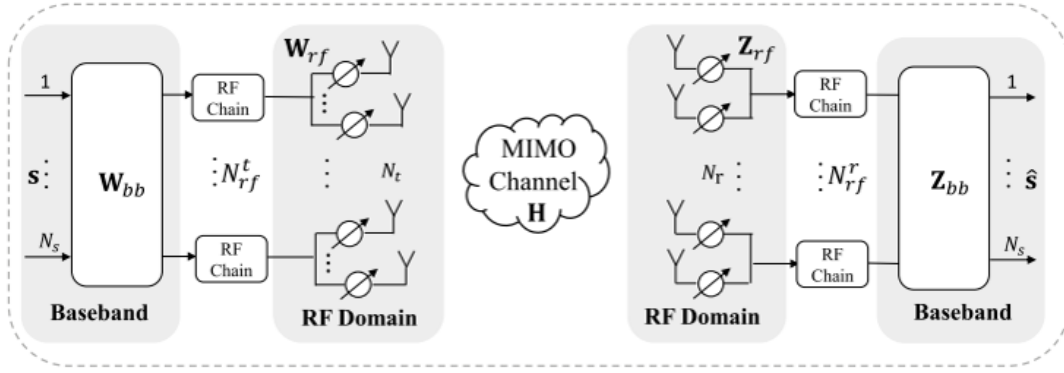


**Figure 4.2:** Block diagram of a large mmWave hybrid spatial processing system

## 4.1.2 Array-of-subarray Structure

### 4.1.2.1 System Model

The system model is illustrated in Fig. 4.2. Each antenna of the uniform linear array (ULA) is equipped with a phase shifter. These phase shifters are used to manipulate the phase of the RF signal radiation through antennas. The  $N_t$  transmitter antennas are partitioned into  $N_{rf}^t$  subarrays with each of the subarrays being driven by a digital baseband processing module. At the receiver, we employ a similar structure as that at the transmitter. The  $N_r$  receiver antennas are grouped into  $N_{rf}^r$  subarrays. The output of the subarrays are processed by a digital baseband (BB) post-processing module. The input bit stream is modulated to generate  $N_s$  parallel data streams denoted by  $\mathbf{s}$ . The  $N_s$  parallel data streams are processed by a  $N_{rf}^t \times N_s$  BB precoding matrix  $\mathbf{W}_{bb}$ . At the transmitter, each RF chain is only routed to one antenna subarray while the routing can be represented by a  $N_t \times N_{rf}^t$  matrix  $\mathbf{W}_{rf}$ . The elements of this matrix are correspondingly given by  $\mathbf{W}_{rf}(m, n) = \sqrt{1/M_t} e^{j\theta_{m,n}}$  if the  $n$ th output of BB processing module is routed to the  $m$ th antenna, and  $\mathbf{W}_{rf}(m, n) = 0$  otherwise. Then,  $\mathbf{W}_{rf}$  is given by

$$\mathbf{W}_{rf}(m, n) = \begin{cases} \frac{1}{\sqrt{M_t}} e^{j\theta_{m,n}}, & n = 1 : N_{rf}^t, \\ & m = M_t(n - 1) + 1 : M_t \times n \\ 0, & otherwise \end{cases}$$

where  $M_t = N_t / N_{rf}^t$  denotes the number of antennas in each subarray.

Similarly at the receiver, the RF post-processing matrix  $\mathbf{Z}_{rf}$  can be represented as

$$\mathbf{Z}_{rf}(m, n) = \begin{cases} \frac{1}{\sqrt{M_r}} e^{j\phi_{m,n}}, & m = 1 : N_{rf}^r, \\ & n = M_r(m - 1) + 1 : M_r \times m \\ 0, & otherwise \end{cases}$$

where  $M_r = N_r/N_{rf}^r$  denotes the number of antennas in each subarray at the receiver side. For a MIMO channel, the processed signal at the receiver is

$$\hat{\mathbf{s}} = \mathbf{Z}_{bb}\mathbf{Z}_{rf}\mathbf{H}\mathbf{W}_{rf}\mathbf{W}_{bb}\mathbf{s} + \mathbf{Z}_{bb}\mathbf{Z}_{rf}\mathbf{n} \quad (4.41)$$

where  $\mathbf{H}$  denotes the  $N_r \times N_t$  channel matrix and  $\mathbf{n}$  denotes the  $N_r \times 1$  noise vector of i.i.d.  $\mathcal{CN}(0, \mathbf{R}_{nn})$ .  $\mathbf{R}_{nn} = \sigma_n^2 \mathbf{I}_{N_r}$  is the noise covariance matrix. The total power is constrained by  $\text{Tr}(\mathbf{F}_{bb}\mathbf{F}_{bb}^H) \leq \mathcal{P}_0$ , where  $\mathcal{P}_0$  is the total power available at the transmitter. In this section, we assume that the channel state information (CSI) is perfectly known at both the transmitter and the receiver. In addition, a perfect synchronization is implicitly assumed.

For the simplicity and preciseness of analysis, we apply the most widely used modified Saleh-Valenzuela (S-V) model for channel modeling at 60 GHz [55, 96, 104]. The impulse response of the channel is given by

$$h(t, \phi) = \sum_{l=0}^{L-1} \sum_{k=0}^{K_l-1} \alpha_{k,l} \delta(t - T_l - \tau_{k,l}) \delta(\phi - \Psi_l - \psi_{k,l}) \quad (4.42)$$

where  $L$  refers to the number of clusters. In the  $l$ th cluster,  $K_l$  is the number of multipath components,  $\alpha_{k,l}$  denotes the multipath gain coefficient of the  $k$ th multipath component, which follows a log-normal distribution.  $T_l$  shows the arrival time of the first ray in the  $l$ th cluster, while  $\tau_{k,l}$  is the delay of the  $k$ th multipath component within cluster relative to the first path arrival time  $T_l$ .  $\Psi_l$ , which follows a uniform distribution  $U[0, 2\pi)$ , stands for the mean angle of arrival of  $l$ th cluster.  $\psi_{k,l}$  is the angle of arrival of the  $k$ th multipath component within cluster and follows zero mean Laplacian distribution. Its distribution is given by [96]

$$p(\psi_{k,l}) = \frac{1}{\sqrt{2}\sigma_G} \exp(-|\sqrt{2}\psi_{k,l}/\sigma_G|) \quad (4.43)$$

where  $\sigma_G$  is the standard deviation.

In this section, we consider the non-line-of-sight (NLOS) channel model for the residential scenario based on the measurements by IEEE task group 802.15.3c [124].

#### 4.1.2.2 Problem Formulation

Hybrid beamforming system design is firstly conducted in this section by means of formulation. Then we propose a two step approach to this problem in which the baseband beamforming optimization is followed by optimizing beamforming design in RF domain.

As mentioned in the introduction, the aim of this hybrid beamforming design is to maximize the information rate of the system. The information rate achieved by this system can be expressed as

$$\mathcal{I} = \log_2(|\mathbf{I} + \mathbf{\Gamma}|) \quad (4.44)$$

where  $\mathbf{\Gamma}$  is the SNR matrix defined as

$$\mathbf{\Gamma} = (\mathbf{Z}_{bb}\mathbf{Z}_{rf}\mathbf{H}\mathbf{W}_{rf}\mathbf{W}_{bb})^H \cdot (\mathbf{Z}_{bb}\mathbf{Z}_{rf}\mathbf{R}_{nn}\mathbf{Z}_{rf}^H\mathbf{Z}_{bb}^H)^{-1}(\mathbf{Z}_{bb}\mathbf{Z}_{rf}\mathbf{H}\mathbf{W}_{rf}\mathbf{W}_{bb})$$

It is assumed that the channel matrix  $\mathbf{H}$  is fixed and perfectly known at both the transmitter and the receiver. Mathematically, the optimization problem can be formulated as

$$\begin{aligned} \max_{\mathbf{W}_{bb}, \mathbf{W}_{rf}, \mathbf{Z}_{bb}, \mathbf{Z}_{rf}} \quad & \mathcal{I} = \log_2(|\mathbf{I} + \mathbf{\Gamma}|) \\ \text{s.t.} \quad & \text{Tr}(\mathbf{W}_{bb}\mathbf{W}_{bb}^H) \leq \mathcal{P}_0 \\ & \mathbf{W}_{rf}(m, n) = \frac{1}{\sqrt{M_t}} e^{j\theta_{m,n}}, \quad m, n \in \mathcal{Q}_t \\ & \mathbf{Z}_{rf}(m, n) = \frac{1}{\sqrt{M_r}} e^{j\phi_{m,n}}, \quad m, n \in \mathcal{Q}_r \end{aligned} \quad (4.45)$$

where  $\mathcal{Q}_t$  and  $\mathcal{Q}_r$  denote the set of indices in which the  $n$ th output of BB processing module is routed to the  $m$ th antenna.

#### 4.1.2.3 Baseband Beamforming Design

Suggested by Equation (4.45), the baseband and RF domain beamforming design have to be optimized jointly for an optimized hybrid beamforming design.

However, this joint optimization problem is a non-convex one for which usually no globally optimal solution is guaranteed. Additionally, general solutions to this problem with uniform elemental power constraint employed in the RF domain are not known. Therefore, we propose a two step approach to obtain a hybrid beamforming design.

Considering  $\mathbf{G} = \mathbf{Z}_{rf}\mathbf{H}\mathbf{W}_{rf}$  as the equivalent digital MIMO channel of size  $N_{rf}^r \times N_{rf}^t$ , the optimization problem can be simplified as

$$\begin{aligned} \max_{\mathbf{W}_{bb}, \mathbf{Z}_{bb}} \quad & \mathcal{I} = \log_2(|\mathbf{I}_{N_s} + \mathbf{\Gamma}|) \\ \text{s.t.} \quad & \text{Tr}(\mathbf{W}_{bb}\mathbf{W}_{bb}^H) \leq \mathcal{P}_0 \end{aligned} \quad (4.46)$$

where

$$\mathbf{\Gamma} = (\mathbf{Z}_{bb}\mathbf{G}\mathbf{W}_{bb})^H (\mathbf{Z}_{bb}\tilde{\mathbf{R}}_{nn}\mathbf{Z}_{bb}^H)^{-1} (\mathbf{Z}_{bb}\mathbf{G}\mathbf{W}_{bb})$$

and the equivalent noise covariance matrix is

$$\tilde{\mathbf{R}}_{nn} = \mathbf{Z}_{rf}\mathbf{R}_{nn}\mathbf{Z}_{rf}^H \quad (4.47)$$

It can be observed from (4.46) that both the equivalent digital MIMO channel matrix  $\mathbf{G}$  and the noise covariance matrix  $\tilde{\mathbf{R}}_{nn}$  are deterministic, if  $\mathbf{W}_{rf}$  and  $\mathbf{Z}_{rf}$  are set to values.

Once  $\mathbf{W}_{rf}$  and  $\mathbf{Z}_{rf}$  are determined, (4.46) can be solved according to the well known waterfilling solution. The closed form solution of  $\mathbf{W}_{bb}$  and  $\mathbf{Z}_{bb}$  is given by [112].

For obtaining the optimum  $\mathbf{W}_{bb}$  and  $\mathbf{Z}_{bb}$ , the eigenvalue decomposition (ED) of  $\mathbf{G}^H \tilde{\mathbf{R}}_{nn}^{-1} \mathbf{G}$  can be expressed as

$$\mathbf{G}^H \tilde{\mathbf{R}}_{nn}^{-1} \mathbf{G} = (\mathbf{V} \ \tilde{\mathbf{V}}) \begin{pmatrix} \Lambda & \mathbf{0} \\ \mathbf{0} & \tilde{\Lambda} \end{pmatrix} (\mathbf{V} \ \tilde{\mathbf{V}})^H \quad (4.48)$$

where  $\mathbf{V}$  is constructed from the first  $N_s$  columns of singular vector matrix and represents an orthogonal matrix of size  $N_{rf}^t \times N_s$ . It should be noted that  $N_s \leq \text{rank}(\mathbf{G})$  is assumed.  $\Lambda$  denotes a diagonal matrix, in which the  $N_s$  eigenvalues are in a decreasing order along the diagonal and  $\tilde{\Lambda}$  describes the zero eigenvalues.

**Lemma 2.** *The solution of  $\mathbf{W}_{bb}$  and  $\mathbf{Z}_{bb}$  can be represented as*

$$\mathbf{W}_{bb} = \mathbf{V} \Phi_f \quad (4.49)$$

$$\mathbf{Z}_{bb} = \Phi_w \mathbf{V}^H \mathbf{G}^H \tilde{\mathbf{R}}_{nn}^{-1} \mathbf{G} \mathbf{V} \quad (4.50)$$

where  $\Phi_f$  and  $\Phi_w$  are diagonal matrices described by

$$\Phi_f = (\mu^{-1/2} - \Lambda^{-1})_+^{1/2} \quad (4.51)$$

$$\Phi_w = (\mu^{1/2} \Lambda^{-1} - \mu \Lambda^{-2})_+^{1/2} \Lambda^{-1/2} \quad (4.52)$$

where  $\mu$  is the Lagrange multiplier given by

$$\mu^{1/2} = \frac{N_s}{\mathcal{P}_0 + \text{Tr}(\Lambda^{-1})} \quad (4.53)$$

*Proof.* See [82]. □

Once  $\mathbf{W}_{bb}$  and  $\mathbf{Z}_{bb}$  are obtained and plugged into the process of baseband beamforming, the optimization of our beamforming system can be extended to RF domain.

#### 4.1.2.4 RF Domain Beamforming Design

Substituting (4.49) and (4.50) in (4.44), we can express the information rate as follows [112]

$$\mathcal{I} = \log_2 \left( \left| \frac{\mathcal{P}_0 + \text{Tr}(\Lambda^{-1})}{N_s} \Lambda \right| \right) \quad (4.54)$$

The optimization of (4.54), which is a non-linear problem, serves as an aspect of the entire RF domain optimization. It is shown in [112] that this optimization problem is equivalent to maximizing the  $\text{Tr}(\Lambda)$  with

$$\begin{aligned} \text{Tr}(\Lambda) &= \text{Tr}(\mathbf{G}^H \tilde{\mathbf{R}}_{nn}^{-1} \mathbf{G}) \\ &= \text{Tr} \left( \frac{1}{\sigma_n^2} \mathbf{W}_{rf}^H \mathbf{H}^H \mathbf{Z}_{rf}^H \mathbf{Z}_{rf} \mathbf{H} \mathbf{W}_{rf} \right) \end{aligned} \quad (4.55)$$

On this basis the optimization problem is simplified to

$$\begin{aligned} \max_{\mathbf{W}_{rf}, \mathbf{Z}_{rf}} \quad & \text{Tr}(\mathbf{W}_{rf}^H \mathbf{H}^H \mathbf{Z}_{rf}^H \mathbf{Z}_{rf} \mathbf{H} \mathbf{W}_{rf}) \\ \text{s.t.} \quad & \mathbf{W}_{rf}(m, n) = \frac{1}{\sqrt{M_t}} e^{j\theta_{m,n}}, \quad m, n \in \mathcal{Q}_t \\ & \mathbf{Z}_{rf}(m, n) = \frac{1}{\sqrt{M_r}} e^{j\phi_{m,n}}, \quad m, n \in \mathcal{Q}_r \end{aligned} \quad (4.56)$$

To the best of our knowledge, the above optimization problem with the two constraints has no closed-form solutions. Therefore an iterative scheme is proposed in the following section to obtain the optimum  $\mathbf{W}_{rf}$  and  $\mathbf{Z}_{rf}$ . In this approach, given equal gain combining (EGC) at the receiver, we can obtain  $\mathbf{W}_{rf}$  while  $\mathbf{Z}_{rf}$  is attained given equal gain transmission (EGT) at the transmitter.

**1) Transmit RF Beamforming Design:** With the help of equal gain combining (EGC) at the receiver, the maximization of effective channel gain in (4.56) under the uniform elemental power constraint is equivalent to

$$\begin{aligned} \max_{\mathbf{W}_{rf}} \quad & \text{Tr}(\mathbf{W}_{rf}^H \mathbf{P} \mathbf{W}_{rf}) \\ \text{s.t.} \quad & \mathbf{W}_{rf}(m, n) = \frac{1}{\sqrt{M_t}} e^{j\theta_{m,n}}, \quad m, n \in \mathcal{Q}_t \end{aligned} \quad (4.57)$$

where  $\mathbf{P} = \mathbf{H}^H \mathbf{Z}_{rf}^H \mathbf{Z}_{rf} \mathbf{H}$ .

By analyzing the objective function in (4.57), the objective function is modified into

$$\text{Tr}(\mathbf{W}_{rf}^H \mathbf{P} \mathbf{W}_{rf}) = \sum_{n=1}^{N_t} \sum_{i=1}^{N_t} \mathbf{w}_n^H \mathbf{p}_i \mathbf{w}_n(i) \quad (4.58)$$

where  $\mathbf{w}_n$  is the  $n$ th column of  $\mathbf{W}_{rf}$  and  $\mathbf{w}_n(i)$  is the  $i$ th element in the  $N_t \times 1$  vector  $\mathbf{w}_n$ . The  $i$ th column of  $\mathbf{P}$  is denoted as  $\mathbf{p}_i$ .

The contribution of the  $n$ th RF chain to the objective function in (4.57) can be expanded as

$$\begin{aligned} & \sum_{i=1}^{N_t} \mathbf{w}_n^H \mathbf{p}_i \mathbf{w}_n(i) \\ &= \sum_{i=1}^{N_t} \left( \mathbf{w}_n^H(-i) \mathbf{p}_i(-i) + \mathbf{w}_n^*(i) \mathbf{p}_i(i) \right) \mathbf{w}_n(i) \\ &= \sum_{i=1}^{N_t} \left( \underbrace{\mathbf{w}_n^H(-i) \mathbf{p}_i(-i) \mathbf{w}_n(i)}_{(a)} + \underbrace{\mathbf{w}_n^*(i) \mathbf{p}_i(i) \mathbf{w}_n(i)}_{(b)} \right) \end{aligned} \quad (4.59)$$

where  $\mathbf{w}_n(-i)$  denotes the vector  $\mathbf{w}_n$  with the element  $\mathbf{w}_n(i)$  removed while similarly,  $\mathbf{p}_i(-i)$  denotes the column vector  $\mathbf{p}_i$  with the element  $\mathbf{p}_i(i)$  removed. We notice that

term (b) in (4.59),  $\mathbf{w}_n^H(i)\mathbf{p}_i(i)\mathbf{w}_n(i) = M_t^{-1}\mathbf{p}_i(i)$ , has no influence on  $\mathbf{w}_n(i)$  which is the weight allocated to the  $i$ th antenna. The dependence of the objective in (4.57) on the  $i$ th antenna's phase shift is completely captured in term (a), which can be maximized by co-phasing  $\mathbf{p}_i(-i)^H\mathbf{w}_n(-i)$  and  $\mathbf{w}_n(i)$ . Therefore, the optimal weighting factor  $\mathbf{w}_n(i)$  is [74]

$$\mathbf{w}_n(i) = \frac{1}{\sqrt{M_t}} e^{j(\angle \mathbf{p}_i(-i)^H \mathbf{w}_n(-i))} \quad (4.60)$$

Based on the optimal condition in (4.60), an iterative procedure can be set up to find the optimal equal gain weighting vector  $\mathbf{w}_n$ .

**2) Receive RF Beamforming Design:** The maximization of the objective function in (4.56) can be re-formulated under equal gain transmission (EGT) at the transmitter in the following manner

$$\begin{aligned} \max_{\mathbf{Z}_{rf}} \quad & \text{Tr}(\mathbf{Z}_{rf}\mathbf{Q}\mathbf{Z}_{rf}^H) \\ \text{s.t.} \quad & \mathbf{Z}_{rf}(m, n) = \frac{1}{\sqrt{M_r}} e^{j\phi_{m,n}}, \quad m, n \in \mathcal{Q}_r, \end{aligned} \quad (4.61)$$

where  $\mathbf{Q} = \mathbf{H}\mathbf{W}_{rf}\mathbf{W}_{rf}^H\mathbf{H}^H$ .

By employing a similar procedure as before, the optimal weighting factor of the  $i$ th antenna at the receiver can be expressed as

$$\mathbf{z}_m(i) = \frac{1}{\sqrt{M_r}} e^{j(\angle \mathbf{z}_m(-i)\mathbf{q}_i(-i))} \quad (4.62)$$

where  $\mathbf{z}_m(-i)$  denotes the  $m$ th row vector  $\mathbf{z}_m$  with the element  $\mathbf{z}_m(i)$  removed and  $\mathbf{q}_i(-i)$  denotes the column vector  $\mathbf{q}_i$  with the element  $\mathbf{q}_i(i)$  removed.

So far, a scheme to obtain optimum  $\mathbf{W}_{rf}$  and  $\mathbf{Z}_{rf}$  has been introduced. The iterative algorithm is summarized as Algorithm 1.

#### 4.1.2.5 Complexity Analysis

Two major factors should be taken into consideration to evaluate the complexity of the proposed scheme: the complexity of the pre- and post-processing operations and the complexity of hardware implementation.

**Hybrid Beamforming Processing Operations:** As discussed earlier, the hybrid beamforming is split and carried out in two procedures, namely, the baseband processing and the RF domain processing. The baseband processing is dominated by the SVD of the equivalent channel matrix  $\mathbf{G}$  and the complexity of one SVD is  $\mathcal{O}(\min(N_{rf}^t \times (N_{rf}^r)^2, N_{rf}^r \times (N_{rf}^t)^2))$ .

The complexity of the RF domain processing is mainly dependent on the iterative algorithm. For analysis purposes, we assume that the average processing complexity of evaluating (4.60) and (4.62) is  $\mathcal{C}_u$ . Then the complexity of evaluating  $\mathbf{W}_{rf}$  is referred as  $(N_t \times N_{rf}^t) \times \mathcal{C}_u$  and similarly for  $\mathbf{Z}_{rf}$ , the complexity is  $(N_r \times N_{rf}^r) \times \mathcal{C}_u$ . Therefore, the complexity of one inner iteration, which is denoted by  $\mathcal{C}_{II}$ , should be  $(N_t \times N_{rf}^t +$



**Algorithm 1** The Iterative Algorithm for MIMO Hybrid Beamforming Design

---

```

1: Initilize: Set  $\mathbf{W}_{rf}$  and  $\mathbf{Z}_{rf}$  to an initial value (e.g. it can be constructed using the
   left and right singular vectors of  $\mathbf{H}$  corresponding to the first  $N_{rf}$  largest singular
   value). Choose the maximal number of iterations for inner-loop  $\mathcal{K}_i$  and outer-loop
    $\mathcal{K}_o$ ;
2: for  $k = 1 : \mathcal{K}_o$  do
3:   for  $i = 1 : \mathcal{K}_i$  do
4:     Set  $\mathbf{Z}_{rf}$  at its most recent value and calculate  $\mathbf{W}_{rf}$ 
5:     using equation (4.60).
6:   end for
7:   for  $j = 1 : \mathcal{K}_i$  do
8:     Set  $\mathbf{W}_{rf}$  at its most recent value and calculate  $\mathbf{Z}_{rf}$ 
9:     using equation (4.62).
10:  end for
11: end for
12: Set  $\mathbf{W}_{rf}$  and  $\mathbf{Z}_{rf}$  at their most recent values, compute beamforming matrix  $\mathbf{W}_{bb}$ 
   and  $\mathbf{Z}_{bb}$  with Lemma 1

```

---

$N_r \times N_{rf}^r) \times \mathcal{C}_u$ . Furthermore, we denote the complexity of one outer iteration as  $\mathcal{C}_{OI}$  and is given by  $\mathcal{C}_{II} \times \mathcal{K}_i$ , where  $\mathcal{K}_i$  is the maximum number of inner iterations. In the end, the total complexity can be concluded into  $\mathcal{C}_{OI} \times \mathcal{K}_o$ , where  $\mathcal{K}_o$  stands for the maximum number of outer iterations.

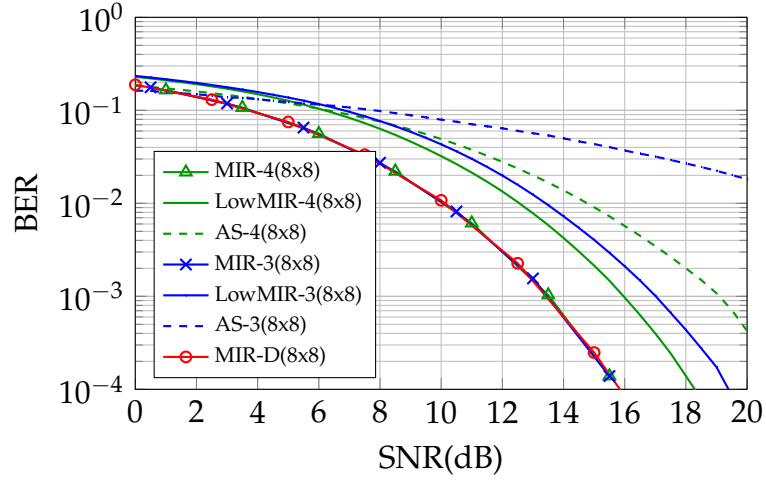
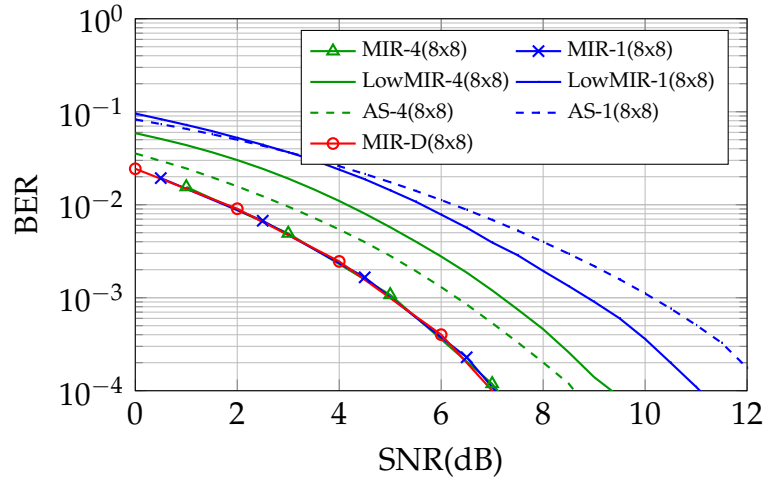
**Hardware Implementation:** The baseband implementation requires  $N_{rf}^t \times N_s$  multiplications and  $N_{rf}^t \times (N_s - 1)$  additions at the transmitter side. At the receiver side, it requires  $N_s \times N_{rf}^r$  multiplications and  $N_s \times (N_{rf}^r - 1)$  additions. The RF domain implementation requires  $(N_t + N_r)$  phase shifters in total.

### 4.1.3 Performance Evaluation

In this section, numerical simulation results are forwarded to illustrate the performance of different criteria, i.e., the information rate and uncoded bit error rate (BER). We consider a wireless transceiver system operating at 60 GHz in an indoor non-line-of-sight (NLOS) environment. For demonstration purposes, we assume that the transmit power across all transmit antennas is normalized to unity with  $\mathcal{P}_0 = 1$ . Each transmitter or receiver channel impulse response is generated using the 60 GHz NLOS multipath channel model for the residential scenario CM2.3 [121]. Here, each channel realization of  $\mathbf{H}$  is assumed to be known at both the transmitter and receiver. The pre-processing and post-processing are adaptive to each channel realization.

#### 4.1.3.1 Performance with Fully-Connected Structure

Now, we compare our proposed schemes with an exhaustive search antenna selection (AS) scheme [60]. We adopt a fully digital transceiver whose performance is used as a benchmark for the following comparisons. In the fully digital transceiver, the number

(a) BER performance with  $N_s = 3$ (b) BER performance with  $N_s = 1$ 

**Figure 4.3:** Information rate and BER performance achieved by fully digital, hybrid, low-complexity hybrid and AS schemes with maximum information rate criterion. (MIR<sub>1</sub>-4(8x8) denotes the  $8 \times 8$  mmWave system with 4 RF chains employing MIR criterion; MIR<sub>1</sub> represents the first subchannel; The low-complexity hybrid system with MIR criterion is denoted as LowMIR; The fully digital transceiver with MIR criterion is denoted as MIR-D.)

of RF chains is equal to the number of antennas. An  $8 \times 8$  mmWave system with the MIR criterion is employed. Firstly, the relation of the number of RF chains and the performance achieved by the optimum scheme is assessed. For simplification, we assume the same number of RF chains at both transmitter and receiver.

According to the optimum  $\mathbf{F}_{rf}$  and  $\mathbf{W}_{rf}$  determined by MIR criterion, the pre- and post-processing in the RF domain diagonalize  $\mathbf{H}$  into eigen subchannels. Note that only the power allocation across the eigen subchannels needs to be performed in

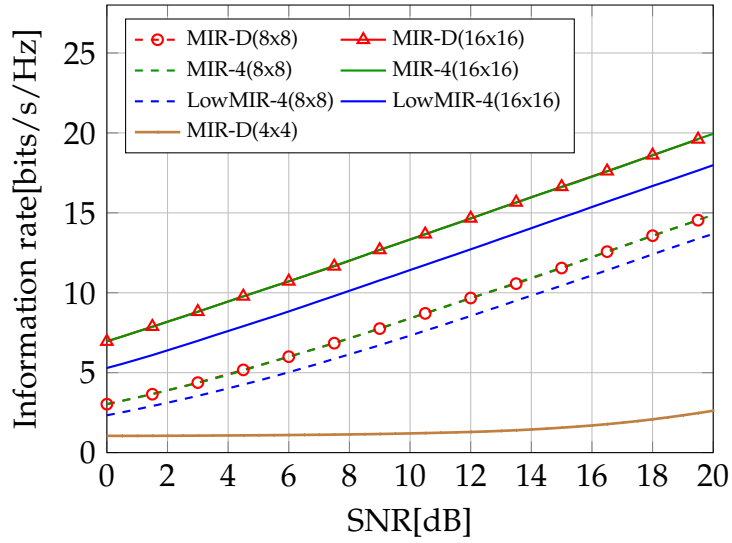


**Figure 4.4:** Information rate achieved by fully digital, hybrid and low-complexity hybrid system with maximum information rate criterion (MIR)

digital baseband. Therefore, the number of RF chains does not influence the performance of the hybrid system when  $N_s \leq N_{rf}^t \leq N_t$  holds.

As shown in Fig. 4.3a and Fig. 4.3b, no performance degradation is observed in the optimum scheme denoted by MIR with different  $N_{rf}$ . However, the performance of the low complexity scheme and antenna selection scheme decreases as  $N_{rf}$  is decreased. For a BER of  $10^{-3}$  depicted in Fig. 4.3a, our optimum scheme outperforms the AS scheme by five and more than 10 dB with four and three RF chains, respectively, when  $N_s = 3$ . Concerning the BER performance with  $N_s = 1$  in Fig. 4.3b, we notice once again that our optimum scheme exceeds the AS scheme in every manner. In addition, the low complexity scheme attains consentaneously a better performance than the AS scheme when the number of data streams  $N_s \geq 2$ , as depicted in Fig. 4.3a. Last but not least, in the case of  $N_{rf} = N_s = 1$ , the low complexity scheme also transcends the AS scheme, as shown in Fig. 4.3b.

The information rate in a MIMO mmWave system with  $N_s = 2$  is evaluated as a function of the number of RF chains and the number of antennas at both the transmitter and receiver. The results are presented in Fig. 4.4, where we compare our proposed hybrid spatial processing strategy with a fully digital transceiver. With 4 RF chains, we observe that the information rate of our optimum scheme is very close to that of a fully digital transceiver in both  $8 \times 8$  and  $16 \times 16$  hybrid systems. Moreover, the low complexity transceiver strategy exhibits an acceptable performance loss. In addition, a  $4 \times 4$  fully digital system with 4 RF chains is simulated. Fig. 4.4 depicts that with the same number of RF chains and an increasing number of antennas, the information rate increases significantly.

Consider an application where  $N_s = 3$  data streams with 4-QAM modulation are transmitted over a MIMO spatial multiplexing system. Fig. 4.5 illustrates the BER performance obtained from different MIMO transmission systems using an un-

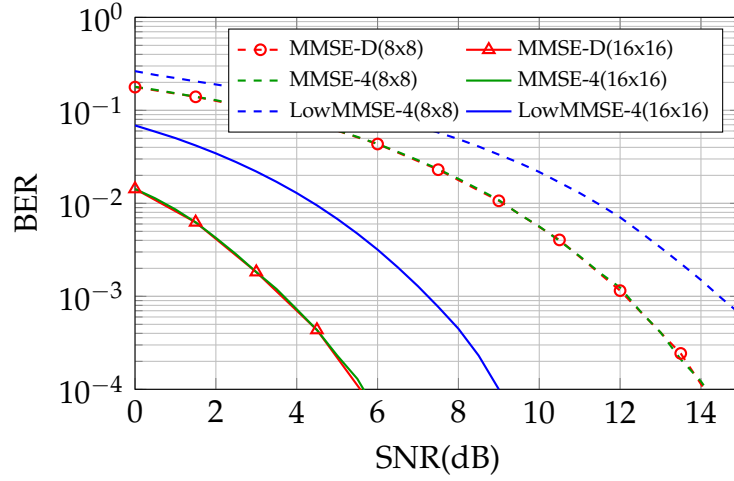


**Figure 4.5:** BER performance comparison under different transceiver setting with unweighted MMSE design criterion

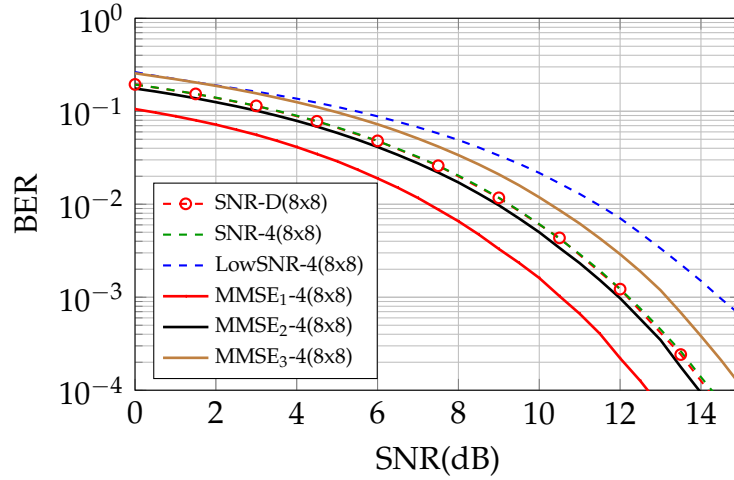


**Figure 4.6:** BER performance obtained by equal-SNR design vs. unweighted MMSE designs:  $N_s = 3$  subchannels

weighted MMSE design criterion. Compared with an  $8 \times 8$  fully digital transceiver (8 RF chains), the performance loss is negligible in an  $8 \times 8$  hybrid system even after reducing to half the number of RF chains. At a BER of  $10^{-3}$ , the performance loss is 2.5 dB when the low complexity transceiver is used. In spite of some performance loss as predicted, this low complexity transceiver reduces the complexity of the hardware design significantly. In practical system design, the trade-offs between hardware complexity and system performance should be well considered. When the antennas increase to  $16 \times 16$  with the same number of RF chains, the significant performance improvement can be attributed to the increase in transmit diversity and array gain.

We adopt the equal-SNR design ( $\mathcal{S} = 1/N_s \mathbf{I}$ ) where each of the  $N_s$  data streams is transmitted with equal error, for any channel realization. An  $8 \times 8$  spatial multiplexing system is applied here to transmit  $N_s = 3$  independent data streams. As

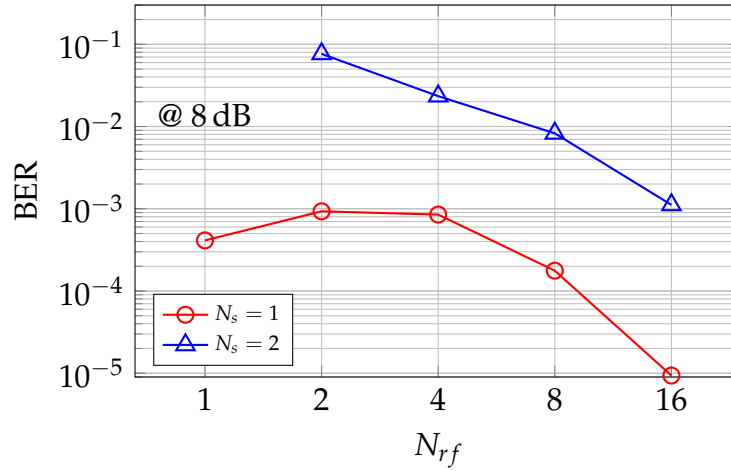


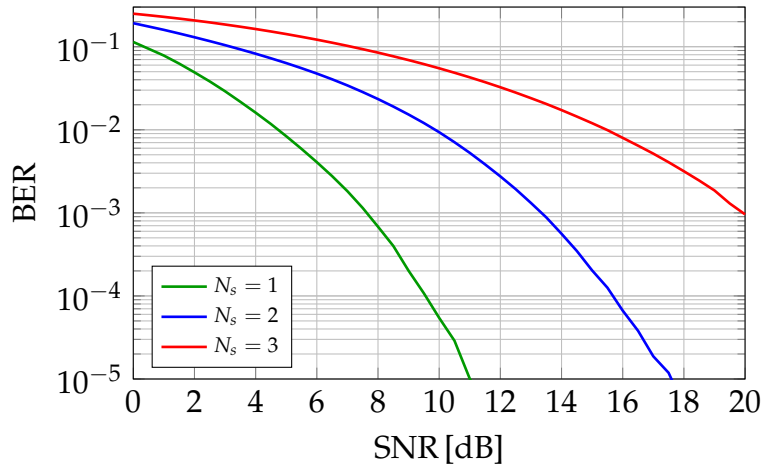
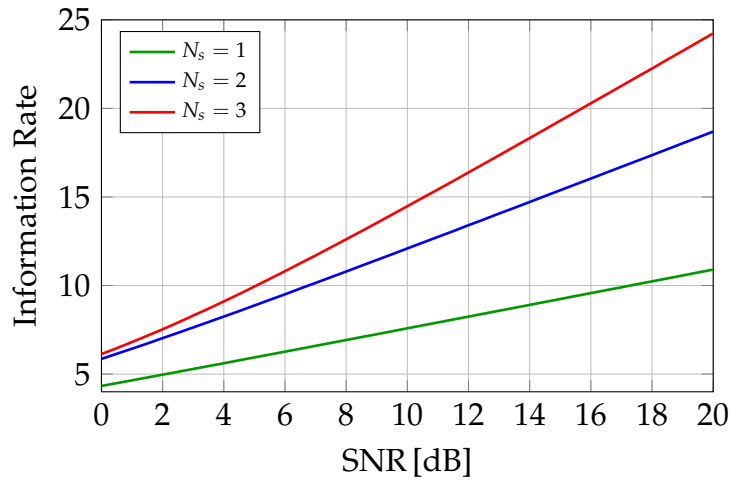
**Figure 4.7:** Average uncoded BER of a  $16 \times 16$  MIMO system with various number of RF chains at both transmitter and receiver side.

shown in Fig. 4.6, while the hybrid system is exploited, there is no performance loss compared with a fully digital system. As the low complexity hybrid system is employed, 2.5 dB performance loss occurs at a BER of  $10^{-3}$ . In addition, Fig. 4.6 depicts the BER performance comparisons conducted by respectively employing two different design criteria, namely equal-SNR and MMSE. It can be verified that the equal-SNR and MMSE design have similar total average BERs. However, the main difference lies in the subchannel BER for each of the 3 data streams, as illustrated in Fig. 4.6. For a fixed-rate system, equal error transmission for all subchannels is realized by equal SNR design. For a multimedia application where different types of information need to be transmitted simultaneously on different subchannels, the MMSE design is a better choice.

#### 4.1.3.2 Performance with Array-of-Subarray Structure

For demonstration purposes, we assume that the total transmits power across all transmit antennas are normalized to unity with  $\mathcal{P}_0 = 1$ , and a rectangular 16-QAM modulation with Gray mapping is used. As mentioned earlier, the channel realization  $\mathbf{H}$  is assumed to be perfectly known at both the transmitter and the receiver. In addition, the impulse response of each transmitter or receiver channel is generated using the 60 GHz NLOS multipath channel model for the residential scenario CM2.3 [124].

Fig. 4.7 depicts how the variation of RF chain numbers at both transmitter and receiver, denoted as  $N_{rf}$  and  $N_s$ , influences the performance of the aforementioned system. Firstly, given  $N_s = 1$ , the BERs of  $N_{rf} = 2$  and  $N_{rf} = 4$  are worse comparing to the case where  $N_{rf} = 1$ . This may be attributed to the fact that the enhancement in diversity gain, which is generated from the increase in the number of RF chains, does not fully compensate for the severe beamforming loss caused by a shrink of antenna numbers in each subarray. However, as the number of RF chains raises to a larger

(a) BER performance with  $N_{rf} = 4$ (b) Information rate with  $N_{rf} = 4$ 

**Figure 4.8:** Relation between the number of data streams  $N_s$  and the performance of the proposed algorithm in a  $16 \times 16$  MIMO system, where the number of RF chain  $N_{rf} = 4$ .

scale of  $N_{rf} = 8$  and  $N_{rf} = 16$ , where the increase in diversity gain surpasses the loss of beamforming gain, the overall gain of the system goes up consequently and leads to a better performance with an ascending BER shown in the figure.

On the other hand, the enhancement of system performance is accompanied by a higher cost of hardware complexity. When it comes to the case of  $N_s \geq 2$ , the system performance increases monotonically with  $N_{rf}$ .

As shown in Fig. 4.8a, the system performance also fluctuates with  $N_s$ . It can be observed from the figure that with the number of RF chains being constant, the BER of the system becomes better with the decrease in the number of  $N_s$ .

Lastly, by comparing Fig. 4.8a with Fig. 4.8b, we can simply come to the conclusion that a trade-off between the information rate and the average BER performance of the system has to be made to pursue an optimal overall system performance. In

addition, the difference between the information rate at different  $N_s$  and the water-filling capacity with a fixed  $N_{rf}$ , which is observed in Fig. 4.8b, could be explained with the fact that rank adaptation has not been considered in our design.

## 4.2 Channel Estimation Based on DFT for Short Range Communication

In Section 4.1, hybrid beamforming structure has shown to be a good compromise in terms of performance and complexity with respect to pure analog or pure digital solutions. The design of the hybrid precoding and combining matrices is usually based on perfect or partial channel state information. However, estimating the millimeter wave (mmWave) channel becomes quite complicated due to the use of large antenna arrays. This leads to the motivation of this section, i.e., developing low-complexity mmWave channel estimation algorithms, which enable hybrid beamforming to approach the performance of digital precoding algorithms.

Several analog beamforming solutions proposed in [43, 51], known as beamforming training, only rely on using networks of analog phase shifters and design weights of these phase shifters without channel knowledge at the transmitter side. Despite the low complexity of these schemes, their performance is generally sub-optimal due to radio frequency (RF) hardware constraints and single beamforming direction coverage. Hence, hybrid beamforming is considered in [14], where a new multi-resolution codebook is designed by leveraging compressed sensing tools to estimate the parameters of mmWave channels with a small number of iterations. Initially, this algorithm assumes the availability of a feedback channel for iteratively exchanging information between the transmitter and receiver. Based on [14], a new algorithm proposed in [13] has no feedback overhead. However, the computational complexity is still rather high by requiring an iterative search within a hierarchical codebook.

In this section, we propose two novel channel estimation algorithms based on two dimensional discrete Fourier transform (2D-DFT) technique: hierarchical beamforming training algorithm and low-complexity beamforming training algorithm. We define a multi-resolution uniform-weighting based codebook, which is similar to a normalized DFT matrix. The proposed algorithms extract mmWave channel parameters such as the angle of arrival (AoA), angle of departure (AoD), and path gain of each path based on the received signal power. The hierarchical beamforming training algorithm jointly estimates the AoAs and AoDs in multiple training stages. To further reduce computational complexity, we propose a low-complexity beamforming training algorithm that separately estimates the AoAs and AoDs with a much lower training overhead. We evaluate the performance of the proposed channel recovery algorithms by simulations, assuming that both the transmitter and receiver adopt hybrid beamforming algorithms proposed in [110]. Numerical results indicate that the proposed algorithms can achieve a comparable spectral efficiency with respect to the case when perfect channel state information is known.

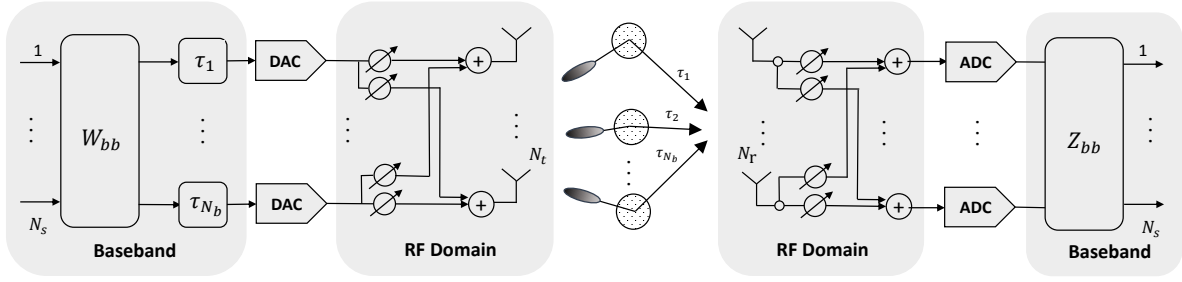


**Figure 4.9:** IEEE 802.15.3c beam maximum gain directions  $\theta_{max}$  in different training level are taken as the original version, so that the maximum gain directions set are obtained to generate uniform weighting based codebook.

### 4.2.1 System Model

In practice, a general single user mmWave MIMO system model can be shown in Fig. 4.9. The access point (AP) is equipped with  $N_t$  antennas while the user with  $N_r$  antennas.  $N_s$  data streams are transmitted from the AP to the user. At the transmitter side,  $N_b$  flat beams are obtained from  $N_s$  data streams using a digital baseband precoding matrix  $\mathbf{W}_{bb}$ , such that  $N_s \leq N_b \leq N_t$  and  $N_s \leq N_b \leq N_r$ . Each flat beam is time-shifted by the input buffer. After that, the phase of the up-converted RF data stream is rotated by the transmit weighting vector, and then emitted into one dominant reflected path. The  $N_t \times N_b$  RF precoder is denoted as  $\mathbf{W}_{rf}$ . Motivated by practical considerations of low power consumption and low-complexity architecture, to generate beam patterns is to simply shift the RF phases, rather than adjust both the amplitude and phase of each element.

To achieve a flat fading channel, the best possible beam separation is needed. In [110], we have proposed an average SIR constrained design to achieve the best possible beam separation to realize transmitting one flat beam on one specific dominant reflected path. With efficient time delay compensation and RF domain beamforming, the equivalent flattened fading channel can be denoted as  $\tilde{\mathbf{H}}$ . The discrete-time transmitted signal is

$$\mathbf{x} = \tilde{\mathbf{H}}\mathbf{W}_{bb}\mathbf{s}, \quad (4.63)$$

where  $\mathbf{s}$  is the  $N_s \times 1$  vector of transmitted symbols, such that  $\mathbb{E}[\mathbf{s}\mathbf{s}^H] = (\mathcal{P}_o/N_s)\mathbf{I}_{N_s}$ , and  $\mathcal{P}_o$  is the total transmit power. Since the RF beamforming is implemented using only analog phase shifters, we assume  $\|\mathbf{W}_{rf}\|^2 = N_t^{-1}\mathbf{I}_{N_b}$ . The total power constraint is enforced by normalizing  $\mathbf{W}_{bb}$ , such that  $\|\mathbf{W}_{rf}\mathbf{W}_{bb}\|_F^2 = N_s$ .

At the user side, the received signal is first combined in the RF domain employing  $N_r \times N_b$  combining matrix  $\mathbf{Z}_{rf}$  followed by a  $N_b \times N_s$  baseband combiner  $\mathbf{Z}_{bb}$ . The constraints on the entries of RF combiner  $\mathbf{Z}_{rf}$  are similar to the RF precoder. If  $\mathbf{Z} = \mathbf{Z}_{rf}\mathbf{Z}_{bb}$ , the received signal after processing can be written as

$$\hat{\mathbf{s}} = \mathbf{Z}^H\tilde{\mathbf{H}}\mathbf{W}_{bb}\mathbf{s} + \mathbf{Z}^H\mathbf{n}, \quad (4.64)$$



where  $\mathbf{n}$  denotes the  $N_r \times 1$  noise vector of i.i.d.  $\mathcal{CN}(0, \mathbf{R}_{nn})$ .  $\mathbf{R}_{nn} = \sigma_n^2 \mathbf{I}_{N_r}$  is the noise covariance matrix. In this section, we implicitly assume perfect synchronization, and both the AP and user have no a priori information of the mmWave channel. Therefore, we will develop channel estimation algorithms to estimate the important channel parameters, such as AoDs, AoAs and path loss in Section 4.2.3. After that, the estimated channel is used to construct the hybrid precoding and decoding matrices as shown in [110].

#### 4.2.1.1 Channel Model

In typical short-range indoor scenarios, signal propagation at 60GHz may exhibit intensive multipath trajectories phenomenon. First, the attenuation of reflecting surfaces is much higher at 60 GHz than in the range below 5 GHz. Thus, multiple reflected rays are not relevant. Secondly, due to high atmospheric absorption at 60 GHz, paths much longer than LOS are negligible. Rather the 60 GHz channel comprises a possible LOS path and a small number of dominating NLOS paths. In the considered indoor environment, most of the reflecting objects ("clusters") are either close to the AP and to the user (e.g. objects on the desk) or near larger objects (walls, boards, etc.). Measurements [55,104] indicate that the number of reflection clusters to be considered is in the range from four to eight. The angular spread for each reflection cluster is small, leading to a small delay spread within a cluster. In conclusion, we assume four to eight dominating clusters with small delay spread of reflections within the cluster but larger delay spread in the range of 3-30 ns between different clusters. Due to the position of reflecting objects, angular separation of clusters may be large at the transmitter and small at the receiver (objects near the transmitter) or vice versa (objects near the receiver) or on both sides (walls, boards, etc.).

As the number of clusters gives an indication about the number of dominant paths, our model considers  $L$  significant clusters, in which the intra-cluster delay spread is minimal. To reduce the delay variations within each cluster and to impart directivity in the direction of the dominant path, the RF domain beamforming is implemented at both the transmitter and receiver. With efficient beam steering, we can assume that there is one dominant path in each cluster, since all rays in a cluster constructively add to the channel gain of the  $l$ th cluster.

Here, we consider the most widely used modified Saleh-Valenzuela (S-V) model for channel modeling at 60 GHz [55, 104]. The  $N_r \times N_t$  frequency-selective MIMO channel between the AP and the user can be expressed as

$$\mathbf{H} = \sqrt{\frac{N_t N_r}{L}} \sum_{l=1}^L \alpha_l \mathbf{a}_r(\phi_l) \mathbf{a}_t^T(\theta_l) \delta(t - \tau_l), \quad (4.65)$$

where  $\alpha_l$  denotes the complex gain of the  $l$ th path, and is assumed to follow the log-normal distribution, with  $\mathbb{E}[|\alpha_l|^2] = \bar{\alpha}$ .  $\phi_l$  and  $\theta_l$  represents the angles of arrival and departure (AoAs/AoDs) of the  $l$ th dominant path, respectively. In order to model AoAs and AoDs, Laplacian distribution with uniformly distributed mean over

$[-\pi, \pi)$ , and angular standard deviation of  $\sigma_{AS}$  are utilized. In this section, we consider the non-line-of-sight (NLOS) channel model for the residential scenario based on the measurements by IEEE task group 802.15.3c [124].

For ease of elaboration, we employ the 1-D uniform spaced antenna array. The array response vectors of the uniform linear arrays, denoted as  $\mathbf{a}_r(\phi_l) \in \mathbb{C}^{N_r \times 1}$  for the receiver and  $\mathbf{a}_t(\theta_l) \in \mathbb{C}^{N_t \times 1}$  for the transmitter, can be expressed as

$$\mathbf{a}(\varphi) = \frac{1}{\sqrt{N}} [1, e^{-jkd \cos(\varphi)}, \dots, e^{-jk(N-1)d \cos(\varphi)}], \quad (4.66)$$

where  $k = 2\pi/\lambda$  and  $d$  is the antenna spacing.

Time delay compensation is implemented in such a way that the beams are time shifted by input buffers. Accordingly, the discrete channel matrix can be expressed as

$$\mathbf{H} = \sqrt{\frac{N_t N_r}{L}} \sum_{l=1}^L \alpha_l \mathbf{a}_r(\phi_l) \mathbf{a}_t^T(\theta_l) \delta(t - \tau_l + \hat{\tau}_l), \quad (4.67)$$

where  $\hat{\tau}_l$  denotes the quantized time delay compensation of the  $l$ th path given by  $\hat{\tau}_l = k_l \cdot T_s$ .  $T_s$  is the sample duration of the buffer and  $k_l$  is an integer. The efficiency of time delay compensation is validated in [107].

After applying the optimized RF domain beamforming with efficient TDC, the equivalent flattened fading channel can be expressed as follows

$$\tilde{\mathbf{H}} = \mathbf{A}_R \text{diag}(\boldsymbol{\alpha}) \mathbf{A}_T^H \mathbf{W}_{rf}, \quad (4.68)$$

where  $\boldsymbol{\alpha} = \sqrt{\frac{N_t N_r}{\bar{L}}} [\alpha_1, \dots, \alpha_l, \dots, \alpha_{\bar{L}}]$  and  $\bar{L}$  is the number of survived path after path selection. During the data transmission, each dominant path only transmits one time-shifted beam, such that the number of active RF chain  $N_b = \bar{L}$ . The matrices  $\mathbf{A}_R$  and  $\mathbf{A}_T$  contain the AP and the user array response vectors with  $\mathbf{A}_R = [\mathbf{a}_r(\phi_1), \dots, \mathbf{a}_r(\phi_l), \dots, \mathbf{a}_r(\phi_{\bar{L}})]$  and  $\mathbf{A}_T = [\mathbf{a}_t(\theta_1), \dots, \mathbf{a}_t(\theta_l), \dots, \mathbf{a}_t(\theta_{\bar{L}})]$ .

The algorithm details of RF domain beamforming design is addressed in Section 4.1. If the channel condition is supposed to be quasi-static, in which both the channel noise and multipath propagations keep invariant during one transmission burst, it is clearly seen that the received signal strength is only determined by the estimated channel.

## 4.2.2 Formulation of the mmWave Channel Recovery Problem

As introduced the geometric mmWave channel model in (4.65), the mmWave channel recovery is equivalent to recovering important parameters of the  $L$  dominant channel paths, namely the path gain, AoA and AoD. We will briefly show how to design the low overhead and low-complexity beamforming training algorithms based on 2D-DFT inspired by the sparse nature of mmWave channel.

#### 4.2.2.1 Previous Work

Generally, for single path channel, given the well-designed beam steering vectors, beamforming actually means to determine the optimal antenna pattern from a pre-scribed codebook. A two-stage beam search technique is commonly exploited by the currently undergoing 60 GHz WPANs standardization IEEE 802.15.3c: sector level beamforming and normal beam refinement. In the first phase, sector level beam patterns are employed to find out the best sector index which is able to obtain the maximum received signal power. The sector level beams can be conveniently realized by using a small portion of antenna elements. Alternatively, the total antenna elements may be adopted with specifically designed phases until all the detection range is covered. Once notifying the best sector index, then the beam level search will be performed by examining the subset beams specified by the sector index.

Let  $N$  be the number of beam level codebook size of the transceiver and the receiver, while  $N_t^{sec}$  and  $N_r^{sec}$  be the number of sector beams of transceiver and receiver, respectively. Generally, the number of beams corresponding to one sector can be given by  $N_t^b = N/N_t^{sec}$  and  $N_r^b = N/N_r^{sec}$ . Hence, the total number of training steps can be easily measured and is given by  $N_{3c} = N_t^{sec} \times N_r^{sec} + N_t^b \times N_r^b$ .

Firstly, it should be noted that there indeed exists the optimal value of sector number for different codebook size. Secondly, although such a two-stage beamforming training scheme may reduce the number of training steps, this search still has a complexity order of  $\mathcal{O}(N^2)$  which means the required overhead may easily become uncontrollable with the further increase of the codebook size  $N$ . Hence, it is still impractical for most realistic applications by taking a large codebook size into account to realize high resolution.

Furthermore, such beamforming training technique employed in IEEE 802.15.3c is only suitable for one data stream transmission. Hence, we propose a novel beamforming training algorithm for the multi-path and multiple data streams case.

#### 4.2.2.2 Design of Uniform-Weighting Codebook

We focus on the design of AP training codebook  $\mathcal{W}^t$ . A similar approach can be followed to construct the user training codebook  $\mathcal{W}^r$ . During beamforming, the best beam pair, or in other words, the best transmit and receive weight vectors, are selected from the known codebooks.

Here, the beam codebook is defined as a  $M \times N$  matrix,  $\mathcal{W}^t$ , which is specified by the number of antenna elements  $M$  and the desired beams number  $N$ . Each column of  $\mathcal{W}^t$  corresponds to one beam steering vector, and rotates the beam to the desired direction  $\theta_n$ . For uniform-weighting based codebook, the  $(m, n)$ th element of  $\mathcal{W}^t$  is given by [114, 129]

$$w_{m,n} = e^{-j2\pi m d \cos(\theta_n)/\lambda}, \quad m = 0, 1, \dots, M-1. \quad (4.69)$$

IEEE 802.15.3c beam main response axis (MRA) directions are taken as the original

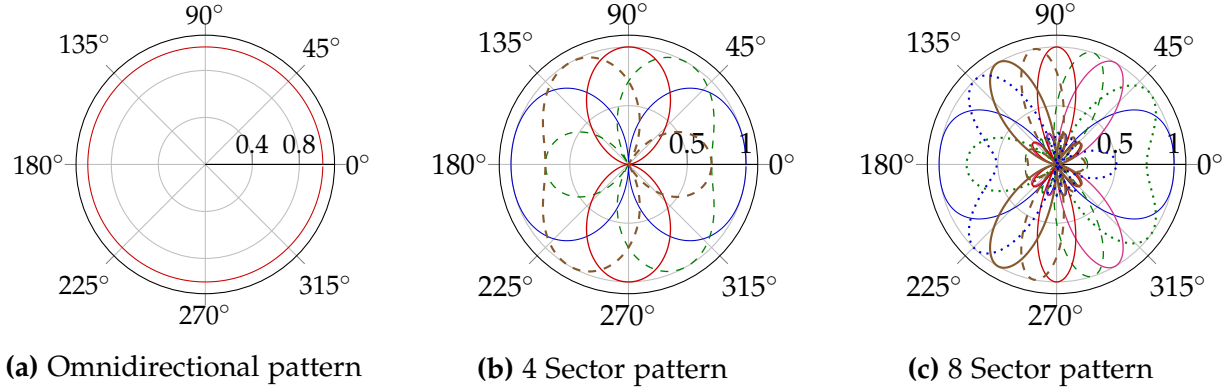


**Figure 4.10:** An example beam patterns of the beamforming vectors with different number of elements. The beam codebook is specified by [129]. (a) The omnidirectional pattern with  $M = 1$ . (b) The sector pattern with  $M = 2$ . (c) The sector beam with  $M = 4$ .

**Table 4.1:** IEEE 802.15.3c beam maximum gain directions  $\theta_{max}$  in different training level

	$\theta_{max}$ (Maximum gain direction)															
$M = 2, N = 4$	0°				60°				90°				120°			
$M = 4, N = 8$	0°		37°		60°		72°		90°		101°		120°		135°	
$M = 8, N = 16$	0°	25°	40°	51°	60°	66°	75°	82°	90°	95°	104°	112°	120°	127°	138°	150°

version to make curve fitting  $f(n), n \in (0, N - 1)$ , then the set of maximum gain directions can be obtained as follows.

$$\Theta = \{\theta_n | \theta_n = f(n), n = 0, \dots, N - 1\}. \quad (4.70)$$

After that, weighting vector based on uniform weighting shown in (4.69) can be obtained to generate a codebook matrix. To minimize the resulting quantization error, the efficient number of beam patterns  $N$  on the performance of the proposed algorithms will be evaluated via numerical simulations in Section 4.2.4.

Similar to the IEEE 802.15.3c regulation, three typical patterns have been shown in Fig.4.10, in which the active antenna elements size  $M$  is set to 1, 2 and 4, respectively. Generally, in order to minimize the resulting bad effect, the number of beam patterns  $N$  and the element size  $M$  are supposed to fulfill the constraint relationship  $N = 2M$ . The omnidirectional pattern is the lowest resolution pattern specified in the codebooks, which is used to refer to an antenna pattern that covers the target area of 360 degrees. Sector level pattern is the second level resolution pattern used to refer to a direction of an array pattern that covers a relatively broad area of multiple beams. Different sectors can overlap. In this work, the training phase consists of  $S$  levels until the highest resolution is reached. The sector in  $s$ th level can be further divided into  $\mathcal{K}$  sub-sectors in the  $(s + 1)$ th level. Fig. 4.10b and Fig. 4.10c show the resulting sector

patterns of beamforming vectors in the first and second codebook levels, respectively. The obtained resolution is approximate to  $\pi/2^{s+1}$ . The beam MRA directions in the first three codebook levels are listed in Table 4.1.

As we know, the radiation pattern of the 1-D uniform spaced antenna array is symmetrical. Therefore, in this training codebook, each column is one beamforming vector directing to  $\theta_n$  in (4.70) with the approximate uniform grid, i.e.  $\theta_n \approx \pi n/N = 2\pi n/N_D, n = 0, 1, \dots, N$ . Here,  $N_D$  represents the DFT size. In each training level  $s$ , sector beams can be conveniently realized by using a small portion of antenna elements, i.e.  $M = 2^s$ , until the total elements are adopted.  $\mathcal{K}$  training beamforming vectors are employed to obtain  $\mathcal{K}$  sector beams which need to cover at least one previous level sector range. The beamforming vectors used in training level  $s$  can be expressed as

$$\mathbf{W}_{rf[m,k]}^s = e^{-j2\pi m d \cos(\theta_k)/\lambda}, \quad k = 1, \dots, \mathcal{K}, \quad (4.71)$$

with  $m = 0, \dots, M^s - 1$  and

$$M^s = \begin{cases} 2^s & 2^s \leq N_t \\ N_t & \text{otherwise} \end{cases} \quad (4.72)$$

representing the number of active antenna elements in training level  $s$ . In fact, all the elements in  $\mathbf{W}_{rf}^s$  can be directly drawn from the training codebook  $\mathcal{W}^t$ . In the  $s$ th training level, one sector range can cover  $\mathcal{N}^s = \frac{N}{2^{s+1}}$  normal beams. Let  $\hat{n}_{s-1}$  denote the index of desired sector in the  $(s-1)$ th training level (i.e.  $\hat{\theta}_{s-1}$  is the corresponding AoD), the mapping can be expressed as  $\mathbf{W}_{rf[m,k]}^s = \mathcal{W}_{[m,n^s]}^t$ , where

$$n^s = \{\hat{n}_{s-1} - \mathcal{N}^s \lceil \frac{\mathcal{K}-2}{2} \rceil : \mathcal{N}^s : \hat{n}_{s-1} + \mathcal{N}^s \lfloor \frac{\mathcal{K}}{2} \rfloor\} \quad (4.73)$$

defines the indices of  $\mathcal{K}$  beamforming vectors associated with AoDs. In order to enforce the total transmit power remaining constant in different training levels, we normalize the entries of  $\mathbf{W}_{rf}^s$ , such that  $|\mathbf{W}_{rf[m,k]}^s| = 1/\sqrt{M^s}$ .

#### 4.2.2.3 Problem Formulation and System Assumption

We consider the system and mmWave channel model described in Section 4.2.1. While the AP employs a beamforming vector  $\mathbf{w}_p$  steering at the direction of  $\theta_p$ , and the user uses a measurement vector  $\mathbf{z}_q$  steering at the direction of  $\phi_q$  to combine the received signal, the resulting signal can be given as

$$y_{q,p} = \mathbf{z}_q^H \mathbf{H} \mathbf{w}_p s_p + \mathbf{z}_q^H \mathbf{n}_{q,p}, \quad (4.74)$$

where  $s_p$  is the training symbol on the beamforming vector  $\mathbf{w}_p$ , such that  $\mathbb{E}[s_p s_p^H] = \mathcal{P}_t$ , with  $\mathcal{P}_t$  being the average total transmit power in the training phase.

By defining for  $l = 1, 2, \dots, L$ ,

$$\vartheta_l = kd \cos(\theta_l) \quad , \quad \varphi_l = kd \cos(\phi_l), \quad (4.75)$$

the  $(n, m)$ th element of the channel matrix  $\mathbf{H}$  in (4.65) can be written as

$$[\mathbf{H}]_{n,m} = \frac{1}{\sqrt{L}} \sum_{l=1}^L \alpha_l e^{-jn\varphi_l} e^{jm\vartheta_l}, \quad (4.76)$$

with  $n = 0, 1, \dots, N_r - 1$ ,  $m = 0, 1, \dots, N_t - 1$ . Hence, the received signal can be rewritten as

$$\begin{aligned} y_{q,p} &= \frac{1}{\sqrt{N_t N_r}} \sum_{m=0}^{N_t-1} \sum_{n=0}^{N_r-1} [\mathbf{H}]_{n,m} e^{jn\varphi_q} e^{-jm\vartheta_p} + n_{q,p} \\ &= C_{q,p} \sum_{l=1}^L \alpha_l \sum_{m=0}^{N_t-1} \sum_{n=0}^{N_r-1} e^{-j(-\varphi_q + \varphi_l)n} e^{-j(\vartheta_p - \vartheta_l)m} + n_{q,p}, \end{aligned} \quad (4.77)$$

where  $C_{q,p} = 1/\sqrt{L N_t N_r}$  denotes the constant coefficient. If  $N$  is large enough, we can write

$$\begin{aligned} \vartheta_l &= \frac{2\pi p_l}{N_D} \quad , \quad \varphi_l = -\frac{2\pi q_l}{N_D}, \\ \vartheta_p &= \frac{2\pi p}{N_D} \quad , \quad \varphi_q = -\frac{2\pi q}{N_D}, \end{aligned} \quad (4.78)$$

for two integers  $p_l$  and  $q_l$ . For a better coverage of the entire user area and smaller overlap between different sectors, the beam MRA directions is not strictly uniform distributed. However, it does not influence such mapping shown in (4.78).

According to (4.77) and (4.78), by neglecting the grid quantization error, the received signal can be represented as

$$y_{q,p} = C_{q,p} \sum_{l=1}^L \alpha_l \underbrace{\sum_{m=0}^{N_t-1} \sum_{n=0}^{N_r-1} e^{-j2\pi(\frac{(p-p_l)m}{N_D} + \frac{(q-q_l)n}{N_D})}}_{\mathcal{F}(q-q_l, p-p_l)} + n_{q,p}. \quad (4.79)$$

Note that for a rectangular function

$$f(n, m) = \begin{cases} 1, & 0 \leq m \leq N_t - 1, 0 \leq n \leq N_r - 1 \\ 0, & \text{otherwise} \end{cases}, \quad (4.80)$$

its 2D-DFT on  $N_D \times N_D$  samples can be expressed as

$$\mathcal{F}(q, p) = \sum_{m=0}^{N_t-1} \sum_{n=0}^{N_r-1} f(n, m) e^{-j2\pi(\frac{pm}{N_D} + \frac{qn}{N_D})}$$

$$= \frac{\sin(\frac{\pi q N_r}{N_D})}{\sin(\frac{\pi q}{N_D})} e^{-j\frac{\pi q(N_r-1)}{N_D}} \times \frac{\sin(\frac{\pi p N_t}{N_D})}{\sin(\frac{\pi p}{N_D})} e^{-j\frac{\pi p(N_t-1)}{N_D}} \quad (4.81)$$

for  $p, q = 0, 1, \dots, N-1$ . Hence, we can rewrite (4.79) as

$$y_{q,p} = \mathcal{C}_{q,p} \sum_{l=1}^L \alpha_l \mathcal{F}(q - q_l, p - p_l) + n_{q,p}. \quad (4.82)$$

Note that detecting  $(\hat{q}_l, \hat{p}_l)$  which maximizes the received signal  $|y_{q,p}|$ , directly implies the detection of AoAs and AoDs of the dominant paths of the channel. The path gains can be also determined by the values of corresponding elements  $|y_{\hat{q}_l, \hat{p}_l}|$ . However, taking a large codebook size  $N$  into account, we need  $N \lceil N/N_b \rceil$  training steps to obtain all the received signal  $y_{q,p}$ ,  $p, q = 0, 1, \dots, N-1$ , which is impractical for most realistic applications. Therefore, we propose two novel hierarchical multi-resolution beamforming training schemes, which invoke some ideas of 2D-DFT to reduce overhead.

### 4.2.3 Adaptive Estimation Algorithm for a Sparse mmWave Channel

In this section, we propose sparse spatial channel recovery algorithms that employ a multi-resolution codebook developed in Section 4.2.2.2 based on the 2D-DFT technique. We firstly address this problem by jointly optimizing the transmit and receive patterns. We then propose a low-complexity algorithm to further reduce the overhead with acceptable performance loss.

#### 4.2.3.1 Hierarchical Beamforming Training Algorithm

We can extract the channel parameters of the different modes by using the iterative cancellation method outlined in Algorithm 2.

According to Section 4.2.2.2, the training codebooks  $\mathcal{W}^t$  and  $\mathcal{W}^r$  of size  $N$  are predefined. The number of beamforming vectors/measurement vectors used in each stage of the hierarchical beamforming training algorithm equals  $\mathcal{K}$ . In the  $s$ th sector level, the AP employs  $\mathcal{K}$  training beamforming vectors of the first level of the codebook  $\mathcal{W}^t$ . For each of those vectors, the user uses  $\mathcal{K}$  measurement vectors of the first level of the codebook  $\mathcal{W}^r$  to combine the received signal. After  $\mathcal{K}^2$  preamble transmission of this level, the user obtains  $\mathcal{K}^2$  received signals

$$y_{q,p}^s = \mathcal{C}_{q,p}^s \sum_{l=1}^L \alpha_l \underbrace{\sum_{m=0}^{M_t^s-1} \sum_{n=0}^{M_r^s-1} e^{-j2\pi(\frac{(p-p_l)m}{N_D} + \frac{(q-q_l)n}{N_D})}}_{\mathcal{F}^s(q-q_l, p-p_l)} + n_{q,p}^s, \quad (4.83)$$

**Algorithm 2** Hierarchical beamforming training algorithm

---

```

1: Input: the AP and user have  $\mathcal{W}^t$ ,  $\mathcal{W}^r$ , and know  $N$ ,  $\mathcal{K}$ ;
2: Initialization:  $M_t^s = M_r^s = 2$ ,  $S = \log_2 N - 1$ ;
    $n_{AP}^s = n_{user}^s = \{1 : \mathcal{N}^1 : N\}$ ;
3: for  $l=1$  to  $L$  do
4:   for  $s=1$  to  $S$  do
5:     Drawn  $\mathbf{W}_{rf[m,p]}^s$ ,  $p \in n_{AP}^s$  from  $\mathcal{W}^t$ ;
6:     Drawn  $\mathbf{Z}_{rf[m,q]}^s$ ,  $q \in n_{user}^s$  from  $\mathcal{W}^r$ ;
7:     After  $\mathcal{K}^2$  training steps, the received signal
        $y_{q,p}^s = \mathcal{C}_{q,p}^s \sum_{l=1}^L \alpha_l \mathcal{F}^s(q - q_l, p - p_l) + n_{q,p}^s$ ;
8:     for  $k = 1$  to  $l - 1$  do
9:        $y_{q,p}^s = y_{q,p}^s - \mathcal{C}_{q,p}^s \hat{\alpha}_l \mathcal{F}^s(q - \hat{q}_l, p - \hat{p}_l)$ ;
10:    end for
11:     $(\hat{q}_l^s, \hat{p}_l^s) = \arg \max_{q \in n_{user}^s, p \in n_{AP}^s} |y_{q,p}^s|$ ;
12:    Update  $n_{AP}^{s+1}$  and  $n_{user}^{s+1}$  according to (4.73);
13:  end for
14:   $\hat{p}_l = \hat{p}_l^S$ ,  $\hat{q}_l = \hat{q}_l^S$ ;
15:   $\hat{\theta}_l = \Theta(\hat{p}_l)$ ,  $\hat{\phi}_l = \Theta(\hat{q}_l)$ ;
16:   $\hat{\alpha}_l = y_{\hat{q}_l, \hat{p}_l} / (\mathcal{C}_{\hat{q}_l, \hat{p}_l} N_t N_r)$ ;
17: end for
18: Output: the estimated AoAs, AoDs and the path gains. Based on (4.65), the
    estimated channel is reconstructed.

```

---

where  $\mathcal{C}_{q,p}^s = 1/\sqrt{LM_t^s M_r^s}$ ,  $p \in n_{AP}^s$  and  $q \in n_{user}^s$ . The number of active antenna elements in sth training level can be obtained as

$$M_a^s = \begin{cases} 2^s & 2^s \leq N_a \\ N_a & \text{otherwise} \end{cases}, a = \{t, r\}. \quad (4.84)$$

We compare the power to determine the one with the maximum received power, i.e.,

$$(\hat{q}_l^s, \hat{p}_l^s) = \arg \max_{q \in n_{user}^s, p \in n_{AP}^s} |y_{q,p}^s|. \quad (4.85)$$

As each beamforming/measurement vector is associated with a certain sector of the quantized AoA/AoD, the selection of the maximum power received signal implies that the corresponding range of the quantized AoA/AoD is highly likely to contain the dominant path of the channel. The output of the maximum power problem  $(\hat{q}_l^s, \hat{p}_l^s)$  is then used to determine the subsets of the beamforming vectors of the next sector level  $s + 1$  based on (4.73). The user then feeds back the selected subset of the beamforming vectors to the AP to employ it in the next level. As the next levels have higher and higher resolution, the AoA/AoD are determined in the last stage with the desired resolution being achieved. Until now, only one path is estimated in this iteration. In the next iteration, a similar training step is repeated. However, at each level  $s$ , the contribution of paths that have been already estimated in the previous iteration is



projected out before determining the new promising AoA and AoD ranges. At the  $l$ th iteration, we can obtain the optimum index pair  $(\hat{p}_l, \hat{q}_l)$  that maximizes  $|y_{p,q}|$ . Then, the AoA and AoD of the  $l$ th dominant path can be drawn from (4.70) as

$$\hat{\theta}_l = \Theta(\hat{p}_l) , \quad \hat{\phi}_l = \Theta(\hat{q}_l). \quad (4.86)$$

After estimating the AoAs/AoDs with the desired resolution, the complex gain of the  $l$ th dominant path turns out to be

$$\hat{\alpha}_l = y_{\hat{q}_l, \hat{p}_l} / (C_{\hat{q}_l, \hat{p}_l} \mathcal{F}^S(0, 0)) = y_{\hat{q}_l, \hat{p}_l} / (C_{\hat{q}_l, \hat{p}_l} N_t N_r). \quad (4.87)$$

The algorithm proceeds in the same way until all of  $L$  paths are estimated.

Based on the proposed algorithm, in each iteration the total number of levels required to estimate the AoA/AoD with a approximate resolution  $\frac{\pi}{N}$  is  $S = \log_2 \frac{N}{2}$ . Also, since we need  $\mathcal{K}^2$  training steps in each level, the total number of required steps becomes  $L\mathcal{K}^2 \log_2 \frac{N}{2}$ . Moreover, since  $N_b$  RF chains can be simultaneously used at the user to combine the measurements, the required number of steps can be further reduced to  $L\mathcal{K} \lceil \mathcal{K}/N_b \rceil \log_2 \frac{N}{2}$ .

In practical environment the number of modes  $L$  should be estimated by stopping the cancellation method while  $|\hat{\alpha}_l|$  becomes too weak which can be ignored. Here, we assume that  $L$  is less than six.

#### 4.2.3.2 Low Complexity Beamforming Training Algorithm

To further reduce the protocol overhead and power consumption, we propose a low-complexity beamforming training algorithm, in which we estimate the AoAs and AoDs separately.

In the first phase, the omnidirectional pattern with  $M = 1$  is employed at the AP. In the  $s$ th sector level, the user uses  $\mathcal{K}$  measurement vectors of the  $s$ th level of the codebook  $\mathcal{W}'$  to perform the received signal. After  $\lceil \mathcal{K}/N_b \rceil$  preamble transmission at this level, the user compares the power of the  $\mathcal{K}$  received signals to determine the one with the maximum received power. The output of the maximum power problem is then used to determine the subsets of measurement vectors of the next sector level  $s + 1$  until the highest resolution is achieved. In the next iteration, a similar training step is repeated. However, at each level  $s$ , we need to remove the contribution of paths that have already been estimated in the previous iteration before determining the new AoA ranges. The algorithm proceeds in the same way until  $L$  paths are estimated.

In the second phase, the user obtains the omnidirectional pattern. A similar training step is repeated to estimate all of AoDs at the AP side. In this algorithm, the total number of levels required to estimate the AoA/AoD with a resolution  $\frac{\pi}{N}$  is still  $\log_2 \frac{N}{2}$ . Also, since we need  $\lceil \mathcal{K}/N_b \rceil$  training steps in each level, the total number of needed steps becomes  $2L \lceil \mathcal{K}/N_b \rceil \log_2 \frac{N}{2}$ . Obviously, the number of preamble transmission is significantly reduced due to  $\mathcal{K} > 2$ . Furthermore, compared with the Algorithm 2, the low-complexity beamforming training algorithm can also avoid the feedback overhead during the training phase.

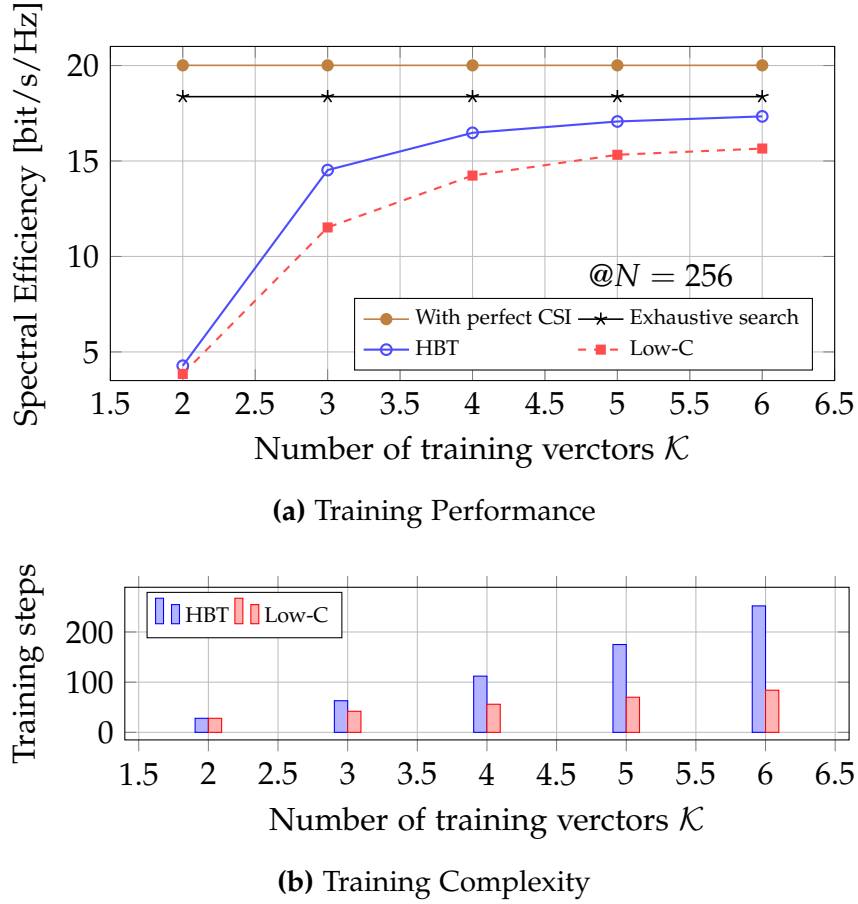


**Figure 4.11:** The effect of number of training vectors  $\mathcal{K}$  on the spectral efficiency and training iterations with  $N_t = 64$ ,  $N_r = 32$ ,  $N_b = 3$  and  $L = 3$ .

#### 4.2.4 Performance Evaluation

In this section, the efficiency of the proposed beamforming training algorithms is validated by numerical simulations. The hierarchical beamforming training (HBT) algorithm and low-complexity (Low-C) beamforming training algorithm are used to recover the channel parameters and further reconstruct the estimated channel. After that, the hybrid beamforming algorithm developed in [110] is then adopted to obtain the AP and the user precoding matrices. For illustration purposes, we adopt the time consuming exhaustive search (i.e.,  $\mathcal{K} = N$ , and  $S = 1$ ), used as benchmarks for the following comparisons.

First, we assess the relation of the number of training vectors  $\mathcal{K}$  and the spectral efficiency achieved by the proposed algorithms. In general, more training vectors in each training stage can achieve higher spectral efficiency. The spectral efficiency obtained by the proposed algorithms with different  $\mathcal{K}$  is depicted in Fig. 4.11. The performance loss between the perfect CSI and the exhaustive search is due to the AoAs and AoDs quantization error. It should be noted that with  $\mathcal{K} \geq 4$  comparable gains can be achieved using a hierarchical beamforming training algorithm despite the need for a much smaller training overhead and computational cost compared with

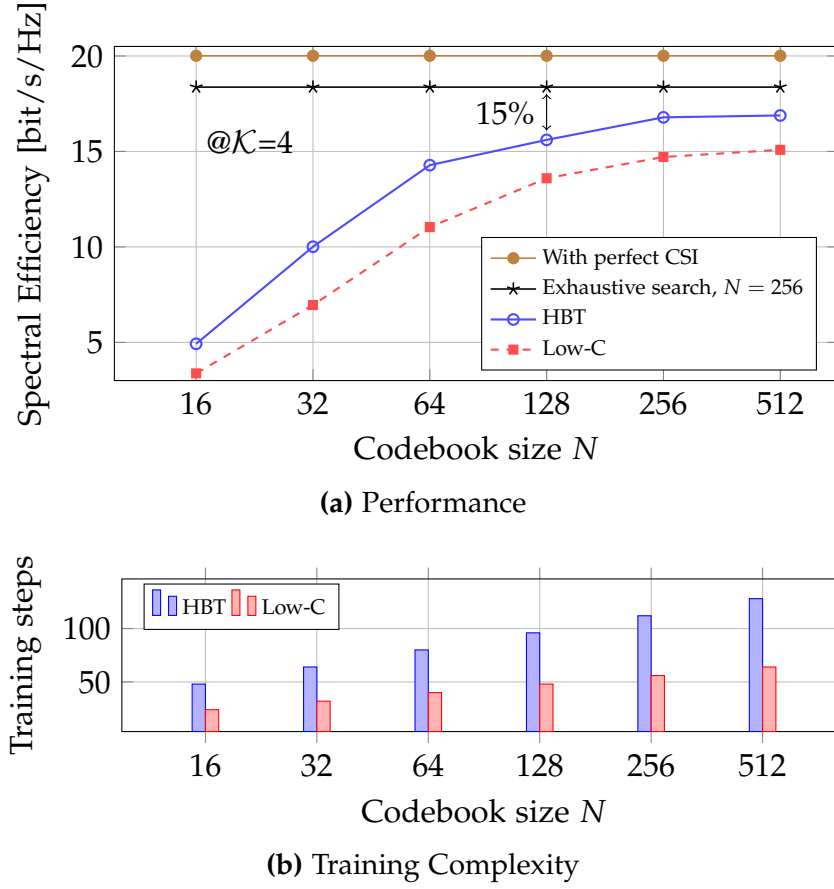


**Figure 4.12:** The effect of codebook size  $N$  on the spectral efficiency with  $N_t = 64$ ,  $N_r = 32$ ,  $N_b = 3$ ,  $\mathcal{K} = 4$  and  $L = 3$ .

the exhaustive search solution, which requires  $N \lceil N/N_b \rceil$  training steps. Moreover, the low-complexity beamforming training algorithm results in an acceptable performance loss with a very low training complexity, as illustrated in Fig. 4.11b.

In Fig. 4.12a, the improvement of spectral efficiency achieved by the proposed algorithms for  $L = 3$  with the codebook size  $N$  is simulated. The results show that more than 85% of the exhaustive search gain can be achieved by the HBT algorithm with only 96 iterations. These results also illustrate that a wise choice of codebook size  $N$  (i.e., to obtain the desired resolution) is necessary in order to have a good compromise between the performance and training overhead. For example, the figure shows that by doubling the number of codebook size, i.e., from 128 to 256, an improvement of less than 1 bit/s/Hz in the spectral efficiency is achieved. In addition, the spectral efficiency obtained by the Low-C algorithm with  $N = 512$  is very close to that of the HBT algorithm with  $N = 128$ . The training overhead associated with the Low-C algorithm is much smaller than that of the HBT algorithm shown in Fig. 4.12b. However, a larger codebook size also leads to higher computational complexity and hardware cost. In ultra-high data rates communication system, such low training overhead can be

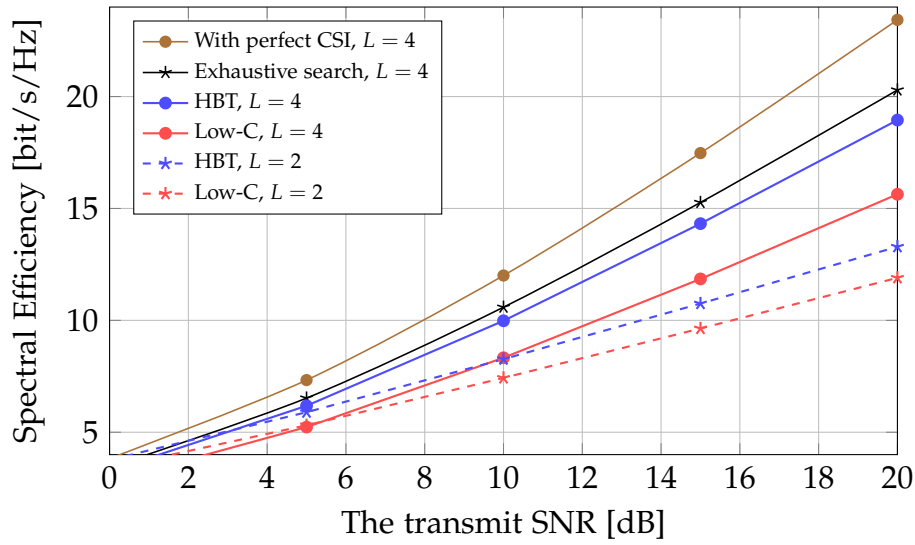


**Figure 4.13:** Spectral efficiency achieved when the precoding matrices are constructed using the estimated channel by proposed algorithms with  $L = 2$  or 4, where  $N_t = 64$ ,  $N_r = 32$ ,  $N_b = 3$ ,  $\mathcal{K} = 4$  and  $N = 256$ .

negligible. According to these criteria, the performance, computational complexity, and hardware cost have a much higher priority than training overhead.

After that, the spectral efficiency given by proposed algorithms is simulated when the desired number of estimated paths  $L$  equals 2 and 4, as illustrated in Fig. 4.13. The simulation results demonstrate that comparable gains are obtained using the proposed algorithms, not mentioning their low-complexity and smaller training overhead. The spectral efficiency degradation obtained by Algorithm 2 is less than 1 bit/s/Hz in a high SNR regime compared with the exhaustive search solution, which requires much more training steps. Fig. 4.13 also shows, with increasing  $L$ , the performance degradation between HBT and Low-C algorithms becomes larger. As we extract channel parameters of the different modes, the error propagation occurs during the iterative cancellation.

### 4.3 Low Complexity Equalization Algorithms

In our previous works, we have discussed different precoding/combining techniques, designed and proposed a new technology to combat the frequency selectivity, named time delay compensation (TDC). The TDC approach as a method to mitigate the effects of frequency selective channel at 60GHz band has been presented in [108]. The simulation results indicate that the approximate flat fading channel obtained by TDC has the advantage of both of the ergodic and outage capacity. Employing even just a one-tap MMSE equalizer [75] at the user side can achieve comparable BER performance to the flattened fading case when the sample duration is equal to or less than the symbol rate, which is not a challenge for hardware implementation at 60 GHz. This supports our proposal that TDC makes the channel flat, reduces the receiver com-

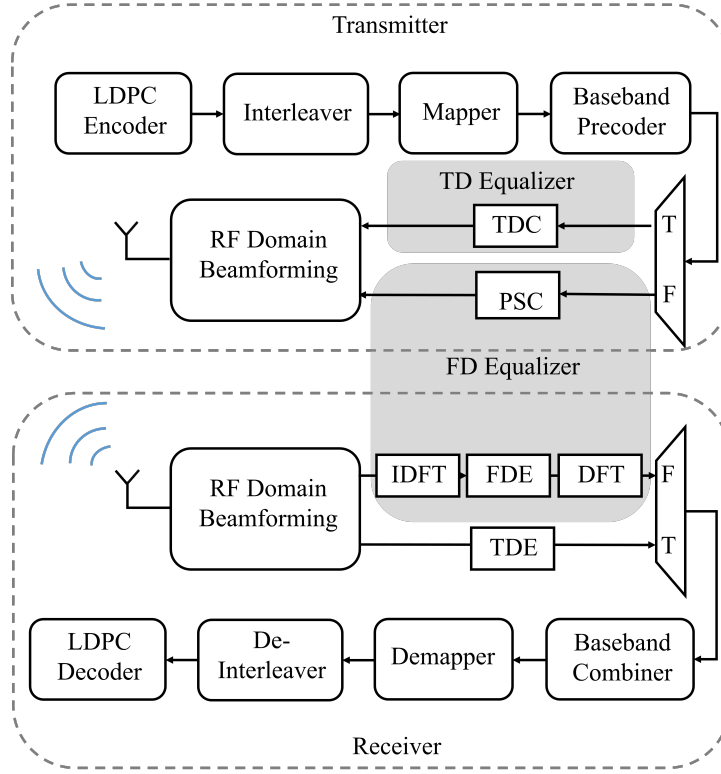


**Figure 4.14:** Block diagram and data path for TDE and FDE in digital baseband transceiver architecture of SC mode.

plexity, and improves the system performance. For the first time, TDC is adopted for mitigating the frequency selectivity to further reduce receiver complexity.

This section focuses on the extension to multiple data streams transmission over wideband channels with frequency selectivity. First, we develop two hybrid precoding solutions, namely TDC based TDE and phase shift compensation (PSC) based FDE, for such wideband mmWave systems, as illustrated in Fig. 4.14. The computational complexity of TDC based TDE is greatly reduced compared to the channel inversion and multi-tap FIR filter of conventional TDE. Our aim is to maximize the achievable capacity of the given system. During one block transmission, the RF precoder design is independent of the time delay spread. By adopting TDC for TDE and PSC for FDE in digital baseband, the flat fading channel is obtained. And then, the baseband precoder can be designed as the flat fading case by solving the capacity maximization problem. Due to energy savings and time considerations, we focus on the quantized precoder and combiner coefficients. Additionally, the proposed FDE requires a pair of FFT and IFFT. The time delay on each data stream in the time domain can be considered as a phase shift, which increases linearly with frequency, in the frequency domain. Second, we consider a frequency selective hybrid precoding system with the RF domain beamforming vectors taken from a quantized codebook. Finally, we validate two proposed equalizers' efficiency via simulations and compare them with the frequency flat case.

### 4.3.1 60 GHz Wideband MIMO Fading Channel

In this section, the channel model for 60 GHz wideband MIMO channels with frequency selectivity based on previous work reported in [55,96,104] is introduced.

#### 4.3.1.1 Propagation Scenario

Consider a wideband MIMO wireless system with one single access point (AP) in an indoor environment. Due to the large transmission bandwidth at 60 GHz, such a system will likely operate on wideband channels with frequency selectivity, making it challenging to use MIMO technology. To combat the effects of frequency selectivity, we propose two low complexity alternative methods: 1) a TDE with TDC, which, if implemented precisely, provides no delay differences between different paths; 2) an FDE with PSC based precoder. Fig. 4.14 illustrates the block diagram and data path for TDE and FDE in the digital baseband transceiver architecture of SC mode.

In such a propagation environment, we assume there are finite scatterer clusters. And the paths emanating from the same cluster suffer smaller delay differences. For the sake of simplicity, throughout this section, we restrict our attention to the downlink case. The TDC and PSC are done at the AP side for both the uplink and downlink transmission. Obviously, the complexity is only at the AP side in such a system.

#### 4.3.1.2 Beam Steering

We assume a uniform linear array (ULA) at both the AP and user side with  $N_t$  transmitter antennas and  $N_r$  receiver antennas. In order to achieve high directionality, beam steering is employed in this work. Shifting the RF phase is a very practical and feasible approach to achieving beam steering, especially considering the low-power consumption and low-complexity structure for 60 GHz compliant devices. Here, a uniform-weighting based codebook design [114,129] is adopted. The weighting vector can be described as follows

$$w_m = e^{-j\frac{2\pi}{\lambda}md\sin(\theta_{max})}, \quad m = 1, \dots, M.$$

The array factor now can be derived as

$$AF(\theta) = \sum_{m=0}^{M-1} w_m e^{j\frac{2\pi}{\lambda}md\sin(\theta)}, \quad (4.88)$$

where  $d$  is the antenna spacing,  $\lambda$  is the wavelength,  $M$  denotes the number of antennas, and  $\theta_{max}$  is the desired direction. Here,  $\theta_{max}$  can be set to angles of arrival and departure (AoA/ AoD).

#### 4.3.1.3 Channel Model

We adopt the modified Saleh-Valenzuela (S-V) model [55,96,104] for channel modeling at 60 GHz. We consider that there are  $L$  clusters and each channel cluster is composed of  $K_l$  rays. Under this model, the delay- $n$  MIMO channel matrix can be given by:

$$\mathbf{H}[n] = \sum_{l=1}^L \sum_{k=1}^{K_l} \alpha_{k,l} \delta(nT_s - \tau_l - t_{k,l}) \times \mathbf{a}_r(\phi_l - \varphi_{k,l}) \mathbf{a}_t^T(\theta_l - \vartheta_{k,l}),$$

where  $\alpha_{k,l}$  is the multipath gain coefficient of the  $k$ th multipath component in the  $l$ th cluster which follows the log-normal distribution.  $\tau_l$  denotes the arrival time of the first ray in the  $l$ th cluster. And the delay of the  $k$ th multipath component within the  $l$ th cluster relative to the first path arrival time  $\tau_l$  denoted as  $t_{k,l}$ .  $\phi_l$  and  $\theta_l$  represent the mean AoA and AoD of  $l$ th cluster respectively which follow uniform distribution  $U[0, 2\pi)$ .  $\varphi_{k,l}$  and  $\vartheta_{k,l}$  denote the AoA and AoD of the  $k$ th multipath component within the  $l$ th cluster. They follow the zero mean Laplacian distribution. The distribution of  $\varphi_{k,l}$  and  $\vartheta_{k,l}$  is given by [96]

$$p(\psi) = \frac{1}{\sqrt{2}\sigma_G} \exp(-|\sqrt{2}\psi/\sigma_G|),$$

where  $\sigma_G$  is the standard deviation. For the convenience of our simulations, the power delay profile of the channel used in this section derived from the non-line-of-sight (NLOS) channel model for the residential scenario based on the measurements by IEEE task group 802.15.3c [124].

Here, the number of clusters  $L$  gives us an indication about the number of dominant paths. Local scatterers in the cluster introduce micro delay variations ( $\tau_{k,l}$  is very small). And they can be even further reduced by employing beam steering for each cluster which focuses the power in the direction of dominant path. If we obtain a narrower beam, then we can achieve lesser delay spread in each cluster. Therefore, we can consider each cluster to be frequency flat over wider bandwidth. Consequently, all the rays in one cluster constructively add the channel gain of the  $l$ th cluster and then we seem to have one single propagation path in each cluster. With RF domain beamforming, the channel can be given as

$$\mathbf{H}[n] = \sum_{l=1}^L \alpha_l \delta(nT_s - \tau_l) \mathbf{a}_r(\phi_l) \mathbf{a}_t^T(\theta_l).$$

In this section, we assume that the AP has perfect channel state information.

#### 4.3.2 Problem Statement

In order to mitigate the effects of frequency selective channels, we consider SC zero-padded (ZP) block transmissions over time-flat but frequency-selective fading channels [65]. Consider a MIMO system with  $N_t$  transmitter antennas and  $N_r$  receiving

antennas. Assuming the number of data streams is  $N_s$ , the information bearing sequence is grouped into blocks  $\mathbf{x}_n = [x_n(1), \dots, x_n(k), \dots, x_n(M_s)]^T$  of size  $M_s$ , where  $k$  denotes the time index and  $n$  denotes the index of data streams,  $n = 1, \dots, N_s$ . To mitigate the inter block interference (IBI), we pad  $M_0$  zeros at the end of each information block to obtain transmitted blocks of size  $M_b = M_s + M_0$ . The length of ZP  $M_0$  is chosen to be at least  $L - 1$  to avoid IBI.

We adopt the hybrid beamforming system architecture illustrated in our previous work [110, Fig. 1]. Therefore the  $N_s \times 1$  transmitted signal vector at time index  $k$  can be expressed as  $\mathbf{x}(k) = [\mathbf{x}_1(k), \dots, \mathbf{x}_{N_s}(k)]$ . The complex signal at output of the baseband precoder  $\mathbf{W}_{bb}$ , of size  $N_{rf} \times N_s$ , at time index  $k$  can be expressed as

$$\mathbf{s}(k) = \mathbf{W}_{bb}(k)\mathbf{x}(k), \quad (4.89)$$

where  $N_{rf}$  is the number of RF chain.

At the receiver side, the received signal is first combined in the RF domain using the  $N_{rf} \times N_r$  combining matrix  $\mathbf{Z}_{rf}$ . Then, the ZPs are discarded to yield the processed signal vector [126] expressed by

$$\begin{bmatrix} \mathbf{r}_1 \\ \vdots \\ \mathbf{r}_{N_{rf}} \end{bmatrix} = \begin{bmatrix} \mathbf{H}_{1,1} & \dots & \mathbf{H}_{1,N_{rf}} \\ \vdots & \ddots & \vdots \\ \mathbf{H}_{N_{rf},1} & \dots & \mathbf{H}_{N_{rf},N_{rf}} \end{bmatrix} \cdot \begin{bmatrix} \mathbf{s}_1 \\ \vdots \\ \mathbf{s}_{N_{rf}} \end{bmatrix} + \begin{bmatrix} \mathbf{n}_1 \\ \vdots \\ \mathbf{n}_{N_{rf}} \end{bmatrix}. \quad (4.90)$$

It is important to emphasize here that the RF domain precoding and combining matrices  $\mathbf{W}_{rf}$  and  $\mathbf{Z}_{rf}$  is the same for all time index  $k$ , which means that the RF domain beamforming is assumed to be frequency flat and only depends on the channel characteristics (e.g., AoA/AoD). The received signal at time index  $k$  after processing can be written as

$$\hat{\mathbf{s}}(k) = \mathbf{Z}_{bb}(k)^H \mathbf{Z}_{rf}^H \mathbf{H}(k) \mathbf{W}_{rf} \mathbf{W}_{bb}(k) \mathbf{x}(k) + \mathbf{Z}_{bb}(k)^H \mathbf{Z}_{rf}^H \mathbf{n}(k), \quad (4.91)$$

The main objective of this section is to maximize the achievable mutual information for such hybrid analog/digital architecture, by selecting the best RF matrix  $\mathbf{W}_{rf}$  from predefined codebook and optimize the baseband precoding matrix  $\mathbf{W}_{bb}(k)$ . The information rate achieved by this system [15] can be expressed as

$$\mathcal{I} = \log_2(|\mathbf{I} + (\mathbf{Z}_{bb}(k) \mathbf{Z}_{rf} \mathbf{H}(k) \mathbf{W}_{rf} \mathbf{W}_{bb}(k))^H \mathbf{R}_n^{-1} (\mathbf{Z}_{bb}(k) \mathbf{Z}_{rf} \mathbf{H}(k) \mathbf{W}_{rf} \mathbf{W}_{bb}(k))|).$$

Note that,  $\mathbf{R}_n = \mathbf{Z}_{bb}(k) \mathbf{Z}_{rf} \mathbf{R}_{nn} \mathbf{Z}_{rf}^H \mathbf{Z}_{bb}(k)^H$  is the post-processing noise variance matrix. Obviously, the computational complexity is extremely high to solve this optimization problem at each symbol duration. In the following, we develop two low complexity hybrid precoding solutions: TDC based TDE and PSC based FDE.



### 4.3.3 Time-Delay Compensation based Time Domain Equalizer

Appreciating to the highly directional characteristic and/or beamforming technique, the combined architecture of TDC and simplified SVD based equalization is proposed in this section to realize TDE in SC mode of 60 GHz systems. Comparing to the "classical" digital equalizers such as zero-forcing (ZF), MMSE and least-mean-squares (LMS) TDE, the computational complexity of TDC based TDE is not proportional to the RMS delay spread of multipath fading channel.

#### 4.3.3.1 Path Selection Algorithm

In order to employ TDC efficiently to obtain a flat fading channel, best possible beam separation is necessary to guarantee the signal-to-interference ratio (SIR). This leads to the optimization of RF domain beamforming at the transmitter side, namely path selection algorithm proposed in our previous work [110]. We use average SIR as a performance metric to maintain the signal quality for each beam.

Suppose that, via each individual dominant path, we transmit only one data stream to bring down the dependency between different dominant paths. However, the side lobes of one beam induces interference to the beams of other dominant paths. We utilize average signal-to-interference ratio (SIR) as a performance metric to maintain the signal quality for each beam. In order to fulfill an SIR constraint denoted as  $\delta$ , e.g.  $\delta = 10\text{dB}$ , the beam inducing higher interference to other beams and the corresponding path undergoing higher attenuation is set aside. The higher SIR constraint we set, the lower dependency between different dominant paths we can obtain. Nevertheless, once the SIR threshold is too high, the capacity achieved by the system is decreased due to the decrements of diversity. Therefore, it is essential to adjust the SIR threshold to balance the dependency between different dominant path and the capacity. Due to the limited SIR threshold, though the dependency between different dominant paths is significantly eliminated, the interference still exists.

#### 4.3.3.2 Time Delay Compensation

Time Delay Compensation (TDC) technique, if implemented precisely without considering the hardware limitations, yields no delay differences between different paths and obtains a flat fading channel over a wide bandwidth. According to indoor channel measurements, the geometric modeling approach [55] consists of multiple clusters, each with multiple rays. To reduce the delay spread both, intra- and intercluster, we employ beamforming in RF domain and a TDC in digital baseband. Generally, the local scatterers in each cluster only introduce very small delay variations and firstly we can further minimize their delay spread by employing RF beamforming. By increasing the number of antennas, a narrower beam can be obtained, which reduces the delay spread. Therefore, in each cluster the channel becomes frequency flat over a wider bandwidth. Meanwhile, we compensate the intercluster time delay difference by adopting an adjustable buffer in digital baseband.

The relative time delay on each individual path is compensated by input buffer. The time delay vector  $\tau$  can be expressed as  $\tau = [\tau_1, \dots, \tau_l, \dots, \tau_L]^T$ . Instead of the absolute time delay on each path, we consider the relative time delay with reference to minimum one to decrease the implementation complexity. Therefore, we obtain

$$\tau = \tau_{min} + [\tilde{\tau}_1, \dots, 0, \dots, \tilde{\tau}_L]^T, \quad (4.92)$$

where  $\tilde{\tau}_l = \tau_l - \tau_{min}$  with  $l = 1, \dots, L$ . Obviously, precision of the buffer depends on the sample duration  $T_b$ . The quantization error vector can be denoted as

$$\tau_e = \tilde{\tau} - \text{round}(\tilde{\tau}/T_b) \cdot T_b, \quad (4.93)$$

where  $\text{round}(x)$  rounds  $x$  to the nearest integer. Experiment results show that the quantization error follow Gaussian distribution. Here, the absolute value of maximum quantization error is equal to  $T_b/2$ . Hence, the possible maximum length of CIR spread with TDC can be written as

$$\mathcal{L} = \lceil (\tau_{e,max} - \tau_{e,min})/T_s \rceil = \lceil T_b/T_s \rceil, \quad (4.94)$$

where  $T_s$  denotes the symbol duration.

To obtain flat channel, we shall have  $\mathcal{L} < 1$ . This inequality can be guaranteed if the buffer sample duration is smaller than symbol duration. During 60 GHz band transmission,  $T_s$  is in the range of few nanoseconds to reach beyond gigabit per second throughout. Obviously, the frequency selectivity of the channel depends on the time resolution of the buffer yielding a trade-off between processing power and performance (both increase with time resolution of the buffer) [108].

#### 4.3.3.3 Capacity Maximization Criterion

After obtaining a flat fading channel, the optimization of remaining precoding and combining matrices is formulated based on the capacity maximization criterion under a total transmit power constraint. Take into consideration the negligible interference and approximate diagonal property of  $\mathbf{H}_{m,n}$  with  $m, n \in \{1, \dots, N_{rf}\}$ , we can obtain

$$\mathbf{H}(k) = \begin{bmatrix} H_{1,1;k} & \dots & H_{1,N_{rf};k} \\ \vdots & \ddots & \vdots \\ H_{N_{rf},1;k} & \dots & H_{N_{rf},N_{rf};k} \end{bmatrix}, \quad (4.95)$$

where  $H_{m,n;k}$  denotes the  $k$ th diagonal element of  $\mathbf{H}_{m,n}$ . As can be seen from (4.90), the diagonal elements in  $\mathbf{H}_{m,n}$  is time invariant, making it much more computationally efficient to solve the optimization problem.

Adopting a similar procedure to [105, 112], the AP can build its hybrid data precoders  $\mathbf{W}_{rf}$ ,  $\mathbf{W}_{bb}$  and combiners  $\mathbf{Z}_{rf}$ ,  $\mathbf{Z}_{bb}$  to approximate the dominant singular vectors of the channel  $\mathbf{W}_{opt}$  and  $\mathbf{Z}_{opt}$ , respectively.

### 4.3.4 Phase-Shift Compensation based Frequency Domain Equalizer

The time delay on each data stream in time domain can be considered as phase shift, which increases linearly with frequency, in the frequency domain. With the assumption of zero padded block transmissions (see Section 4.3.2), we can use DFT and IDFT of length  $N$  equal to this block length for a delay compensation in the frequency domain. Furthermore, additional components are not required adopting the PSC. Let  $\mathbf{F}_N$  denote the normalized DFT matrix of size  $N \times N$ , with the  $(p, q)$ th element equals to  $(1/\sqrt{N}) \exp(-j2\pi(p-1)(q-1)/N)$ . Thus, the equality  $\mathbf{F}_N^H \mathbf{F}_N = \mathbf{I}_N$  holds. By left multiplying (4.90) by  $\text{diag}\{\mathbf{F}_N \dots \mathbf{F}_N\}$ , the FD representations can be expressed as

$$\begin{bmatrix} \mathbf{Y}_1 \\ \vdots \\ \mathbf{Y}_{N_{rf}} \end{bmatrix} = \begin{bmatrix} \mathbf{H}_{1,1}^{\mathcal{F}} & \dots & \mathbf{H}_{1,N_{rf}}^{\mathcal{F}} \\ \vdots & \ddots & \vdots \\ \mathbf{H}_{N_{rf},1}^{\mathcal{F}} & \dots & \mathbf{H}_{N_{rf},N_{rf}}^{\mathcal{F}} \end{bmatrix} \cdot \begin{bmatrix} \mathbf{S}_1 \\ \vdots \\ \mathbf{S}_{N_{rf}} \end{bmatrix} + \begin{bmatrix} \mathbf{N}_1 \\ \vdots \\ \mathbf{N}_{N_{rf}} \end{bmatrix}$$

where  $\mathbf{Y}_m = \mathbf{F}_N \mathbf{y}_m$ ,  $\mathbf{H}_{m,n}^{\mathcal{F}} = \mathbf{F}_N \mathbf{H}_{m,n} \mathbf{F}_N^H$ ,  $\mathbf{S}_n = \mathbf{F}_N \mathbf{s}_n$  and  $\mathbf{N}_m = \mathbf{F}_N \mathbf{n}_m$ .

*Remark 1:* If the block time duration  $(M_s + L - 1)T_s$  less than the channel coherence time, then we can consider the CIR during one block transmission keep invariant so that  $\mathbf{H}_{m,n}$  is a circulant matrix. Meanwhile,  $\mathbf{H}_{m,n}^{\mathcal{F}}$  is a diagonal matrix with the  $k$ th diagonal element

$$H_{m,n,k}^{\mathcal{F}} = \sum_{l=1}^{M_l} h_{m,n}(l) \exp(-j2\pi(l-1)(k-1)/N).$$

In order to enhance the computational efficiency, similar to TD equalizer, SVD can be applied to sub-channels which can be determined by taking out the  $k$ th diagonal element from the corresponding position of each  $\mathbf{H}_{m,n}^{\mathcal{F}}$ , and these elements compose the matrix of  $k$ th sub-channel  $\mathbf{H}^{\mathcal{F}}(k)$ ,  $k = 1, 2, \dots, N$ , i.e.

$$\mathbf{H}^{\mathcal{F}}(k) = \begin{bmatrix} H_{1,1;k}^{\mathcal{F}} & \dots & H_{1,N_{rf};k}^{\mathcal{F}} \\ \vdots & \ddots & \vdots \\ H_{N_{rf},1;k}^{\mathcal{F}} & \dots & H_{N_{rf},N_{rf};k}^{\mathcal{F}} \end{bmatrix}. \quad (4.96)$$

Nevertheless, in practical system, it is still not computationally efficient to execute  $N$  times SVD of size  $N_{rf} \times N_{rf}$  during one block transmission.

Here, due to the RF domain beamforming and path selection algorithm,  $h_{m,n}(\hat{l})$  with  $\hat{l} = m = n$  is a dominant figure, of which the amplitude is much larger than other coefficients. Therefore the contribution to  $H_{m,n,k}^{\mathcal{F}}$  of other elements  $h_{m,n}(l)$  with  $l \neq \hat{l}$  are ignorable, i.e.

$$H_{m,n,k}^{\mathcal{F}} \approx h_{m,n}(\hat{l}) \exp(-j2\pi(\hat{l}-1)(k-1)/N) \quad (4.97)$$

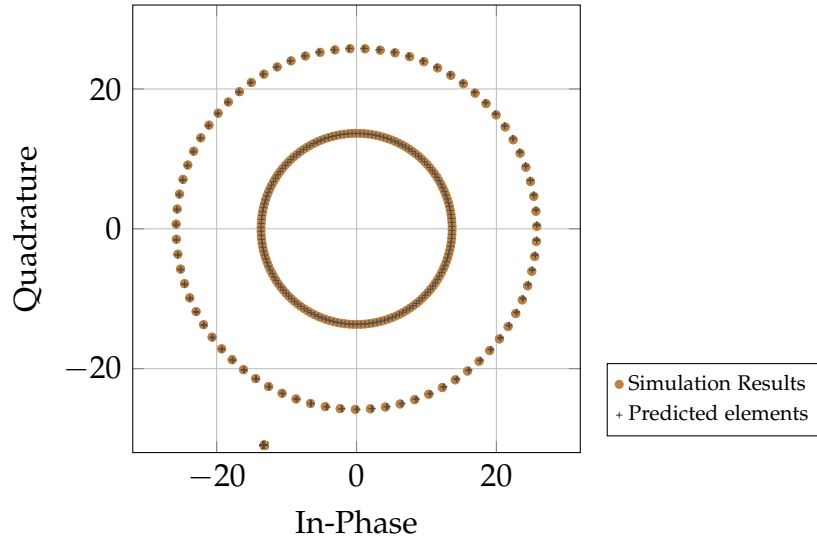


**Figure 4.15:** The scatter plot of diagonal elements of channel matrix with 3 dominant paths. There exists an approximately constant phase shift between adjacent sub-channel.

Therefore, the relation among  $\{H_{m,n;k}^{\mathcal{F}}, H_{m,n;k-1}^{\mathcal{F}}\}$  can be determined as  $H_{m,n;k}^{\mathcal{F}} = H_{m,n;k-1}^{\mathcal{F}} \Delta\phi_{m,n}$  with  $\Delta\phi_{m,n} = \exp(-j2\pi(\hat{l}-1)/N)$ . Obviously,  $\Delta\phi_{1,1} = 0$ .

*Remark 2:* There exists an approximately constant phase shift between adjacent sub-channel matrix  $\mathbf{H}^{\mathcal{F}}(k-1)$  and  $\mathbf{H}^{\mathcal{F}}(k)$ , which means  $\mathbf{H}^{\mathcal{F}}(k)$  can be determined from  $\mathbf{H}^{\mathcal{F}}(k-1)$  by element-by-element multiplying a phase shift matrix  $\Phi$  with  $\Delta\phi_{m,n}$

$$\Delta\phi_{m,n} = \begin{cases} \exp(-j2\pi(\hat{l}-1)/N), & m = n, \hat{l} = m \\ 0, & \text{otherwise} \end{cases}. \quad (4.98)$$

Based on the aforementioned two properties, we propose a very low complexity SVD based FD equalizer.

#### 4.3.4.1 Phase Shift Compensation

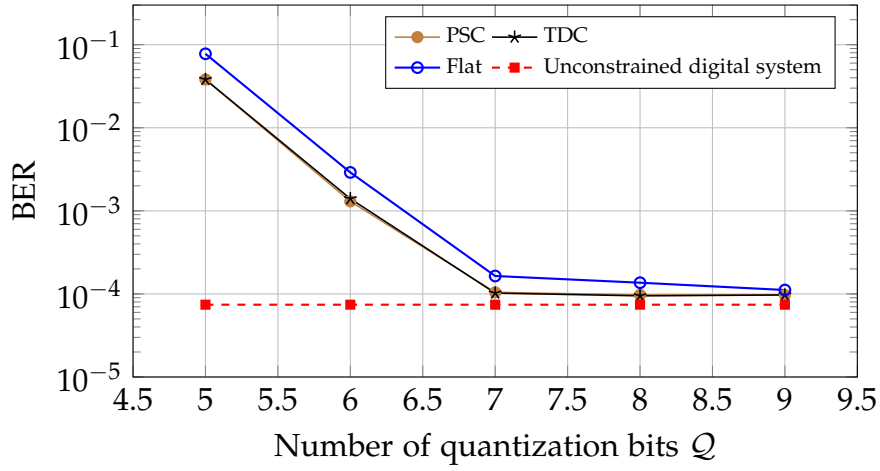
With considering the baseband precoder and combiner, the equivalent channel  $\tilde{\mathcal{H}}(k-1)$  can be expressed as

$$\tilde{\mathcal{H}}(k-1) = \mathbf{Z}_{bb}(k-1) \cdot \mathbf{H}^{\mathcal{F}}(k-1) \cdot \mathbf{W}_{bb}(k-1) \quad (4.99)$$

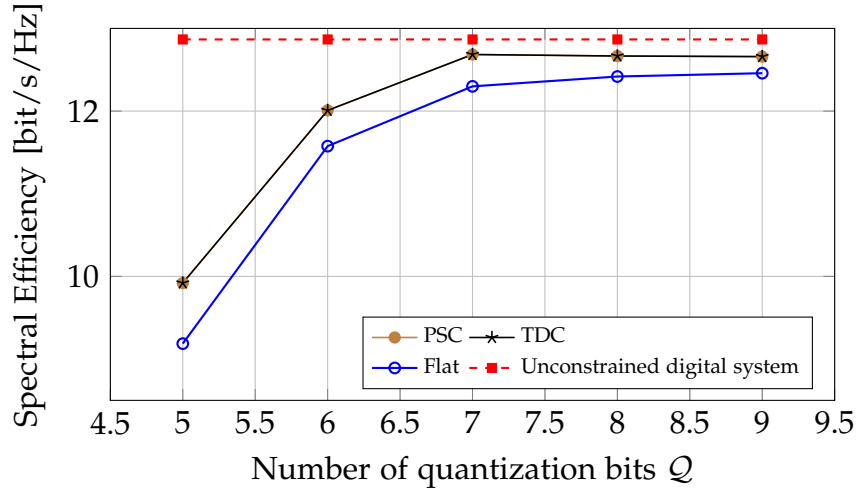
where  $\tilde{\mathcal{H}}(k-1)$  is a approximately diagonal matrix with ordered positive elements, which means several parallel independent channels are obtained.

Suppose that  $\mathbf{W}_{bb}(k) = \Phi^{-1} \mathbf{W}_{bb}(k-1)$  and  $\mathbf{Z}_{bb}(k) = \mathbf{Z}_{bb}(k-1)$ , the equivalent channel  $\tilde{\mathcal{H}}(k)$  can be written as

$$\tilde{\mathcal{H}}(k) = \mathbf{Z}_{bb}(k) \cdot \mathbf{H}^{\mathcal{F}}(k) \cdot \mathbf{W}_{bb}(k) = \tilde{\mathcal{H}}(k-1) \quad (4.100)$$



(a) BER Performance



(b) Spectral Efficiency

**Figure 4.16:** BER performance and spectral efficiency as a function of phase quantization bits in a hybrid system with only quantized analog phase control. Results compare the BER performance of proposed algorithms with the unconstrained system. The SNR is at 18dB

Therefore, once one sub-channel matrix and phase shift matrix are known, all other sub-channel matrices can be determined. Moreover, the difference between original diagonal elements and reproduced diagonal elements is very small, as shown in Fig. 4.15. It can be seen  $\tilde{\mathcal{H}}(k)$  is also flattened by only multiplying a diagonal phase shift matrix to pre-processing matrix instead of performing SVD again, which is much more computationally efficient.

### 4.3.5 Performance Evaluation

In this section, we present numerical results to evaluate the performance of proposed SVD based TDE and FDE. We consider the case when there is only one AP and one

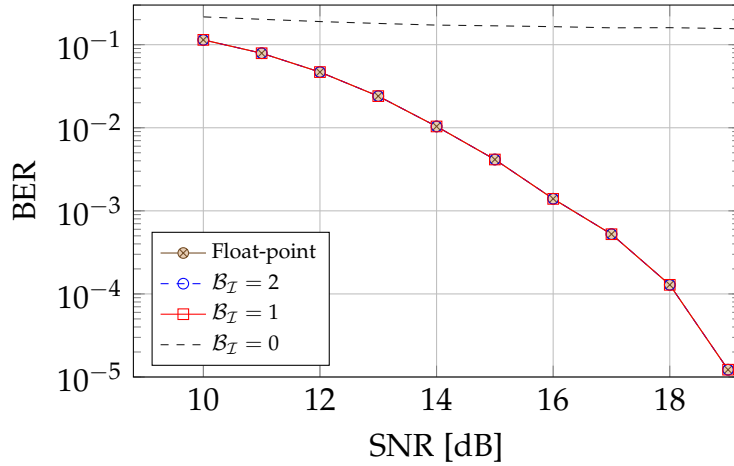


**Figure 4.17:** The influence of integer bit-length on the BER performance. We consider 8 bit fractional part for all the cases.

user without any interference. We adopt the hybrid beamforming system architecture illustrated in [110, Fig. 1]. The AP has  $N_t = 32$  antennas, and the user has  $N_r = 16$  antennas. The antenna array is ULAs, with spacing between antennas equal to  $\lambda/2$ . We focus on the quantized precoder and combiner coefficients since it is more important for hardware realization due to energy savings and time considerations. The baseband precoder and combiner adopt a fixed bit-length message quantization with sign-magnitude representation. The quantization scheme is described by the bit-length  $\mathcal{B}$ . The precoder and combiner coefficients and processed signals use saturating arithmetic to prevent wrapping. And the RF phase shifters are assumed to have only quantized phases. As mentioned earlier, each channel realization is generated using the 60 GHz NLOS multipath channel model for the residential scenario CM2.3 [124]. In addition, the channel realization  $\mathbf{H}$  is assumed to keep invariant during one codeword transmission. The LDPC code used in the WiMAX IEEE 802.16e standard with the rate of 2/3 and codeword bits 576, and Gray mapped 16 QAM modulation are employed for the transmission. Two data streams are simultaneously transmitted with  $N_{rf} = 3$ .

#### 4.3.5.1 Influence of Parameter Setting

The BER performance and spectral efficiency as a function of phase quantization bits in a hybrid system with only quantized analog phase control are depicted in Fig. 4.16. For illustration purposes, we adopt the time consuming unconstrained digital system. Their decoding performance and spectral efficiency are used as benchmarks for the following comparisons. Here, the impact of the RF system limitations on the performance of proposed equalization algorithms is evaluated. We consider 6 bit quantization with sign-magnitude representation for digital baseband processing. Simulation results show that the proposed algorithms can achieve near-optimal spectral efficiency if the quantization bits is larger than or equal to 7. Also, the results show that five

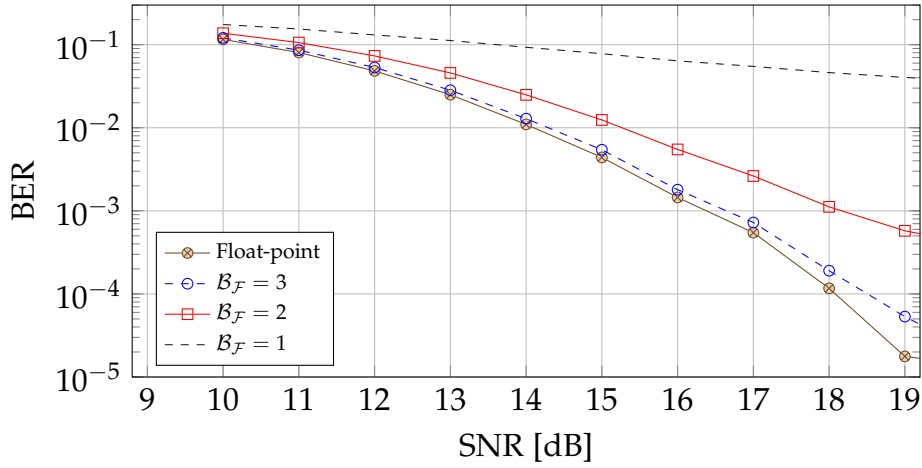


**Figure 4.18:** The influence of bit-length of fractional part on the BER performance. We consider 2 bit integer part for all the cases.

quantization bit may be sufficient to accomplish more than 90% of the maximum gain. However, the BER performance loss is unacceptable.

The subsequent step is to examine the impact of word-length  $B$  on the BER performance. The BER performance over the signal to noise ratio SNR for different fixed-point word-length is shown in Fig. 4.17. The 16 bit floating-point representation is used as a reference. Firstly, it can be seen in Fig. 4.17 that the communication performance shows no degradation for  $B_I = 1$  bit integer part with 8 bit fractional part. Secondly, in Fig. 4.18 different bit length of fractional part cases are shown. When  $B_F = 4$ , there is no performance loss with 2 bit integer part. The degradation in communications performance for  $B_F = 3$  is just 0.4dB as the target BER is  $10^{-4}$ . In the following, we set the number of phase quantization bits to  $Q = 7$ . For baseband precoder and combiner, the bit-length of integer part and fractional part to  $B_I = 1$ , and  $B_F = 4$ . This quantization scheme results in a communication loss of 0.1dB compared to floating-point representation.

#### 4.3.5.2 Comparison: TDE and FDE

After identifying the optimal word-length at digital baseband and number of phase quantization bits, we further compare the decoding performance and spectral efficiency of the proposed algorithms. The decoding performance comparisons are conducted in the context of a  $N_s = 2$  MIMO system combined with capacity achieving channel code. As we can observe, from Fig. 4.19, the proposed algorithms yield BERs very close to that of flat fading channel, where only some marginal BER loss occurs at high SNRs. In Fig. 4.20, the frequency selective channel can achieve slightly higher spectral efficiency than the flat fading case due to the increment of diversity.

Besides BER performance and spectral efficiency, computational algorithm complexity is also one of the most important factors. The components and computational complexity of two proposed equalization algorithms are listed in Table 4.2 and 4.3. The FDE requires a pair of FFT and IFFT to transform data to the frequency do-

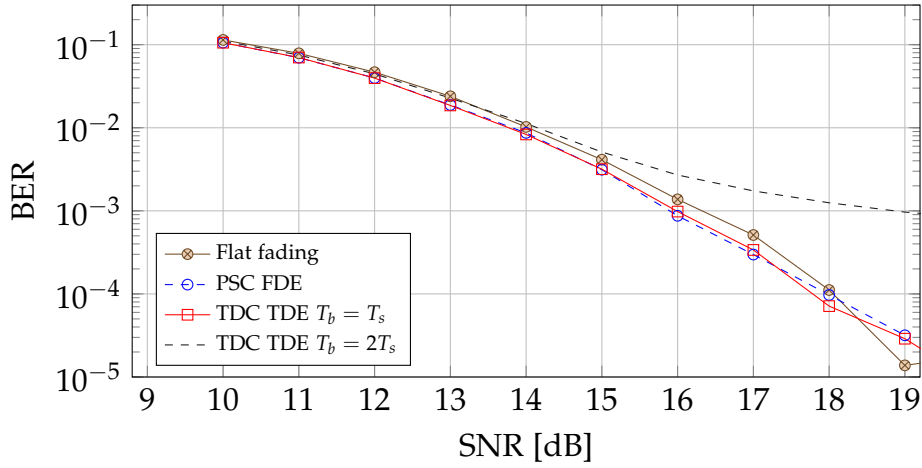


**Figure 4.19:** The BER performance of different algorithms. The BER performance loss exists when the resolution of the buffer is low.

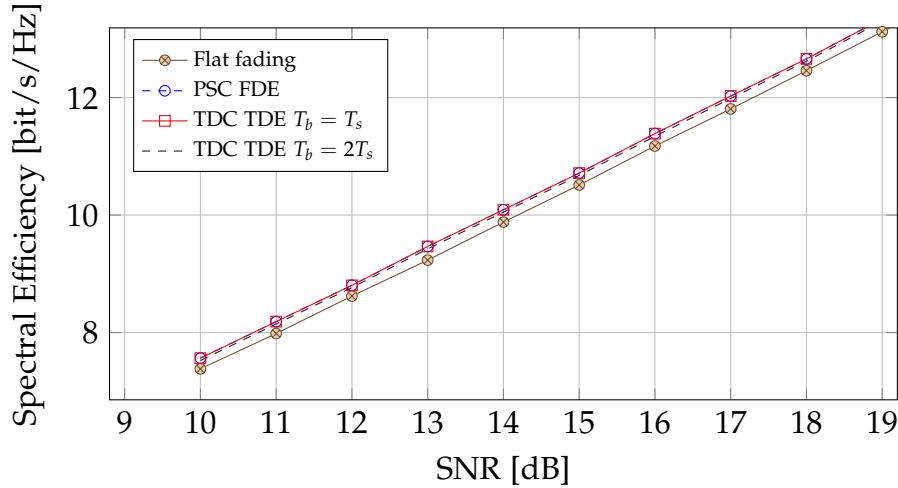


**Figure 4.20:** The spectral efficiency of different algorithms. The frequency selective channel can achieve slightly higher spectral efficiency.

main for equalization and back to time domain for data demodulation, respectively. With a block length of  $M_b = 512$ , the number of operations during one block transmission at the receiver side is shown in Fig. 4.21. The PSC based FDE requires a higher implementation complexity due to DFT. According to the criteria for low power consumption, computational complexity has a higher priority than decoding performance. Therefore, the additional complexity related to FDE is the cost of its BER gain.

## 4.4 Summary

In this chapter, we have analyzed the performance of a single user MIMO system (point-to-point transmission) with hybrid pre- and post-processing, in which a limited

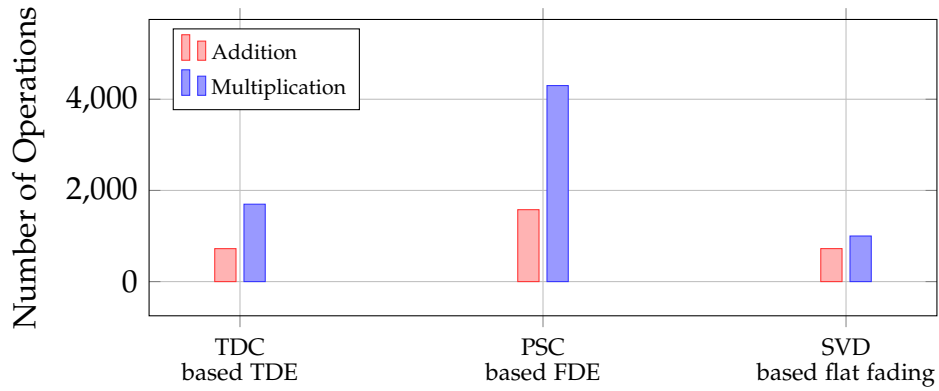


**Table 4.2:** Computational complexity: TDC based TDE

Component	Addition	Multiplication
Pre-processing	$N_{rf} \times (N_s - 1)$	$N_{rf} \times N_s$
Post-processing	$N_s \times (N_{rf} - 1)$	$N_{rf} \times N_s$
Input buffer	Implemented by register	
SVD	$\mathcal{O}(N_{rf}^3)$	

**Table 4.3:** Computational complexity: PSC based FDE

Component	Addition	Multiplication
Pre-processing	$N_{rf} \times (N_s - 1)$	$N_{rf} \times N_s$
Post-processing	$N_s \times (N_{rf} - 1)$	$N_{rf} \times N_s$
DFT / IDFT	$\mathcal{O}(M_b \log M_b)$	
SVD	$\mathcal{O}(N_{rf}^3)$	

**Figure 4.21:** The number of operations during one block transmission at the receiver side with  $N_s = 2$ ,  $N_{rf} = 3$ , and  $M_b = 512$ .

number of RF chains drives a large number of antennas array. There are two kinds of common structures: fully-connected structure and array-of-subarray structure.

For a fully-connected structure, three joint optimum pre- and post-processing design criteria have been derived for a hybrid spatial processing system under total transmit power constraint. After optimizing digital baseband pre- and post-processing with a weighted minimum mean square error (MMSE) criterion, the optimization in the RF domain is performed based on three criteria subject to various error weights. Besides, a low hardware complexity transceiver has been constructed. Relative to a fully digital pre-processing architecture, the performance loss of our hybrid scheme is negligible. For array-of-subarray structure, the two-step scheme consists of a base-

band beamforming design similar to a fully-connected structure and a counterpart in the RF domain using an iterative algorithm. Numerical results to assess the performance of the proposed system in terms of uncoded BER and information rate have been presented.

After that, we have developed two novel mmWave channel recovery algorithms that efficiently determine different parameters of the mmWave channel with a very low training overhead based on the 2D-DFT technique. The proposed algorithms take into account practical radio frequency (RF) hardware limitations and computational complexity reduction during the training phases with comparable performance. For further work, it would be interesting to seek the design of robust channel recovery algorithms.

Last, we have proposed two frequency selective hybrid precoding solutions, namely TDC based TDE and PSC based FDE. Compared to the "classical" digital equalizers such as ZF, MMSE, and LMS TDE, the equalization algorithms we derived aim to maximize the data rate. The RF precoder is frequency flat during one block transmission due to the independence of RF precoder design on the time delay spread. The flat fading channel is obtained by adopting TDC for TDE and PSC for FDE in digital baseband. After that, the baseband precoder can be designed as the flat fading case in our previous work to maximize the achievable capacity. The proposed two novel mmWave channel equalization algorithms efficiently reduce the computational complexity. We focused on the quantized precoder and combiner coefficients since it is more critical for hardware realization due to energy and time savings. Furthermore, the RF phase shifters are assumed to have only quantized phases. Numerical simulations validate the performance of the proposed algorithms with quantized precoding and combining. It would be interesting to design efficient hybrid precoding for wideband multi-user mmWave systems, which will be addressed in Chapter 6.

## Chapter 5

# Power Efficiency Analysis of Millimeter Wave Transmission Systems

---

Large scale antenna systems in the mmWave band provide a solution to the severe shortage of spectrum experienced in the conventional microwave bands. In a practical large scale antenna deployment, implementation of hybrid beamforming structure is critical as it provides high array gains to overcome the high path loss and achieve sufficient link margins. However, while implementing this structure, we also encounter quite a few challenges, such as complexity, cost, and energy consumption. In this chapter, the spectrum efficiency of the hybrid beamforming approach is introduced in Section 5.2. After that, a power consumption model for the large scale antenna mmWave system is presented and analyzed in Section 5.3. With the help of this model, we maximize the energy efficiency of the overall system. As the optimization of energy efficiency is a crucial factor in system optimization and design of the power-hungry devices, the spectral efficiency goes through a reduction with the increasing energy efficiency. Thus, an analysis of the relation between energy and spectral efficiency becomes a critical task, and we aim to optimize energy efficiency constraining the spectral efficiency being fixed, as addressed in Section 5.4. The numerical results in Section 5.5 can then be utilized to guide the practical energy/spectrum efficiency trade-off for the LSAS design.

The results presented in the chapter have been published in part by the author in [106,107,110].

## 5.1 Introduction

60 GHz band offers a promising future for the ever-increasing demands of the local and personal area networks related to the high data rates, low power consumption and high spectrum efficiency (SE) [58]. Unfortunately, owing to many differentiating factors such as increased hardware complexity, large bandwidth at millimeter wave (mmWave) resulting in frequency selectivity, MIMO processing in mmWave systems differs significantly from it in the traditional microwave systems. Moreover, the channel at mmWave is sparse in the angular domain [76,96]. All these factors make the traditional system architectures implausible at mmWave. With high data rates which are enabled by the available bandwidths in the mmWave bands, limiting the processing power in an affordable range becomes an issue. The processing power consumption should be on the scale of a few Watt to avoid forced cooling. Allowing as little as 10 pJ for processing 1 bit, we need 1 W of processing power for 100 Gb/s. Thus, driven

by the aim of high spectral efficiency and maximizing data rate under strict energy constraint, a novel Large Scale Antenna System (LSAS) transceiver architecture employing hybrid beamforming with time-delay compensation (TDC) technology has been proposed in [110].

Due to the requirement of low power consumption for battery operated devices, access points (APs) undertake most major computation procedures such as various estimation works, precoding, etc [16]. Fundamentally, the users (e.g. mobile) are relatively small scale communication units while APs are physically large scale communication units. When targeting data rates are on the scale of Gbps, the overall power consumption of the system suffers dramatically. Therefore, the proposed transceivers should be optimized to achieve a maximum data rate under a strict overall energy constraint, which implies that transmit energy as well as processing energy is limited for a given data rate [105]. In this chapter, we aim at the optimization of the system parameters, such as the number of user antennas, the number of RF chains and the number of data streams in order to maximize the energy efficiency (EE) for the novel proposed transceiver architecture.

In the previous work [107], the LSAS architecture employing hybrid beamforming with TDC has been proposed, which combats the frequency selectivity to flatten the channel over a wide bandwidth as well as maximizes the capacity. The analysis of the power requirements for this system is still an important consideration which needs to be investigated.

Thus, the motivation of this chapter comes to devising a suitable power consumption model and optimizing the EE of the system. To enhance the EE while guaranteeing a certain SE, it is required to study the fundamental EE-SE relationship to design practical energy-saving strategies. Furthermore, the different system parameters influencing the EE-SE relationship such as the number of receive and transmitter antennas, the average signal-to-interference ratio (SIR) threshold, and the bandwidth, are studied. Numerical simulations comparing the EE and SE under different system parameters are also presented. Accordingly, an optimum set of system parameters is obtained, which observes the practical EE/SE trade-off and maximizing the performance of the proposed LSAS system architecture.

## 5.2 Spectrum Efficiency

The channel model for broad-band fading channels is introduced in this chapter accompanied by the novel LSAS transceiver architecture employing hybrid beamforming with TDC technology.

Based on the experimental investigations, the clustering approach is directly applicable to channel models for 60 GHz indoor wireless local area network (WLAN) systems with each cluster actually consisting of a number of rays closely spaced to each other in the time and angular domains. Therefore, the number of clusters gives an indication about the number of dominant paths. Our model considers that there are  $L$  significant clusters with minimal intra-cluster delay spread. RF domain beam-

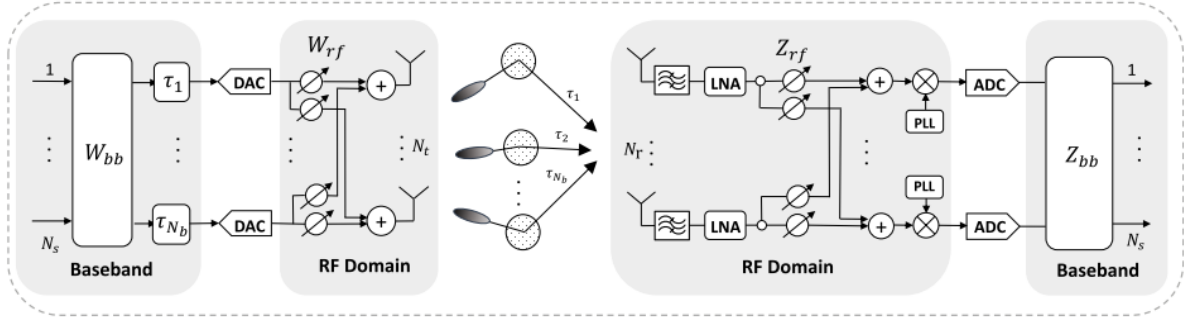


**Figure 5.1:** Block diagram of a large mmWave system employing beamforming and time-delay compensation

forming can then be exploited which focuses the power in the direction of the dominant path and the delay variations can further be reduced. With efficient beam steering, we can assume that there is one dominant path in each cluster, since all the rays in a cluster constructively add the channel gain of the  $l$ th cluster.

Here, we consider the most widely used modified Saleh-Valenzuela (S-V) model for channel modeling at 60 GHz [55, 96, 104]. Using this model, the  $N_r \times N_t$  dimensional frequency-selective MIMO channel between the AP and the user can be expressed as

$$\mathbf{H} = \sqrt{\frac{N_t N_r}{L}} \sum_{l=1}^L \alpha_l \mathbf{a}_r(\phi_l) \mathbf{a}_t^T(\theta_l) \delta(t - \tau_l) \quad (5.1)$$

where  $\alpha_l$  denotes the complex gain of the  $l$ th path.

The complex gains  $\alpha_l$  are assumed to follow the log-normal distribution, with  $\mathbb{E}[|\alpha_l|^2] = \bar{\alpha}$ . The angles of arrival and departure (AoAs/AoDs) of the  $l$ th dominant path are represented by  $\phi_l$  and  $\theta_l$  respectively. In order to model AoAs and AoDs, Laplacian distribution with uniformly distributed mean over  $[-\pi, \pi)$  and angular standard deviation of  $\sigma_{AS}$  is utilized. Here, we consider the non-line-of-sight (NLOS) channel model for the residential scenario based on the measurements by IEEE task group 802.15.3c [124]. The array response vectors of the uniform linear arrays denoted as  $\mathbf{a}_r(\phi_l) \in \mathbb{C}^{N_r \times 1}$  for the receiver and  $\mathbf{a}_t(\theta_l) \in \mathbb{C}^{N_t \times 1}$  for the transmitter equal to

$$\mathbf{a}(\varphi) = \frac{1}{\sqrt{N}} [1, e^{jkd \sin(\varphi)}, \dots, e^{jk(N-1)d \sin(\varphi)}] \quad (5.2)$$

where  $k = \frac{2\pi}{\lambda}$  and  $d$  is the antenna spacing.

Time delay compensation is implemented in such a way that the beams are time shifted by input buffers. Accordingly, the discrete channel matrix is

$$\mathbf{H} = \sqrt{\frac{N_t N_r}{L}} \sum_{l=1}^L \alpha_l \mathbf{a}_r(\phi_l) \mathbf{a}_t^T(\theta_l) \delta(t - \tau_l + \hat{\tau}_l) \quad (5.3)$$

where  $\hat{\tau}_l$  denotes the quantized time delay compensation of the  $l$ th path given by  $\hat{\tau}_l = k_l \cdot T_b$ , in which  $T_b$  is the sample duration of the buffer and  $k_l$  is an integer. The efficiency of time delay compensation is validated in [107].

Moreover, we try to achieve the best possible beam separation in order to get a flat fading channel. An SIR constrained path selection algorithm to implement this has been proposed in [110] which includes optimization of the number of antennas to get the best possible directivity. Since the RF beamforming is implemented using only analog phase shifters, it holds that

$$|\mathbf{W}_{rf}(m, l)|^2 = M_l^{-1} \quad (5.4)$$

where  $M_l$  represents the optimized number of active antennas for the  $l$ th beam after the completion of the algorithm. During data transmission, each dominant path only transmits one time-shifted beam such that the number of active RF chains is  $N_b = \bar{L}$ . The algorithm details of RF domain beamforming design, namely to obtain the best beam separation and to guarantee the SIR in the direction of dominant paths satisfying a certain threshold, is beyond the scope of this article and will not be introduced in this work.

After applying optimized RF domain beamforming with efficient TDC, the equivalent flattened fading channel can be expressed as

$$\tilde{\mathbf{H}} = \mathbf{A}_R \text{diag}(\boldsymbol{\alpha}) \mathbf{A}_T^H \mathbf{W}_{rf} \quad (5.5)$$

where

$$\boldsymbol{\alpha} = \sqrt{\frac{N_t N_r}{\bar{L}}} [\alpha_1, \dots, \alpha_l, \dots, \alpha_{\bar{L}}]$$

and  $\bar{L}$  is the number of resolved paths after path selection. The matrices  $\mathbf{A}_R$  and  $\mathbf{A}_T$  contain the AP and the user array response vectors with

$$\mathbf{A}_R = [\mathbf{a}_r(\phi_1), \dots, \mathbf{a}_r(\phi_l), \dots, \mathbf{a}_r(\phi_{\bar{L}})]$$

and

$$\mathbf{A}_T = [\mathbf{a}_t(\theta_1), \dots, \mathbf{a}_t(\theta_l), \dots, \mathbf{a}_t(\theta_{\bar{L}})]$$

The RF domain beamforming vector is designed such that a constant projection on the corresponding array response vector and zero projection on the other directions are generated. Hence, by applying optimized RF domain beamforming design with an efficient SIR threshold, we can obtain

$$\mathbf{A}_T^H \mathbf{W}_{rf} \approx \mathbf{I}_{\bar{L}} \quad (5.6)$$

Based on (5.5), we can derive  $\mathbb{E}[\|\tilde{\mathbf{H}}\|_F^2] \approx \bar{\alpha} N_t N_r$ .

A single-user mmWave MIMO system model is illustrated in Fig 5.1. The focus of this section lies in the downlink transmission. A transmitter with  $N_t$  antennas can be observed to communicate  $N_s$  data streams to a receiver with  $N_r$  antennas. At the transmitter side,  $N_b$  flat beams are obtained from  $N_s$  data streams using a digital

baseband precoding matrix  $\mathbf{W}_{bb}$ , such that  $N_s \leq N_b \leq N_t$  and  $N_s \leq N_b \leq N_r$ . The  $N_b$  flat beams are time-shifted by the input buffer and then processed by an  $N_t \times N_b$  RF precoder  $\mathbf{W}_{rf}$ . With efficient TDC and RF domain beamforming, the equivalent flattened fading channel can be denoted as  $\tilde{\mathbf{H}}$ .

The discrete-time transmitted signal is then

$$\mathbf{x} = \tilde{\mathbf{H}}\mathbf{W}_{bb}\mathbf{s} \quad (5.7)$$

where  $\mathbf{s}$  is the  $N_s \times 1$  vector of transmitted symbols, such that  $\mathbb{E}[\mathbf{s}\mathbf{s}^H] = (\mathcal{P}_o/N_s)\mathbf{I}_{N_s}$ , and  $\mathcal{P}_o$  stands for the total transmit power. The total power constraint is enforced by normalizing  $\mathbf{W}_{bb}$  such that  $\|\mathbf{W}_{rf}\mathbf{W}_{bb}\|_F^2 = N_s$ .

At the user side, the received signal is first combined in the RF domain employing the  $N_b \times N_r$  combining matrix  $\mathbf{Z}_{rf}$  followed by a  $N_s \times N_b$  baseband combiner  $\mathbf{Z}_{bb}$ . The constraints on the entries of RF combiner  $\mathbf{Z}_{rf}$  are similar to the RF precoder. If  $\mathbf{Z} = \mathbf{Z}_{bb}\mathbf{Z}_{rf}$ , the received signal after processing can be then written as

$$\hat{\mathbf{s}} = \mathbf{Z}\tilde{\mathbf{H}}\mathbf{W}_{bb}\mathbf{s} + \mathbf{Z}\mathbf{n} \quad (5.8)$$

where  $\mathbf{n}$  denotes the  $N_r \times 1$  noise vector of i.i.d.  $\mathcal{CN}(0, \mathbf{R}_{nn})$ . The noise covariance matrix is represented by  $\mathbf{R}_{nn} = \sigma_n^2 \mathbf{I}_{N_r}$ .

In this section, it is assumed that the channel state information (CSI) is perfectly known at both the transmitter and the receiver. In addition, we implicitly assume perfect synchronization. In literature, mmWave-specific channel estimation has been proposed [14]. The important channel parameters such as AoDs, AoAs, time delay and path loss can be estimated by sparse channel estimation. Effectively, we further assume ideal decoding at the receiver side based on the  $N_s$ -dimensional processed received signal  $\hat{\mathbf{s}}$ . Under the stated assumptions, the information rate, achieved by this system, can be formulated as

$$\mathcal{I} = \log_2 \left| \mathbf{I} + \frac{(\mathbf{Z}\tilde{\mathbf{H}}\mathbf{W}_{bb})^H(\mathbf{Z}\tilde{\mathbf{H}}\mathbf{W}_{bb})}{(\mathbf{Z}\mathbf{R}_{nn}\mathbf{Z}^H)} \right| \quad (5.9)$$

In order to improve the data rate obtained in (5.9), the number of data streams  $N_s$  needs to be optimized rather than constant.

### 5.3 Power Consumption Model

In this section, an approximated power consumption model for the system in Fig. 5.1 is developed. We focus only on the receiver part. In order to estimate the total energy consumption, all signal processing blocks at the receiver side need to be considered in the model. However, in order to keep the model from being over-complicated at this stage, baseband signal processing blocks such as channel coding, pulse-shaping, and digital modulation are intentionally omitted. The methodology used here can be extended to include those blocks in future research work.

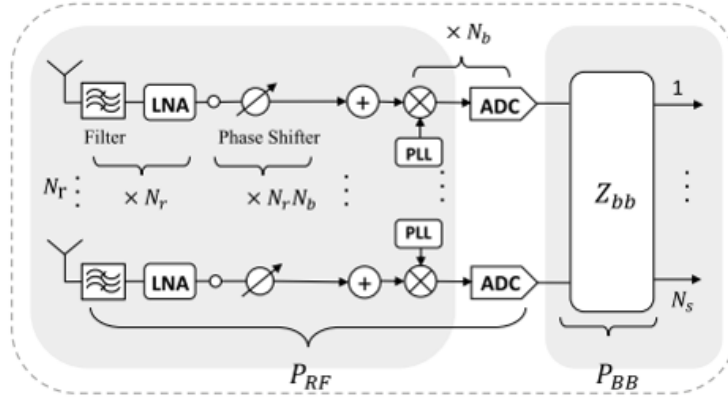


**Figure 5.2:** Block Diagram of the Receiver Chain

The total average power consumption along the signal path can be divided into two main components: the power consumption of all the circuit blocks  $P_{RF}$  in the analog part and the power consumption of the baseband combiner  $P_{BB}$ . The first term  $P_{RF}$  in the total power consumption is given by

$$P_{RF} = N_r(P_{\text{filter}} + P_{\text{LNA}}) + N_r N_b P_{\text{shifter}} + N_b P_{\text{PLL}} + N_b(P_{\text{mix}} + P_{\text{ADC}}) \quad (5.10)$$

where  $P_{\text{filter}}$ ,  $P_{\text{LNA}}$ ,  $P_{\text{shifter}}$ ,  $P_{\text{PLL}}$ ,  $P_{\text{mix}}$  and  $P_{\text{ADC}}$  denote the power consumption values for the filter, the low noise amplifier (LNA), the phase shifter, the phase-locked loop and the mixer and the ADC respectively. The exact computation of the dissipated power is difficult in general, thus we approximate the power consumption of each hardware component here and elaborate it further in Section 5.5.

It is known that a baseband combiner is designed and implemented in complementary metal-oxide-semiconductor (CMOS). The power consumption per operation unit depends tightly on the feature sizes of CMOS technology. During data transmission, the baseband combining matrix is multiplied with the vector of processed symbols of size  $N_b \times 1$ . Accordingly, it requires  $N_s \times N_b$  multiplications of complex numbers and  $N_s \times (N_b - 1)$  addition of complex numbers. Let  $P_m$  and  $P_a$  be the power consumption per multiplier and adder operation for a real value, respectively. Then the second term  $P_{BB}$  in the total power consumption is given by

$$P_{BB} = 4N_s N_b P_m + 2N_s(2N_b - 1)P_a \quad (5.11)$$

The related circuit and system parameters are defined in section 5.5, where the power consumption values of various circuit blocks are quoted from the corresponding references.

Based on (5.10) and (5.11), the total power consumption equals to

$$P_{\text{total}} = P_{RF} + P_{BB} \quad (5.12)$$



## 5.4 Energy Efficiency

For given system parameters  $(N_t, N_r, N_b, N_s)$ , the hybrid precoders or combiners are designed to maximize the spectral efficiency of the system in Fig. 5.1. In [105,112], the joint precoding and combining optimization have been presented. The entries of RF matrices  $\mathbf{W}_{rf}$  and  $\mathbf{Z}_{rf}$  have equal norm, of which the columns are selected to focus the power in the direction of the dominant path to achieve best beam separation. Then the popular singular value decomposition and water-filling power allocation are employed to obtain the baseband matrices  $\mathbf{W}_{bb}$  and  $\mathbf{Z}_{bb}$ . From eigenvalue decomposition theorem,  $\tilde{\mathbf{H}}\tilde{\mathbf{H}}^H$  has  $N$  nonzero eigenvalues with  $N_s \leq N \leq N_b$ . Hence the achievable data rate can be written as

$$\mathcal{I} = \sum_{i=1}^N \log_2 \left( 1 + \frac{\lambda_i P_i}{\sigma_n^2} \right) \quad (5.13)$$

where  $\lambda_i$  denotes the  $i$ th eigenvalue and  $P_i$  denotes the power allocated on the  $i$ th eigenmode under the power constraint  $\sum_{i=1}^N P_i \leq \mathcal{P}_o$ . By applying the derivation for achievable data rate and the assumed power consumption model, the energy efficiency  $\eta_{EE}$  can be formulated as

$$\eta_{EE} = \frac{\mathcal{I}}{P_{\text{total}}} \quad (5.14)$$

In the mmWave MIMO systems, a trade-off between the power consumption and the achievable rate can be observed. The achievable data rate increases with the increasing number of receive antennas while the power consumption also increases accordingly, which results in a concave shape of energy efficiency curve. Based on that, the number of receive antennas that maximizes the EE are discussed in this chapter. We validate the efficiency of our proposed solution via simulations.

### 5.4.1 The Energy Efficiency Optimization Algorithm

It is difficult to see the direct relation between the EE and  $N_r$  from (5.13). As a consequence, the EE with respect to  $N_r$  is optimized by observing the bounds on the data rate  $\mathcal{I}$ . The lower bound can be satisfied with equality if only the strongest modes are filled up by waterfilling, corresponding to a rank-one channel. It can be expressed as

$$\mathcal{I} \geq \log_2 \left( 1 + \frac{\mathcal{P}_o \sum_{i=1}^N \lambda_i}{\sigma_n^2} \right) \quad (5.15)$$

On the other hand, if the channel has equal eigenvalues, i.e. if all the eigenmodes are identical, the upper bound is achieved in the following manner

$$\mathcal{I} \leq N \log_2 \left( 1 + \frac{\mathcal{P}_o \sum_{i=1}^N \lambda_i}{N^2 \sigma_n^2} \right) \quad (5.16)$$

where  $\sum_{i=1}^N \lambda_i = \|\tilde{\mathbf{H}}\|_F^2 = \text{Tr}(\tilde{\mathbf{H}}^H \tilde{\mathbf{H}})$ .

The best possible beam separation is necessary to achieve a flat fading channel. In [110], we have proposed an average SIR constrained design to achieve the best possible beam separation. As is known, the SIR of a particular beam is related to the number of transmit antennas used. In the proposed design algorithm, the number of antennas is optimized to achieve the best possible directivity and at the same time satisfy the SIR constraint, which also contributes to minimizing the processing power.

The effect of the SIR threshold on the number of average paths that can be resolved is illustrated in [110]. There are two competing effects. On one hand, when increasing the threshold, the average number of paths reduces since weak paths are dropped. This reduction is followed by a decrease of the channel rank and, thus, leads to lower data rates. On the other hand, increasing the SIR threshold leads to a higher received signal-to-noise ratio (SNR) and a significant reduction of frequency selectivity. Hence, the equalization complexity at the user side reduces. While the threshold is high enough, the frequency selectivity becomes negligible and the equalizer becomes unnecessary. As a supplement, a further positive effect of increasing the threshold is that the gain in each subchannel is higher and, therefore, higher order modulation can be employed. This results in an increase in the overall data rate, followed by a co-occurrence of positive and negative effects. After taking all the factors into consideration, the overall data rate is reduced by increasing SIR threshold.

Note that after the implementation of hybrid beamforming with TDC, the channel can be considered as a diagonal composing of  $L$  independent paths. With the consideration of SIR threshold being sufficient, at which the interference can be neglected,  $\mathbf{A}_T^H \mathbf{W}_{rf} = \mathbf{I}_{N_b}$  is further assumed.

Under this assumption, the total power gain of the channel matrix can be reformulated as

$$\begin{aligned} \sum_{i=1}^N \lambda_i &= \text{Tr} \left( (\mathbf{A}_R \text{diag}(\boldsymbol{\alpha}) \mathbf{A}_T^H \mathbf{W}_{rf})^H (\mathbf{A}_R \text{diag}(\boldsymbol{\alpha}) \mathbf{A}_T^H \mathbf{W}_{rf}) \right) \\ &= \frac{N_t N_r}{N_b} \sum_{i=1}^{N_b} \alpha_i^2 \end{aligned} \quad (5.17)$$

The data rate  $\mathcal{I}$  is accordingly bounded as

$$\log_2 (1 + \mathcal{C} N_r) \leq \mathcal{I} \leq N \log_2 \left( 1 + \frac{\mathcal{C} N_r}{N^2} \right) \quad (5.18)$$

where  $\mathcal{C} = \mathcal{P}_o N_t \sum_{i=1}^{N_b} \alpha_i^2 / (N_b \sigma_n^2)$ .

Now the case of upper bound is observed and the optimization problem can be expressed from (5.14) as

$$\underset{N_r}{\text{maximize}} \quad \frac{\mathcal{C}_5 \log_2 (\mathcal{C}_1 + \mathcal{C}_2 N_r)}{\mathcal{C}_3 + \mathcal{C}_4 N_r}, \quad (5.19)$$

where

$$\begin{aligned}\mathcal{C}_1 &= 1, \\ \mathcal{C}_2 &= \mathcal{P}_o N_t \sum_{i=1}^{N_b} \alpha_i^2 / (N^2 N_b \sigma_n^2), \\ \mathcal{C}_3 &= 4N_s N_b P_m + 2N_s (2N_b - 1) P_a + P_{\text{PLL}} + N_b (P_{\text{mix}} + P_{\text{ADC}}), \\ \mathcal{C}_4 &= P_{\text{filter}} + P_{\text{LNA}} + N_b P_{\text{shifter}}, \\ \mathcal{C}_5 &= N.\end{aligned}$$

The objective function  $f(N_r)$  can be expressed as follows

$$f(N_r) = \frac{\mathcal{C}_5 \log_2(\mathcal{C}_1 + \mathcal{C}_2 N_r)}{\mathcal{C}_3 + \mathcal{C}_4 N_r} \quad (5.20)$$

where  $\mathcal{C}_1, \mathcal{C}_2, \mathcal{C}_3, \mathcal{C}_4, \mathcal{C}_5 > 0$ .

A function  $f: \mathbf{R}^n \rightarrow \mathbf{R}$  is called *quasiconcave* if its domain and its superlevel sets

$$S_\alpha = \{x \in \mathbf{dom} f \mid f(x) \leq \alpha\} \quad (5.21)$$

for  $\alpha \in \mathbf{R}$ , are convex [25, Section 3.4].

Based on that, the objective function  $f(N_r)$  is a quasiconcave, i.e. a unimodal function. It can be said that if a  $N_r^{\text{opt}}$  exists, which means  $f'(N_r^{\text{opt}}) = 0$ , then  $N_r^{\text{opt}}$  is the global maximizer and the function is increasing for  $N_r < N_r^{\text{opt}}$  and decreasing for  $N_r > N_r^{\text{opt}}$ .

Now,

$$f'(N_r) = \frac{\mathcal{C}_2(\mathcal{C}_3 + \mathcal{C}_4 N_r)}{(\mathcal{C}_1 + \mathcal{C}_2 N_r) \ln 2} - \mathcal{C}_4 \log_2(\mathcal{C}_1 + \mathcal{C}_2 N_r) \quad (5.22)$$

In order to derive  $N_r^{\text{opt}}$ , consider  $f'(N_r^{\text{opt}}) = 0$  and we get

$$\frac{(\mathcal{C}_2 \mathcal{C}_3 - \mathcal{C}_1 \mathcal{C}_4)}{\mathcal{C}_1 + \mathcal{C}_2 N_r} - \mathcal{C}_4 = \mathcal{C}_4 (\ln(\mathcal{C}_1 + \mathcal{C}_2 N_r) - 1) \quad (5.23)$$

By substituting  $z = \ln(\mathcal{C}_1 + \mathcal{C}_2 N_r) - 1$ , we derive

$$\frac{(\mathcal{C}_2 \mathcal{C}_3 - \mathcal{C}_1 \mathcal{C}_4)}{\mathcal{C}_5 \mathcal{C}_4} = z e^z \quad (5.24)$$

where  $e$  is the natural number.

Therefore the optimization problem has a closed form solution as

$$N_r^{\text{opt}} = \frac{e^{W(\frac{\mathcal{C}_2 \mathcal{C}_3 - \mathcal{C}_1 \mathcal{C}_4}{\mathcal{C}_5 \mathcal{C}_4}) + 1} - \mathcal{C}_1}{\mathcal{C}_2} \quad (5.25)$$

To sum up, the derivation of the optimization problem leads finally to the Lambert  $W$  function  $W(z)$  defined by the equation  $z = W(z)e^{W(z)}$  for any  $z \in \mathbb{C}$ .

The aforementioned function can be described as a concave function, while EE is an increasing function for  $N_r < N_r^{opt}$  as well as a decreasing function for  $N_r > N_r^{opt}$ . The proposed solution is validated by providing the numerical examples in the section of simulation results.

## 5.5 Performance Evaluation

In this section, we evaluate EE for our proposed transmission scheme and compare the performances along different system configurations. Here, to compute the power consumption in a realistic way, the hardware characterization described in Section 5.3 is employed. We consider the wireless transceiver system operating at 60 GHz in an indoor NLOS environment. For demonstration purposes, the total transmit power across all transmit antennas is also assumed to be normalized to unity with  $\mathcal{P}_0 = 1$ . As mentioned earlier, each channel realization is generated using the 60 GHz NLOS multipath channel model for the residential scenario CM2.3 [124]. In addition, the channel realization  $\mathbf{H}$  is assumed to keep invariant during one codeword transmission.

### 5.5.1 Parameters in Power Consumption Model

In [89], a very low power consumption LNA designed in the 65nm CMOS process has been presented. LNA determines the total noise figure at the receiver. High gain LNA with less NF can be achieved with minimizing the transistor size [29]. Measurements in [89] show that the proposed direct conversion receiver chip takes  $0.34mm^2$  area on the board and the LNA has 12dB gain, 4.2dB NF gain, and 5.4mW power consumption which is relatively low.

The second important block in the receiver front-end is the down-conversion mixer that has a great deal of effect on the receiver's performance. In conventional microwave systems, *Gilbert* mixer is widely used due to the high power consumption of the Gilbert mixer at 60GHz, thus in [89] the *transconductance* mixer is proposed for low-power design at 60GHz. However, the only drawback of this kind of mixer is the large chip area requirements in comparison with conventional Gilbert mixers. Measurements in [89] show that the transconductance mixer with 65nm CMOS process has 6dB gain, 10dB NF, and consumes only 0.5mW power.

In [35,73] proposed a phased-array receiver for 60GHz, fabricated in 40nm low-power CMOS technology. [73] implies the power consumption of phase shifter is 7mW including a mixer. However, as phase shifters in the analog domain can be assumed as passive devices that consume very low power, thus in this project, the power consumption of phase shifter is assumed to be 2mW.

In addition, for the power consumption of mmWave ADCs [66], observations have been done on devices which can be used in a 60 GHz system with at least a 500 MHz

**Table 5.1:** Energy Consumption per Operation(f) [118]

Benchmark Circuits	Energy Consumption per Operation(f)				
	FinFet 7nm		CMOS 14nm		NCSU 45nm
$V_{dd}$	0.30V	0.45V	0.55V	0.80V	1.10V
16-bit adder	0.111	0.384	0.762	1.44	495.8
16-bit multiplier	0.964	3.276	6.244	13.23	2954.9

bandwidth and an effective resolution (ENOB) larger than 5 bits. The power estimated for an ADC, according to the method mentioned in [32] is given below

$$P_{ADC} = \frac{3V_{DD}^2 L_{min}(2BW + f_{cor})}{10^{-0.1525n+4.838}} \quad (5.26)$$

where  $V_{DD}$  is the supply voltage,  $L_{min}$  denotes the minimal channel length for CMOS technology,  $f_{cor}$  is the corner frequency of  $1/f$  noise and  $BW$  represents signal bandwidth. The following values,  $V_{DD} = 1.2V$ ,  $L_{min} = 0.16 \times 10^{-6}$ ,  $f_{cor} = 1MHz$  and  $n = 5$ , are applied to all cases.

Recently considerable research efforts have been invested in FinFet devices with superior performance and power reduction in sub-20nm technology [118]. Synthesis results show that 7nm FinFet technology resulting in 10X and 1000X energy consumption reduction in comparison with 14nm and 45nm bulk CMOS technology. Although these results are anticipated of power consumption of 7nm FinFet but are promising replacement of conventional bulk CMOS-based devices. [118] provides power consumption comparison between 7nm FinFet and 14nm, 45nm CMOS standard cell libraries (AND, OR, XOR). Table 5.1 summarizes the energy consumption result of a 16-bit adder and a 16-bit multiplier synthesized using different libraries. Results clearly show that 7nm FinFet technology has a remarkable superiority in energy consumption. Results are shown for two supply voltages, one for low power usage and the other for high-performance applications.

**Table 5.2:** List of Simulation Parameters

Parameter	Value	Parameter	Value
$P_{filter}$	2.5 mW [50]	$P_{PLL}$	30 mW [128]
$P_{shifter}$	2 mW [48]	$P_a$	0.49 mW [118]
$P_{LNA}$	5.4 mW [89]	$P_m$	2.05 mW [118]
$P_{mixer}$	0.5 mW [125]		

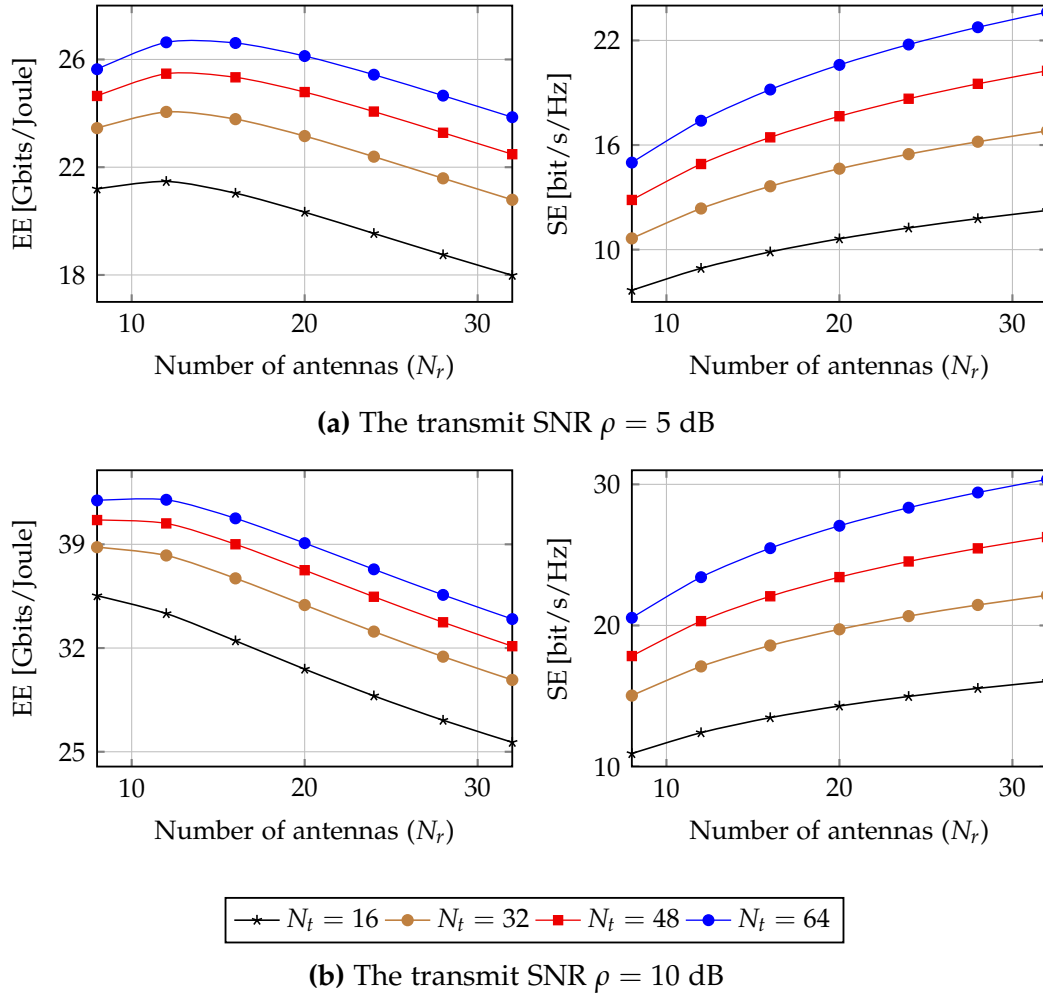


**Figure 5.3:** Maximal EE and the corresponding spectral efficiency for different number of transmit and receiver antennas, where the Bandwidth is set to 1 GHz and  $\delta = 11$  dB.

The power consumption for each component is listed in Table 5.2 along with the settings mentioned in the corresponding references. In the case of the adder and multiplier, the energy consumption per operation unit is listed in [118]. The corresponding power consumption is shown deeply dependent on the symbol rate. Besides, the performance degradation resulting from fixed-point quantization was evaluated using extensive Monte-Carlo simulations, which suggested that 16bit is fully sufficient to maintain overall system performance. The choice of word-width for CMOS power consumption is motivated by above results.

### 5.5.2 Impact of Increase in Antennas

Fig. 5.3 shows the variation of EE as a function of the number of transmit antennas and the number of receive antennas, where the bandwidth is 1 GHz. Another variable is the amount of transmit SNR, which are set to  $\rho = 5$  dB and  $\rho = 10$  dB respectively.

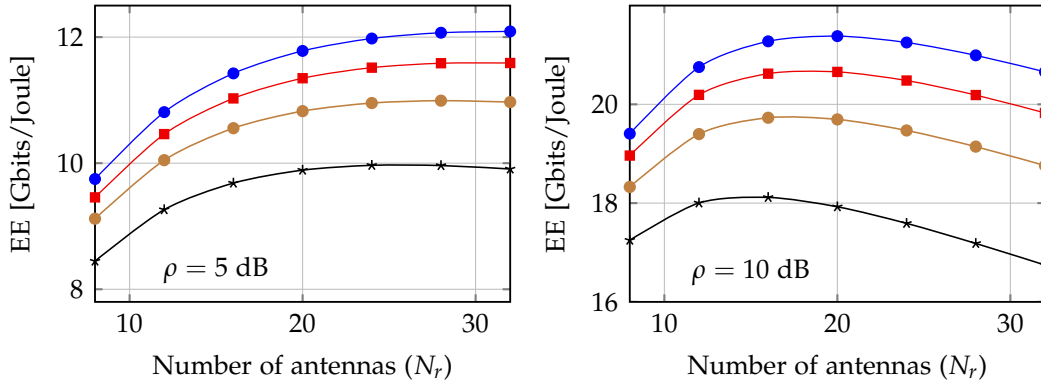


**Figure 5.4:** Maximal EE for different number of transmit and receiver antennas, where the Bandwidth is set to 5 GHz.

It can be easily understood that the increase of  $N_t$  has a positive influence on EE. Correspondingly, an optimum point behaviour of EE curve is observed with respect to  $N_r$ . Since not only the data rate but also the circuit operating power consumption are increasing by the increment of the number of receive antennas, the tendency of EE shows a concave shape with respect to the transmit SNR as expected. Therefore, the optimal point for EE can be determined.

Although the absolute value of EE is increasing along with the transmit SNR, the number of receive antennas to maximize the EE is decreased. The reason is that the rate of increase of data rate is bigger than the power consumption. It is worth noting that EE curves more sharply for higher SNR. What's more, the SE of the system will obviously be enhanced with larger  $N_r$  as well as  $N_t$ .

In Fig. 5.4, we depict the EE when the bandwidth is set to 5 GHz. Compared with the EE illustrated in Fig. 5.3, the wider the bandwidth is, the slower the convergence of EE to the optimal point will be. Meanwhile, increasing the SNR at this bandwidth helps to accelerate the convergence of EE. This is due to the fact that increasing bandwidth power consumption increases dramatically and can be seen that in high SNR regime increasing  $N_t$  leads to significant EE reduction.

### 5.5.3 Influence of SIR Threshold in EE and SE

Now the effect of SIR threshold on SE and the processing energy per bit along with varying SNRs are demonstrated in Fig. 5.5. It is obvious that increasing the SIR threshold results in a decrease in SE, since the rank of the channel decreases with an increasing  $\delta$ . As for the case of the processing energy, two types of behaviors are observed based on the received SNR. At the low SNR region, where the SIR threshold is increased, the processing energy per bit decreases. When the SNR is larger than  $-6$  dB, the processing energy per bit becomes smaller for lower SIR threshold. Furthermore, we can see that with the increase in SNR, the gap between SE for the two SIR thresholds increases significantly.

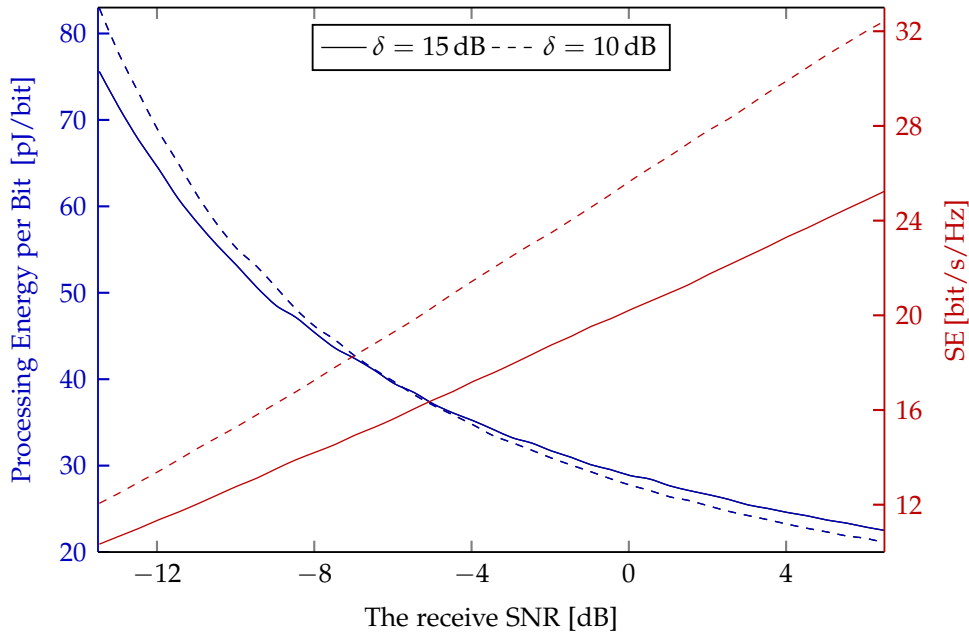


**Figure 5.5:** The effect of SIR threshold on the processing energy per bit and the spectral efficiency under various receive SNRs, where the bandwidth is set to 1 GHz.

## 5.6 Summary

As power consumption at the user side is a crucial factor for power-hungry devices, a power consumption model for the receiver side has been first formulated in this chapter. The total average power consumption along the signal path can be divided into two main components: the power consumption of all the circuit blocks in the analog part and the power consumption of baseband combiner. The RF chain consists of the filter, the low noise amplifier (LNA), the phase shifter, the phase-locked loop, and the mixer and the ADC, where each of these components is scaled with different system parameters (such as the number of receiver antennas and the number of RF chains). We also have investigated the total number of operations at the digital baseband, which scales with the power consumption of the adders and multipliers. Thus, a total power expenditure at the receiver side for our system model has been presented.

We then have formulated the EE with respect to our considered hybrid analog/digital beamforming structure, and we have optimized it over different parameters. 1) Optimization over the number of receive antennas was the only case that we could find a closed-form solution. We showed that the optimal value is presented by Lambert W function, and the objective function is a quasi-concave function that, with increasing the number of receiver antennas more than the optimal value, EE decreases and vice versa. 2) The optimization problem for the number of transmit antennas is not a linear function and cannot be formulated as a closed-form solution. However, simulation results show that with increasing the number of transmit antennas, EE



improves monotonically; thus, the maximum available number of transmit antennas provides the best results. However, when we consider the proper access point (AP) design, power consumption, and system complexity, more than 64 transmit antennas are not recommended. 3) For the number of RF chains as another optimization parameter, we concluded that this value is dynamic and with respect to the SIR ratio and the number of available transmit antennas. 4) For the case of the number of data streams as a design factor, we know that  $1 \leq N_s \leq 3$ ; thus, optimization is an irrelevant case for it.

To keep the power model from being over-complicated at this stage, baseband signal processing blocks such as channel coding, pulse-shaping, and digital modulation are intentionally omitted. We mainly focus on the methodology of EE/SE analysis to guide the practical EE/SE trade-off for the LSAS design. The methodology used here can be extended to include those blocks in future research work.



## Chapter 6

# Energy-Efficient Design of Multi-user Millimeter Wave and sub-THz System

---

Until now, the research focuses on the 60 GHz range, in particular, for the radio frequency (RF) architecture and channel characteristics. As proof of concept for the methodology and because of its high relevance, the proposed approach is applied towards systems operating beyond the 100 GHz carrier frequency range. In this chapter, a new higher frequency band, 120 GHz, is explored, both in the mmWave band and sub-Terahertz (sub-THz) band and provides a wide frequency band to achieve ultra-high data rates. The impact of an extension to 120 GHz carrier frequency ranges is considered. Except that, an extension from the point-to-point MIMO transmission to multi-user case [61, 100] (MIMO multiple access channel for uplink and broadcast channel for downlink) is addressed.

This chapter has first studied the channel characteristics and channel models at 120 GHz published in the literature, as shown in Section 6.2. Compared to 60 GHz, the shorter wavelength of 120 GHz allows more antennas employed, and larger bandwidth used in the system. Based on literature research, we employ the ray-tracing method to generate the channel model. Moreover, the planar antenna array is used instead of the linear antenna array. After comparing different system architectures, a multi-user low RF complexity hybrid beamforming MIMO system at 120 GHz is applied in our work, with two structures: fully-connected structure and array-of-subarray structure. Several algorithms with CSI are proposed to maximize the capacity of such systems in Section 6.3. Besides, we propose an iterative power precoding algorithm without CSI. Its performance seems better since the complexity of the hardware is much higher. Finally, we explore the influence of some parameters on the system performance, such as the number of antennas, the number of users, and quantization-bits, as illustrated in Section 6.4.

The algorithms employed in this chapter have been published in part by the author in [105, 109, 111–113] and more comprehensive investigations has been presented in the supervised thesis [31].

## 6.1 Introduction to Terahertz Band

As mentioned before, the critical frequency range for communication systems at mm-Wave is operated at 60 GHz band, since several companies, such as SiBEAM, LG, IBM, Sony, have many products under these developments [127]. Besides, there are various standards for 60 GHz WLAN/ WPAN applications. For example, IEEE 802.11ad,

which provided up to 6.75 Gbps throughput using approximately 2 GHz of the spectrum at 60 GHz over a short-range; IEEE 802.15.3c, which indicates that mmWave WPAN can operate in the new and clear band including 57-64 GHz unlicensed band; Wireless HD, which is based on a 7 GHz channel in the 60 GHz; the WiGig standard, which develops and promotes the adoption of multi-Gbps speed wireless communications technology operating over the unlicensed 60 GHz frequency band; and ECMA 387, which specifies a physical layer (PHY), distributed medium access control (MAC) sublayer, and an HDMI protocol adaptation layer (PAL) for 60 GHz wireless networks. There are also efforts done in the adjacent sub-THz and THz range. The spectrum around 120 GHz has gained some interest since the NTT group in Japan has done multi-gigabit systems experiments. And the system InP HEMT MMICs was successfully used in the Beijing Olympic Games for the broadcasting HDTV, whose error-free transmission rate was up to 10 Gbps [127]. 120 GHz band is also included in the D-band, whose spectral range is between 110 GHz and 170 GHz. This frequency band is suited for short-range communications and is typically used in atmosphere applications. It may also have some potential possibility of applications, such as precision positioning, velocity sensors [84], and passive millimeter-wave camera [49]. In 2008 the IEEE 802.15 Terahertz Interest Group (IGthz) has been established to explore whether the Terahertz band is feasible for wireless communications [44]. Until January 2014, an official IEEE standardization committee called 100 Gbps was proposed. The THz band, in general, covers the frequency range from 100 GHz to 10 THz. The potential applications at the THz band include biomedical, industrial, consumer, ecological and military [88].

With the demand for higher data rates and spectral efficiency, it is necessary to develop the wireless communication system to a higher frequency. Systems working in the unlicensed 60 GHz frequency band have provided data rates of more than 1.5 Gbps, transmitting the uncompressed video signals [45]. In addition, the research has demonstrated that the data rates can be up to 10 Gbps at 120 GHz, which is required for transmissions for a 10-Gb Ethernet (10 GbE) signal or multiplex transmission of HD-SDI signals [42]. Furthermore, the largely unexploited sub-THz and THz regions with wider bandwidth may become leaders to even higher data rates in wireless communications.

Due to the development of the mmWave in wireless communications and much attention pay to the 60 GHz frequency band, 120 GHz can be used in the beam space MIMO system as an alternative. To reduce the hardware complexity and power consumption at the user side, we will design a low RF complexity mmWave beamspace MIMO system at 120 GHz. Two hybrid beamforming architectures, fully-connected structure and array-of-subarray structure, are mainly investigated. The system aims at achieving the maximum spectral efficiency, as well as good BER performance. Here, to further achieve the maximum capacity of the system, We have proposed several hybrid beamforming designs to minimize the signal-to-interference-noise ratio (SINR). Besides, we compare the performance related to different parameters, such as system structures, hybrid beamforming designs, antenna number, user number by simula-

tion. And the performance of the system with an estimated channel is evaluated as a contrast.

## 6.2 Channel Model and System Model

In this section, the channel models at 120 GHz published in the literature are introduced, and the system models are investigated.

### 6.2.1 Channel Model at 120 GHz

Compared with so many mature channel models for the 60 GHz band, the channel models for 120 GHz published by other research groups are fewer. Here we introduce two kinds: ray-tracing based channel model and modified S-V channel model.

#### 6.2.1.1 Ray tracing based channel model

Ray-tracing is based on the geometrical optics to explore the characteristics of the wireless communication channels. This tool is deterministic in the practical deployment, since it is more accurate than the theoretical models. Essentially, the ray-tracing is to build a channel model based on the measurements in a specific site. Furthermore, the shorter the wavelength, the more accurate the modeling.

In [127], the simulation scenario for sub-THz cells is in an office room. The room's size and all things in the room should be considered, such as window, door, ceiling, table, people. Through tracking the propagation path (LOS or NLOS) at a time, we can get the receiving power in the coverage area. The LOS path or once-reflected path determines the final received power for most areas, but the NLOS paths are more robust to shadowing, while the LOS path is easy to be broken by moving people or other objects.

In this dissertation, three ray-tracing based channel models published in the literature are studied. In [39], ray-tracing is used to develop the multi-ray channel model, unified in the (0.06-10) THz band. The channel model is based on tracing the propagation of LOS, reflected, diffusely scattered, and diffracted EM waves. The frequency band is split into several sub-bands. When the sub-bands are narrow enough, each channel can be seen as a flat channel. In [59], a channel model for the indoor environment at 0.1-1 THz band is proposed. This model captures the LOS and NLOS (or reflected) propagation paths. Here, we use the ray-tracing method proposed in [34] to build the channel model for 120 GHz channels. The channel matrix can be expressed as

$$\begin{aligned} \mathbf{H} &= \mathbf{H}_{LOS} + \mathbf{H}_{NLOS} \\ &= \alpha_L(f, d) G_t G_r \mathbf{a}_r(\theta_L) \mathbf{a}_t^H(\phi_L) + \sum_{i=1}^{N_{ray}-1} \alpha_i(f, d) G_t G_r \mathbf{a}_r(\theta_i) \mathbf{a}_t^H(\phi_i) \end{aligned} \quad (6.1)$$

where  $\mathbf{H}_{LOS}$  and  $\mathbf{H}_{NLOS}$  are the channel transfer functions of LOS path and NLOS paths, respectively.  $N_{ray}$  is the number of propagation paths.  $\alpha$  is the complex gain of the component, where  $f$  is the carrier frequency.  $G_t$  and  $G_r$  are the transmit and receiver antenna gain, respectively.  $\mathbf{a}_t$  and  $\mathbf{a}_r$  are the antenna array steering vectors at the transmitter and receiver side, respectively.  $\phi$  and  $\theta$  are the angles of departure/arrival (AOD/AOA) for the rays, respectively.

- (1) Path gain: in the sub-THz band, the atmospheric absorption cannot be neglected. Thus, the LOS path loss consist of spreading loss and absorption loss, as [46]

$$|\alpha_L(f, d)|^2 = L_{spread}(f, d)L_{abs}(f, d), \text{ with} \quad (6.2)$$

$$L_{spread} = \left(\frac{c}{4\pi fd}\right)^2, \quad L_{abs} = e^{-k_{abs}(f)r}$$

where  $c$  is the light speed in free space,  $k_{abs}$  is the absorption coefficient. For the lower sub-THz band, the major atmospheric absorption is from oxygen molecules [69]. The absorption coefficient is about 0.4 for 120 GHz band [46]. For NLOS path gain, the reflection loss is considered. The  $i$ th NLOS path gain can be given by

$$|\alpha_i(f, d)|^2 = \Gamma_i^2 |\alpha_L(f, d)|^2$$

where  $\Gamma$  is the product of the Fresnel reflection coefficient and the Rayleigh roughness factor and can be calculated as in [39]. Comparing to LOS path, the power of once-reflected path is attenuated by 5-10 dB on average and at least 15 dB for twice-reflected paths [119], [72]. Although NLOS path gain is also affected by the scattering loss and diffraction loss, the reflection loss is determinant.

- (2) AOA/AOD: the AOA/AOD for sub-THz channels generally follow Laplacian distribution or zero-mean second order Gaussian mixture model (GMM) [53].  $\phi$  and  $\theta$  are both limited in  $[0, 2\pi)$ .
- (3) Array steering vector: for an uniform linear array (ULA), the array steering vector can be expressed as

$$\mathbf{a}_{ULA}(\phi) = [1, \dots, e^{j\frac{2\pi r}{\lambda} m \sin(\phi)}, \dots, e^{j\frac{2\pi r}{\lambda} (M-1) \sin(\phi)}]^T$$

where  $M$  is the number of array element, with  $m = 0, \dots, M-1$ .  $r$  is the antenna spacing, generally,  $r = \frac{\lambda}{2}$  and  $\lambda$  is the wavelength.

### 6.2.1.2 Modified S-V model

The S-V model is used for modeling the multi-path propagation in an indoor environment. Here, the amplitudes of the received signal have independent Rayleigh distribution. The phases have an independent uniform distribution [79]. Based on the limited measurement data in the THz band (0.1-10 THz), a modified S-V model is proposed to characterize the indoor THz channel.

The indoor THz communication architecture is shown in [53, Fig.1]. One access point (AP) serves several users. The AP is equipped with multiple antennas and can be decomposed into  $K$  disjoint subarrays. Each subarray consists of  $M_t \times N_t$  antennas. In such a system, the modified S-V model is applied, and the channel response for one antenna subarray can be given by

$$H(f, d) = \sum_{i=0}^{M-1} \sum_{l=0}^{N^i-1} \alpha_{il}(f, d) G_t(\phi_{il}^t, \theta_{il}^t) G_r(\phi_{il}^r, \theta_{il}^r) \times \mathbf{a}_r(\phi_{il}^r, \theta_{il}^r) \mathbf{a}_t^\dagger(\phi_{il}^t, \theta_{il}^t) \quad (6.3)$$

where  $M$  and  $N$  are the number of clusters and rays within the  $i$ th cluster, respectively.  $\alpha_{il}$  denotes the path gain of the  $l$ th arrival ray in  $i$ th cluster.  $\phi_{il}^t / \theta_{il}^t$  and  $\phi_{il}^r / \theta_{il}^r$  represent the azimuth/elevation angles of the departure and arrival, respectively.  $G_t$  and  $G_r$  refer to the transmit and receive antenna gains, respectively.  $\mathbf{a}_t$  and  $\mathbf{a}_r$  are the array steering vectors at the Tx and Rx, respectively.  $(\cdot)^\dagger$  denotes the conjugate transpose.

- Time of Arrival: if we set the arrival time of the first cluster  $T_0 = 0$  as the reference time, then the arrival time of the  $i$ th cluster and the  $l$ th ray in the  $i$ th cluster are denoted as  $T_i$  and  $\tau_{il}$ , respectively. Then the time of the arrival of each ray can be written as  $t_{il} = T_i + \tau_{il}$ . For the S-V model [79], the clusters, as well as the rays within the cluster, form Poisson arrival processes with cluster arrival rate  $\Lambda$  and ray arrival rate  $\lambda$ , respectively. So

$$p(T_i | T_{i-1}) = \Lambda e^{-\Lambda(T_i - T_{i-1})}, \quad T_i > T_{i-1}$$

$$p(\tau_{il} | \tau_{i(l-1)}) = \lambda e^{-\lambda(\tau_{il} - \tau_{i(l-1)})}, \quad \tau_{il} > \tau_{i(l-1)}.$$

$\Lambda$  and  $\lambda$  are frequency-dependent and sensitive to the surface material in the indoor building due to the small wavelength of the THz waves. In general, the rougher the surface of the material, the smaller the reflectivity. Then the arrival rate is smaller [70].

- Path Gain: the path gain  $\alpha$  is related to the path loss. As in [127], the path loss consists of the spreading loss and molecular absorption loss.
- AOA/AoD: in this modified S-V model, the departure/arrival time and angle are assumed independent. Then the azimuth angle of departure/arrival for each ray  $\phi_{il}^t / \phi_{il}^r$ , consist of the mean azimuth angle of departure/arrival for each cluster  $\Phi_i^t / \Phi_i^r$  and the azimuth angle of departure/arrival for the ray within the cluster  $\phi_{il}^t / \phi_{il}^r$ . Similarly, the elevation angle of departure/arrival for each ray  $\theta_{il}^t / \theta_{il}^r$ , consist of the mean elevation angle of departure/arrival for each cluster  $\Theta_i^t / \Theta_i^r$  and the elevation angle of departure/arrival for the ray within the cluster  $\theta_{il}^t / \theta_{il}^r$  [71]. Therefore,

$$\phi_{il}^t = \Phi_i^t + \phi_{il}^t, \quad \phi_{il}^r = \Phi_i^r + \phi_{il}^r \quad (6.4)$$

$$\theta_{il}^t = \Theta_i^t + \theta_{il}^t, \quad \theta_{il}^r = \Theta_i^r + \theta_{il}^r \quad (6.5)$$

where  $\Phi_i^t/\Phi_i^r$  and  $\Theta_i^t/\Theta_i^r$  follow the uniform distribution on  $(-\pi, \pi]$  and  $[-\frac{\pi}{2}, \frac{\pi}{2}]$ , respectively.  $\phi_{il}^t/\phi_{il}^r$  and  $\theta_{il}^t/\theta_{il}^r$  follow a zero-mean second order Gaussian mixture model (GMM) [71]. It can be given by

$$GMM(x) = \frac{w_1}{\sqrt{2\pi}\sigma_1} e^{-\frac{x^2}{2\sigma_1^2}} + \frac{w_2}{\sqrt{2\pi}\sigma_2} e^{-\frac{x^2}{2\sigma_2^2}} \quad (6.6)$$

where  $w_1$  and  $w_2$  are the associated coefficients. Unlike the conventional S-V model, where the AoA/AoD follow the Laplace distribution, the GMM model can provide higher angular resolution for the THz beams. Even the angle close to zero, although it is limited by the azimuth and elevation angular ranges.

- Antenna Gain: under the insurance of the directivity of the antennas, the sector antennas are employed in this system. Thus,

$$G_t(\phi_{il}^t, \theta_{il}^t) = \begin{cases} \sqrt{G_t^0}, & \text{if } \phi_{il}^t, \theta_{il}^t \text{ are both in the sector range of the antenna} \\ 0, & \text{otherwise} \end{cases} \quad (6.7)$$

In addition, the sector range should be small enough to guarantee the antenna directivity.

- Array Steering Vector: the antenna array steering vector at the transmitter and at the receiver side are denoted as  $\mathbf{a}_t^t(\phi_{il}^t, \theta_{il}^t)$  and  $\mathbf{a}_r(\phi_{il}^r, \theta_{il}^r)$ , respectively. For a uniform planar array (UPA), with  $M \times N$  antennas, its array steering vector can be denoted as

$$\mathbf{a}_{UPA}(\phi, \theta) = \frac{1}{\sqrt{MN}} [1, \dots, e^{\frac{2\pi a}{\lambda} [m \cos \phi \sin \theta + n \sin \phi \sin \theta]}, \dots, e^{\frac{2\pi a}{\lambda} [(M-1) \cos \phi \sin \theta + (N-1) \sin \phi \sin \theta]}],$$

where  $\lambda$  is the wavelength.  $m$  and  $n$  are the antenna element indexes, defined as  $0 \leq m \leq M-1$ ,  $0 \leq n \leq N-1$ , respectively.

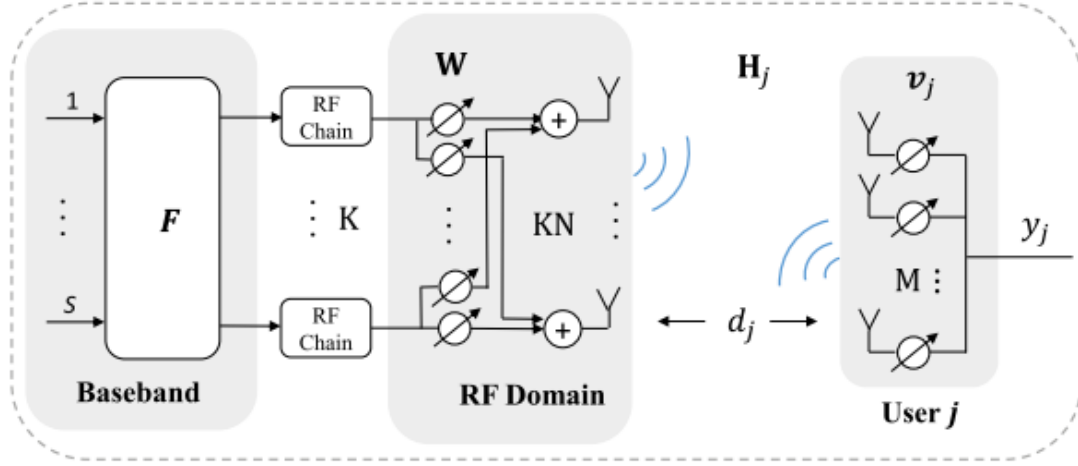
## 6.2.2 System Model

For the 120 GHz frequency band, there are two research directions. One is similar to the 60 GHz frequency band for mmWave communications in picocells, the other as sub-THz is applied for nanonetwork. In the following, we introduce these two kinds of systems that are published by other research groups.

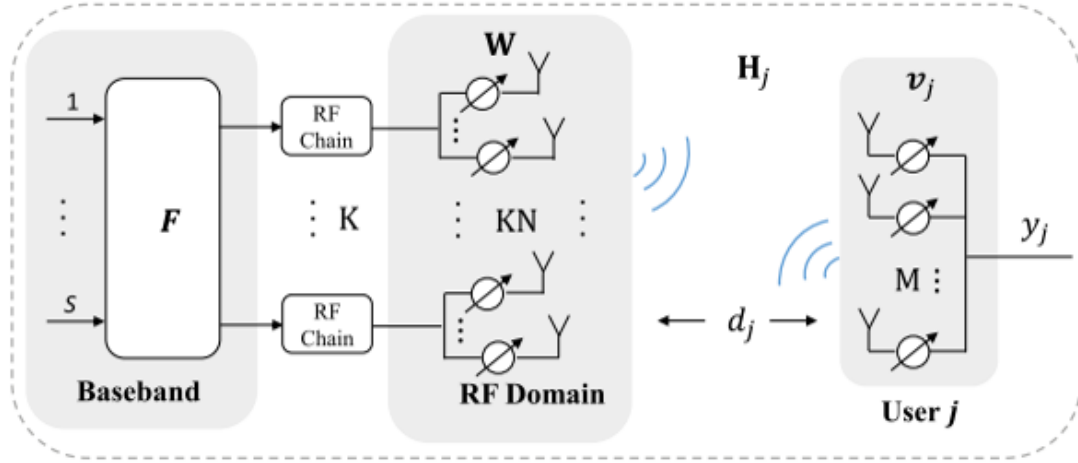
### 6.2.2.1 Millimeter-wave system

Compared to the conventional cellular system, the mmWave wireless communication system can promise higher data rate transmission due to the large bandwidth. And





(a) Fully-connected structure



(b) Array-of-subarray structure

**Figure 6.1:** Two kinds of low complexity hybrid beamforming structures, where the beam pattern is generated only by the phase shifter other than adjusting both the amplitude and phase of the signal.

Multiple-input multiple-output (MIMO) and beamforming techniques have been deployed in modern wireless networks to improve reliability and capacity. Beamforming is a technique that multiple antennas form a directional beam pattern. The published beamforming structure can be divided: analog-only beamforming, full-digital beamforming, and hybrid beamforming. Besides, adding the power amplifier (PA) in the RF domain will increase the complexity of the structure.

**1) Analog-only beamforming structure:** let  $K$  is the RF chain number, and  $KN$  is the antenna number. The data streams are up-converted to the RF domain, and then their phases are rotated by the weight vector. Finally, the signal is emitted by the antennas to the wireless channel. Considering the practice in the project, we aim at

low-power consumption and low complexity. The generation of the beam pattern is only to shift the RF phase by the phase shifter other than adjusting both the amplitude and phase of the signal [51].

**2) Full-digital beamforming structure:** for the full-digital beamforming structure as in [98], it requires the RF chain number the same as the antenna number (one per antenna element) and each beamforming weights are applied digitally. Although the digital beamforming offers the greatest flexibility, it demands more power and cost, especially in the large antenna system.

**3) Hybrid beamforming structure:** Similar to 60 GHz systems, there are two kinds of common hybrid beamforming structures: fully-connected structure and array-of-subarray structure, as shown in Fig. 6.1a and Fig. 6.1b, respectively. The system includes digital baseband beamforming and analog domain beamforming.

**Fully-connected structure:** for the fully-connected structure in Fig. 6.1a, each RF chain is connected to all antennas, and  $KN$  more adders are needed. In order to decrease the complexity of the system, the beam pattern is generated only by the phase shifter other than adjusting both the amplitude and phase of the signal.

**Array-of-subarray structure:** As shown in Fig. 6.1b, the array-of-subarray structure is more practical for the antenna deployment of the base station in the 3G and 4G LTE systems [41], where each RF chain is generally connected to an antenna array [40]. The subarray antenna element spacing is assumed to be smaller than the wavelength, thus there exists a high level of antenna correlation. We further assume the space between adjacent subarrays is much larger than the wavelength so that the channels of different subarrays are independent. In addition, the distance from any user to the AP is assumed to be much larger than the spaces among different subarrays. The complexity of the array-of-subarray structure is decreased compared to the fully-connected structure. In addition, we are only using the phase shifter instead of the combining of the phase shifter and PA can further decrease the complexity of the system.

### 6.2.3 Nanonetwork Architecture

In the terahertz frequency band, the wavelength is so short that the concept of the internet of nano-things is proposed [12]. There are two main alternatives for communications in this field: molecular communication and nano-electromagnetic communication. Many potential applications for those communications have been explored, such as health monitoring, environment sensing, and surveillance systems [47]. We focus on the architecture of electromagnetic communication among nano-devices.

We introduce an example of the application of electromagnetic communication, as shown in Fig. 6.2 [12]. It shows a desktop environment with nano-devices as transceivers connected to the internet. The user can keep track of the location and status of all the things on the desktop by the interconnect of the nano-devices with very low power consumption.

As shown in Fig. 6.3 [91], the components in the nano network architecture is illustrated. Nano-nodes are the smallest and simplest nanomachines, which can be

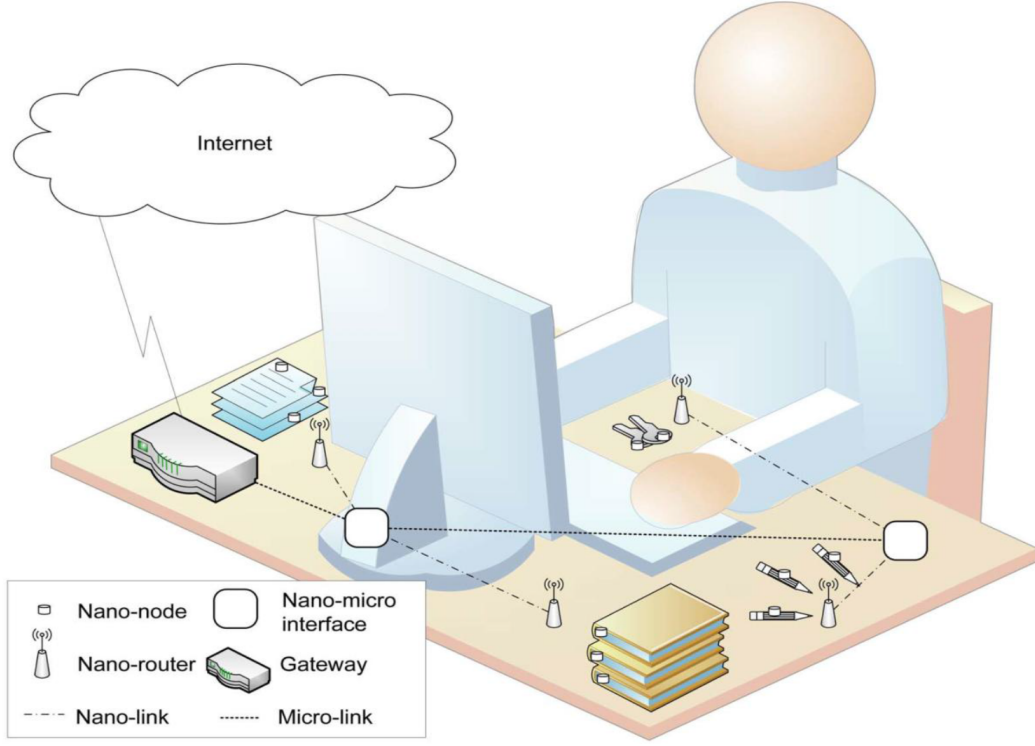


**Figure 6.2:** Nanonetwork in the interconnected office [12].

integrated into almost all types of things, such as pens, keys, books. Considering the power consumption and their limiting capability, they can only communicate in a very short distance. Nano-routers can aggregate information from several nanomachines and send some simple control commands to nanomachines, with having larger computation resources and capabilities. They can also communicate with nano-micro interface devices, conveying the information from nano-routers to the gateway as a relay station. Another function of the nano-micro interface is to make frequency conversions between THz band frequency and lower band frequency [91]. Gateway is connected with the internet, with controlling the whole system remotely. Since the larger the capacity, the bigger the size of the nano-devices, the nano-devices with small size should be deployed more invasive.

Based on the proposed channel model in the THz frequency band, the total bandwidth can be divided into several sub-bands. Thus, the capacity of the nanonetwork can be obtained by the summation of the capacity of each sub-band. Then the capacity of the nanonetwork can be given by [46]

$$C(d) = \sum_i \Delta f \log_2 \left[ 1 + \frac{S(f_i) A(f_i, d)^{-1}}{N(f_i, d)} \right] \quad (6.8)$$

where  $f_i$  is the central frequency of the  $i$ th sub-band, and the bandwidth of each sub-band is  $\Delta f$ .  $\Delta f$  should be small enough, then the channel can be seen as a flat fading

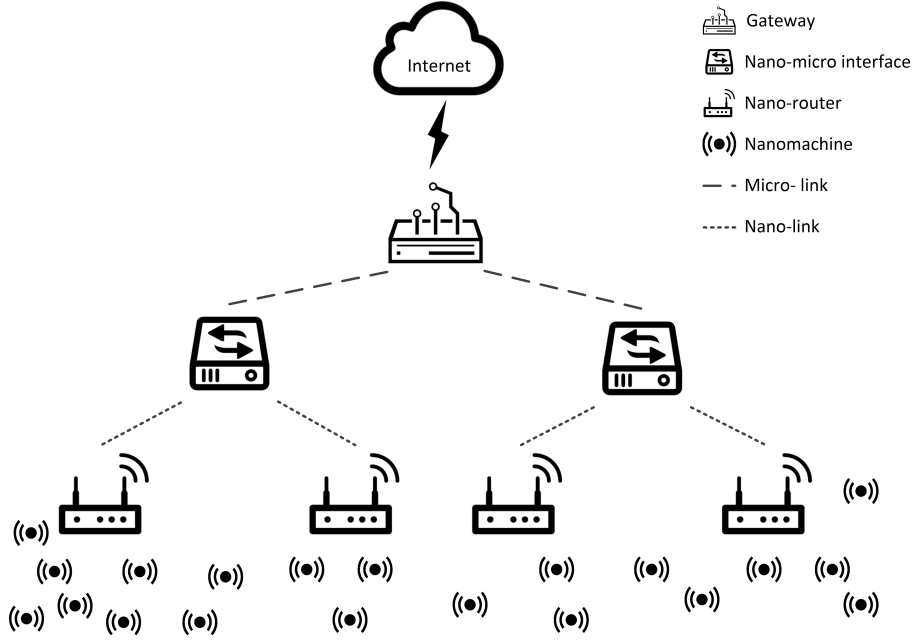


Figure 6.3: Nanonetwork architecture

channel.  $d$  is the total path length;  $S$  and  $N$  are the power spectral density of the transmitted signal and noise, respectively;  $A$  is the channel path loss.

As shown in Fig. 6.4 [46], we see that the capacity of nanonetwork can be up to several hundreds of thousand Gbps when the distance is less than 0.1 mm with the optimal power allocation. For the case in which a transmission window at 350 GHz with considering a standard medium with 1% of water vapor molecule, the capacity is about several thousand Gbps, which is still large enough. Besides, for a larger transmission distance than 1 cm, the molecular absorption cannot be neglected.

As for the 120 GHz frequency band, the communication range is larger than the microscale for the THz frequency band but smaller than the picocells for the lower frequency band. We can do a compromise between these two fields, aiming at larger capacity and medium size of the devices.

## 6.3 Hybrid Beamforming Design

This section addresses the problem formulation and proposes the hybrid beamforming design based on the system configuration. Here, we introduce two kinds of algorithms: with perfect channel state information (CSI) and without CSI.

### 6.3.1 System Configuration

We consider an indoor communication system at 120 GHz, where an access point (AP) serves multiple users. The AP is equipped with  $K$  RF chains and  $KN$  antennas with a fully-connected structure, as shown in Fig. 6.1a or a array-of-subarray structure as

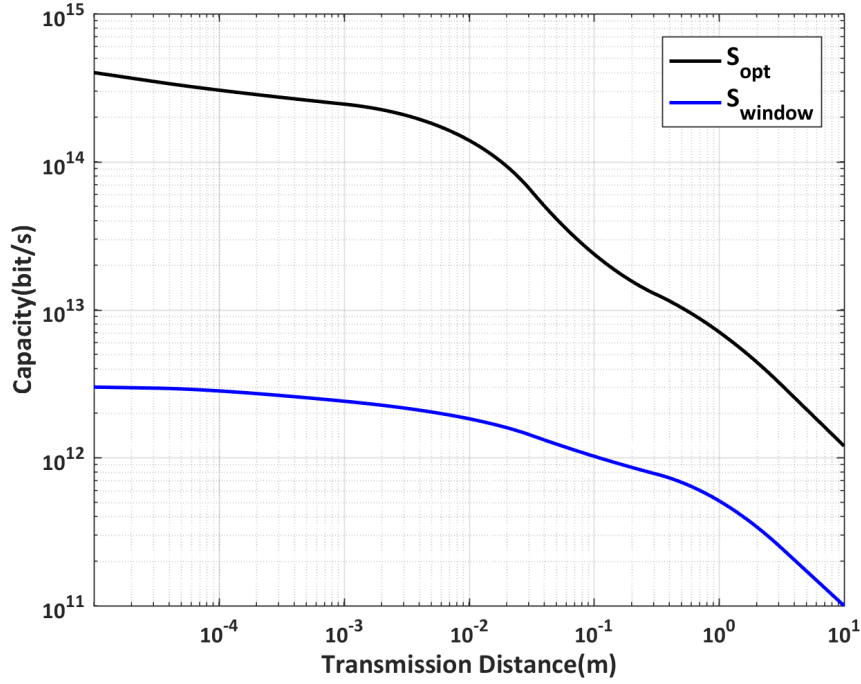


**Figure 6.4:** Capacity as a function of the distance for the optimal power spectral density  $S_{opt}$  and a transmission window at 350 GHz with 1%  $H_2O$   $S_{window}$  [46]

in Fig. 6.1b. At the receiver side (user side), due to the processing limitation of the receiver, there is only one RF chain equipped with  $M$  antennas,  $M \ll KN$ .

In Fig. 6.1, we denote the number of user is  $J$  and the distance between the AP and the  $j$ th user is  $d_j$ ,  $K \geq J$ . Then the received signal of user  $j$  can be given by

$$y_j = \mathbf{v}_j^H \mathbf{H}_j \mathbf{W} \mathbf{f} \mathbf{s} + \mathbf{v}_j^H \mathbf{n}_j,$$

where  $\mathbf{s}$  is the  $J \times 1$  transmitted signal,  $H_j$  is the  $M \times KN$  channel matrix between the AP and the  $j$ th user, and  $W$  is the  $KN \times K$  transmit analog beamforming matrix. For the fully-connected structure,  $W$  can be expressed as

$$\mathbf{W} = [\mathbf{w}_1, \mathbf{w}_2, \dots, \mathbf{w}_K],$$

where  $\mathbf{w}_k$  is a  $KN \times 1$  vector. For the array-of-subarray structure,  $W$  is block diagonal and given by

$$\mathbf{W} = \begin{bmatrix} \mathbf{w}_1 & \mathbf{0} & \cdots & \mathbf{0} \\ \mathbf{0} & \mathbf{w}_2 & \cdots & \mathbf{0} \\ \vdots & \vdots & \ddots & \vdots \\ \mathbf{0} & \mathbf{0} & \cdots & \mathbf{w}_K \end{bmatrix},$$

where  $\mathbf{w}_k$  is an  $N \times 1$  vector.  $\mathbf{F}$  is the  $K \times J$  baseband digital beamforming matrix,  $\mathbf{v}_j$  is the  $M \times 1$  receive analog beamforming vector at user  $j$ , and  $\mathbf{n}_j$  is the Gaussian noise at user  $j$ , i.e.,  $\mathbf{n}_j \sim \mathcal{N}(0, \sigma_j^2 \mathbf{I})$ .

### 6.3.2 Problem Formulation

Given the system model, the channel model and equal power allocation, the data rate of the user  $j$  for the system can be expressed as [61]

$$R_j = B \log_2 \left( 1 + \frac{\frac{P_t}{J} |\mathbf{v}_j^H \mathbf{H}_j \mathbf{W} \mathbf{f}_j|^2}{\sum_{i \neq j} \frac{P_t}{J} |\mathbf{v}_j^H \mathbf{H}_j \mathbf{W} \mathbf{f}_i|^2 + \sigma_j^2} \right) \quad (6.9)$$

where  $P_t$  is the transmit power and  $B$  is the bandwidth. We can see that the information rate is jointly determined by beamforming matrix  $F$ ,  $W$  and  $V$ . Our goal is to maximize the system sum-rate under the transmitted power constraint. Then the optimization problem can be expressed as

$$\begin{aligned} \arg \max_{\mathbf{F}, \mathbf{W}, \mathbf{V}_j} & \sum_{j=1}^J \log_2 \left( 1 + \frac{\frac{P_t}{J} |\mathbf{v}_j^H \mathbf{H}_j \mathbf{W} \mathbf{f}_j|^2}{\sum_{i \neq j} \frac{P_t}{J} |\mathbf{v}_j^H \mathbf{H}_j \mathbf{W} \mathbf{f}_i|^2 + \sigma_j^2} \right). \\ \text{s.t. } & \text{Tr}\{\mathbf{W} \mathbf{F} \mathbf{F}^H \mathbf{W}^H\} \leq P_t \end{aligned} \quad (6.10)$$

### 6.3.3 Optimization Algorithms with Perfect CSI

Since the objective function (6.10) is a non-convex problem, it is very difficult or with very high complexity to solve the problem. Thus, we concerned more about low complexity sub-optimal solutions. With the perfect CSI, we see different sub-optimal solutions with different settings.

#### 6.3.3.1 Optimal Transmit Beamforming with MRC Receiver Design

First, we analyze a simple system structure, full-digital structure. The received signal at user  $j$  can be expressed as

$$y_j = \hat{\mathbf{h}}_j^H \left( \sum_{j=1}^J \mathbf{f}_j s_j \right) + \hat{\mathbf{n}}_j \quad (6.11)$$

where  $\hat{\mathbf{h}}_j^H = \mathbf{v}_j^H \mathbf{H}_j$  denotes the equivalent channel for user  $j$  and  $\hat{\mathbf{n}}_j = \mathbf{v}_j^H \mathbf{n}_j$  is the equivalent noise with zero mean and variance  $\sigma^2$ . Then the SINR at user  $j$  can be represented as

$$\text{SINR}_j = \frac{|\hat{\mathbf{h}}_j^H \mathbf{f}_j|^2}{\sum_{i \neq j} |\hat{\mathbf{h}}_j^H \mathbf{f}_i|^2 + \sigma^2}. \quad (6.12)$$

The objective function can be given as

$$\begin{aligned} \arg \max_{\mathbf{f}_1, \dots, \mathbf{f}_J} & \sum_{j=1}^J \log 2(1 + \text{SINR}_j) \\ \text{s.t.} & \sum_{j=1}^J \|\mathbf{f}_j\|^2 \leq P_t. \end{aligned} \quad (\text{P1})$$

Since the problem (P1) is challenging to solve directly, we use a trick by employing maximum ratio transmission (MRT) beamforming from [23]. Before addressing the issue (P1), we prepare by solving a power maximization problem

$$\begin{aligned} \arg \max_{\mathbf{f}_1, \dots, \mathbf{f}_J} & \sum_{j=1}^J \|\mathbf{f}_j\|^2 \\ \text{s.t.} & \text{SINR}_j \geq \gamma_j \end{aligned} \quad (\text{P2})$$

where  $\gamma_j$  is the SINR at user  $j$  that should be achieved at the optimum of (P2). The key point of the solution of (P2) is to reformulate it as a convex problem. It is clear that  $\sum_{j=1}^J \|\mathbf{f}_j\|^2$  is a convex function of the beamforming vectors. To the convexity of the SINR constraints, we rewrite the formula  $\text{SINR}_j \geq \gamma_j$  as [21]

$$\frac{1}{\gamma_j \sigma^2} |\hat{\mathbf{h}}_j^H \mathbf{f}_j|^2 \geq \sum_{i \neq j} \frac{1}{\sigma^2} |\hat{\mathbf{h}}_j^H \mathbf{f}_i|^2 + 1. \quad (6.13)$$

Thus, the strong duality and Karush-Kuhn-Tucker (KKT) are sufficient for the optimal solution. We define the Lagrangian function of (P2) as

$$\mathcal{L}(\mathbf{f}_1, \dots, \mathbf{f}_J, \lambda_1, \dots, \lambda_J) = \sum_{j=1}^J \|\mathbf{f}_j\|^2 + \sum_{j=1}^J \lambda_j \left( \sum_{i \neq j} \frac{1}{\sigma^2} |\hat{\mathbf{h}}_j^H \mathbf{f}_i|^2 + 1 - \frac{1}{\gamma_j \sigma^2} |\hat{\mathbf{h}}_j^H \mathbf{f}_j|^2 \right) \quad (6.14)$$

where  $\lambda_j \geq 0$  is the Lagrange multiplier associated with the  $\text{SINR}_j$ . According to the stationarity KKT conditions, that is  $\partial \mathcal{L} / \partial \mathbf{f}_j = 0$ , we can obtain

$$\mathbf{f}_j + \sum_{i \neq j} \frac{\lambda_i}{\sigma^2} \hat{\mathbf{h}}_i \hat{\mathbf{h}}_i^H \mathbf{f}_j - \frac{\lambda_j}{\gamma_j \sigma^2} \hat{\mathbf{h}}_j \hat{\mathbf{h}}_j^H \mathbf{f}_j = 0 \quad (6.15)$$

$$\Leftrightarrow \left( \mathbf{I} + \sum_{j=1}^J \frac{\lambda_j}{\sigma^2} \hat{\mathbf{h}}_j \hat{\mathbf{h}}_j^H \right) \mathbf{f}_j = \frac{\lambda_j}{\sigma^2} \left( 1 + \frac{1}{\gamma_j} \right) \hat{\mathbf{h}}_j \hat{\mathbf{h}}_j^H \mathbf{f}_j \quad (6.16)$$

$$\Leftrightarrow \mathbf{f}_j = \left( \mathbf{I} + \sum_{j=1}^J \frac{\lambda_j}{\sigma^2} \hat{\mathbf{h}}_j \hat{\mathbf{h}}_j^H \right)^{-1} \hat{\mathbf{h}}_j \times \frac{\lambda_j}{\sigma^2} \left( 1 + \frac{1}{\gamma_j} \right) \hat{\mathbf{h}}_j^H \mathbf{f}_j. \quad (6.17)$$

Since  $\frac{\lambda_j}{\sigma^2}(1 + \frac{1}{\gamma_j})\hat{\mathbf{h}}_j^H \mathbf{f}_j$  is a scalar, the optimal  $\mathbf{f}_j$  must be parallel to  $(\mathbf{I} + \sum_{j=1}^J \frac{\lambda_j}{\sigma^2} \hat{\mathbf{h}}_i \hat{\mathbf{h}}_i^H)^{-1} \hat{\mathbf{h}}_j$ . Then the optimal beamforming vectors  $\mathbf{f}_1^*, \dots, \mathbf{f}_J^*$  are given by

$$\mathbf{f}_j^* = \sqrt{p_j} \frac{\left(\mathbf{I} + \sum_{j=1}^J \frac{\lambda_j}{\sigma^2} \hat{\mathbf{h}}_i \hat{\mathbf{h}}_i^H\right)^{-1} \hat{\mathbf{h}}_j}{\left\| \left(\mathbf{I} + \sum_{j=1}^J \frac{\lambda_j}{\sigma^2} \hat{\mathbf{h}}_i \hat{\mathbf{h}}_i^H\right)^{-1} \hat{\mathbf{h}}_j \right\|} = \sqrt{p_j} \hat{\mathbf{f}}_j^*$$

where  $p_j$  is the beamforming power and  $\hat{\mathbf{f}}_j^*$  is the beamforming direction for user  $j$ . The  $J$  unknown beamforming powers are computed by SINR constraints in Eq. (6.13) with equality at the optimal solution. That is  $\frac{1}{\gamma_j} p_j |\hat{\mathbf{h}}_j^H \mathbf{f}_j|^2 - \sum_{i \neq j} p_i |\hat{\mathbf{h}}_j^H \mathbf{f}_i|^2 = \sigma^2$ . Then we can obtain the  $J$  powers as

$$\begin{bmatrix} p_1 \\ \vdots \\ p_J \end{bmatrix} = \mathbf{M}^{-1} \begin{bmatrix} \sigma^2 \\ \vdots \\ \sigma^2 \end{bmatrix} \quad (6.18)$$

where

$$\mathbf{M}_{i,j} = \begin{cases} \frac{1}{\gamma_i} |\mathbf{h}_i^H \hat{\mathbf{f}}_i^*|^2, & i = j \\ -|\mathbf{h}_i^H \hat{\mathbf{f}}_j^*|^2, & i \neq j \end{cases}. \quad (6.19)$$

We note that the Lagrange multiplier can be computed by convex optimization [21].

Next, we can solve the problem (P1) based on the solution of (P2). Suppose that we know the optimal SINR values  $\text{SINR}_1^*, \dots, \text{SINR}_J^*$ , which are the solutions of problem (P1). If we set  $\gamma_j = \text{SINR}_j^*$ , the beamforming vectors that solve (P2) will also address (P1). Although the optimal SINR values are unknown unless we have solved (P1), we can obtain the optimal beamforming for (P1) as

$$\mathbf{f}_j^* = \sqrt{p_j} \frac{\left(\mathbf{I} + \sum_{j=1}^J \frac{\lambda_j}{\sigma^2} \hat{\mathbf{h}}_i \hat{\mathbf{h}}_i^H\right)^{-1} \hat{\mathbf{h}}_j}{\left\| \left(\mathbf{I} + \sum_{j=1}^J \frac{\lambda_j}{\sigma^2} \hat{\mathbf{h}}_i \hat{\mathbf{h}}_i^H\right)^{-1} \hat{\mathbf{h}}_j \right\|}. \quad (6.20)$$

The strong duality of (P2) implies  $\sum_{j=1}^J \lambda_j = P_t$ . We note that  $\sum_{j=1}^J \frac{\lambda_j}{\sigma^2} \hat{\mathbf{h}}_i \hat{\mathbf{h}}_i^H = \frac{1}{\sigma^2} \hat{\mathbf{H}} \Lambda \hat{\mathbf{H}}$  to obtain a simple structure of the optimal beamforming, where  $\hat{\mathbf{H}} = [\hat{\mathbf{h}}_1, \dots, \hat{\mathbf{h}}_J]$  is the equivalent channel matrix and  $\Lambda = \text{diag}(\lambda_1, \dots, \lambda_J)$  is a diagonal matrix with the  $\lambda$ -parameters. A closed-form expression can be obtained as [23]

$$\mathbf{F}^* = \left(\mathbf{I} + \frac{1}{\sigma^2} \hat{\mathbf{H}} \Lambda \hat{\mathbf{H}}^H\right)^{-1} \hat{\mathbf{H}} \mathbf{P}^{\frac{1}{2}} \quad (6.21)$$



where  $\mathbf{P} = \text{diag}(p_1/\|(\mathbf{I} + \frac{1}{\sigma^2}\hat{\mathbf{H}}\Lambda\hat{\mathbf{H}}^H)^{-1}\hat{\mathbf{h}}_1\|, \dots, p_J/\|(\mathbf{I} + \frac{1}{\sigma^2}\hat{\mathbf{H}}\Lambda\hat{\mathbf{H}}^H)^{-1}\hat{\mathbf{h}}_J\|)$  is the power allocation matrix. The MRC receiver which is to maximize the received signal power can be denoted as [30]

$$\mathbf{v}_j = \frac{\mathbf{H}_j \mathbf{f}_j}{\|\mathbf{H}_j \mathbf{f}_j\|}. \quad (6.22)$$

Here, we also apply this method to hybrid beamforming design since the digital and analog beamforming can be jointly designed to obtain the optimal transmit beamforming  $\mathbf{F}_{opt}$ . The objective function is

$$\begin{aligned} \arg \min_{\mathbf{W}, \mathbf{F}} \quad & \|\mathbf{F}_{opt} - \mathbf{W}\mathbf{F}\| \\ \text{s.t.} \quad & \text{Tr}\{\mathbf{W}\mathbf{F}\mathbf{F}^H\mathbf{W}^H\} \leq P_t. \end{aligned} \quad (6.23)$$

### 6.3.3.2 Nulling Interference Hybrid Beamforming Design

To simplify the objective function (6.10), we obtain the suboptimal solutions by designing the digital beamforming matrix to cancel the inter-user interference. Then the objective function can be rewritten as

$$\begin{aligned} \arg \max_{\mathbf{W}, \mathbf{v}_j} \quad & \sum_{j=1}^J \log_2 \left( 1 + \frac{|\mathbf{v}_j^H \mathbf{H}_j \mathbf{W} \mathbf{f}_j|^2}{J\sigma_j^2/P_t} \right) \\ \text{s.t.} \quad & \text{Tr}\{\mathbf{W}\mathbf{F}\mathbf{F}^H\mathbf{W}^H\} \leq P_t. \end{aligned} \quad (6.24)$$

When the digital beamforming matrix is fixed, we must jointly optimize the objective function (6.24) to obtain the analog beamforming matrix both at the transmitter and the receiver. Thus, the next step is to choose analog beamforming matrix  $\mathbf{W}$  and  $\mathbf{V}$  to maximize  $\sum_{j=1}^J |\mathbf{v}_j^H \mathbf{H}_j \mathbf{W}|^2$ , as

$$\arg \max_{\mathbf{W}, \mathbf{v}_j} \sum_{j=1}^J |\mathbf{v}_j^H \mathbf{H}_j \mathbf{W}|^2. \quad (6.25)$$

In the following, we will introduce the digital beamforming design and the analog beamforming design respectively.

**Nulling interference digital beamforming design:** in general, there are two kinds of designs to null the inter-user interference in the multiuser scenario: zero-forcing (ZF) precoder and block diagonalization (BD) precoder [95].

1) ZF precoder: the ZF precoder can be expressed as [54]

$$\mathbf{F} = [\mathbf{f}_1, \mathbf{f}_2, \dots, \mathbf{f}_J] = \hat{\mathbf{H}}\Delta \quad (6.26)$$

$$\hat{\mathbf{F}} = [\hat{\mathbf{f}}_1, \hat{\mathbf{f}}_2, \dots, \hat{\mathbf{f}}_J] \triangleq \hat{\mathbf{H}}^H(\hat{\mathbf{H}}\hat{\mathbf{H}}^H)^{-1} \quad (6.27)$$

$$\hat{\mathbf{H}} = [\hat{\mathbf{h}}_1, \hat{\mathbf{h}}_2, \dots, \hat{\mathbf{h}}_J]^T \quad (6.28)$$

$$\hat{\mathbf{h}}_j^T = \mathbf{v}_j^H \mathbf{H}_j \mathbf{W} \quad (6.29)$$

where  $\hat{\mathbf{H}}$  is the equivalent channel matrix,  $\Delta$  is a diagonal matrix to regulate the digital beamforming power such that  $\|\mathbf{W}\mathbf{f}_j\|^2 = 1$  and  $\Delta_{j,j} = \frac{1}{\|\mathbf{W}\hat{\mathbf{f}}_j\|}$ . The algorithm's performance decreases with the high noise, and the system capacity is limited with the increasing number of users.

2) Block diagonalization (BD) precoder: the critical concept of BD is to make the precoding vector  $\mathbf{f}_i$  orthogonal to the equivalent channel  $\hat{\mathbf{h}}_j^T = \mathbf{v}_j^H \mathbf{H}_j \mathbf{W}$ , which can cancel the inter-user interference. It is given by

$$\hat{\mathbf{h}}_j^T * \mathbf{f}_i = 0, \forall 1 \leq i, j \leq J, i \neq j. \quad (6.30)$$

We define the complementary channel matrix  $\tilde{\mathbf{H}}$  that contains the equivalent channel gains of all users except for the  $j$ th user as

$$\tilde{\mathbf{H}} = [\hat{\mathbf{h}}_1, \dots, \hat{\mathbf{h}}_{j-1}, \hat{\mathbf{h}}_{j+1}, \dots, \hat{\mathbf{h}}_J]^T. \quad (6.31)$$

To satisfy the constraint in (6.30),  $\mathbf{f}_i$  should lie in the null space of  $\tilde{\mathbf{H}}$  in (6.31). Let  $\tilde{N} = \text{rank}(\tilde{\mathbf{H}})$  and we use the singular value decomposition (SVD) on  $\tilde{\mathbf{H}}$  as in [115]

$$\tilde{\mathbf{H}} = \tilde{\mathbf{U}} \tilde{\Sigma} [\tilde{\mathbf{V}}^{(1)} \tilde{\mathbf{V}}^{(0)}]^H \quad (6.32)$$

where  $\tilde{\mathbf{U}}$  is a unitary matrix with  $\tilde{\mathbf{U}}\tilde{\mathbf{U}}^H = \mathbf{I}$ ,  $\tilde{\Sigma}$  is a diagonal matrix, matrix  $\tilde{\mathbf{V}}^{(1)}$  consists of the first  $\tilde{N}$  right singular vectors of  $\tilde{\mathbf{H}}$  and  $\tilde{\mathbf{V}}^{(0)}$  consists of the last  $(K - \tilde{N})$  right singular vectors of  $\tilde{\mathbf{H}}$ , whose columns are in the null space of  $\tilde{\mathbf{H}}$ . Thus,  $\mathbf{f}_j$  can be chosen from the column vectors of  $\tilde{\mathbf{V}}^{(0)}$ .

**Analog beamforming design with nulling interference precoder:** before we obtain the digital precoder matrix  $\mathbf{F}$ , we should determine the problem in (6.25). Here, we only employ phase shifters for the analog beamformers. According to different system structures, the analog beamforming design is different. In the following, two kinds of algorithms will be introduced: RF beam steering codebook based searching algorithm and modified generalized low-rank approximation of matrices (MGLRAM) algorithm.

1) RF beam steering codebook based searching algorithm: the beam steering codebook based searching algorithm for fully-connected structure, as shown in Algorithm 3, is developed to obtain the analog beamforming matrices [54], [17]. In order to ensure fairness and overall performance, the RF chain will be assigned firstly to the longer-distance user. There should be a guarantee that the beam generated at the user side is wide enough to receive multiple narrow beams from AP since  $M \ll KN$ . Unlike the fully-connected structure, in an array-of-subarray structure, each subarray instead of each antenna has one beam steering direction. The channel matrix of user  $j$  is

$$\mathbf{H}_j = [\mathbf{H}_{j,1}, \dots, \mathbf{H}_{j,K}] \quad (6.33)$$

where  $\mathbf{H}_{j,k}$  is the channel from the  $k$ th subarray to the user  $j$ . The analog beamforming design for the array-of-subarray structure is described in the Algorithm 4 [54]. It is

**Algorithm 3** Analog Beamforming Searching for the Fully-Connected Structure

---

```

1: Initialize the transmit beamsteering codebook for user  $j$ ,  $\mathcal{W}_j = \mathcal{W}$  and the receive
   beamsteering codebook  $\mathcal{V}$ ;
2: for  $k = 1 : K$  do
3:    $j = (k - 1) \bmod J + 1$ ;
4:   if  $k \leq J$  then
5:      $\{\mathbf{a}_t(\hat{\phi}_k), \mathbf{a}_r(\hat{\theta}_j)\} = \arg \max_{\hat{\phi}_k \in \mathcal{W}_j, \hat{\theta}_j \in \mathcal{V}} \left| \mathbf{a}_r^H(\theta_j) \mathbf{H}_j \mathbf{a}_t(\phi_k) \right|^2$ 
6:   else
7:      $\mathbf{a}_t(\hat{\phi}_k) = \arg \max_{\hat{\phi}_k \in \mathcal{W}_j} \left| \mathbf{a}_r^H(\theta_j) \mathbf{H}_j \mathbf{a}_t(\phi_k) \right|^2$ 
8:   end if
9:   Update  $\mathcal{W}_j = \mathcal{W}_j - \{\hat{\phi}_k\}$ ;
10: end for
11: return  $\mathbf{w}_k = \frac{1}{\sqrt{KN}} \mathbf{a}_t(\hat{\phi}_k)$  and  $\mathbf{v}_j = \frac{1}{\sqrt{M}} \mathbf{a}_r(\hat{\theta}_j)$ ;

```

---

**Algorithm 4** Analog Beamforming Searching for the Array-of-Subarray Structure

---

```

1: Initialize the transmit beamsteering codebook  $\mathcal{W}$  and the receive beamsteering
   codebook  $\mathcal{V}$ ;
2: for  $k = 1 : K$  do
3:    $j = (k - 1) \bmod J + 1$ ;
4:   if  $k \leq J$  then
5:      $\{\mathbf{a}_t(\hat{\phi}_k), \mathbf{a}_r(\hat{\theta}_j)\} = \arg \max_{\hat{\phi}_k \in \mathcal{W}_j, \hat{\theta}_j \in \mathcal{V}} \left| \mathbf{a}_r^H(\theta_j) \mathbf{H}_{j,k} \mathbf{a}_t(\phi_k) \right|^2$ 
6:   else
7:      $\mathbf{a}_t(\hat{\phi}_k) = \mathbf{a}_t(\hat{\phi}_j)$ 
8:   end if
9: end for
10: return  $\mathbf{w}_k = \frac{1}{\sqrt{N}} \mathbf{a}_t(\hat{\phi}_k)$  and  $\mathbf{v}_j = \frac{1}{\sqrt{M}} \mathbf{a}_r(\hat{\theta}_j)$ ;

```

---

**Algorithm 5** Analog Beamforming Design based on MGLRAM

---

```

1: Initialize  $\mathbf{v}_j$  by solving (25);
2:  $\mathbf{P} = \sum_{j=1}^J \mathbf{H}_j^H \mathbf{v}_j \mathbf{v}_j^H \mathbf{H}_j$ ;
3:  $\mathbf{P} = \mathbf{U}_P \mathbf{\Sigma}_P \mathbf{U}_P^H$ ;
4:  $\mathbf{W} = \frac{1}{\sqrt{KN}} e^{j \cdot \text{angle}\{\mathbf{U}_P(:, 1:K)\}}$ 
5: for  $i = 1 : J$  do
6:    $\mathbf{Q} = \mathbf{H}_i \mathbf{W} \mathbf{W}^H \mathbf{H}_i^H$ ;
7:    $\mathbf{Q} = \mathbf{U}_Q \mathbf{\Sigma}_Q \mathbf{U}_Q^H$ ;
8:    $\mathbf{v}_i = \frac{1}{\sqrt{M}} e^{j \cdot \text{angle}\{\mathbf{U}_Q(:, 1)\}}$ ;
9: end for
10: return  $\mathbf{W}$  and  $\mathbf{v}_i$ ;

```

---

noticed that users can receive multiple beams from different subarrays, but the beam steering harvests only the strongest path.

2) Modified generalized low-rank approximation of matrices algorithm: considering a particular case that  $\mathbf{W}$  and  $\mathbf{v}_j$  are unitary, the objective function can be written as

$$\begin{aligned} \arg \max_{\mathbf{W}, \mathbf{v}_j} \sum_{j=1}^J |\mathbf{v}_j^H \mathbf{H}_j \mathbf{W}|^2 \\ \text{s.t. } \mathbf{W}^H \mathbf{W} = \mathbf{I}, \quad \mathbf{v}_j^H \mathbf{v}_j = \mathbf{I}, \forall j. \end{aligned} \quad (6.34)$$

The MGLRAM algorithm proposed in [94] can be used to determine the problem. According to [120], (6.34) can be rewritten as

$$\begin{aligned} \arg \max_{\mathbf{W}} \text{Tr} \left\{ \mathbf{W}^H \sum_{j=1}^J \mathbf{H}_j^H \mathbf{v}_j \mathbf{v}_j^H \mathbf{H}_j \mathbf{W} \right\} \\ \text{s.t. } \mathbf{W}^H \mathbf{W} = \mathbf{I} \end{aligned} \quad (6.35)$$

$$\begin{aligned} \arg \max_{\mathbf{v}_j \in \mathcal{V}} \text{Tr} \left\{ \sum_{j=1}^J \mathbf{v}_j^H \mathbf{H}_j \mathbf{W} \mathbf{W}^H \mathbf{H}_j^H \mathbf{v}_j \right\} \\ \text{s.t. } \mathbf{v}_j^H \mathbf{v}_j = \mathbf{I}, \forall j. \end{aligned} \quad (6.36)$$

The concept of generalized low-rank approximation of matrices (GLRAM) is to iteratively update  $\mathbf{W}$  and  $\mathbf{v}_j$  so that the effective array gain can be maximal. MGLRAM is a sub-optimal but low complexity method. In Algorithm 5, initialize  $\mathbf{v}_j$  by solving the problem

$$\arg \max_{\mathbf{v}_j \in \mathcal{V}} |\mathbf{v}_j^H \mathbf{H}_j|^2 \quad (6.37)$$

where  $\mathcal{V}$  is the receive beam steering codebook. Then apply one iteration based on MGLRAM to solve  $\mathbf{W}$  and  $\mathbf{v}_j$ .

### 6.3.3.3 Interference Suppression with MMSE-based Hybrid Precoding Design

The proposed hybrid precoder is to minimize the sum-MSE of all data streams  $E\|\mathbf{s} - \hat{\mathbf{s}}\|^2$ , suppressing both the inter-user interference and the noise. The sum-MSE is [90]

$$E\|\mathbf{s} - \hat{\mathbf{s}}\|^2 = \|\mathbf{I} - \bar{\mathbf{H}}\mathbf{W}\mathbf{B}\|^2 + J\gamma\sigma^2 \quad (6.38)$$

where  $\bar{\mathbf{H}} = [\bar{\mathbf{h}}_1, \bar{\mathbf{h}}_2, \dots, \bar{\mathbf{h}}_J]^T$ ,  $\bar{\mathbf{h}}_j^T = \mathbf{v}_j^H \mathbf{H}_j$ ,  $\mathbf{B}$  is an unnormalized digital precoder, and  $\gamma$  is a power scaling factor such that  $\mathbf{F} = \sqrt{1/\gamma}\mathbf{B}$ . The objective function can be expressed as

$$\begin{aligned} \arg \min_{\mathbf{F}, \mathbf{W}, \gamma} \text{Tr} \{ (\mathbf{I} - \bar{\mathbf{H}}\mathbf{W}\mathbf{B})(\mathbf{I} - \bar{\mathbf{H}}\mathbf{W}\mathbf{B})^H \} + J\gamma\sigma^2 \\ \text{s.t. } \text{Tr} \{ \mathbf{W}\mathbf{B}\mathbf{B}^H \mathbf{W}^H \} \leq \gamma P_t. \end{aligned} \quad (6.39)$$

Suppose that we know  $\mathbf{W}$ , the optimal solution of  $\mathbf{B}$  in a closed-form is [62]

$$\mathbf{B}^* = (\mathbf{W}^H \bar{\mathbf{H}}^H \bar{\mathbf{H}} \mathbf{W} + \frac{J\sigma^2}{P_t} \mathbf{W}^H \mathbf{W})^{-1} \mathbf{W}^H \bar{\mathbf{H}}^H \quad (6.40)$$

where  $\mathbf{F}^* = \sqrt{1/\gamma^*} \mathbf{B}^*$  and  $\gamma^* = \|\mathbf{W}\mathbf{B}\|^2/P$ . Then we utilize the orthogonal matching pursuit (OMP) [101] to solve the joint problem (6.39) as the Algorithm 6.  $\mathbf{A}_t = [\mathbf{a}_t(\phi_1), \dots, \mathbf{a}_t(\phi_{KN})]$  is the matrix of the transmit array steering vectors.  $K$  columns of  $\mathbf{A}_t$  consist of the RF analog beamforming matrix  $\mathbf{W}$ .

---

**Algorithm 6** Hybrid MMSE Precoding via OMP

---

```

1: Input:  $\bar{\mathbf{H}}, \mathbf{A}_t$ 
2: Output:  $\mathbf{W}, \mathbf{F}$ 
3: Initialize  $\mathbf{V}_{res} = \mathbf{I}, \mathbf{W} = \text{empty};$ 
4: for  $k = 1 : K$  do
5:    $\Phi = \mathbf{A}_t^H \bar{\mathbf{H}}^H \mathbf{V}_{res};$ 
6:    $i = \arg \max_l [\Phi \Phi^H]_{l,l};$ 
7:    $\mathbf{W} = [\mathbf{W} | \mathbf{A}_t^{(i)}];$ 
8:    $\mathbf{B}^* = (\mathbf{W}^H \bar{\mathbf{H}}^H \bar{\mathbf{H}} \mathbf{W} + \frac{J\sigma^2}{P_t} \mathbf{W}^H \mathbf{W})^{-1} \mathbf{W}^H \bar{\mathbf{H}}^H;$ 
9:    $\mathbf{V}_{res} = \frac{\mathbf{I} - \bar{\mathbf{H}} \mathbf{W} \mathbf{B}^*}{\|\mathbf{I} - \bar{\mathbf{H}} \mathbf{W} \mathbf{B}^*\|};$ 
10: end for
11:  $\gamma = \frac{\text{Tr}\{\mathbf{W} \mathbf{B} \mathbf{B}^H \mathbf{W}^H\}}{P};$ 
12: return  $\mathbf{F} = \frac{1}{\gamma} \mathbf{B}, \mathbf{W};$ 

```

---

At the receiver side, the analog beamforming vector  $\mathbf{v}_j$  can be obtained to maximize the channel gain  $\|\bar{\mathbf{h}}^T\|$

$$\mathbf{v}_j = \arg \max_{\mathbf{v}_j \in \mathcal{V}} \|\bar{\mathbf{h}}^T\| \quad (6.41)$$

where  $\mathcal{V}$  is the receive beam steering codebook for users.

### 6.3.3.4 SVD based Precoding Design

Considering only one user in the system, the objective function can be written as

$$\begin{aligned} \arg \max_{\mathbf{F}, \mathbf{W}, \mathbf{v}_j} \sum_{j=1}^J \log_2 \left| \mathbf{I} + \frac{\mathbf{f}_j^H \mathbf{W}^H \mathbf{H}_j^H \mathbf{v}_j \mathbf{v}_j^H \mathbf{H}_j \mathbf{W} \mathbf{f}_j}{J\sigma_j^2 / P_t} \right| \\ \text{s.t. } \text{Tr}\{\mathbf{W} \mathbf{F} \mathbf{F}^H \mathbf{W}^H\} \leq P_t \end{aligned} \quad (6.42)$$

Let  $\mathbf{G} = \mathbf{W}^H \mathbf{H}_j^H \mathbf{v}_j \mathbf{v}_j^H \mathbf{H}_j \mathbf{W}$ ,  $\mathbf{G}$  is a Hermitian matrix. According to SVD,  $\mathbf{G} = \mathbf{U} \mathbf{\Sigma} \mathbf{U}^H$ . Then  $\mathbf{f}_j$  should be the first column vector of  $\mathbf{U}$  which is corresponding to the maximum eigenvalue [34], [37]. After that, the received signal can be maximized as (6.25). However, for a multi-user scenario, the performance will be getting worse due to the inter-user interference.

### 6.3.4 Optimization Algorithm without CSI

This power iteration method is based on the numerical matrix analysis to assess the eigenvalue and singular value decomposition of the matrix [116]. The channel  $\mathbf{H}$  can be written as

$$\mathbf{H} = \sigma_1 \mathbf{u}_1 \mathbf{v}_1^H + \sigma_2 \mathbf{u}_2 \mathbf{v}_2^H + \cdots + \sigma_P \mathbf{u}_P \mathbf{v}_P^H \quad (6.43)$$

where  $\mathbf{u}_1, \dots, \mathbf{u}_P$  are left singular vectors of size  $M \times 1$ ,  $\mathbf{v}_1, \dots, \mathbf{v}_P$  are right singular vectors of size  $KN \times 1$  and  $\sigma_1 \geq \sigma_2 \geq \dots \sigma_P$  are singular values in a decreasing order. We define

$$\mathbf{G} = \mathbf{H}^H \mathbf{H}. \quad (6.44)$$

For a positive integer  $m$ , we define

$$\begin{aligned} \mathbf{H}^{2m} &= \mathbf{G}^m = (\mathbf{H}^H \mathbf{H})^m \\ \mathbf{H}^{2m-1} &= \mathbf{H} \mathbf{G}^{m-1} = \mathbf{H} (\mathbf{H}^H \mathbf{H})^{m-1}. \end{aligned} \quad (6.45)$$

Since the singular vectors are orthogonal to each other, we can get

$$\begin{aligned} \mathbf{H}^{2m} &= \sigma_1^{2m} \mathbf{v}_1 \mathbf{v}_1^H + \sigma_2^{2m} \mathbf{v}_2 \mathbf{v}_2^H + \cdots + \sigma_P^{2m} \mathbf{v}_P \mathbf{v}_P^H \\ \mathbf{H}^{2m-1} &= \sigma_1^{2m-1} \mathbf{u}_1 \mathbf{v}_1^H + \sigma_2^{2m-1} \mathbf{u}_2 \mathbf{v}_2^H + \cdots + \sigma_P^{2m-1} \mathbf{u}_P \mathbf{v}_P^H \end{aligned} \quad (6.46)$$

$\sigma_i^{2m} / \sigma_1^{2m}$  decreases exponentially as  $m$  increases,  $i = 1, 2, \dots, P$ . When  $m$  is approaching infinity, then

$$\begin{aligned} \lim_{m \rightarrow \infty} \mathbf{H}^{2m} &= \sigma_1^{2m} \mathbf{v}_1 \mathbf{v}_1^H \\ \lim_{m \rightarrow \infty} \mathbf{H}^{2m-1} &= \sigma_1^{2m-1} \mathbf{u}_1 \mathbf{v}_1^H. \end{aligned} \quad (6.47)$$

We can see that when  $m$  is large enough, only the strongest eigenmode  $\mathbf{u}_1, \mathbf{v}_1$  remains. Thus, we can obtain  $\mathbf{u}_1, \mathbf{v}_1$  by utilizing the power iteration method. For an arbitrary vector  $\mathbf{q}$  in the column space of  $\mathbf{H}$  can be represented by  $\mathbf{q} = \sum_{i=1}^P c_i \mathbf{v}_i$ , where  $c_i \mathbf{v}_i$  is contributed to  $\mathbf{v}_i$  by  $\mathbf{q}$ . Due to the orthogonality between singular vectors, we have that

$$\begin{aligned} \lim_{m \rightarrow \infty} \mathbf{H}^{2m} \mathbf{q} &= \sigma_1^{2m} \mathbf{v}_1 \mathbf{v}_1^H \left( \sum_{i=1}^P c_i \mathbf{v}_i \right) \\ &\propto \mathbf{v}_1. \end{aligned} \quad (6.48)$$

If we normalize the result after each iteration, the converged result will be equal to  $\mathbf{v}_1$ . Similarly, we can get  $\mathbf{u}_1$  by

$$\begin{aligned} \lim_{m \rightarrow \infty} \mathbf{H}^{2m-1} \mathbf{q} &= \sigma_1^{2m-1} \mathbf{u}_1 \mathbf{v}_1^H \left( \sum_{i=1}^P c_i \mathbf{v}_i \right) \\ &\propto \mathbf{u}_1. \end{aligned} \quad (6.49)$$

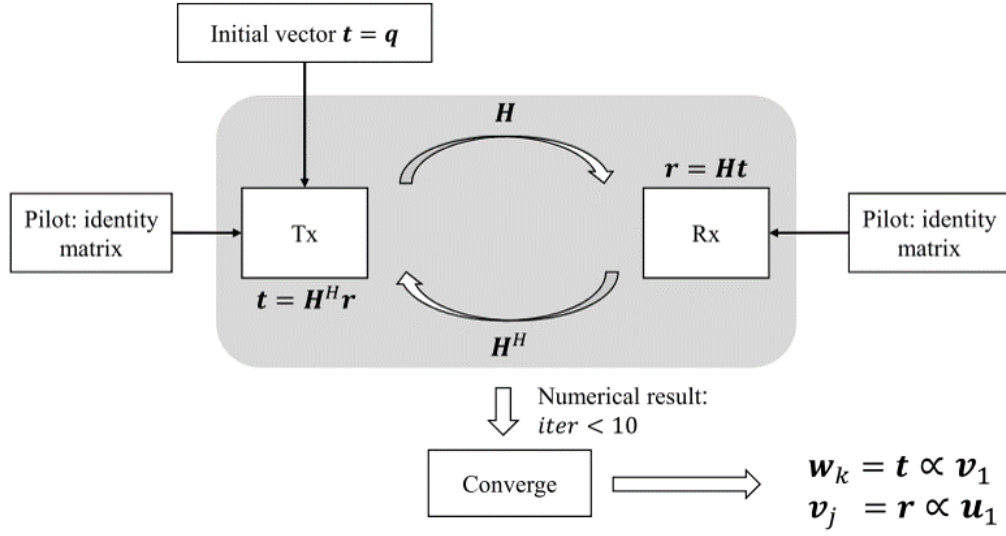


**Figure 6.5:** Iterative analog precoding training algorithm procedure: the convergence speed is validated by the simulation.

Note that  $\mathbf{q}$  is random, thus the possibility that  $\mathbf{q}$  is coincident with the column space of  $\mathbf{H}$  is 1. According to Equation 6.48 and 6.49, the analog precoder  $\mathbf{v}_1$  and the receiver combiner  $\mathbf{u}_1$  are obtained without CSI. Furthermore, the SVD decomposition of  $\mathbf{H}$  is no longer necessary.

The iterative process includes two steps, as shown in Fig. 6.5, optimizing the transmit precoding vector by receiving the signal with the receive combining vector at the transmitter and optimizing the receive combining vector by receiving the signal with the transmit precoding vector at the receiver. Until the convergence of the process, we can get  $\mathbf{v}_1$  and  $\mathbf{u}_1$ .

In addition, the algorithm can be extended to get  $\mathbf{v}_2, \dots, \mathbf{v}_P$  and  $\mathbf{u}_1, \dots, \mathbf{u}_P$ . We generate a random vector  $\mathbf{t}_1$  orthogonal to  $\mathbf{v}_1$  to obtain  $\mathbf{v}_2$ . In other words,  $\mathbf{t}_1$  can be represented by

$$\mathbf{t}_1 = \mathbf{t} - (\mathbf{v}_1^H \mathbf{t}) \mathbf{v}_1 = \sum_{i=2}^P c_i \mathbf{v}_i \quad (6.50)$$

where  $\mathbf{t}_1$  is orthogonal to  $\mathbf{v}_1$ . Similarly,

$$\lim_{m \rightarrow \infty} \mathbf{H}^{2m} \mathbf{t}_1 = c_2 \sigma_2^{2m} \mathbf{v}_2 \propto \mathbf{v}_2 \quad (6.51)$$

$$\lim_{m \rightarrow \infty} \mathbf{H}^{2m-1} \mathbf{t}_1 = c_2 \sigma_1^{2m-1} \mathbf{u}_2 \propto \mathbf{u}_2 \quad (6.52)$$

We can obtain  $\mathbf{v}_2, \mathbf{u}_2$  when the algorithm is applied until the convergence.

Although the algorithm seems less complicated than that based on RF codebook searching, it needs more amplifiers. Since each element's amplitudes in both  $\mathbf{v}$  and  $\mathbf{u}$

are not identical, only equipped with phase shifters is not enough. That means both the hardware cost and the power consumption will increase.

## 6.4 Performance Evaluation

In this section, we analyze the complexity and evaluate the performance of algorithms with different system structures. The algorithms are evaluated first with the perfect CSI, and then with the estimated channel. At last, the performance of the power iteration algorithms without CSI is validated for two different structures.

We consider the transceiver model for the indoor environment on a 120 GHz mmWave frequency band, where the ray tracing channel model is applied. Different multi-user system structures, such as the fully-digital beamforming structure, the analog-only beamforming structure, and the hybrid beamforming structure, are compared. We assume that the channel is flat for narrow bandwidth. The total transmit power is normalized to unity (i.e.,  $P_0 = 1$ ) and equally allocated to each RF chain. 16 QAM and LDPC are utilized as a modulation scheme and channel coding scheme, respectively. Sphere detection is employed at the receiver side. Besides, other detailed parameters are listed in Table 6.1.

**Table 6.1:** System settings

Carrier frequency	120GHz
Frame length	576
Channel coding rate	2/3
Modulation type	16QAM
Type of antenna array	UPA
Maximum number of dominant path	4
Number of transmit antennas ( $N_t$ )	64
Number of transmit antennas ( $N_r$ )	16
Number of users	1 ~ 4
Quantization bits of RF beamforming codebook	3 ~ 7
SNR range	0 dB ~ 30 dB



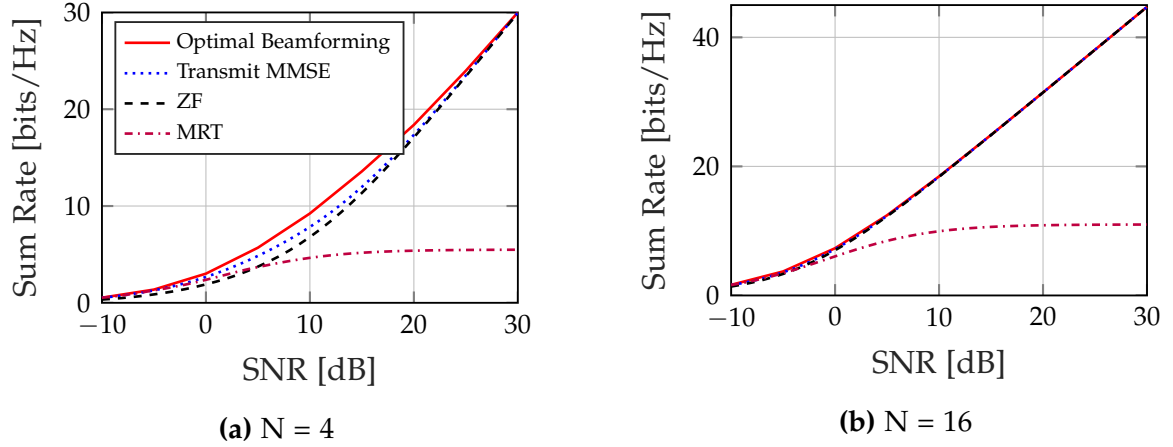


**Figure 6.6:** Spectral efficiency of different precoding design algorithms

### 6.4.1 Performance and Complexity Comparison

**Performance Comparison:** according to the asymptotic beamforming property, we discuss the optimal beamforming from two extreme cases: MRT beamforming and ZF beamforming.

In the low SNR case (i.e., represented by  $\sigma^2 \rightarrow \infty$ ), the system is noise-limited and  $\text{SINR} \approx \text{SNR}$ . MRT beamforming is the optimal beamforming, which can maximize the transmit signal power (i.e., maximizing the SNR and the system capacity). In the high SNR case (i.e., represented by  $\sigma^2 \rightarrow 0$ ), the system is interference-limited and  $\text{SINR} \approx \text{SIR}$ . ZF beamforming is the optimal beamforming that can cancel the inter-user interference (i.e., maximizing the SIR and the system capacity).

In a word, when the noise dominates over the interference, we employ MRT beamforming to maximize the signal power. On the contrary, when the interference dominates over the noise, we operate ZF beamforming to eliminate the interference. The optimal beamforming is a trade-off between noise reduction and interference elimination. Therefore, at arbitrary SNR, the optimal beamforming balance between these two extremes, MRT and ZF.

The performance of different precoding designs is shown in Fig. 6.6, that the number of transmit antennas is 4 and 16, respectively. It gives the sum rate of the system with four users as a function of the SNR. In Fig. 6.6a, the performance of MRT is better than that of ZF at the low SNR. On the contrary, ZF's performance is much better than that of MRT at the high SNR. The transmit MMSE performance is between the performance of optimal beamforming and that of ZF when there is an effective power allocation scheme in the system. Comparing Fig. 6.6a to 6.6b, the larger the number of transmit antennas, the larger the sum rate of the system. We can see that in Fig. 6.6b, the performance of ZF beamforming performance is almost the same as that of optimal beamforming, especially at the high SNR. Furthermore, the gaps among the performance of those algorithms are approaching zero at the low SNR.

**Table 6.2:** The complexity of algorithms

Algorithm		+	$\times$	SVD/ $(\cdot)^{-1}$
Single-user SVD		-	-	$\mathcal{O}(N_r N_t^2)$
<b>Analog beamforming</b>				
With perfect CSI	RF codebook based analog beamforming with fully-connected structure	$J(2^{2q-1}N_r N_t + 2^{4q-2}N_t)$	$J(2^{2q-1}N_r N_t + 2^{4q-2}N_t)$	-
	RF codebook based analog beamforming with array-of-subarray structure	$2^{2q-1}N_r N_t + 2^{4q-2}N_t$	$2^{2q-1}N_r N_t + 2^{4q-2}N_t$	-
Without CSI	Iterative analog precoding training	$2mN_r N_t$	$2mN_r N_t$	$\mathcal{O}(JN_r N_t^2)$
<b>Digital beamforming</b>				
ZF precoding		$JN_r N_t$	$JN_r N_t$	$\mathcal{O}(J^3)$
MMSE precoding		$JN_r N_t + 2(J^3 + JN_t)$	$JN_r N_t + 2(J^3 + JN_t)$	$\mathcal{O}(J^3)$

**Complexity Comparison:** the complexity of the system is one of the most critical factors in evaluating the system. Here, we calculate the number of additions and multiplications to describe system complexity.

The complexity of algorithms is shown in Table. 6.2, where  $q$  is the number of quantization-bits, and  $m$  is the iteration number when the algorithm converges. The single-user SVD algorithm's complexity is related to the number of antennas both at the transmitter and receiver.

Other algorithms consist of analog beamforming and digital beamforming. With the same antennas equipped in the system, the RF codebook-based analog beamforming complexity is mainly determined by the quantization-bits  $q$ . With a large number of antennas, high spatial resolution is necessary. Thus  $q$  increases, and the complexity of the algorithm increases exponentially. For the array-of-subarray structure, the complexity is lower than that for the fully-connected structure due to the smaller subarray antenna number. Without CSI,  $m$  is the determinant factor of the iterative power precoding training algorithm's complexity. It is related to the number of paths in the channel. The higher the path number, the larger the iteration number. In our system, the number of paths is less than 4. Therefore,  $m$  is less than 10, according to the sim-

ulation results. The RF codebook searching algorithm's complexity is much higher than that of the iterative analog beamforming training algorithm. On the contrary, the hardware complexity of the iterative analog beamforming training algorithm is higher than that of the RF codebook searching algorithm, since it needs the combination of power amplifiers and phase shifters in the RF domain to shape not only the phase of the signal but also the amplitude of the signal.

In the digital baseband processing, we use ZF precoding and MMSE precoding to reduce the noise and interference. The complexity of the ZF algorithm is lower than that of the MMSE algorithm. The number of antennas and users influences the complexity of ZF precoding. In contrast, for MMSE precoding, it is independent of the number of receive antennas since the algorithm's principle is to use the duality of the MMSE algorithm at the receiver, and there is no digital baseband processing at the receiver in our system.

### 6.4.2 Performance Analysis

**Convergence Speed:** according to the algorithm in Section 6.3.4, the analog beamforming design can be achieved without CSI. Fig. 6.7 illustrates the convergence speed of this algorithm. Usually, the iteration number in this algorithm is less than 10. The path number influences the convergence speed. The larger the path number, the slower the convergence speed.

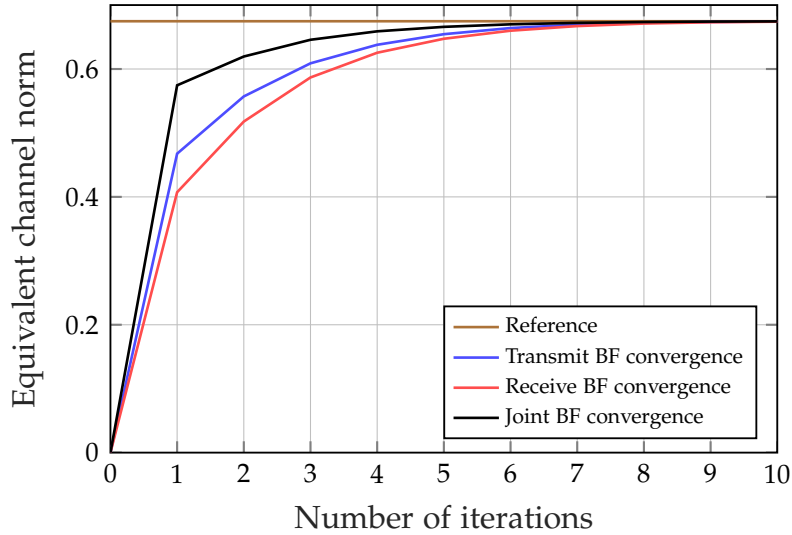
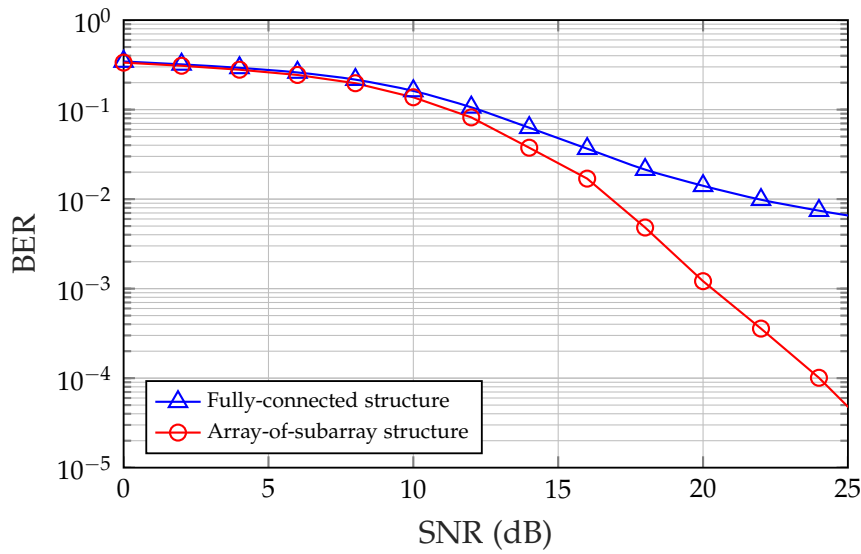
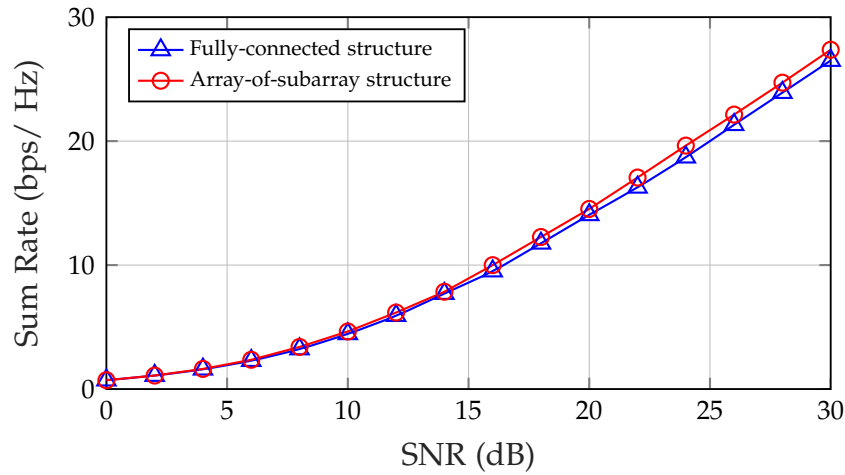


**Figure 6.7:** The convergence speed comparison of the equivalent channel norm

**System Structures:** Fig. 6.8 provides the achievable sum rate and BER performance of two different system structures. Here, we consider ZF precoder at the digital baseband and RF codebook based algorithm at the analog part. The performance of the array-of-subarray structure is better than that of the fully-connected structure. For the array-of-subarray structure, the channels of different subarrays are independent. Besides, for the fully-connected structure, the correlation of the channel matrix



(a) BER Performance



(b) Sum rate

**Figure 6.8:** Performance comparison of two different system structures

elements is much higher than that for the array-of-subarray structure since there are many zero-elements in the channel matrix for the array-of-subarray structure. In the following, the trend of the results for the two structures is the same. Hence, we only show the numerical results for the array-of-subarray structure.

The influence of the number of users on the system performance (i.e., the achievable sum rate and BER performance), is illustrated in Fig. 6.9. As the number of users increases, both the sum-rate of the system and the inter-user interference increase. The more the users, the larger the throughput of the system, the worse the quality of service.

The influence of the number of codebook quantization bits on the system performance (i.e., the achievable sum rate and BER performance) is depicted in Fig. 6.10. Here,

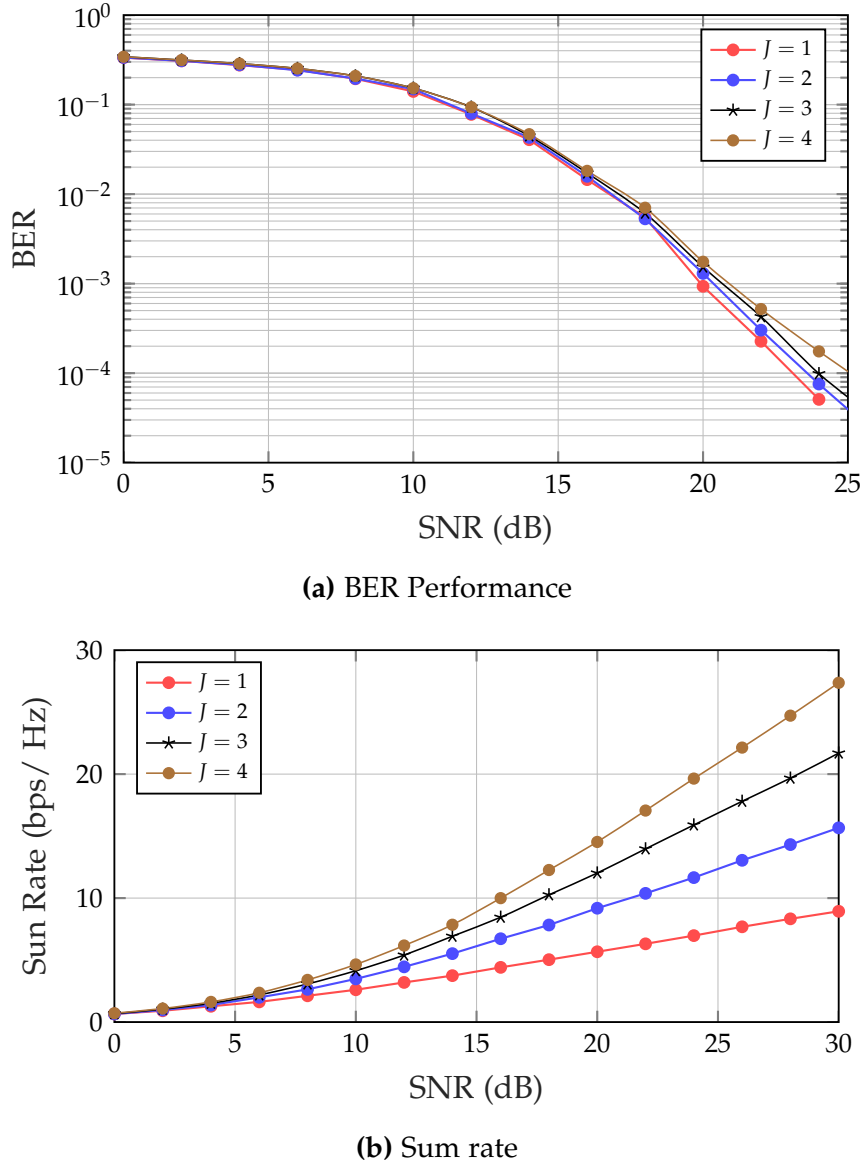
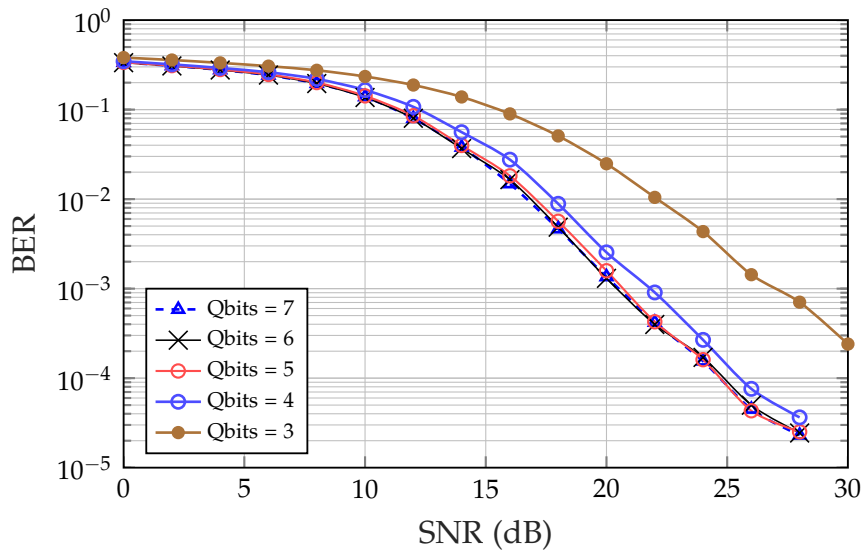


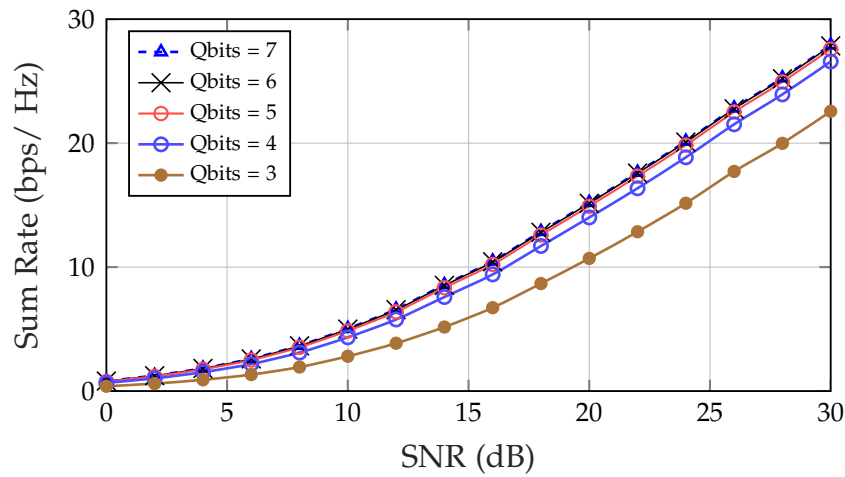
**Figure 6.9:** The influence of the number of users on the system performance: sum rate and BER performance.

we mainly consider the low complexity analog beamforming based on the RF codebook based searching algorithm. As the number of quantization-bits decreases, the system's sum-rate decreases, and the BER performance is worse. When the number of quantization-bits drops, the decreasing spatial resolution leads to a larger estimation error of the AOA/AOD. Thus, the performance of the system becomes worse. We can see that the number of quantization-bits cannot be less than 5. Otherwise, the performance loss grows unacceptable.

After identifying the optimal parameters (e.g., the number of quantization bits is 5), we compare the achievable sum rate and BER performance of different algorithms, as depicted in Fig. 6.11. The RF codebook based searching algorithm with an estim-



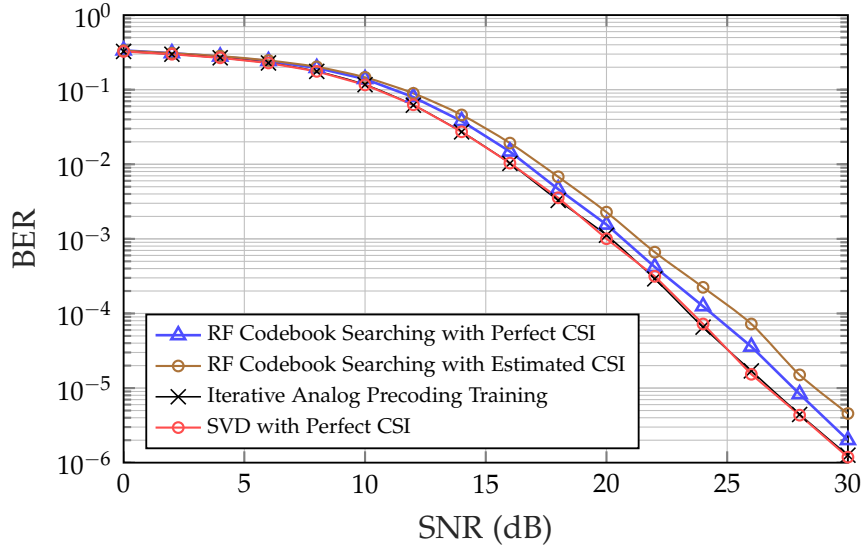
(a) BER Performance



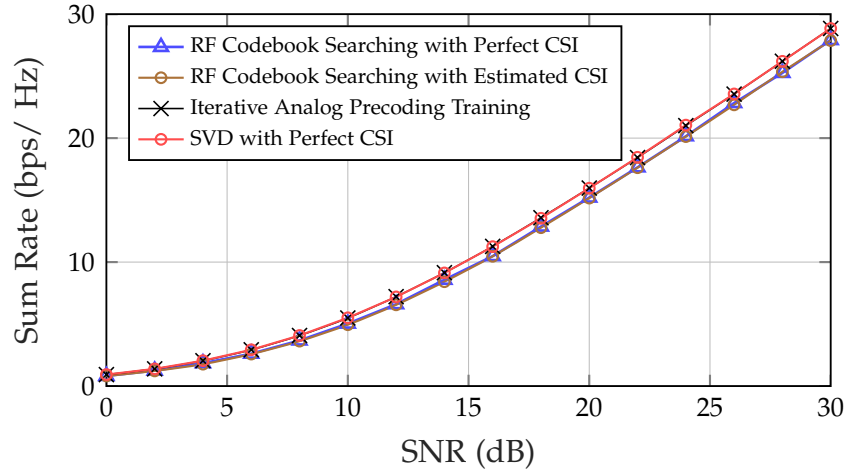
(b) Sum rate

**Figure 6.10:** The influence of the number of codebook quantization bits on the system performance (Array-of-subarray structure): sum rate and BER performance.

ated CSI based on the adaptive compressed sensing (CS) channel estimation algorithm is validated, and its control group is with perfect CSI. Except that, we show the performance of the iterative analog precoding training algorithm in Fig. 6.11, and its control group is to do SVD directly with perfect CSI. For the former, the achievable sum-rate almost has no performance gap. However, the system's BER performance with estimated CSI gets worse due to the estimation error. For the latter, the system performance is almost the same since there is only one RF chain at the receiver so that only the most robust mode is needed, and we can see that the algorithm is feasible for the system.



(a) BER Performance



(b) Sum rate

**Figure 6.11:** The performance comparison of different algorithms with the array-of-subarray structure

## 6.5 Summary

This chapter has first studied the channel characteristics and channel models at 120 GHz published in the literature. We have considered the indoor scenario due to the high propagation attenuation. Compared to 60 GHz, the shorter wavelength of 120 GHz allows more antennas employed, and larger bandwidth used in the system. Based on literature research, we have employed the ray-tracing method to generate the channel model. Moreover, the planar antenna array has been used instead of the linear antenna array. It lays the foundation for the investigations in the following algorithms.

After comparing different system architectures, a multi-user low RF complexity hybrid beamforming MIMO system at 120 GHz has been applied in our work, with two structures: fully-connected structure and array-of-subarray structure. The simulation results have shown that the system's performance with the array-of-subarray structure is better than that with the fully-connected structure. The array-of-subarray structure is more straightforward and more practical in 3G and 4G LTE systems.

Several algorithms have been proposed to maximize the capacity of such a system. The design of the digital baseband processing includes ZF precoding and MMSE precoding. Considering a multi-user system, we have used the ZF algorithm to cancel the inter-user interference. Moreover, the simulation results have also demonstrated that the ZF precoding algorithm's performance is slightly better. The analog beamforming design is based on the RF codebook searching, with low complexity in the RF domain. Besides, the iterative power precoding algorithm without CSI has been evaluated by the simulation. Its performance seems better since the complexity of the hardware is much higher. Furthermore, we have explored the influence of some parameters on the system performance, such as the number of antennas, the number of users, and quantization-bits.

**Outlook** This chapter has simplified the channel as a flat-fading channel, which is different from the practical case. At the transmitter, the equal power allocation has been exploited in this system considering the low complexity but sacrificing the performance. Furthermore, until now, there are very few applications for the 120 GHz frequency band in wireless communications, and it is more complicated to apply the system to the practice. Thus, a large amount of work needs to be done in the future.



## Chapter 7

# Conclusion and Outlook

---

### 7.1 Summary and Contributions

The focus of our research is on communication system architectures for data rates of 100 Gb/s and beyond under a processing energy constraint. As a scenario in LP100, short-range wireless transmitters working at carrier frequencies around 60 GHz and bandwidths between 1 GHz and 10 GHz are initially assumed.

As the start of our work, we have presented an introduction to 60 GHz technology, which started with the worldwide regulatory and frequency allocation of the 60 GHz band in Chapter 2. The direct comparisons between typical 60 GHz system and other Gigabits systems such as UWB and IEEE 802.11n technologies have been shown in terms of the transmit power, bandwidth, and spectrum efficiency. The large bandwidth simplifies the design of the systems that deliver a multi-Gigabytes transmission with much lower spectral efficiency. This makes it an ideal candidate for ultra-high data rate (e.g., 100 Gbps and beyond) transmission systems with strict power limitation. Next, various standardization efforts for the 60 GHz band already developed by multiple international standards groups and industry alliances have been discussed, and a comparison of their physical layer features has been provided. After that, we have presented an overview of 60 GHz channel modeling, which lays the foundation of the investigation of 60 GHz based wireless communications system design in the following chapters. In particular, the PL and shadowing effects impose huge losses on the communication link at the mmWave band. Take the path loss for an example, in the residential environment (NLOS case) in the IEEE 802.15.3c channel model for example, at a distance of 10 m, a total of 110.4 dB loss is incurred. Such high PLs need to be compensated to achieve ultra-high data rate transmission. By employing beamforming technology, it can provide significant directivity gain over the space of interest at one end of the link, if a large scale antennas array is employed. Therefore, beamforming technology is very critical to the 60 GHz communications design shown in Chapter 3. Finally, a few examples of the different channel models proposed by IEEE 802.15.3c have been given (see Appendix A.1 for more details) for Residential, Office, Desktop, and Library environments, respectively, which will be used in this thesis for the numerical simulations in the following chapters. All the channel model parameters are extracted from measurement data over a specific specified range of distance and around a particular frequency range.

In Chapter 3, a novel transmission scheme, namely hybrid beamforming with TDC, has been developed. We have proposed the TDC technology to mitigate the severe frequency selectivity effects at the 60 GHz band. The simulation results in-

indicate that the approximate flat fading channel obtained by TDC has advantages for both the ergodic and outage capacity. Even just one-tap MMSE equalizer employed at the user side can achieve comparable BER performance to the flattened fading case when the sample duration is equal to or less than the symbol rate, which is not a challenge for hardware implementation at 60 GHz. This performance evaluation supports our proposal that TDC makes the channel flat, reduces the receiver complexity, and improves the system performance. Meanwhile, in order to achieve a flat fading channel, the best possible beam separation is necessary. A SIR constrained capacity maximization algorithm has been proposed, devoted to a joint design of the precoder and combiner, which is implemented with a two-fold aim of flattening the channel and maximizing the capacity. Numerical results to evaluate the performance of the proposed system, i.e., hybrid beamforming with TDC, have also been presented in terms of the FER and information rate.

In Chapter 4, we have mainly focused on performance analysis on the hybrid beamforming approach proposed in Chapter 3, such as MIMO pre-/post-processing, channel estimation, and equalization for such large scale MIMO systems. To obtain the maximum information rate, we have proposed a joint design of digital baseband pre- and post-processing based on a weighted minimum mean square error (MMSE) criterion on the transmit power constraint. Further, the optimization in the RF domain has been specified into three criteria by taking various error weights into account. For ease of hardware implementation, we also have developed a transceiver with lower complexity where pre-processing in the RF domain after upconversion is implemented merely using analog phase shifters. While employing such large antenna arrays, it becomes challenging to estimate the mmWave channel using conventional algorithms. Hence, we have proposed two novel multi-resolution mmWave channel estimation algorithms that exploit two dimensional discrete Fourier transform (DFT) technique inspired by the sparse nature of the mmWave channel. The proposed algorithms take into account practical radio frequency (RF) hardware limitations and computational complexity reduction during the training phases. Except that, we have proposed two frequency selective hybrid precoding solutions, namely time delay compensation (TDC) based time-domain equalization (TDE) and phase shift compensation (PSC) based frequency domain equalization (FDE). Numerical simulations validate the performance of the proposed algorithms with quantized precoding and combining.

As power consumption at the user side is a crucial factor for power-hungry devices, a power consumption model for the receiver side has been first formulated in Chapter 5. The total average power consumption along the signal path can be divided into two main components: the power consumption of all the circuit blocks in the analog part and the power consumption of baseband combiner. The RF chain consists of the filter, the low noise amplifier (LNA), the phase shifter, the phase-locked loop, the mixer, and the ADC, where each of these components is scaled with different system parameters (such as the number of receiver antennas and the number of RF chains). We also have investigated the total number of operations at the digital baseband, which scales with the power consumption of the adders and multipliers. Thus, a total power expenditure at the receiver side for our system model has been presented. We then have

formulated the EE with respect to our considered hybrid analog/digital beamforming structure, and we have optimized it over different parameters. 1) Optimization over the number of receive antennas was the only case that we could find a closed-form solution. We showed that the optimal value is presented by the Lambert W function, and the objective function is a quasi-concave function that, with increasing the number of receiver antennas more than the optimal value, EE decreases and vice versa. 2) The optimization problem for the number of transmit antennas is not a linear function and cannot be formulated as a closed-form solution. However, simulation results show that with increasing the number of transmit antennas, EE improves monotonically; thus, the maximum available number of transmit antennas provides the best results. However, when we consider the proper access point (AP) design, power consumption, and system complexity, more than 64 transmit antennas are not recommended. 3) For the number of RF chains as another optimization parameter, we concluded that this value is dynamic and with respect to the SIR ratio and the number of available transmit antennas. 4) For the case of the number of data streams as a design factor, we know that  $1 \leq N_s \leq 3$ ; thus, optimization is an unrelated case for it. Here, We have mainly focused on the methodology of EE/SE analysis to guide the practical EE/SE trade-off for the LSAS design.

As proof of concept for the methodology and because of its high relevance, the proposed approach has been applied towards systems operating beyond the 100 GHz carrier frequency range. In Chapter 6, the impact of an extension to 120 GHz carrier frequency ranges and an extension from the point-to-point MIMO transmission to multi-user case has been addressed. This chapter has first studied the channel characteristics and channel models at 120 GHz published in the literature. Based on literature research, we have employed the ray-tracing method to generate the channel model. Moreover, the planar antenna array has been used instead of the linear antenna array. It lays the foundation for the investigations in the following algorithms. After comparing different system architectures, a multi-user low RF complexity hybrid beamforming MIMO system at 120 GHz has been applied with two structures: fully-connected structure and array-of-subarray structure. The simulation results have shown that the system's performance with the array-of-subarray structure is better than that with the fully-connected structure. The array-of-subarray structure is more straightforward and more practical in 3G and 4G LTE systems. Several algorithms have been proposed to maximize the capacity of such a system. The design of the digital baseband processing includes ZF precoding and MMSE precoding. Considering a multi-user system, we have used the ZF algorithm to cancel the inter-user interference. Moreover, the simulation results have also demonstrated that the ZF precoding algorithm's performance is slightly better. The analog beamforming design is based on the RF codebook searching, with low complexity in the RF domain. Besides, the iterative power precoding algorithm without CSI has been evaluated by the simulation. Its performance seems better since the complexity of the hardware is much higher. Furthermore, we have explored the influence of some parameters on the system performance, such as the number of antennas, the number of users, and quantization-bits.

## 7.2 Outlook

Within this dissertation, we have performed the critical concepts for transceivers operating at 60 GHz in bandwidth between 1-10 GHz, which are optimized for maximum information bit rates under transmit and processing power constraints (i.e., 10-100pJ / information bit). Due to technical difficulties, the proposed system has some trade-offs and requires extra effort in practice. Therefore, we consider the following important challenges remaining for future work.

**Compensation and robust design for PHY hardware imperfection:** The fulfillment of data throughput in the Gbps range comes at the price not only of bandwidth and promising technology at mmWave band, but also with high accuracy in the carrier modulated signal processing. However, the PHY hardware imperfection includes oscillator phase noise, high IQ phase and amplitude imbalance (I/Q mismatch), power amplifier nonlinearity, and quantization noise in data converters (DAC/ADC) and so on unfortunately exists. For example, the ADC sampling rate has already been a bottleneck for Gbps 60 GHz wireless systems, which is more challenging to achieve even higher data rates. As we know, calibration schemes and compensation algorithms can partially mitigate these imperfections. It is essential to take RF imperfection into account in the 60 GHz (or higher) system design and establish their behavioral models, proposing simple and efficient compensation algorithms to evaluate system performance on link-level without computationally complex circuit-level simulations.

# Acronyms

---

## Acronyms

ABF	analog beamforming
ADC	analog-to-digital converter
AoA	angle of arrival
AoD	angle of departure
AP	access point
AS	antenna selection
AWGN	additive white Gaussian noise
BB	baseband
BER	bit error rate
BF	beamforming
CDF	cumulative distribution functions
CMOS	complementary metal-oxide-semiconductor
CSI	channel state information
DAC	digital-to-analog converter
DBF	digital beamforming
ED	eigenvalue decomposition
EE	energy efficiency
EGC	equal gain combining
EGT	equal gain transmission
i.i.d.	independent and identically distributed
IBI	inter block interference
LOS	line-of-sight
LSAS	large scale antenna system
MAP	maximum a-posteriori
MIMO	multi-input and multi-output
MIR	maximum information rate
MMSE	minimum mean square error
mmWave	millimeter wave
NLOS	non-line-of-sight

---

OFDM	orthogonal frequency-division multiplexing
PAPR	peak-to-average power ratio
PL	path loss
PoE	probability of error
QAM	quadrature amplitude modulation
RAF	RF array factor
RF	radio frequency
RMS	root mean square
S-V model	Saleh-Valenzuela channel model
SC-FDE	single carrier with frequency domain equalization
SE	spectrum efficiency
SIR	signal-to-interference ratio
SNR	signal-to-noise ratio
SSP	spatial signal processing
SVD	singular value decomposition
TDC	time delay compensation
TDD	time division duplex
ULA	uniform linear array
VGA	variable gain amplifier
VPS	variable phase shifter
WLAN	wireless local area networks
WPAN	wireless personal area networks
ZP	zero padded

# Bibliography

---

- [1] "802.15.3 - 2016 - IEEE standard for high data rate wireless multi-media networks," *IEEE Std 802.15.3-2016*.
- [2] Airplay homepage. <https://www.apple.com/de/airplay/>. 2020.
- [3] DLNA guidelines. <https://spirespark.com/dlna/guidelines>.
- [4] High rate 60 GHz PHY, MAC and HDMI PAL. <https://www.ecma-international.org/activities/index.html>.
- [5] "Millimeter-wave data transmission equipment for specified low power radio station (ultra high speed wireless LAN system, november," *ARIB STD-T74 (2005)*.
- [6] "Millimeter-wave video transmission equipment for specified low power radio station," *ARIB STD-T69 (2005)*.
- [7] WiGig alliance. <http://wirelessgigabitalliance.org>.
- [8] Wireless high-definition (wirelessHD). <http://www.wirelesshd.org/>.
- [9] "IEEE standard for information technology–telecommunications and information exchange between systems–local and metropolitan area networks–specific requirements–part 11: Wireless LAN medium access control (MAC) and physical layer (PHY) specifications Amendment 3: Enhancements for very high throughput in the 60 GHz band," *IEEE Std 802.11ad-2012 (Amendment to IEEE Std 802.11-2012, as amended by IEEE Std 802.11ae-2012 and IEEE Std 802.11aa-2012)*, pp. 1–628, 2012.
- [10] "Cisco visual networking index: Global mobile data traffic forecast update, 2015–2020," Tech. Rep., February 3, 2016.
- [11] A. Adhikary, E. Al Safadi, M. K. Samimi, R. Wang, G. Caire, T. S. Rappaport, and A. F. Molisch, "Joint spatial division and multiplexing for mm-Wave channels," *IEEE J. on Select. Areas in Commun.*, vol. 32, no. 6, pp. 1239–1255, 2014.
- [12] I. F. Akyildiz and J. M. Jornet, "The internet of nano-things," *IEEE Wireless Commun.*, vol. 17, no. 6, 2010.
- [13] A. Alkhateeb, O. E. Ayach, G. Leus, and R. W. Heath, "Single-sided adaptive estimation of multi-path millimeter wave channels," in *Signal Process. Advances in Wireless Commun. (SPAWC), 2014 IEEE 15th Int. Workshop on*, June 2014, pp. 125–129.
- [14] A. Alkhateeb, O. El Ayach, G. Leus, and R. Heath, "Channel estimation and hybrid precoding for millimeter wave cellular systems," *Select. Topics in Signal Process., IEEE J. of*, vol. 8, no. 5, pp. 831–846, Oct 2014.

- [15] A. Alkhateeb and R. W. Heath, "Frequency selective hybrid precoding for limited feedback millimeter wave systems," *IEEE Trans. on Commun.*, vol. 64, no. 5, pp. 1801–1818, 2016.
- [16] A. Alkhateeb, J. Mo, N. Gonzalez-Prelcic, and R. W. Heath, "MIMO precoding and combining solutions for millimeter-wave systems," *IEEE Commun. Mag.*, vol. 52, no. 12, pp. 122–131, December 2014.
- [17] A. Alkhateeb, G. Leus, and R. W. Heath, "Limited feedback hybrid precoding for multi-user millimeter wave systems," *IEEE trans. on wireless commun.*, vol. 14, no. 11, pp. 6481–6494, 2015.
- [18] O. E. Ayach, R. W. Heath, S. Abu-Surra, S. Rajagopal, and Z. Pi, "Low complexity precoding for large millimeter wave MIMO systems," in *2012 IEEE Int. Conference on Commun. (ICC)*, 2012, pp. 3724–3729.
- [19] T. Bai, A. Alkhateeb, and R. W. Heath, "Coverage and capacity of millimeter-wave cellular networks," *IEEE Commun. Mag.*, vol. 52, no. 9, pp. 70–77, 2014.
- [20] C. A. Balanis, *Antenna theory: analysis and design*. John Wiley & Sons, 2016.
- [21] M. Bengtsson and B. Ottersten, "Handbook of antennas in wireless communications," *Optimal and Suboptimal Transmit Beamforming: Boca Raton, FL: CRC*, 2001.
- [22] S. Birke, W. Chen, G. Wang, D. Auras, C. Shen, R. Leupers, and G. Ascheid, "VLSI implementation of channel estimation for millimeter wave beamforming training," in *2018 IEEE 9th Latin American Symp. on Circuits Syst. (LASCAS)*, 2018, pp. 1–4.
- [23] E. Björnson, M. Bengtsson, and B. Ottersten, "Optimal multiuser transmit beamforming: A difficult problem with a simple solution structure [lecture notes]," *IEEE Signal Process. Mag.*, vol. 31, no. 4, pp. 142–148, 2014.
- [24] H. Bolcskei, D. Gesbert, and A. J. Paulraj, "On the capacity of OFDM-based spatial multiplexing systems," *IEEE Trans. on Commun.*, vol. 50, no. 2, pp. 225–234, 2002.
- [25] S. Boyd and L. Vandenberghe, *Convex Optimization*. Cambridge University Press, 2004.
- [26] S.-K. Chia-Chin Chong, "Generalization and parameterization of the mmWave channel models," 2005.
- [27] C.-C. Chong, C.-M. Tan, D. I. Laurenson, S. McLaughlin, M. A. Beach, and A. R. Nix, "A new statistical wideband spatio-temporal channel model for 5-GHz band WLAN systems," *Select. Areas in Commun., IEEE Journal on*, vol. 21, no. 2, pp. 139–150, 2003.
- [28] S. S. Christensen, R. Agarwal, E. de Carvalho, and J. M. Cioffi, "Weighted sum-rate maximization using weighted MMSE for MIMO-BC beamforming design," in *2009 IEEE Int. Conference on Commun.*, 2009, pp. 1–6.
- [29] E. Cohen, S. Ravid, and D. Ritter, "An ultra low power LNA with 15dB gain and 4.4 dB NF in 90nm CMOS process for 60 GHz phase array radio," in *Radio Frequency Integrated Circuits Symp., 2008. RFIC 2008. IEEE*. IEEE, 2008, pp. 61–64.
- [30] A. Coskun and C. Candan, "Transmit precoding for flat-fading mimo multiuser systems with maximum ratio combining receivers," *IEEE Trans. on Veh. Technology*, vol. 60, no. 2, pp. 710–716, 2011.



- [31] N. Cui, "Design of low RF complexity millimeter wave beamspace MIMO system at 120 GHz," Master's thesis, RWTH Aachen University, Aachen, Germany, June, 2017.
- [32] S. Cui, A. J. Goldsmith, and A. Bahai, "Energy-constrained modulation optimization," *IEEE Trans. Wireless Commun.*, vol. 4, no. 5, pp. 2349–2360, Sept 2005.
- [33] C. H. Doan, S. Emami, D. A. Sobel, A. M. Niknejad, and R. W. Brodersen, "Design considerations for 60 GHz CMOS radios," *IEEE Commun. Mag.*, vol. 42, no. 12, pp. 132–140, 2004.
- [34] O. El Ayach, S. Rajagopal, S. Abu-Surra, Z. Pi, and R. W. Heath, "Spatially sparse precoding in millimeter wave MIMO systems," *IEEE Trans. on Wireless Commun.*, vol. 13, no. 3, pp. 1499–1513, 2014.
- [35] S. Emami, R. F. Wiser, E. Ali, M. G. Forbes, M. Q. Gordon, X. Guan, S. Lo, P. T. McElwee, J. Parker, J. R. Tani *et al.*, "A 60GHz CMOS phased-array transceiver pair for multi-Gb/s wireless communications," in *Solid-State Circuits Conference Digest of Technical Papers (IS-SCC), 2011 IEEE International*. IEEE, 2011, pp. 164–166.
- [36] K. Fan, "On a theorem of weyl concerning eigenvalues of linear transformations i," *Proc. of the Nat. Academy of Sci. of the United States of America*, vol. 35, no. 11, p. 652, 1949.
- [37] X. Gao, L. Dai, S. Han, I. Chih-Lin, and R. W. Heath, "Energy-efficient hybrid analog and digital precoding for mmwave mimo systems with large antenna arrays," *IEEE J. on Select. Areas in Commun.*, vol. 34, no. 4, pp. 998–1009, 2016.
- [38] M. Ghaddar, L. Talbi, and G. Delisle, "Coherence bandwidth measurement in indoor broadband propagation channel at unlicensed 60 GHz band," *Electron. Lett.*, vol. 48, no. 13, pp. 795 – 797, 2012.
- [39] C. Han, A. O. Bicen, and I. F. Akyildiz, "Multi-ray channel modeling and wideband characterization for wireless communications in the terahertz band," *IEEE Trans. on Wireless Commun.*, vol. 14, no. 5, pp. 2402–2412, 2015.
- [40] S. Han, I. Chih-Lin, Z. Xu, and C. Rowell, "Large-scale antenna systems with hybrid analog and digital beamforming for millimeter wave 5G," *IEEE Commun. Mag.*, vol. 53, no. 1, pp. 186–194, 2015.
- [41] S. Han, C. Lin, C. Rowell, Z. Xu, S. Wang, Z. Pan *et al.*, "Large scale antenna system with hybrid digital and analog beamforming structure," in *Commun. Workshops (ICC), 2014 IEEE Int. Conference on*. IEEE, 2014, pp. 842–847.
- [42] A. Hirata, T. Kosugi, H. Takahashi, R. Yamaguchi, F. Nakajima, T. Furuta, H. Ito, H. Sugahara, Y. Sato, and T. Nagatsuma, "120-GHz-band millimeter-wave photonic wireless link for 10-Gb/s data transmission," *IEEE trans. on microw. theory and tech.*, vol. 54, no. 5, pp. 1937–1944, 2006.
- [43] S. Hur, T. Kim, D. J. Love, J. V. Krogmeier, T. A. Thomas, and A. Ghosh, "Millimeter wave beamforming for wireless backhaul and access in small cell networks," *IEEE Trans. Commun.*, vol. 61, no. 10, pp. 4391–4403, October 2013.
- [44] IEEE-802.15-WPAN, "Terahertz interest group (igthz)," <http://www.ieee802.org/15/pub/IGthzOLD.html>, 2014.

- [45] M. Jacob, S. Priebe, T. Kurner, C. Jastrow, T. Kleine-Ostmann, and T. Schrader, "An overview of ongoing activities in the field of channel modeling, spectrum allocation and standardization for mm-Wave and Thz indoor communications," in *GLOBECOM Workshops, 2009 IEEE*. IEEE, 2009, pp. 1–6.
- [46] J. M. Jornet and I. F. Akyildiz, "Channel modeling and capacity analysis for electromagnetic wireless nanonetworks in the terahertz band," *IEEE Trans. on Wireless Commun.*, vol. 10, no. 10, pp. 3211–3221, 2011.
- [47] J. Kokkonen, J. Lehtomäki, K. Umebayashi, and M. Juntti, "Frequency and time domain channel models for nanonetworks in terahertz band," *IEEE Trans. on Antennas and Propag.*, vol. 63, no. 2, pp. 678–691, 2015.
- [48] L. Kong, "Energy-efficient 60GHz phased-array design for multi-Gb/s communication systems," Ph.D. dissertation, EECS Department, University of California, Berkeley, Dec 2014.
- [49] E. Laskin, M. Khanpour, S. T. Nicolson, A. Tomkins, P. Garcia, A. Cathelin, D. Belot, and S. P. Voinigescu, "Nanoscale cmos transceiver design in the 90–170-GHz range," *IEEE Trans. on Microw. Theory and Tech.*, vol. 57, no. 12, pp. 3477–3490, 2009.
- [50] E. Lauwers and G. Gielen, "ACTIF: a high-level power estimation tool for analog continuous-time filters," in *Proc. of IEEE Int. Conf. Compu. Aided Design*, Nov 2000, pp. 193–196.
- [51] B. Li, Z. Zhou, W. Zou, X. Sun, and G. Du, "On the efficient beam-forming training for 60 GHz wireless personal area networks," *IEEE Trans. Wireless Commun.*, vol. 12, no. 2, pp. 504–515, February 2013.
- [52] Y. Liang, "Ergodic and outage capacity of narrowband MIMO gaussian channels," 01 2005.
- [53] C. Lin and G. Y. Li, "Indoor terahertz communications: How many antenna arrays are needed?" *IEEE Trans. on Wireless Commun.*, vol. 14, no. 6, pp. 3097–3107, 2015.
- [54] C. Lin and G. Y. Li, "Energy-efficient design of indoor mmwave and sub-thz systems with antenna arrays," *IEEE Trans. on Wireless Commun.*, vol. 15, no. 7, pp. 4660–4672, 2016.
- [55] C. Liu, E. Skafidas, T. Pollock, and R. Evans, "Angle of arrival extended S-V model for the 60 GHz wireless desktop channel," *Personal, Indoor and Mobile Radio Commun., 2006 IEEE 17th Int. Symp. on*, pp. 1–6, 2006.
- [56] Y. Luechao, W. Gaojiang, G. Ascheid, L. Cang, and X. Zuocheng, "A flexible low-complexity robust THP approach for MISO downlinks with imperfect CSI," in *2015 IEEE/CIC Int. Conference on Commun. in China (ICCC)*, 2015, pp. 1–5.
- [57] H. R. M. Fiacco, M. Parks and S. R. Saunders, "Final report: Indoor propagation factors at 17 and 60 GHz," in *Tech. report and study carried out on behalf of the Radio commun. Agency, University of Surrey*. IEEE, Aug. 1998.
- [58] S. Misra, "Millimeter wave wireless communications (Rappaport, T., et al; 2014) [Book review]," *IEEE Wireless Commun.*, vol. 22, no. 5, pp. 6–7, October 2015.

- [59] A. Moldovan, M. A. Ruder, I. F. Akyildiz, and W. H. Gerstacker, "LOS and NLOS channel modeling for terahertz wireless communication with scattered rays," in *Globecom Workshops (GC Wkshps)*, 2014. IEEE, 2014, pp. 388–392.
- [60] A. Molisch and M. Win, "MIMO systems with antenna selection," *Microwave Mag., IEEE*, vol. 5, no. 1, pp. 46–56, Mar 2004.
- [61] D. H. N. Nguyen, L. B. He, and T. Le-Ngoc, "Multiuser MISO precoding for sum-rate maximization under multiple power constraints," in *2015 IEEE Wireless Commun. and Networking Conference (WCNC)*, 2015, pp. 729–734.
- [62] D. H. Nguyen, L. B. Le, and T. Le-Ngoc, "Hybrid MMSE precoding for mmWave multi-user MIMO systems," in *Commun. (ICC), 2016 IEEE Int. Conference on.* IEEE, 2016, pp. 1–6.
- [63] J. Nsenga, A. Bourdoux, and F. Horlin, "Mixed analog/digital beamforming for 60 GHz MIMO frequency selective channels," in *Commun. (ICC), 2010 IEEE Int. Conf. on.* IEEE, 2010, pp. 1–6.
- [64] C. Oestges, "Validity of the Kronecker model for MIMO correlated channels," in *Veh. Technology Conference, 2006. VTC 2006-Spring. IEEE 63rd*, vol. 6, May 2006, pp. 2818–2822.
- [65] S. Ohno, "Performance of single-carrier block transmissions over multipath fading channels with linear equalization," *IEEE Trans. on Signal Process.*, vol. 54, no. 10, pp. 3678–3687, 2006.
- [66] O. Orhan, E. Erkip, and S. Rangan, "Low power analog-to-digital conversion in millimeter wave systems: Impact of resolution and bandwidth on performance," in *2015 Informa. Theory and Applicat. Workshop (ITA)*, 2015, pp. 191–198.
- [67] S. I. M. N. Pagani, P. and W. Li, "(2006) Adaptation of the France Telecom 60 GHz channel model to the TG3c framework," April, 2006.
- [68] J.-Y. Park, Y. Wang, and T. Itoh, "A 60 GHz integrated antenna array for high-speed digital beamforming applications," in *Microwave Symp. Dig., 2003 IEEE MTT-S Int.*, vol. 3. IEEE, 2003, pp. 1677–1680.
- [69] Z. Pi and F. Khan, "An introduction to millimeter-wave mobile broadband systems," *IEEE Commun. Mag.*, vol. 49, no. 6, 2011.
- [70] R. Piesiewicz, T. Kleine-Ostmann, N. Krumbholz, D. Mittleman, M. Koch, and T. Kürner, "Terahertz characterisation of building materials," *Electronics Letters*, vol. 41, no. 18, pp. 1002–1004, 2005.
- [71] S. Priebe, M. Jacob, and T. Kürner, "AoA, AoD and ToA characteristics of scattered multipath clusters for THz indoor channel modeling," in *Wireless Conference 2011-Sustainable Wireless Technologies (European Wireless), 11th European.* VDE, 2011, pp. 1–9.
- [72] S. Priebe and T. Kurner, "Stochastic modeling of Thz indoor radio channels," *IEEE Trans. on Wireless Commun.*, vol. 12, no. 9, pp. 4445–4455, 2013.
- [73] K. Raczkowski, W. De Raedt, B. Nauwelaers, and P. Wambacq, "A wideband beamformer for a phased-array 60GHz receiver in 40nm digital CMOS," in *Solid-State Circuits Conference Dig. of Tech. Papers (ISSCC), 2010 IEEE Int.* IEEE, 2010, pp. 40–41.

- [74] Y. R. Ramadan, A. S. Ibrahim, and M. M. Khairy, "Minimum outage RF beamforming for millimeter wave MISO-OFDM systems," in *2015 IEEE Wireless Commun. and Networking Conference (WCNC)*, 2015, pp. 557–561.
- [75] R. Rana, "Study and analysis of performance of spatial multiplexing equalizer for transmit - receive diversity," *Int. J. of Emerging Trends Technology in Comput. Sci. (IJETTCS)*, vol. 3, p. 50, 03 2014.
- [76] T. S. Rappaport, S. Sun, R. Mayzus, H. Zhao, Y. Azar, K. Wang, G. N. Wong, J. K. Schulz, M. Samimi, and F. Gutierrez, "Millimeter wave mobile communications for 5G cellular: It will work!" *IEEE Access*, vol. 1, pp. 335–349, 2013.
- [77] T. Rappaport, *Wireless Communications: Principles and Practice*, 2nd ed. USA: Prentice Hall PTR, 2001.
- [78] T. S. Rappaport, R. W. Heath Jr, R. C. Daniels, and J. N. Murdock, *Millimeter wave wireless communications*. Pearson Education, 2014.
- [79] A. A. Saleh and R. Valenzuela, "A statistical model for indoor multipath propagation," *IEEE J. on select.areas in commun.*, vol. 5, no. 2, pp. 128–137, 1987.
- [80] H. Sampath, P. Stoica, and A. Paulraj, "A generalized space-time linear precoder and decoder design using the weighted MMSE criterion," in *Signals, Syst. and Comput., 2000. Conference Record of the Thirty-Fourth Asilomar Conference on*, vol. 1. IEEE, 2000, pp. 753–758.
- [81] H. Sampath, P. Stoica, and A. Paulraj, "Generalized linear precoder and decoder design for MIMO channels using the weighted MMSE criterion," *Commun., IEEE Trans. on*, vol. 49, no. 12, pp. 2198–2206, 2001.
- [82] H. Sampath, P. Stoica, and A. Paulraj, "Generalized linear precoder and decoder design for MIMO channels using the weighted MMSE criterion," *IEEE Transactions on Communications*, vol. 49, no. 12, pp. 2198–2206, 2001.
- [83] S. Sandhu and M. Ho, "Analog combining of multiple receive antennas with OFDM," in *Commun., 2003. ICC '03. IEEE Int. Conference on*, vol. 5, May 2003, pp. 3428–3432 vol.5.
- [84] I. Sarkas, E. Laskin, J. Hasch, P. Chevalier, and S. Voinigescu, "Second generation transceivers for D-band radar and data communication applications," in *Microw. Symp. Dig. (MTT), 2010 IEEE MTT-S Int.* IEEE, 2010, pp. 1328–1331.
- [85] A. Scaglione, S. Barbarossa, and G. B. Giannakis, "Filterbank transceivers optimizing information rate in block transmissions over dispersive channels," *IEEE Trans. on Inform. Theory*, vol. 45, no. 3, pp. 1019–1032, 1999.
- [86] A. Scaglione, P. Stoica, S. Barbarossa, G. B. Giannakis, and H. Sampath, "Optimal designs for space-time linear precoders and decoders," *IEEE Trans. on Signal Process.*, vol. 50, no. 5, pp. 1051–1064, 2002.
- [87] D. Seethaler, H. Artés, and F. Hlawatsch, "Detection techniques for MIMO spatial multiplexing systems," *e i Elektrotechnik und Informationstechnik*, vol. 122, pp. 91–96, 03 2005.
- [88] K. Sergii and Y. Yuriy, "Nanonetwork: Organisation of communication channels between nano-objects," in *Electronics and Nanotechnology (ELNANO), 2014 IEEE 34th Int. Conference on*. IEEE, 2014, pp. 238–241.

- [89] Y. Shang, D. Cai, W. Fei, H. Yu, and J. Ren, "An 8mW ultra low power 60 GHz direct-conversion receiver with 55dB gain and 4.9 dB noise figure in 65nm CMOS," in *Radio-Frequency Integration Technology (RFIT), 2012 IEEE Int. Symp. on.* IEEE, 2012, pp. 47–49.
- [90] S. Shi, M. Schubert, and H. Boche, "Rate optimization for multiuser MIMO systems with linear processing," *IEEE Trans. on Signal Process.*, vol. 56, no. 8, pp. 4020–4030, 2008.
- [91] A. P. Shrestha, S.-J. Yoo, H. J. Choi, and K. S. Kwak, "Enhanced rate division multiple access for electromagnetic nanonetworks," *IEEE Sensors J.*, vol. 16, no. 19, pp. 7287–7296, 2016.
- [92] P. Smulders, "The road to 100 Gb/s wireless and beyond: basic issues and key directions," *IEEE Commun. Mag.*, vol. 51, no. 12, pp. 86–91, 2013.
- [93] P. Smulders, "Broadband wireless LANs : a feasibility study," Ph.D. dissertation, Department of Electrical Engineering, 1995.
- [94] N. Song, H. Sun, and T. Yang, "Coordinated hybrid beamforming for millimeter wave multi-user massive MIMO systems," in *Global Commun. Conference (GLOBECOM), 2016 IEEE.* IEEE, 2016, pp. 1–6.
- [95] Q. H. Spencer, A. L. Swindlehurst, and M. Haardt, "Zero-forcing methods for downlink spatial multiplexing in multiuser MIMO channels," *IEEE Trans. on Signal Process.*, vol. 52, no. 2, pp. 461–471, 2004.
- [96] Q. Spencer, B. Jeffs, M. Jensen, and A. Swindlehurst, "Modeling the statistical time and angle of arrival characteristics of an indoor multipath channel," *IEEE J. Select. Areas in Commun.*, vol. 18, no. 3, pp. 347–360, 2000.
- [97] M. Steinbauer, A. F. Molisch, and E. Bonek, "The double-directional radio channel," *IEEE Antennas and Propagation Mag.*, vol. 43, no. 4, pp. 51–63, 2001.
- [98] S. Sun, T. S. Rappaport, R. W. Heath, A. Nix, and S. Rangan, "MIMO for millimeter-wave wireless communications: beamforming, spatial multiplexing, or both?" *IEEE Commun. Mag.*, vol. 52, no. 12, pp. 110–121, 2014.
- [99] A. R. Tharek and J. P. McGeehan, "Propagation and bit error rate measurements within buildings in the millimeter wave band about 60 GHz," in *8th European Conference on Electrotechnics, Conference Proc. on Area Commun.*, 1988, pp. 318–321.
- [100] A. Thornburg, T. Bai, and R. W. Heath, "Performance analysis of outdoor mmWave Ad Hoc networks," *IEEE Trans. on Signal Process.*, vol. 64, no. 15, pp. 4065–4079, 2016.
- [101] J. A. Tropp and S. J. Wright, "Computational methods for sparse solution of linear inverse problems," *Proc. of the IEEE*, vol. 98, no. 6, pp. 948–958, 2010.
- [102] J. Vía, V. Elvira, I. Santamaria, and R. Eickhoff, "Analog antenna combining for maximum capacity under OFDM transmissions," in *Commun., 2009. ICC'09. IEEE Int. Conf. on.* IEEE, 2009, pp. 1–5.
- [103] J. Vía, V. Elvira, I. Santamaria, and R. Eickhoff, "Minimum BER beamforming in the RF domain for OFDM transmissions and linear receivers," in *Acoust., Speech and Signal Process., 2009. ICASSP 2009. IEEE Int. Conf. on.* IEEE, 2009, pp. 2513–2516.

- [104] J. Wallace and M. Jensen, "Modeling the indoor MIMO wireless channel," *Antennas and Propagation, IEEE Trans. on*, vol. 50, no. 5, pp. 591–599, 2002.
- [105] G. Wang and G. Ascheid, "Hybrid beamforming under equal gain constraint for maximizing sum rate at 60 GHz," in *Proc. of IEEE Veh. Tech. Conf. (VTC Spring)*, May 2015, pp. 1–5.
- [106] G. Wang, A. Bytyn, D. Khajavi, Y. Wang, R. Negra, and G. Ascheid, "Power efficiency of millimeter wave transmission systems with large number of antennas," in *2016 IEEE 84th Vehicular Technology Conference (VTC-Fall)*, 2016, pp. 1–6.
- [107] G. Wang, P. Karanjekar, and G. Ascheid, "Beamforming with time-delay compensation for 60 GHz MIMO frequency-selective channels," in *proc. of IEEE Int. Symp. on Personal, Indoor, and Mobile Radio Commun. (PIMRC)*, Aug 2015, pp. 387–391.
- [108] G. Wang, P. Karanjekar, and G. Ascheid, "Beamforming with time-delay compensation for 60 GHz MIMO frequency-selective channels," in *Proceedings of IEEE International Symposium on Personal, Indoor, and Mobile Radio Communications (PIMRC)*, aug 2015.
- [109] G. Wang, S. A. Naeimi, and G. Ascheid, "Low complexity channel estimation based on DFT for short range communication," in *2017 IEEE Int. Conference on Commun. (ICC)*, 2017, pp. 1–7.
- [110] G. Wang, J. Sun, and G. Ascheid, "Hybrid beamforming with time delay compensation for millimeter wave MIMO frequency selective channels," in *2016 IEEE 83rd Veh. Technol. Conf. (VTC Spring)*, May 2016, pp. 1–6.
- [111] G. Wang, J. Sun, and G. Ascheid, "Low complexity equalization algorithms for frequency selective millimeter wave channel," in *2017 IEEE 28th Annu. Int. Symp. on Personal, Indoor, and Mobile Radio Commun. (PIMRC)*, 2017, pp. 1–7.
- [112] G. Wang and G. Ascheid, "Joint pre/post-processing design for large millimeter wave hybrid spatial processing systems," in *European Wireless 2014; 20th European Wireless Conference; Proc. of*, May 2014, pp. 1–6.
- [113] G. Wang, G. Ascheid, Y. Wang, O. Hanay, R. Negra, M. Herrmann, and N. Wehn, "Optimization of wireless transceivers under processing energy constraints," *Frequenz*, vol. 71, 01 2017.
- [114] J. Wang, Z. Lan, C. Sum, C. Pyo, J. Gao, T. Baykas, A. Rahman, R. Funada, F. Kojima, I. Lakkis, H. Harada, and S. Kato, "Beamforming codebook design and performance evaluation for 60GHz wideband WPANs," in *2009 IEEE 70th Veh. Technology Conference Fall*, 2009, pp. 1–6.
- [115] X. Wang, R. F. Schaefer, L. Thiele, T. Haustein, and Y. Wang, "Ergodic secrecy sum rate for multiuser MIMO downlink systems using block diagonalization," in *Commun. and Network Security (CNS), 2016 IEEE Conference on*. IEEE, 2016, pp. 636–640.
- [116] P. Xia, R. W. Heath, and N. Gonzalez-Prelcic, "Robust analog precoding designs for millimeter wave MIMO transceivers with frequency and time division duplexing," *IEEE Trans. on Commun.*, vol. 64, no. 11, pp. 4622–4634, 2016.
- [117] Xiaoli Ma, Liuqing Yang, and G. B. Giannakis, "Optimal training for MIMO frequency-selective fading channels," *IEEE Trans. on Wireless Commun.*, vol. 4, no. 2, pp. 453–466, 2005.

- [118] Q. Xie, X. Lin, Y. Wang, S. Chen, M. J. Dousti, and M. Pedram, "Performance comparisons between 7-nm FinFET and conventional bulk CMOS standard cell libraries," *IEEE Trans. Circuits Syst. II: Exp. Briefs*, vol. 62, no. 8, pp. 761–765, Aug 2015.
- [119] H. Xu, V. Kukshya, and T. S. Rappaport, "Spatial and temporal characteristics of 60 GHz indoor channels," *IEEE J. on select. areas in commun.*, vol. 20, no. 3, pp. 620–630, 2002.
- [120] J. Ye, "Generalized low rank approximations of matrices," *Machine Learning*, vol. 61, no. 1-3, pp. 167–191, 2005.
- [121] S. Yong, "TG3c channel modeling sub-committee final report," *IEEE802. 15-07-0584-00-003c*, 2007.
- [122] S.-K. Yong, P. Xia, and A. Valdes-Garcia, *60 GHz Technology for Gbps WLAN and WPAN: From Theory to Practice*, September, 2010.
- [123] S.-K. Yong, "Channel modeling sub committee final report," 2007.
- [124] S.-K. Yong, "TG3c channel modeling sub-committee final report," *IEEE 802.15-07-0584-01-003c*, vol. 2007, no. 1, 2007.
- [125] F. Zhang, E. Skafidas, W. Shieh, B. Yang, B. Wicks, and Z. Liu, "A 60-GHz double-balanced mixer for direct up-conversion transmitter on 130-nm CMOS," in *Proc. of IEEE Compound Semiconductor Integrated Circuits Symp.*, Oct 2008, pp. 1–4.
- [126] J. Zhang, Y. R. Zheng, C. Xiao, and K. B. Letaief, "Channel equalization and symbol detection for single-carrier MIMO systems in the presence of multiple carrier frequency offsets," *IEEE Trans. on Veh. Technology*, vol. 59, no. 4, pp. 2021–2030, 2010.
- [127] C. Zhen and C. Jun-Cheng, "Channel characterization at 120 GHz for future indoor communication systems," *Chinese Physics B*, vol. 22, no. 5, p. 059201, 2013.
- [128] B. Zhou, L. Zhang, Y. Wang, and Z. Yu, "A 56-to-66 GHz quadrature phase-locked loop with a wide locking range divider chain in 65nm CMOS," in *IEEE Int. Conf. on Electron. Devices and Solid-State Circuits (EDSSC)*, June 2015, pp. 455–458.
- [129] W. Zou, Z. Cui, B. Li, Z. Zhou, and Y. Hu, "Beamforming codebook design and performance evaluation for 60GHz wireless communication," in *Commun. and Inform. Technologies (ISCIT), 2011 11th Int. Symp. on*, Oct 2011, pp. 30–35.





# Publication List

---

## Journal Publications

G. Wang, G. Ascheid, Y. Wang, et al. (2017). Optimization of Wireless Transceivers under Processing Energy Constraints. *Frequenz*, 71(9-10), pp. 379-388. Retrieved 26 Sep. 2017, from doi:10.1515/freq-2017-0150.

## Conference Publications

D. Zhang, G. Wang, G. Ascheid and H. Meyr, "Searching for optimal scheduling of MIMO doubly iterative receivers: An ant colony optimization-based method," 2012 IEEE Global Communications Conference (GLOBECOM), Anaheim, CA, USA, 2012, pp. 4658-4664.

G. Wang and G. Ascheid, "Joint Pre/Post-processing Design for Large Millimeter Wave Hybrid Spatial Processing Systems", in Proceedings of European Wireless Conference (EW) pp. 1–6, VDE , 2014, ISBN: 978-3-80073-621-8, ©2014 IEEE.

G. Wang and G. Ascheid, "Hybrid Beamforming under Equal Gain Constraint for Maximizing Sum Rate at 60 GHz", in Proceedings of IEEE Vehicular Technology Conference (VTC-Spring) (Glasgow, Scotland), May 2015.

G. Wang, P. karanjekar, and G. Ascheid, "Beamforming with Time-Delay Compensation for 60 GHz MIMO Frequency-Selective Channels", in Proceedings of IEEE International Symposium on Personal, Indoor, and Mobile Radio Communications (PIMRC) Aug. 2015.

L. Yuan, G. Wang, G. Ascheid, C. Liu, and Z. Xing, "A flexible low-complexity robust THP approach for MISO downlinks with imperfect CSI, in ICC pp. 1–5, IEEE, Nov. 2015.

G. Wang, J. Sun and G. Ascheid, "Hybrid Beamforming with Time Delay Compensation for Millimeter Wave MIMO Frequency Selective Channels," 2016 IEEE 83rd Vehicular Technology Conference (VTC Spring), Nanjing, 2016, pp. 1-6.

G. Wang, A. Bytyn, D. Khajavi, Y. Wang, R. Negra and G. Ascheid, "Power Efficiency of Millimeter Wave Transmission Systems with Large Number of Antennas," 2016 IEEE 84rd Vehicular Technology Conference (VTC Fall), Montreal, 2016, pp. 1-6.

G. Wang, S. A. Naeimi and G. Ascheid, "Low complexity channel estimation based on DFT for short range communication," 2017 IEEE International Conference on Communications (ICC), Paris, 2017, pp. 1-7.

G. Wang, J. Sun and G. Ascheid, " Low Complexity Equalization Algorithms for Frequency Selective Millimeter Wave Channel", in Proceedings of IEEE International Symposium on Personal, Indoor, and Mobile Radio Communications (PIMRC), pp. 1-7, IEEE , Oct. 2017.

S. Birke, W. Chen, G. Wang, D. Auras, C. Shen, R. Leupers, G. Ascheid, "VLSI Implementation of Channel Estimation for Millimeter Wave Beamforming Training", 9th Latin Amer. Symp. on Circuits & Syst. (LASCAS), Puerto Vallarta, Mexico, 2018, pp.1-4.

# Curriculum Vitae

---

Name	Gaojian Wang
Geburtsdatum	02.02.1988
Geburtsort	Liaocheng, China
Since 11/2020	Senior System Engineer OPPO research center, Peking
10/2012-09/2019	Research Assistant and PhD Candidate Chair for Integrated Signal Processing Systems RWTH Aachen University, Germany
09/2009-08/2012	Master of Science in Communication Engineering RWTH Aachen University, Germany
03/2012-08/2012	Internship Project: 3D Beamforming measurement Alcatel-Lucent, Stuttgart, Germany
05/2011-02/2012	Master Project Iteration Control Algorithm for Iterative MIMO-Receivers RWTH Aachen University, Germany
09/2008-08/2009	Exchange Student Communication and Information Technology Bremen University, Germany
09/2005-09/2008	Bachelor of Science Design of Integrated Circuit and Integrated System Shandong University, China

